DIAGONALLY-REINFORCED CONCRETE COUPLING BEAMS WITH HIGH-STRENGTH STEEL BARS

By
Shahedreen Ameen
Rémy D. Lequesne
Andrés Lepage

Structural Engineering and Engineering Materials
SM Report No. 138
May 2020

THE UNIVERSITY OF KANSAS CENTER FOR RESEARCH, INC.
2385 Irving Hill Road, Lawrence, Kansas 66045-7563

Diagonally-Reinforced Concrete Coupling Beams with High-Strength Steel Bars

By
Shahedreen Ameen
Rémy D. Lequesne
Andrés Lepage

Structural Engineering and Engineering Materials
SM Report No. 138
THE UNIVERSITY OF KANSAS CENTER FOR RESEARCH, INC.
LAWRENCE, KANSAS
May 2020

ABSTRACT

The use of high-strength steel in diagonally reinforced coupling beams was investigated with the aims of minimizing reinforcement congestion and increasing the maximum permissible design shear stress without compromising behavior under large displacement reversals. Five large-scale diagonally reinforced concrete coupling beam specimens with clear span-to-depth ratios of 1.9 were tested under fully reversed cyclic loads. The primary variables were yield stress of the diagonal reinforcement (60 and 120 ksi [420 and 830 MPa]), target beam shear stress (10 and $15\sqrt{f_c'}$ psi [0.83 and $1.25\sqrt{f_c'}$ MPa]), length of the secondary (non-diagonal) longitudinal reinforcement, and axial restraint. All specimens had the same nominal concrete compressive strength and beam dimensions.

Chord rotation capacities exhibited by the specimens with Grade 120 (830) reinforcement were between 5.1 and 5.6%, less than that of the control specimen with Grade 60 (420) diagonal reinforcement (7.1%). Neither development of secondary reinforcement nor increases in design shear stress affected specimen chord rotation capacity. The axially-restrained specimen with Grade 120 (830) diagonal reinforcement showed the same chord rotation capacity as a similar specimen without axial restraint, but 14% larger strength. In specimens with secondary longitudinal reinforcement extended into the wall (such that the embedment length exceeded the calculated development length), the localization of damage evident along the beam-wall interface in tests of specimens with bars terminating near the wall face was not observed. Although damage was more distributed throughout the beam span, deformation capacity was not increased. Among the specimens, it was shown that the initial stiffness, area of the shear force-chord rotation hysteresis

cycles, and residual chord rotation at zero shear force changed in inverse proportion to the diagonal bar yield stress.

A database of results from tests of diagonally reinforced coupling beams was compiled and used to evaluate the sensitivity of coupling beam chord rotation capacity to a range of variables. Variables included aspect ratio, reinforcement grade, transverse confinement reinforcement (type, spacing, and ratio), shear stress, and length of secondary (non-diagonal) reinforcement (whether terminated near the beam-wall interface or developed into the wall). An equation was proposed for calculating coupling beam chord rotation capacity as a function of beam clear span-to-height ratio and the ratio of hoop spacing to diagonal bar diameter. Chord rotation capacity was not correlated with other variables. Modifications are also proposed to the stiffness and deformation capacity modeling parameters recommended in ASCE 41-17 and ACI 369.1-17 for diagonally reinforced coupling beams to account for reinforcement grade.

ACKNOWLEDGMENTS

Primary financial support was provided by the Department of Civil, Environmental & Architectural Engineering and the School of Engineering at The University of Kansas. Partial support was provided by MMFX Technologies Corporation and Commercial Metals Company.

TABLE OF CONTENTS

LIST OF FIGURES

LIST OF TABLES

CHAPTER 1 INTRODUCTION

1.1 BACKGROUND AND MOTIVATION

Coupled structural walls are a commonly used lateral-force-resisting system in seismically active regions due to their strength and stiffness. Coupled walls consist of two or more structural walls arranged in series and linked, over the height of the structure, by a series of short coupling beams. For satisfactory performance of the system in an earthquake, coupling beams are required to sustain high shear forces throughout large displacement demands.

To achieve this behavior, coupling beams are often reinforced with diagonally oriented reinforcing bars confined with closely spaced transverse reinforcement. Such reinforcement detailing has been shown to resist both diagonal tension and sliding shear failures in highly stressed coupling beams with small aspect ratios (clear span-to-overall depth ratios less than approximately 2), resulting in excellent deformation capacity under reversals of load (Paulay and Binney, 1974). In practice, the ACI Building Code requires diagonally reinforced coupling beams to be designed such that the inclined bars resist all the shear and moment demand (ACI Building Code References are to ACI 318-14 unless otherwise noted). Closely spaced hoops are required to confine either each diagonal cage or the entire coupling-beam cross section. These hoops are necessary to maintain integrity of the concrete core and delay buckling of diagonal reinforcement. This reliance on well-confined diagonal reinforcement cages to resist the whole coupling beam shear demand often results in heavy congestion of reinforcement.

Use of high-strength steel (yield strengths up to 120 ksi, or 830 MPa) has the potential to alleviate difficulties with construction of diagonally-reinforced coupling beams by facilitating the use of fewer and smaller reinforcing bars. However, use of steel with a nominal yield strength

larger than 60 ksi (420 MPa) is not permitted in special seismic systems (ACI Building Code) due to lack of experimental data. Coupling beams are good candidates for use of high-strength steel because the concerns associated with use of high strength steel, such as compatibility between reinforcing bars and concrete under compression and control of crack widths at service-level loads, are unlikely to cause problems.

As a result of the reduced reinforcement congestion, it may be feasible to construct coupling beams with high-strength reinforcement that have design shear stresses larger than $10\sqrt{f_c'}$ [psi] ($0.83\sqrt{f_c'}$ [MPa]), the current ACI Building Code limit. For conventionally reinforced beams (with no diagonal bars), this shear stress limit prevents diagonal compression failures. Coupling beams, however, may be less susceptible to diagonal compression failures because of the diagonal bars proportioned to resist all inclined tension and compression forces. Diagonally reinforced coupling beams may, therefore, exhibit adequate deformation capacity under shear stresses larger than $10\sqrt{f_c'}$ [psi] ($0.83\sqrt{f_c'}$ [MPa]).

A concern with the use of high-strength reinforcement is that increases in yield strength are typically associated with decreases in bar strain at fracture. To maximize member deformation capacity, it may be necessary to use reinforcement detailing that limits concentration of strain demands near beam ends to encourage the spread of deformations throughout the beam span when using high-strength reinforcement. It may therefore be problematic that the ACI Building Code (318-14) commentary recommends terminating secondary (non-diagonal) longitudinal reinforcement near the intersection with the wall to limit unexpected overstrength of the member. Tests have indicated that undesirable localized damage may occur along the wall-beam interface as a result of this detail (Lequesne, Parra-Montesinos, and Wight, 2013). This localization was not

evident in recent tests of coupling beams with all reinforcement at the beam-wall interface satisfying development length requirements (Lim, Hwang, Cheng, and Lin, 2016). These tests showed that developing all beam reinforcement into the wall may lead to increased beam strength and deformation capacity. There is a need to evaluate the importance of this reinforcement detailing on the behavior of coupling beams constructed with high-strength steel.

Finally, there is a need to evaluate the effect of axial restraint on the behavior of coupling beams under earthquake-type displacement reversals. Most previously used test setups allowed free elongation of the coupling beam specimen. This is unlike typical in-situ conditions, where stiff structural walls and diaphragms provide some resistance to beam elongation. Among the few tests providing axial force or restraint were those by Tegos and Penelis (1988), who tested twenty-four diagonally reinforced columns under double curvature, twenty-one of which were axially loaded. Lequesne (2011) and Han et al. (2015) tested coupling beam specimens with restraint provided with steel links. None of these studies, however, directly evaluated the effects of restraint on behavior.

1.2 OBJECTIVES

The primary aim of this research was to investigate the use of high-strength steel as diagonal reinforcement in coupling beams. This objective was motivated by the desire to: a) minimize reinforcement congestion by reducing the amount and size of steel bars, and b) increase the maximum permissible design shear stress without compromising behavior under large displacement reversals. To accomplish this aim, the following objectives were set:

1) Quantify, in terms of strength, deformation capacity, and stiffness, how the behavior of coupling beams designed for a shear stress of $10\sqrt{f_c'}$ [psi] ($0.83\sqrt{f_c'}$ [MPa]) and

constructed with Grade 120 (830) bars differs from an ACI Building Code compliant control specimen,

2) Evaluate whether, and to what extent, the behavior of coupling beam specimens designed for a target shear stress of $15\sqrt{f_c'}$ [psi] ($1.25\sqrt{f_c'}$ [MPa]) differs from that of specimens designed for the ACI Building Code limit ($10\sqrt{f_c'}$ [psi], or $0.83\sqrt{f_c'}$ [MPa]), and
3) Determine the impact of terminating secondary beam longitudinal reinforcement near the beam-wall interface, as recommended in the ACI Building Code commentary, on diagonal reinforcing bar strain demand and member deformation capacity.

In addition to these, two complementary secondary objectives were also set:

4) Quantify the effects of axial restraint on coupling beam behavior, again in terms of strength, deformation capacity, and stiffness, and
5) Propose beam deformation capacity limits that account for beam aspect ratio and reinforcement grade for use in non-linear simulation of coupled-wall systems.

1.3 APPROACH

To address Objectives 1 through 4, five large-scale tests of diagonally-reinforced coupling beam specimens (Table 1.1) were conducted. The approximately ½-scale specimens, which had an aspect ratio (clear span-to-overall depth) of 1.9, were tested under fully reversed cyclic loading to simulate earthquake-type demands.

Table 1.1 – Summary of coupling beam specimens (1 ksi = 6.89 MPa, 1 psi = 0.00689 MPa, 1 in. = 25.4 mm)

ID	Diagonal Bar Nominal Yield Stress ksi	Transverse and Longitudinal Bar Nominal Yield Stress ksi	Target Nominal Shear Strength[a] psi	Diagonal Bars[b]	Longitudinal Bars	Transverse Bars	Axially Restrained
CB1	60	60	$10\sqrt{f_c'}A_{cw}$	12#7	8#3[c]	#3@3 in.	No
CB2	120	60	$10\sqrt{f_c'}A_{cw}$	8#6	8#3[c]	#3@3 in.	No
CB2D	120	60	$10\sqrt{f_c'}A_{cw}$	8#6	8#3[d] developed	#3@3 in.	No
CB2AD	120	60	$10\sqrt{f_c'}A_{cw}$	8#6	8#3[d] developed	#3@3 in.	Yes
CB3D	120	60	$15\sqrt{f_c'}A_{cw}$	12#6	8#3[d] developed	#3@3 in.	No

[a] Based on ACI 318-14 Eq. 18.10.7.4 using specified material properties; A_{cw} is the cross-sectional area of the coupling beam.
[b] Includes all bars from both diagonal groups.
[c] Cutoff 2 in. (50 mm) into the wall from the beam-wall interface, consistent with ACI commentary.
[d] Developed into wall per ACI 318-14 Eq. 25.4.2.3a.

The specimens (Table 1.1) included a control specimen compliant with ACI Building Code requirements that used conventional Grade 60 (420) steel as diagonal reinforcement. The other four specimens were constructed with Grade 120 (830) steel as diagonal reinforcement. These specimens were designed for target shear stresses of either $10\sqrt{f_c'}$ [psi] ($0.83\sqrt{f_c'}$ [MPa]), the upper limit permitted by the ACI Building Code, or $15\sqrt{f_c'}$ [psi] ($1.25\sqrt{f_c'}$ [MPa]). Two different reinforcement details were used at the beam-wall interface: either all secondary longitudinal beam reinforcement was cutoff 2 in. (50 mm) into the wall from the beam-wall interface or it was extended into the walls a length equal to the development length. To study the effects of axial restraint, one of the specimens with high-strength steel was tested in parallel with stiff longitudinally-oriented links designed to provide axial restraint. Other specimens were free to elongate.

To address Objective 5, a database was compiled of results from tests of diagonally reinforced coupling beams. Using this database and experimental results reported herein, the sensitivity of coupling beam deformation capacity to several parameters was evaluated. Modifications to ASCE 41-17 and ACI 369.1-17 modeling parameters for diagonally reinforced coupling beams, including stiffness and deformation capacity, are proposed to account for reinforcement grade.

CHAPTER 2 LITERATURE REVIEW

2.1 COUPLING BEAMS

Under earthquake-type or other lateral loading, the deformation of coupled walls causes a differential movement between the supported ends of the coupling beams (Figure 2.1). The chord rotation demand imposed on coupling beams, calculated as the differential movement divided by the length of the beam, is often significantly larger than the global drift demand due to the geometry of the system. A key requirement for attaining the desired behavior from a coupled wall system is therefore the deformation capacity of its coupling beams. Coupling beams also need to maintain adequate strength and stiffness under large flexural and shear deformations in order to spread inelastic deformations over the height of the system and sustain wall coupling throughout the imposed loading.

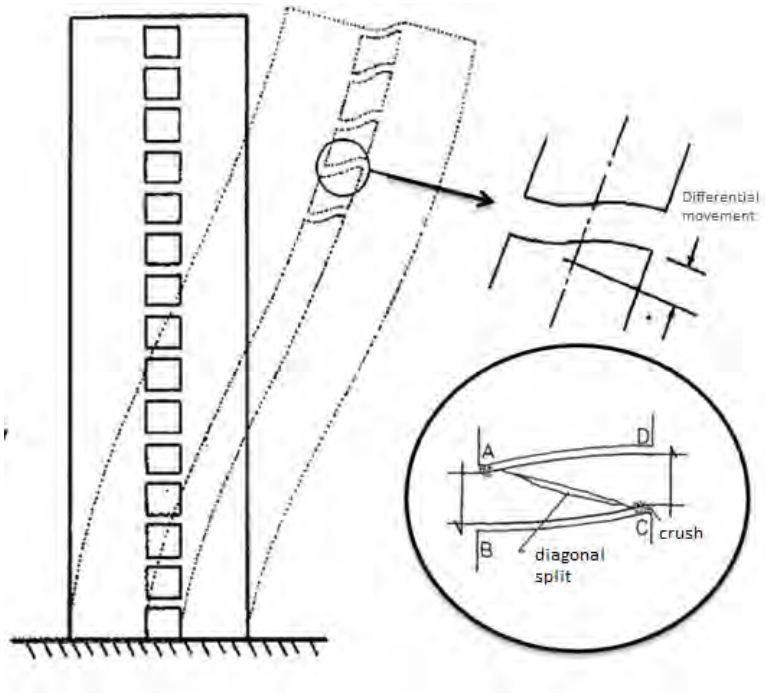

Figure 2.1 – Deformed shape of a coupled shear wall subjected to lateral load (Subedi, 1991)

2.1.1 REINFORCED CONCRETE COUPLING BEAMS

The deformation of reinforced concrete coupling beams is a combination of flexural and shear deformations. Flexural deformations develop because coupling beams are under double curvature bending, with a point of inflection at the center of the beam, when the structure deforms laterally. Flexural deformations are thus expected to be largest at the beams ends, where the use of confinement reinforcement in the expected flexural hinge region can delay degradation of the compression zone and buckling of reinforcement.

Lateral building drifts also impose uniform shear over the length of coupling beams. Shear deformations tend to cause compression along one diagonal (AC in Figure 2.1) and tension along the other diagonal (BD), with both top and bottom surfaces of the beam remaining in tension along the length of the beam when unrestrained axially. To prevent or delay inclined shear failures, transverse or inclined reinforcement must be placed throughout the beam span. In addition, after several cycles of reversing loads, wide flexural cracks near the beam ends are susceptible to developing large sliding shear displacements that can limit the beam deformation capacity. Inclined reinforcement is most effective at preventing or delaying sliding shear failures.

2.1.1.1 ORIGINATION OF DIAGONALLY ORIENTED REINFORCEMENT

In 1969, Paulay reported results from tests of twelve deep reinforced concrete coupling beams with aspect ratios of 1.0, 1.3 and 2.0 under static and cyclic loading. The tests were part of a project initiated to investigate the behavior of coupled shear walls. The results clearly showed the inadequacy of conventional ‘moment-frame-type’ reinforcement layouts (longitudinal bars with transverse steel, as shown in Figure 2.2) for coupling beams with aspect ratios less than 2.0. Because the specimens were relatively deep, short-spanned, and subjected to very high shear

stresses, their behavior was dominated by shear deformations and not flexure. Paulay found that conventional horizontally reinforced (‘moment-frame-type’) coupling beams are likely to exhibit diagonal tension or sliding shear (shear compression) failures after high intensity reversed cyclic loading. The ductility of these beams was inadequate to satisfy the demand in coupled shear wall structures that are expected to be subjected to large earthquakes (Paulay, 1971). Other than at low shear stresses, beams with conventional ‘moment-frame-type’ reinforcement do not exhibit satisfactory performance.

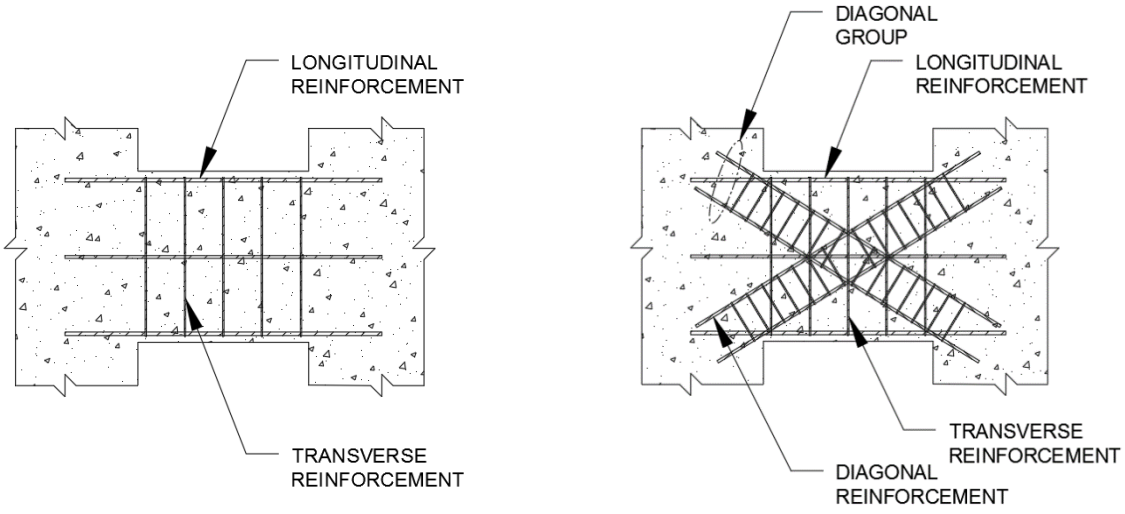

Figure 2.2 - Conventionally (left) and diagonally (right) reinforced coupling beams (wall reinforcement omitted for clarity)

The Paulay test results also showed that instead of developing the strain profile expected based on imposed sectional moments, tensile strain was developed in the longitudinal reinforcement over the entire span of the beam for both top and bottom steel as shown in Figure 2.3. The figure shows the reinforcing bar strain measured at several points along the span of one of the conventionally reinforced beams tested by Paulay. Each curve in the figure is labeled with a circled value to indicate the imposed chord rotation. This shows that traditional reinforced concrete flexural design principles are not applicable to short coupling beams subjected to large

nominal shear stresses. Furthermore, Paulay argued that the presence of compression reinforcement cannot be expected to improve beam ductility if it is, in fact, elongating throughout the loading protocol.

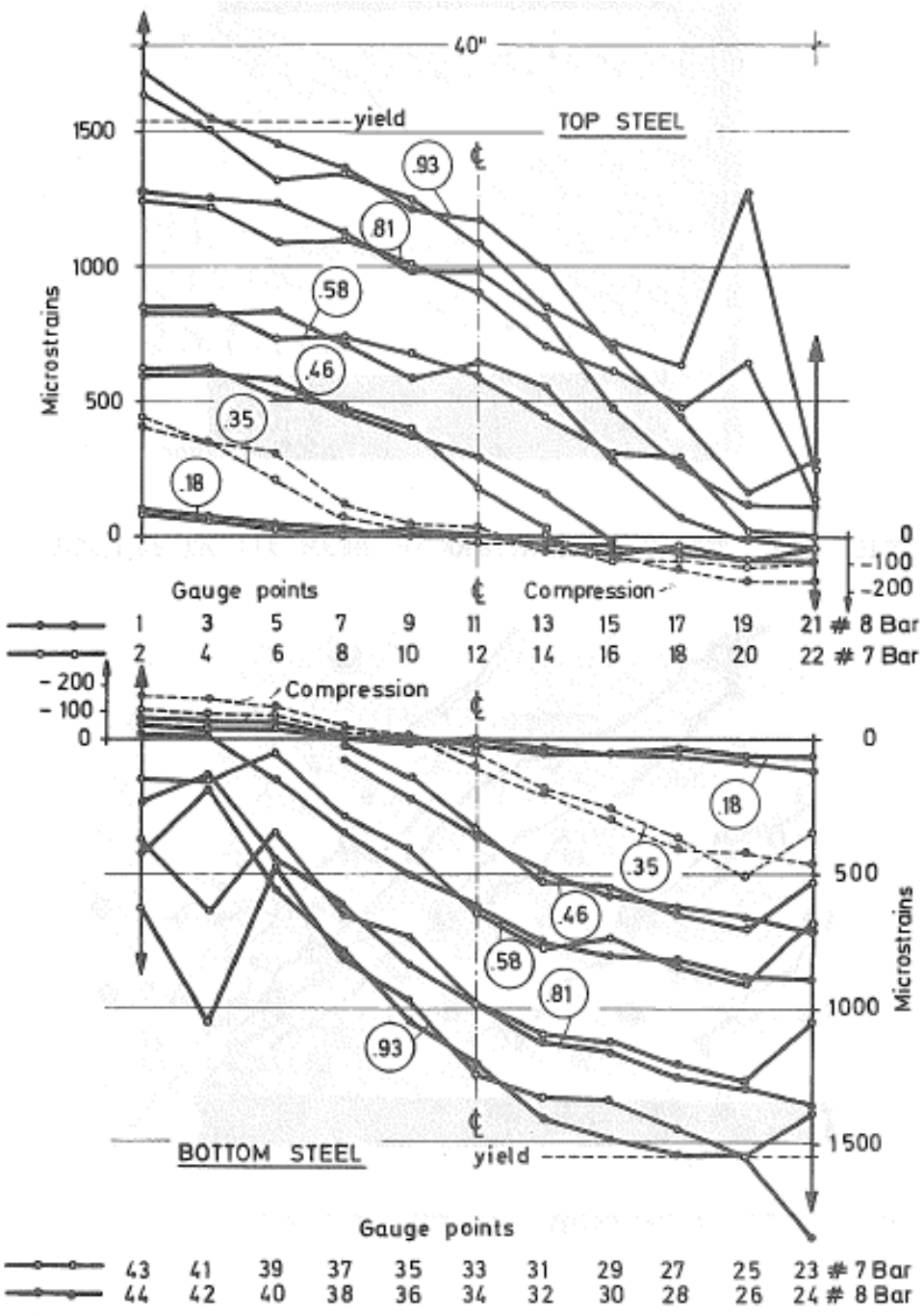

Figure 2.3 – Strain distribution in longitudinal steel in a coupling beam tested by Paulay, 1969

These findings led Paulay and Binney to propose a different reinforcement detailing approach in 1972 aimed at improving coupling beam performance. Paulay and Binney tested three short and deep coupling beams (two with an aspect ratio of 1.29 and one with 1.02) under repeated cyclic loading with the principal reinforcement placed in the form of two intersecting diagonal bars (Figure 2.2). Reinforced in this way, the beam acts as a cross-bracing with equal diagonal tension and compression capacity. For a member experiencing antisymmetric bending with its inflection point at midspan, this reinforcement arrangement is a logical solution because the depth of the primary flexural reinforcement follows the moment distribution. Test results showed that diagonally reinforced coupling beams possess excellent deformation capacity and energy dissipation properties when the inclined reinforcement is adequately restrained from buckling.

The improved behavior exhibited by diagonally reinforced coupling beams is shown in Figures 2.4 and 2.5, which show plots of load versus beam chord rotation for two specimens reported by Paulay in 1969 and Paulay and Binney in 1974, respectively. Strain measurements indicated that steel stresses along the diagonal bars were nearly uniform over the length of the beam after the onset of diagonal cracking. Strain measurements taken on longitudinal (non-diagonal) reinforcement again showed that in beams with an aspect ratio less than 1.5, the flexural reinforcement is subjected to tension over the entire span of the beam (not only at midspan but also in the theoretical compression zones for both top and bottom reinforcement). Specimens tested by Paulay and Binney developed strengths in excess of the calculated nominal strength due to strain hardening.

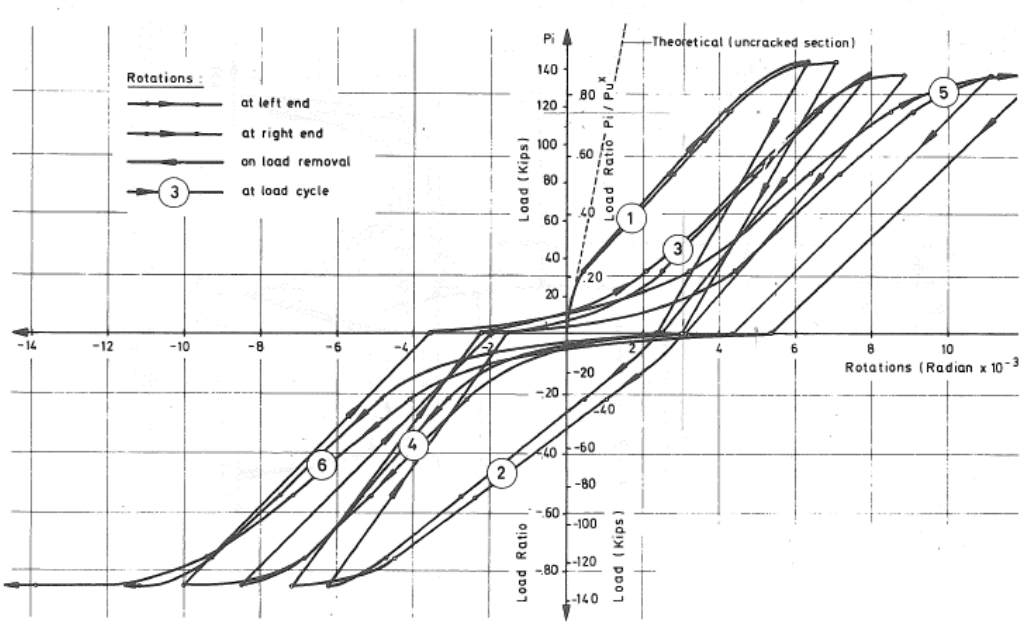

Figure 2.4 – Load-rotation relationship for "Beam 312" with moment-frame-type reinforcement (Paulay, 1969)

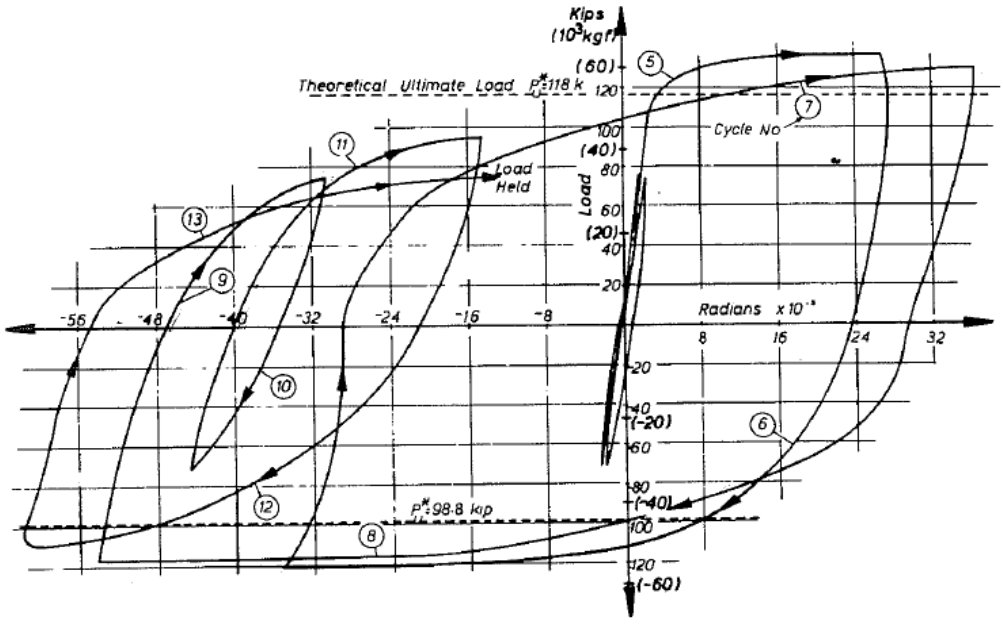

Figure 2.5 – Load-rotation relationship for "Beam 317" with diagonal reinforcement (Paulay and Binney, 1974)

Subsequent experimental work has supported the effectiveness of diagonally oriented reinforcement as a means of improving the deformation capacity of reinforced concrete coupling beams. In 1976, Irwin and Ord reported results from tests of six small-scale reinforced concrete coupled shear wall models. The specimens consisted of two pier segments linked by a series of coupling beams, with the depth of the coupling beams varied among the specimens. It was concluded that diagonally reinforced coupling beams are capable of providing adequate strength and ductility and are thus appropriate for use in coupled walls. Similar tests of large-scale coupled systems, reported by Paulay and Santhakumar in 1976, showed similar results.

In 1988, results were published from two independent research programs designed to study the use of full-length diagonal reinforcement for improving the hysteretic response of short columns subjected to high shear stresses – a situation similar to that of coupling beams. Kuramoto, Minami, and Wakabayashi tested fifteen reinforced concrete short columns subjected to axial compression and lateral cyclic loading. Twelve of the fifteen specimens – all of them having an aspect ratio of 2.0 – were diagonally reinforced. The study confirmed that diagonal reinforcement improves the strength and ductility of short columns if adequately confined. The need for this confinement increases with axial load, because the cause of failure in diagonally reinforced members is typically buckling of diagonally oriented bars. In a separate study, Tegos and Penelis tested twenty-four column specimens to evaluate the use of diagonal reinforcement in short columns. Their results also demonstrated the improved behavior exhibited by diagonally reinforced concrete members relative to those with more conventional reinforcement.

2.1.1.2 ALTERNATIVE REINFORCEMENT LAYOUTS

Despite the excellent behavior consistently exhibited by diagonally reinforced coupling beams, researchers have continued to seek alternatives. This is because diagonally reinforced coupling beams are difficult and time-consuming to construct due to reinforcement congestion (a large amount of confinement reinforcement is needed for the diagonal reinforcement and diagonally oriented beam reinforcement must intersect the densely reinforced wall boundary elements).

In 1978, Shiu, Barney, Fiorato, and Corley reported tests of eight reinforced concrete coupling beam specimens to evaluate the performance of three different reinforcement layouts. Three coupling beam specimens with conventional 'moment-frame-type' reinforcement, three specimens with diagonal bars near the beam-wall interface (Figure 2.6) and two with full-length diagonal reinforcement were subjected to high shear stresses ranging from 7 to $11\sqrt{f_c'}$ [psi] (0.58 to $0.91\sqrt{f_c'}$ [MPa]). The specimens had aspect ratios of 2.5 and 5.0 for each type of detailing. From the results, it was observed that performance of the beams with conventional 'moment-frame-type' reinforcement was limited by sliding-shear in the hinging region, a mode of failure that is not improved by increasing the amount of transverse reinforcement. Damage at the ends of the beams caused by sliding shear was not observed in specimens with diagonal bars near the beam-wall interface, but the overall improvement in hysteretic response was not significant enough to justify the additional cost of detailing. For the beams with an aspect ratio of 2.5, full-length diagonal reinforcement dramatically improved the deformation capacity. Furthermore, the beams with an aspect ratio of 2.5 and full-length diagonal reinforcement reached the predicted shear capacity, whereas most of the other specimens were more than 10% below the expected strength.

The deformation capacity of beams with full-length diagonal reinforcement was limited by buckling and subsequent fracture of diagonal bars. In the case of the beams with an aspect ratio of 5.0, use of full-length diagonal reinforcement did not result in a significant improvement in behavior relative to the beams with 'moment-frame-type' reinforcement. A possible explanation for this difference is that in slender beams, diagonally-oriented reinforcement has a very small angle of inclination relative to the longitudinal beam axis. The contribution of the diagonal bars to shear resistance is therefore small and inefficient. It was concluded that it is not economical to use full-length diagonal reinforcement in coupling beams with aspect ratios larger than 4.0.

In their 1988 paper, Tegos and Penelis also reported results from tests of specimens constructed with an alternative reinforcement detail aimed at preventing premature diagonal-splitting failures in shear-critical columns. The proposed reinforcement detail consisted of arranging the main longitudinal reinforcement into the shape of a rhombus (Figure 2.6). Through tests of twenty-four column specimens with aspect ratios of 2.0, 3.0 and 4.0, eighteen of which had rhombic reinforcement detailing, it was observed that the specimens with inclined rhombic reinforcements and an aspect ratio of more than 1.5 retained strength up to a rotation of 4% with no significant deterioration after reaching their maximum capacity. Three of the eighteen specimens had no imposed axial load, while the others were under large compression, ranging from 20% to 35% of $A_g f_c'$, where A_g is the gross cross-sectional area. Specimens without compression loads had deformation capacities larger than similar specimens under large compression loads, as expected, but the results were not sufficient to evaluate the effect of axial restraint because elongation was not controlled and it was not clear the magnitude of imposed axial force was representative of the axial forces that develop in restrained beams. More important,

introducing inclined rhombic-type reinforcement appeared to prevent explosive inclined shear failures; thereby reducing the amount of hoops required.

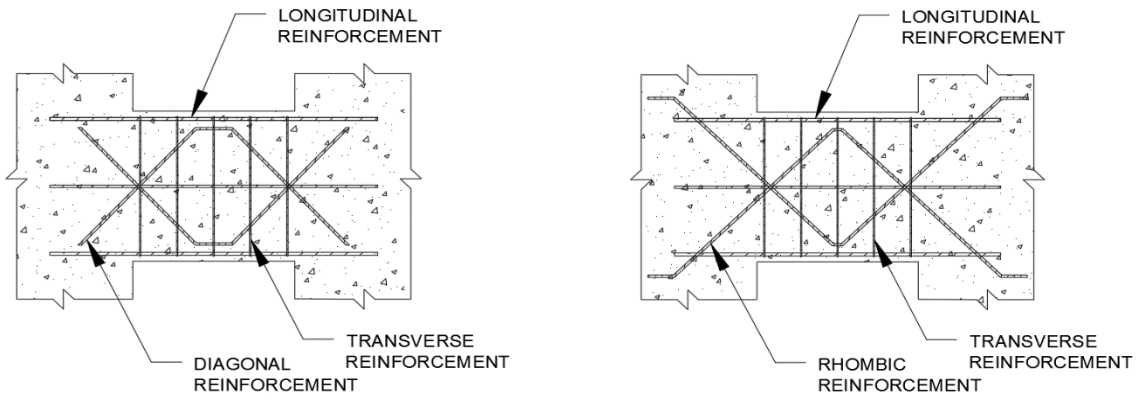

Figure 2.6 – Bent-up bar (left) and rhombic reinforcement (right) at beam-wall interface (wall reinforcement omitted for clarity)

In 1996, Tassios, Moretti, and Bezas reported results from tests of ten coupling beams with five different layouts of reinforcement and two different aspect ratios (1.0 and 1.66). Other than the conventional (moment-frame-type) and "well-established but difficult to construct" diagonal reinforcement detailing, three other reinforcement arrangements were evaluated. Two of those included short and long dowels across the end of the beams (Figure 2.7) aimed at preventing sliding shear failures, and the third had bent-up bars, parallel in the middle and intersecting at the ends, similar to the ones tested by Shiu et al. (Figure 2.6). The specimens were tested in a vertical position with one end fixed to the reaction frame and the other end free to elongate. It was again observed that before development of diagonal cracking, the distribution of strains measured along the primary longitudinal reinforcement was very close to that predicted by flexural theory. After inclined cracking, however, the strain distribution changed such that tensile strains were recorded along the full length of the beam along both the top and bottom of the beams. This abrupt change

in the distribution of longitudinal strains was more evident in specimens with an aspect ratio of 1.0.

The Tassios et al. tests once again showed that use of a diagonal reinforcement layout leads to larger deformation capacity than other layouts, particularly in specimens with lower aspect ratios (less than approximately 1.5). Specimens with bent-up bars had larger strength and deformation capacity than the conventionally reinforced specimens. Although the presence of dowels did prevent sliding at the beam ends, it did not prevent shear compression failures (at the ends for specimens with long dowels and near the middle of the beam span for specimens with short dowels). A severe pinching of the force-displacement relationship was also observed in the response of all specimens with dowel bars. In general, specimens with an aspect ratio of 1.66 exhibited a larger deformation capacity than those with an aspect ratio of 1.0. From the crack patterns, it appears shear was primarily transferred through a diagonal compressive strut in specimens with aspect ratios of 1.0, whereas in specimens with aspect ratios of 1.66, a truss-like mechanism seemed to be a better model. The researchers recommended that for coupling beams with aspect ratios lower than about 1.5, well-confined diagonal reinforcement designed to sustain the entire shear force and bending moment be used. For beams with aspect ratios larger than 1.5, diagonal reinforcement resulted in the best performance, but alternative reinforcement layouts also resulted in satisfactory behavior. For instance, the researchers suggested that use of full-length dowels near mid-depth in combination with bent-up bars near the beam ends and conventional longitudinal reinforcement along the top and bottom of the beam may be adequate. For beams with aspect ratios larger than approximately 2.66, Tassios et al. suggested that conventional ‘moment-frame-type’ detailing may be adequate based on previous research.

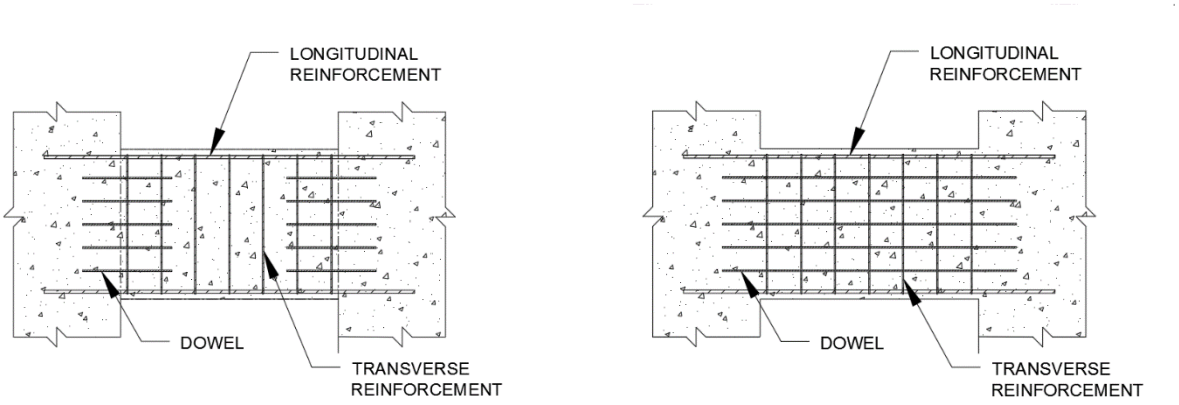

Figure 2.7 – Coupling beam with short (left) and long (right) dowels across the end (wall reinforcement omitted for clarity)

In 2000, Galano and Vignoli published results from tests aimed at comparing the behavior of 15 short coupling beam specimens. The specimen behavior was compared in terms of failure mechanism, deformation capacity, peak strength, and degradation in stiffness. To verify the claim by Tegos and Penelis that specimens with full-length diagonal and rhombic reinforcement layouts exhibited similar behavior, the test series included specimens with four different reinforcement layouts: conventional (moment-frame-type), diagonal without confining ties, diagonal with confining ties, and rhombic. The specimens had an aspect ratio of 1.5 and were subjected to either monotonic or reversed cyclic shear loading. It was found that specimens with the rhombic reinforcement configuration exhibited better strength retention and similar energy dissipation compared to specimens with well-confined diagonal reinforcement. Although not discussed in the Galano and Vignoli paper, the unexpected failure mode (crushing of the concrete strut) exhibited by some of the diagonally reinforced specimens raise questions about the validity of the findings. According to Canbolat's review (2004), the unanticipated crushing of the concrete strut can likely be attributed to the concrete quality, which varied among the specimens.

Tests of beams with a hybrid reinforcement scheme (Figure 2.8) were reported in 2016 by Lim, Hwang, Cheng, and Lin. The series of six coupling beam specimens included two with moment-frame-type reinforcement, two with full-length diagonal reinforcement, and two with conventional (moment-frame-type) detailing combined with diagonal reinforcement, named a 'hybrid layout'. The proposed hybrid reinforcement layout was similar to that proposed previously for beams constructed of high-performance fiber reinforced concrete (Lequesne, 2011). The six specimens included beams with aspect ratios of 3.0 and 4.0. Specimens with the hybrid reinforcement layout exhibited a deformation capacity that was judged to be adequate; larger than that of specimens with conventional (moment-frame-type) detailing but less than that of specimens with full-length diagonal reinforcement. For example, among specimens with aspect ratios of 3.0, it was observed that conventionally reinforced specimens retained 80% of the maximum lateral force until a chord rotation of 4.1%, while diagonally reinforced specimens reached 7% chord rotation. For the hybrid specimens, the limiting chord rotation was 5.5%. The authors argued that a chord rotation of 5.5% is adequate and that the hybrid reinforcement layout is likely to be simpler to construct than a diagonal-bar layout because of the reduced amount of diagonal reinforcement and horizontal longitudinal bar development into the wall boundary element.

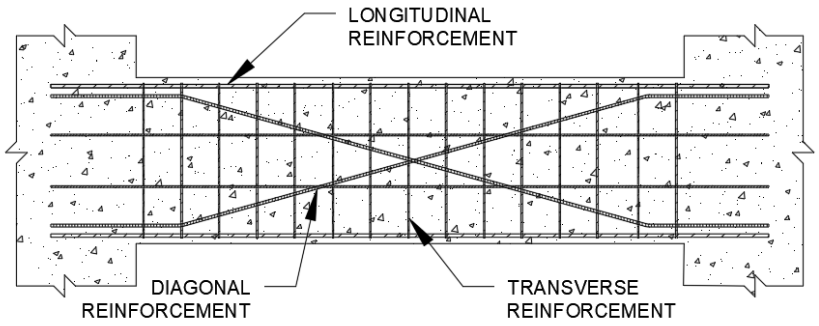

Figure 2.8 – Coupling beams with hybrid layout (wall reinforcement omitted for clarity)

The Lim et al. diagonally reinforced beam specimens deviated from ACI Building Code commentary recommendations in at least two important ways: (1) the diagonal bars were bent near the beam ends and entered the walls horizontally instead of at an inclination, and (2) the development length of the secondary (non-diagonal) longitudinal reinforcement (ACI Building Code references are to ACI 318-14 unless otherwise noted). Instead of terminating near the beam-wall interface, the secondary (non-diagonal) longitudinal reinforcement satisfied ACI Building Code development length requirements. As a result of this second detail, damage was spread throughout the beam spans in the Lim et al. tests while in other tests (Naish, Fry, Klemencic, and Wallace, 2009, Lequesne, Parra-Montesinos, and Wight, 2013) localized damage was observed along the beam-wall interface. It therefore seems possible that developing the non-diagonal reinforcement may be a way to reduce concentrations of deformations near the beam ends. This may be particularly advantageous when less ductile high-strength steel is used.

Recently, a new reinforcement detail for reinforced concrete coupling beams was proposed by Choi, Hajyalikhani, and Chao (2018) that consists of reinforcing a deep coupling beam as if it was two slender ‘moment-frame’-type beams stacked vertically (Figure 2.9). The reinforcement cages are separated by a small unreinforced strip of concrete. Five “double-beam” coupling beam specimens, four with aspect ratios of 2.4 and one with an aspect ratio of 3.3, were tested under reversed cyclic loads. Two of the specimens with aspect ratios of 2.4 and the one with an aspect ratio of 3.3 had 1 in. (25.4 mm) clear spacing between the ends of the transverse reinforcement at midheight; in the other two specimens, the clear spacing was either 0.25 in. (6.35 mm) or 2 in. (51 mm). The results showed that under small displacements the “double-beam” specimens act like conventional coupling beams. Under large displacements, cracks concentrate near midheight at midspan and then propagate toward the beam ends. Eventually, the beam separates into two

relatively slender beams that each have approximately twice the aspect ratio of the original beam. As a result, the shear-dominated deep beam behavior typical of coupling beams becomes flexure-dominated slender beam behavior. As a result, sliding shear failures at the beam-wall interface become less likely. The specimens sustained large rotations (6 to 11%) and large shear stresses between 10 and $12\sqrt{f_c'}$ [psi] (0.83 and $1.0\sqrt{f_c'}$ [MPa]).

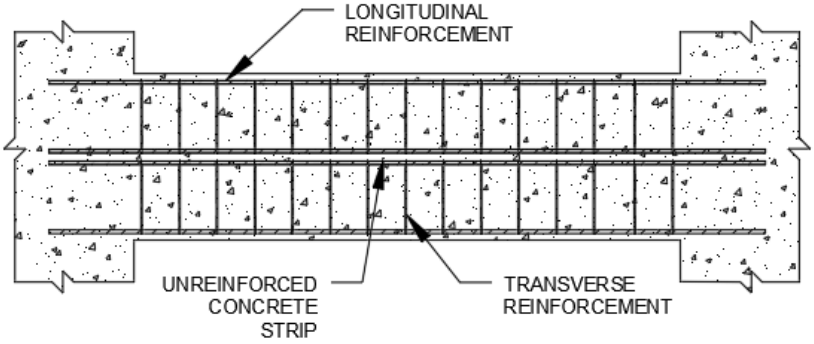

Figure 2.9 – Reinforcement layout in "double-beam" coupling beams (wall reinforcement omitted for clarity)

Several different reinforcement layouts have thus been investigated in an effort to find simpler ways to construct coupling beams that exhibit deformation capacities similar to diagonally reinforced beams. Although several have resulted in deformation capacities close to that of diagonally reinforcement beams, the apparent reduction in reinforcement congestion achieved by some of the alternatives has not been significant enough to motivate their adoption in practice. Diagonally-oriented reinforcement continues to be the primary layout used in construction of reinforced concrete coupling beams.

2.1.1.3 CONFINEMENT

Since the ACI Building Code adopted provisions for diagonally reinforced concrete coupling beams in 1999, their use has become common in multistory buildings. To ensure stability of the diagonal reinforcement under compression, the ACI Building Code (318-99) required that each diagonal cage be confined by hoops with an area and spacing satisfying the requirements for confinement of columns in moment frames classified as special (Figure 2.10a). These requirements remained unchanged until an alternative was added in 2008 (318-08) that allowed the use of hoops to confine the entire coupling beam cross section instead of only the inclined reinforcement cages (Figure 2.10b). This change, justified based on the studies described below, was made to alleviate the reinforcement congestion caused by confinement reinforcement.

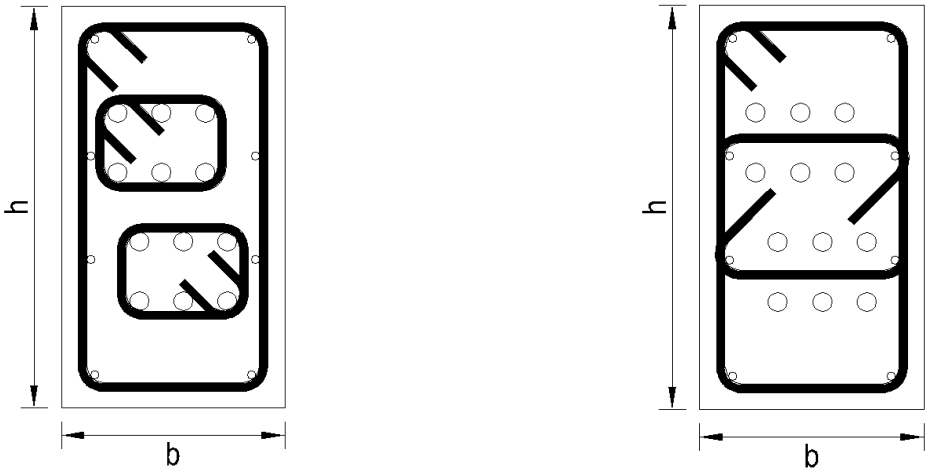

(a) Diagonal confinement (b) Full confinement

Figure 2.10 – Confinement detailing of coupling beam

In 2008, with the aim of promoting relaxed confinement requirements, Fortney, Rassati, and Shahrooz reported results from tests under reversed cyclic loading of two diagonally-

reinforced coupling beam specimens with different transverse reinforcement detailing. One specimen was in full compliance with ACI Building Code (318-05) provisions, whereas the other had fewer hoops around the diagonal bar groups along the length of the beam where the diagonal bar groups intersected. In addition, both the specimens had more than twice the area of transverse reinforcement around the core of the specimens than required by Code provisions (ACI 318-05). The experimental results showed that providing more transverse reinforcement than required beneficially impacted the response of the specimens by ensuring necessary confinement to the concrete core of the beam and delaying buckling. Though the two test results were insufficient to propose a minimum transverse reinforcement ratio, it was clear that the concrete core must remain intact through large deformation cycles. Therefore, contrary to expectations, the final recommendation was to increase the minimum transverse reinforcement ratio above the code specified requirements.

In 2013, Naish, Fry, Klemencic, and Wallace reported results from an experimental study aimed at comparing the behavior of specimens constructed in accordance with the requirements of either ACI 318-05 or ACI 318-08 (diagonal cage confinement or full-section confinement, respectively). The test specimens were designed to simulate common tall-building configurations for residential and office construction. Of the eight specimens tested, five had an aspect ratio of 2.4, which is a typical aspect ratio for coupling beams in residential buildings, and the other three specimens had an aspect ratio of 3.33, intended to represent typical office buildings. Two specimens with each aspect ratio had hoops placed along the intersecting groups of diagonal bars ("diagonal" confinement) whereas other specimens had hoops placed so as to provide confinement for the core of the coupling beam ("full-section" confinement). Test results showed the use of full-section confinement results in behavior that is similar to that of specimens with confinement of

only the diagonal bars. These results supported the ACI Building Code change, adopted in 2008, permitting the use of full-section confinement in coupling beams.

In the Naish et al. tests, the beams were not axially restrained. Three of the five specimens with an aspect ratio of 2.4 were, however, constructed with a 4 in. (100 mm) thick reinforced concrete slab, two of which also contained post-tensioned strands that provided some partial restraint to axial growth along the member length. Most damage experienced by the beams was concentrated at the beam-wall interface in the form of slip/extension of diagonal reinforcement, even when axial load was applied to the beam via post-tensioning.

2.1.1.4 CODE REQUIREMENTS AND LIMITATIONS

According to the ACI Building Code (318-14), coupling beams with aspect ratios less than 2.0 and nominal shear stresses over $4\sqrt{f_c'}$ [psi] ($0.33\sqrt{f_c'}$ [MPa]) shall be diagonally reinforced. For coupling beams with aspect ratios between 2.0 and 4.0, either diagonal or special moment frame reinforcement detailing are permitted. When the aspect ratio is larger than or equal to 4.0, the beam shall be designed with special moment frame detailing. These provisions reflect that use of inclined reinforcement to resist transverse shear becomes increasingly inefficient as the beam aspect ratio increases (and thus the angle of reinforcement inclination decreases).

Where diagonal reinforcement is used, the diagonal bar groups must consist of at least four longitudinal bars arranged to form a rectangle. The diagonal bars have to be designed to resist the entire shear, with the nominal shear capacity thus calculated using Eq. 2.1 (Figure 2.11).

$$V_n = 2A_{vd}\, f_y \sin(\alpha) \leq 10\sqrt{f_c'}\, bh \qquad \text{Eq. 2.1}$$

The ACI Building Code allows coupling beams to be designed for nominal shear strengths up to $10\sqrt{f_c'}$ [psi] ($0.83\sqrt{f_c'}$ [MPa]) with a maximum diagonal bar yield stress f_y of 60 ksi (420 MPa), although Harries, Fortney, Shahrooz, and Brienen (2005) have argued that nominal shear strengths larger than $6\sqrt{f_c'}$ [psi] ($0.5\sqrt{f_c'}$ [MPa]) are difficult to achieve in slender coupling beams due to reinforcement congestion.

For confinement, the ACI Building Code provides the two options shown in Figure 2.10; either a) confine each group of diagonal bars independently with hoops, or b) provide hoops and crossties to confine the entire beam cross section. In either case, the area and spacing of hoops must satisfy the requirements for confinement of special moment frame columns supporting axial loads less than $0.3A_g f_c'$, where A_g is the gross cross-sectional area. Each bar within the diagonal group must be embedded into the wall at least 25 percent more than the calculated development length in tension.

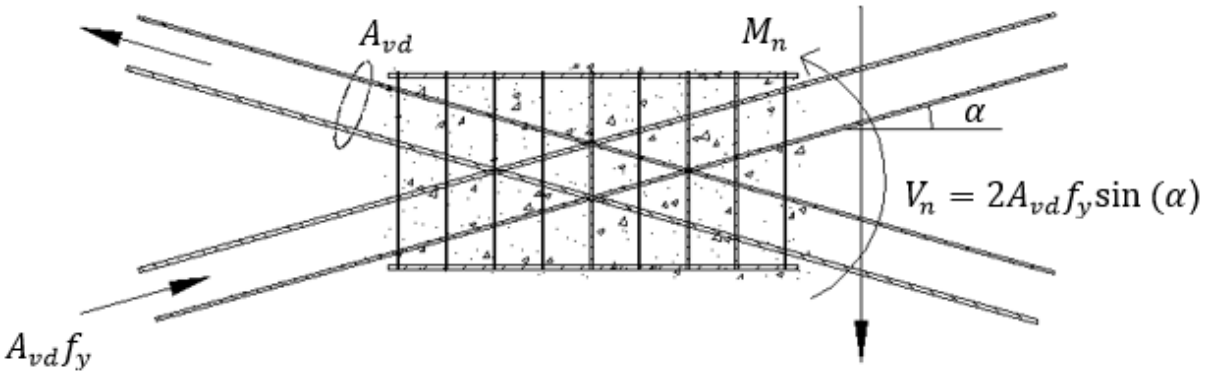

Figure 2.11 – Schematic of diagonally reinforced coupling beam showing end reactions (wall reinforcement omitted for clarity)

2.1.2 STEEL COUPLING BEAMS

Use of steel sections, embedded into reinforced concrete walls, is an alternative to reinforced concrete coupling beams. In 1993, Harries, Mitchell, Cook, and Redwood published results from tests under reversed cyclic loading of two full-scale specimens that demonstrated that use of steel sections as coupling beams can provide excellent deformation capacity and energy dissipation. The beams were designed and detailed following the seismic design requirements for eccentrically braced frames in the Canadian Steel Design Standard. When properly embedded into the adjacent reinforced concrete walls, steel coupling beams can also exhibit larger strength than reinforced concrete beams with shallower depths. Harries et al. argued that use of steel coupling beams may be the only way to provide the required strength and stiffness in structures with height restrictions.

In 1993, Shahrooz, Remmetter, and Qin reported results from tests of three specimens consisting of wall piers and coupling beams. The tests were aimed at investigating the transfer of cyclic forces between the steel coupling beams and reinforced concrete walls. Built-up steel sections were attached to the wall piers by embedment into the boundary element, interfering with the wall reinforcement. According to the test results, the performance of the steel coupling beams was satisfactory in terms of hysteresis and energy dissipation characteristics. Subsequent studies, such as Park and Yun (2005), have proposed models for computing the proper embedment length of steel coupling beams. Though smaller than concrete coupling beams of similar strength and stiffness, steel coupling beams are difficult to place on-site; their embedment causes significant interference with reinforcement in the adjacent wall boundary elements.

2.1.3 COMPOSITE COUPLING BEAMS

Use of composite coupling steel-concrete coupling beams has also been investigated. In 1996, Gong, Shahrooz, and Gillum published results from tests on coupling beams consisting of wide-flanged steel beams encased in lightly reinforced concrete. The composite members exhibited both strength and deformation capacity, while the concrete encasement prevented undesirable web and flange buckling of the steel section. In 2005, Lam, Su, and Pam proposed another alternative consisting of a steel plate encased in concrete. After testing three beams under reversed cyclic loading (one conventionally reinforced and two with embedded steel plates along the whole span, either with or without shear studs), it was concluded that embedded steel plates improved the strength and stiffness of coupling beams.

In 2017, Motter, Fields, Hooper, Klemencic, and Wallace published results from tests of four large-scale steel-reinforced concrete coupling beam specimens to quantify the effects of steel section embedment length, aspect ratio, wall boundary longitudinal and transverse reinforcement amounts, and loading. These results once again confirmed that improved performance was associated with long embedment length as well as heavy wall boundary reinforcement; reduced embedment length and light wall boundary reinforcement led to reduced performance with cyclic degradation evident in the load-deformation response and significant damage in the embedment region.

In general, composite coupling beams have the same limitation as steel coupling beams: the long embedment required to ensure full development of the steel section must pass through, and thus disrupt, the longitudinal and transverse reinforcement in the wall boundary zone.

2.1.4 HPFRC COUPLING BEAMS

Use of high performance fiber reinforced concrete (HPFRC) in construction of coupling beams has gained some traction in practice. In 2005, Canbolat, Parra-Montesinos, and Wight published results from tests four coupling beams with aspect ratios of 1.0. This series of tests included a reinforced concrete specimen detailed to satisfy ACI Building Code (318-02) requirements, an HPFRC specimen with no diagonal reinforcement, and two precast, diagonally reinforced, HPFRC coupling beams. Results demonstrated that HPFRC can provide effective confinement of diagonal reinforcement, thereby significantly reducing the need for transverse reinforcement. HPFRC was also shown to increase the shear strength and energy dissipation of the member, potentially allowing for a reduction in the amount of diagonal reinforcement required to attain a target shear strength. Finally, use of HPFRC was shown to improve the damage tolerance of the member by dispersing damage over more numerous, finer cracks. As a result, HPFRC coupling beams may require less costly repairs than reinforced concrete coupling beams following an earthquake.

In 2007, Zhang, Zhang, and Huang reported similar findings from their tests of nine fiber-reinforced and four high-strength concrete coupling beams with aspect ratios less than 2.5. The variables were aspect ratio, steel fiber volume fraction, hoop content, and loading mode. The test results indicated that the partial replacement of hoops by steel fibers can not only improve the shear resistance of the coupling beams but also change the failure type from brittle shear failure to ductile flexural failure. Another contemporary study by Yun, Kim, Jeon, Park, and Lee (2008) on three coupling beams with aspect ratios of 1.0 and two different reinforcement arrangements also supported the use of HPFRC in shear dominated coupling beams.

Subsequent tests of HPFRC coupling beams with aspect ratios from 1.75 to 3.3 (Parra-Montesinos, Wight, and Setkit, 2010, Lequesne, 2011) have shown that use of HPFRC permits a significant reduction in the amount of diagonal reinforcement required to achieve acceptable performance under earthquake-type loads. For an HPFRC coupling beam with an aspect ratio of 1.75, the area of diagonal reinforcement can be reduced by approximately 2/3 relative to reinforced concrete coupling beams without markedly compromising deformation capacity. For HPFRC coupling beams with aspect ratios larger than approximately 2.5, no diagonal reinforcement is required.

These findings led to the use of HPFRC coupling beams in high-rise structures on the west coast of the United States. However, despite early adoption, widespread use of HPFRC coupling beams has been hindered by the somewhat higher cost of HPFRC and the unfamiliarity of contractors with sourcing and handling it.

2.2 HIGH STRENGTH STEEL

The idea of using high-strength reinforcement in concrete structures can be traced back to at least 1934 when Richart and Brown performed a series of laboratory tests on columns with circular cross sections and spiral reinforcement. The tests showed that longitudinal bars with yield stress close to 100 ksi (690 MPa) were fully effective in columns resisting concentric axial loads. With adequate spiral confinement, the core concrete developed compressive strains large enough for the longitudinal bars to reach their yield point. In 1960, experimental work at the Portland Cement Association (PCA) Laboratory led to similar conclusions. But for tied columns with rectangular sections, PCA reported that the specified yield point needs to be reached at or below a strain of 0.003 if it is to be developed in a concentrically loaded column. As a result, in 1963, the ACI

Building Code limited the yield stress of vertical column reinforcement to 75 ksi (515 MPa), which, in 1971, was increased to 80 ksi (550 MPa) for non-seismic applications. The limit was 60 ksi (420 MPa) for seismic applications.

Recent advances in steel production have made it possible to produce higher strength reinforcement at a price that is competitive with Grade 60 (420) steel. As a result, there has been renewed interest in the use of high-strength steel as a means of reducing reinforcement congestion as well as material, shipping, and placing costs.

In 2012, Rautenberg, Pujol, Tavallali, and Lepage reported the results of four column tests. Two control specimens were reinforced with conventional Grade 60 (420) reinforcement and two specimens had high-strength Grade 120 (830) reinforcement. The strengths of all specimens were approximately equal because the product of the reinforcement ratio and steel yield stress was approximately constant. Transverse reinforcement (No. 3 Grade 60 (420) hoops) was provided to restrain buckling of the longitudinal reinforcement, confine the core concrete, resist shear, and improve bond between concrete and the longitudinal bars. Under fully reversed cyclic loads, all four specimens exhibited drift capacities of at least 4%. Based on the results, Rautenberg et al. argued that use of high-strength reinforcement in columns of earthquake-resistant structures has a high potential to be effective because when columns are sized so that the axial load demand falls below the balanced point, the moment capacity is governed by reinforcement in tension. As a result, the drawbacks of using high-strength reinforcement – crack width and deflection during service – do not control. Other tests of members constructed with high-strength steel have led to similar conclusions regarding the viability of using high-strength steel in columns, beams, and squat walls (Yotakhong, 2003, Tavallali, 2011, Ghannoum, and Slavin, 2015, Cheng, Hung, Lequesne, and Lepage, 2016).

2.3 SUMMARY

The difficulties associated with constructing coupling beams capable of exhibiting the required deformation capacity, strength, and stiffness have resulted in a large body of research aimed at developing simpler and more effective coupling beam designs. Researchers have investigated the use of diagonal reinforcement, a rhombic arrangement of primary bars, steel beams, steel-concrete composite beams, HPFRC coupling beams, and more (including fully unbonded post-tensioned precast concrete coupling beams reported by Weldon and Kurama, 2006, coupling beams with side bolted steel plates reported by Zhu, Zhou, and Su, 2008, coupling beams with a replaceable fuse reported by Chen and Lu, 2012, and bolted steel coupling beams reported by Lim, Kang, and Hong, 2016). Experimental results showed that each of these alternatives exhibited better behavior than conventional 'moment-frame-type' coupling beams but also had other limitations.

The reinforcement detail that consistently exhibits the largest deformation capacity and is most commonly used in practice is diagonal reinforcement. If properly detailed, diagonally-reinforced coupling beams exhibit considerable stiffness, strength, and deformation capacity. However, due to significant reinforcement congestion, diagonally reinforced coupling beams are also often difficult to construct, particularly in more slender members and those with nominal shear stresses near the ACI Building Code limit of $10\sqrt{f_c'}$ [psi] ($0.83\sqrt{f_c'}$ [MPa]).

Use of high-strength steel is believed to be a likely means of significantly reducing the reinforcement congestion common in reinforced concrete coupling beams, and thus simplifying construction and reducing costs. Other structural members have been shown to exhibit high deformation capacity under earthquake-type loads when reinforced with high strength steel (up to

Grade 120 (830)). Use of such high-strength reinforcement is not, however, permitted by the ACI Building Code due to lack of experimental data. There is a need to experimentally evaluate the behavior of coupling beams reinforced with high-strength reinforcement.

In addition to this, the ACI Building Code commentary recommends terminating all the secondary (non-diagonal) longitudinal reinforcement near the beam-wall interface to limit unexpected overstrength. No previous experimental work has directly investigated the effect of this reinforcement detail on beam behavior, although there is evidence that it impacts the failure mechanism. It is plausible that, because it tends to delay concentration of deformation demands near the wall face, developing all reinforcement will tend to increase the deformation capacity of coupling beams – particularly when reinforcement is used that has limited deformation capacity.

Finally, despite the restraint of coupling beam growth provided by walls in practice, the effect of axial restraint on coupling beam behavior has been frequently omitted in past tests of coupling beams. Although axial forces developed in response to the restraint may increase beam flexural and shear strengths, it may also make the beam more prone to exhibit buckling of diagonal reinforcement. The effect of axial restraint on coupling beam deformation capacity needs to be evaluated.

CHAPTER 3 EXPERIMENTAL PROGRAM

3.1 SPECIMENS

3.1.1 DESIGN AND DETAILING

Five coupling beam specimens were tested under reversed cyclic loading (Table 1.1, Table 3.1, and Figure 3.1). For convenience, the specimens were tested oriented as shown in Figure 3.1 instead of their typical horizontal orientation. The specimens had a length of 34 in. (860 mm), depth of 18 in. (460 mm), and width of 10 in. (250 mm), resulting in an aspect ratio (ratio of clear span-to-overall depth) of 1.9. The specimens had either Grade 60 or 120 (420 or 830) steel as diagonal reinforcement and Grade 60 (420) steel for all non-diagonally oriented reinforcement. Four of the five specimens (CB1, CB2, CB2D, and CB2AD) were designed to have nominal shear strengths, calculated assuming the two intersecting diagonal reinforcement cages resist all imposed shear force (Eq. 2.1), of $10\sqrt{f_c'}$ [psi] ($0.83\sqrt{f_c'}$ [MPa]); while the other (CB3D) was designed to have a nominal shear strength near $15\sqrt{f_c'}$ [psi] ($1.25\sqrt{f_c'}$ [MPa]), 50% more than the ACI Building Code limit (ACI Building Code references are to ACI 318-14 unless otherwise noted). Table 3.1 contains the calculated nominal strengths of the specimens.

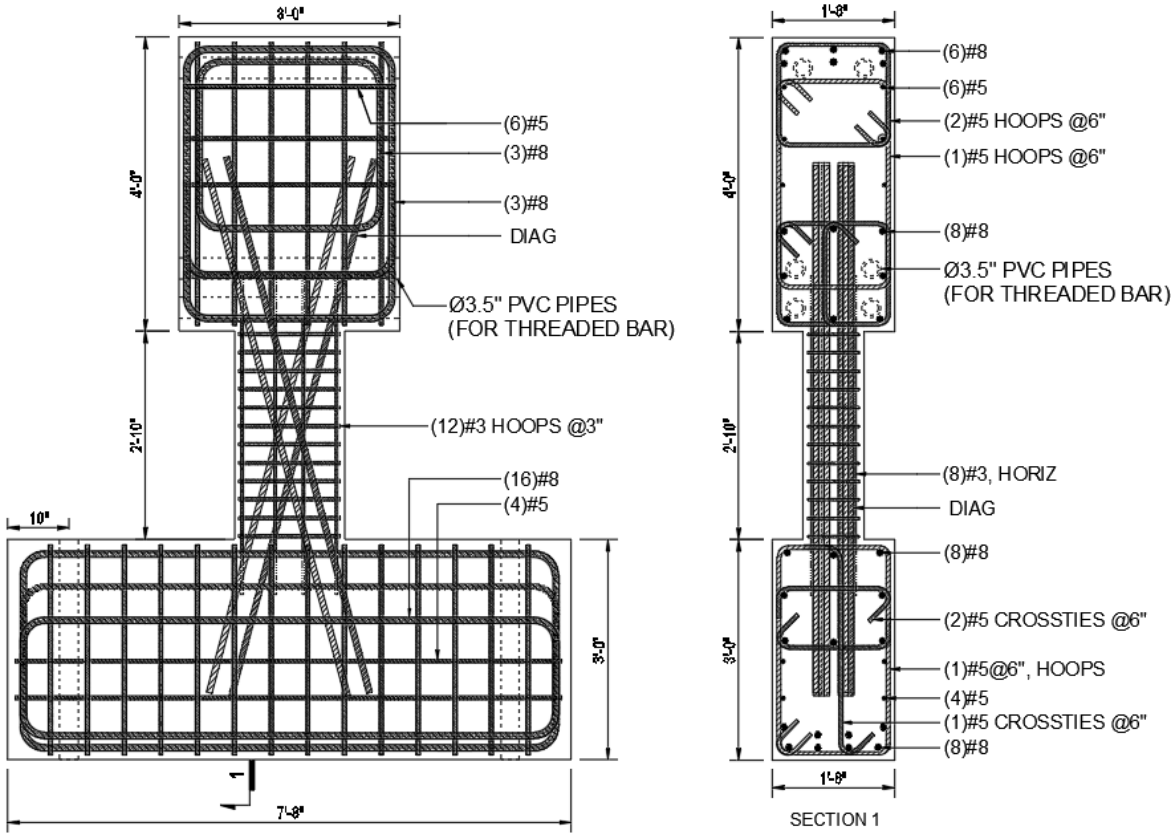

Figure 3.1 – Nominal specimen dimensions and reinforcement (1 in. = 25.4 mm)

Table 3.1 – Specimen nominal strength and transverse reinforcement (1 psi = 0.00689 MPa, 1 kip = 4.45 kN, 1 in. = 25.4 mm)

Specimen ID	Calculated Nominal Shear Strength [a]		Ratio of Transverse Reinforcement Area Provided to Required [b]			
			ACI 318-14 Eq. 18.10.7.4d (i)		ACI 318-14 Eq. 18.10.7.4d (ii)	
	psi	kips	For 10 in.	For 18 in.	For 10 in.	For 18 in.
CB1	$9.6\sqrt{f_c'}A_{cw}$	134	0.96	0.99	1.01	1.05
CB2	$9.4\sqrt{f_c'}A_{cw}$	131	0.96	0.99	1.01	1.05
CB2D	$9.4\sqrt{f_c'}A_{cw}$	131	0.96	0.99	1.01	1.05
CB2AD	$9.4\sqrt{f_c'}A_{cw}$	131	0.96	0.99	1.01	1.05
CB3D	$14.1\sqrt{f_c'}A_{cw}$	197	0.96	0.99	1.01	1.05

[a] Based on ACI 318-14 Eq. 18.10.7.4 using specified material properties; A_{cw} is the cross-sectional area of the coupling beam.

[b] Using specified material properties.

As shown in Figure 3.2, CB1 had 12 No. 7 (22) diagonal bars, CB2, CB2D, and CB2AD had 8 No. 6 (19) diagonal bars, and CB3D had 12 No. 6 (19) diagonal bars. The diagonal bars were inclined 18 degrees relative to the longitudinal beam axis. Transverse reinforcement, provided for the full beam cross section, was nominally identical in all specimens, with Grade 60 (420) No. 3 (10) hoops and crossties spaced at 3 in. (75 mm) on center. The amount of transverse reinforcement was determined according to ACI 318-14 section 18.10.7.4d. The ratio of the amount of transverse reinforcement provided to the amount of transverse reinforcement required for each principal direction is provided in Table 3.1. The 3-in. (75-mm) spacing ended up being $3.4d_b$ for specimens with Grade 60 (420) steel and $4d_b$ for specimens with Grade 120 (830) steel. This difference in spacing in terms of d_b means the No. 6 (19) Grade 120 (830) diagonal bars had longer unbraced lengths and higher stresses than the No. 7 (22) Grade 60 (420) diagonal bars in CB1. The Grade 120 (830) bars are therefore more prone to buckling than the Grade 60 (420) bars. This may result in reduced deformation capacities for CB2, CB2D, CB2AD, and CB3D relative to that of CB1.

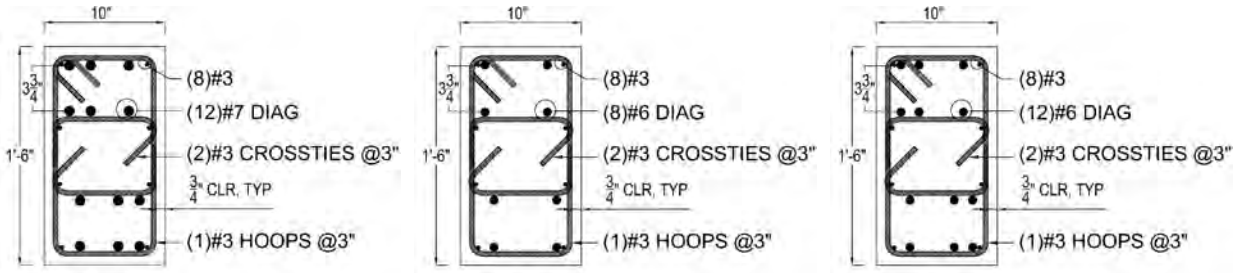

(a) CB1 (b) CB2, CB2D, CB2AD (c) CB3D

Figure 3.2 - Coupling beam cross-sections near wall intersection (1 in. = 25.4 mm)

The specimens also had eight No. 3 bars oriented longitudinally and distributed around the perimeter of the beam such that each bar was supported by either a crosstie or a corner of a hoop. To be consistent with the detailing recommended in the ACI Building Code commentary, the

secondary longitudinal reinforcement was terminated 2 in. (50 mm) into the top and bottom blocks in two specimens (CB1 and CB2). In the other three specimens, the secondary longitudinal reinforcement was extended 9 in. (230 mm) into the walls. This was equal to the development length calculated per ACI 318-14 Eq. 25.4.2.3a with $1.25f_y$ substituted for f_y (extension shown with dotted lines in Figure 3.1). Diagonal bar embedment lengths were 26 in. (660 mm) and 35 in. (890 mm) for Grade 60 (420) No. 7 (22) and Grade 120 (830) No. 6 (19) bars, respectively. These satisfied the ACI 318-14 development length requirements. Because the ACI 318-14 development length equation was not intended for use with Grade 120 (830) reinforcement, the development length for Grade 120 (830) No. 6 bars was also checked against the length calculated using Eq. 4-11b in ACI 408R-03. The provided embedment length was 92% of the development length calculated using ACI 408R-03 recommendations. Although less than recommended, the large concrete cover and dense reinforcement in the top and bottom blocks were believed to justify use of a slightly shorter development length in these tests.

The test setup was designed to test the beam specimens rotated 90 degrees from horizontal, with a top and bottom block designed to simulate wall boundary elements (Figure 3.1). To achieve this, these blocks were reinforced with a dense cage of Grade 60 (420) longitudinal and transverse steel similar to wall boundary element reinforcement near the connection with the coupling beam.

3.1.2 MATERIALS

3.1.2.1 CONCRETE

Ready-mix concrete provided by a local supplier was used to cast the specimens. The concrete had a target compressive strength of 6,000 psi (41 MPa) and a maximum aggregate size of 0.5 in. (13 mm). Concrete mixture proportions are listed in Table 3.2.

The measured concrete compressive strengths, listed in Table 3.3, were obtained from tests of standard concrete cylinders following ASTM standards. Each value is the average results from compressive tests on three 4-in. by 8-in. (100-mm by 200-mm) cylinders conducted on the test dates. Test day values of f_{cm} are used for analysis of results.

Table 3.2 - Batched proportions (per cubic yard) for concrete mixture (1 lb = 0.45 kg, 1 in. = 25.4 mm)

ID	Water	Cementitious Material (*CM*)		Aggregate			Admixtures		Water/ *CM* [h]	Initial Slump	Spread
		Cement [a]	Fly Ash [b]	Fine [c]	Coarse A [d]	Coarse B [e]	Retarder [f]	Water Reducer [g]			
	lb	lb	lb	lb	lb	lb	oz	oz		in.	in.
CB1	284	649	150	1208	507	1177	24	35	0.40	9	18.5
CB2	230	748	0	1727	1111	0	0	30	0.39	6.25	
CB2D	286	647	150	1196	503	1177	24	35	0.40	11	23
CB2AD	284	649	150	1208	507	1177	24	35	0.40	9	18.5
CB3D	286	647	150	1196	503	1177	24	35	0.40	11	23

[a] Type I Portland Cement
[b] Class C
[c] Kansas River sand, meets ASTM C33/C33M-16 requirements for fine aggregate
[d] Pea gravel, maximum aggregate size of 3/8 in. (10 mm)
[e] Crushed limestone, maximum aggregate size of 3/4 in. (19 mm)
[f] Set retarder (compliant with ASTM C494/C494M-16)
[g] High-range water-reducing admixture (compliant with ASTM C494/C494M-16)
[h] Calculated by dividing the weight of water in one cubic yard of concrete, including corrections to account for aggregate moisture content, by total weight of cement and fly ash

Table 3.3 - Concrete strength on the day of testing

Specimen ID	Specified Compressive Strength f_c' psi (MPa)	Compressive Strength at Test Day f_{cm} [a,b] psi (MPa)
CB1	6000 (41)	5990 (41)
CB2		7190 (50)
CB2D		6310 (44)
CB2AD		5640 (39)
CB3D		6180 (43)

[a] Measured from laboratory tests following ASTM C39/39M-17a.
[b] Cylinder size of 4 by 8 in. (100 by 200 mm), reported value is average of three.

3.1.2.2 REINFORCING STEEL

Deformed mild-steel bars were used for all reinforcement. Mill certifications for reinforcing bars used as conventional Grade 60 (420) steel showed compliance with ASTM A706/A706M-15 (2015) Grade 60 (420). Mill certifications for reinforcing bars used as Grade 120 (830) showed compliance with ASTM A1035-16a Grade 120 (830). Reinforcing bar mechanical properties, shown in Table 3.4, were obtained from tensile tests in accordance with ASTM A370-17 and ASTM E8-16a. Figure 3.3 shows samples of tensile test data.

Table 3.4 – Reinforcing steel properties

Bar Size	Nominal Bar Diameter	Yield Stress	Tensile Strength	Uniform Elongation	Fracture Elongation
	d_b	f_y [a]	f_t [a]	ε_{su} [b]	ε_{sf} [c]
No.	in. (mm)	ksi (MPa)	ksi (MPa)		
7 (22)	0.875 (22.2)	63 (434)	90 (621)	12.8%	20.5%
6 (19)	0.750 (19.1)	128 (883)	168 (1158)	5.3%	10.0%
3 (10)[d]	0.375 (9.5)	69 (476)	107 (738)	10.2%	13.0%
3 (10)[e]	0.375 (9.5)	68 (469)	105 (724)	10.8%	12.9%

[a] Measured from laboratory tests following ASTM A370-17.
[b] Corresponds to strain at peak stress following ASTM E8/E8M-16a.
[c] Determined from stress-strain curve as the intersection of the horizontal axis and a line passing through the fracture point with a slope equal to the measured elastic modulus.
[d] Used for the secondary (non-diagonal) longitudinal reinforcement.
[e] Used for the hoops and crossties.

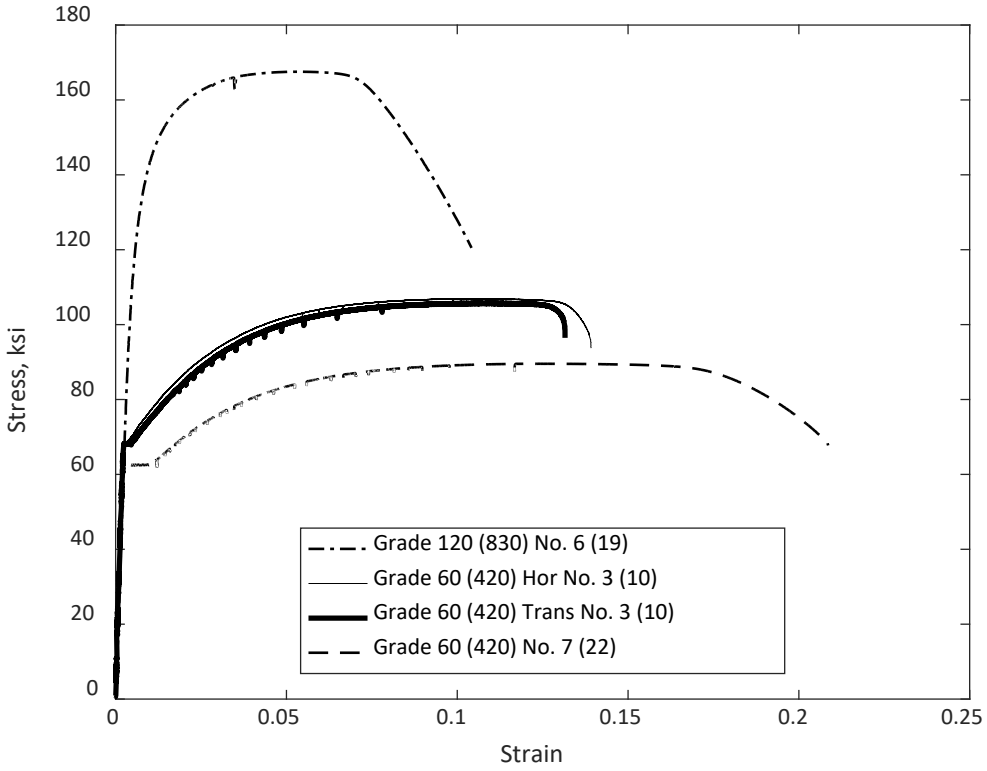

Figure 3.3 – Measured stress versus strain for diagonal bars (1 ksi = 6.89 MPa)

3.1.3 CONSTRUCTION

Photos of the various stages of specimen construction are provided in Appendix A from Figure A.1 through Figure A.11. Construction of each specimen included the assembly of reinforcing bar cages, preparation and erection of wooden formwork, and placement of the concrete. Concrete for the specimen and the top and bottom blocks was placed monolithically (while laying horizontally). After finishing the concrete, specimens and cylinders were covered with wet burlap and plastic sheets until removal of the formwork, which typically occurred three to four days after casting. After formwork was removed, all specimens were kept in the laboratory until they were tested.

CB1 was constructed using Grade 60 (420) diagonal reinforcement, whereas CB2, CB2D, CB2AD, and CB3D were constructed using Grade 120 (830) diagonal reinforcement. The bottom and top blocks of all specimens were built with nominally identical detailing using Grade 60 (420) reinforcement. Two steel pipes with outer diameters of 6.63 in. (170 mm) and inner diameters of 6.07 in. (155 mm) were cast into the blocks for CB2AD to accommodate the axial restraint fixtures described in Section 3.2 (Figure A.8).

3.2 TEST SETUP

The general test setup is shown in Figure 3.4. For testing, the bottom block of each specimen was bolted to the laboratory strong floor with two 2.5-in. (64-mm) diameter high-strength threaded rods passing through the bottom block (Figure 3.4). To distribute the hold-down forces, each of the threaded rods was connected to a steel spreader beam under the strong floor. Two MTS 201.70 hydraulic actuators were used to load the specimens. Each actuator has a stroke length of 40 in. (1020 mm) and a force capacity of 220 kips (980 kN). The two actuators were connected to the laboratory strong wall and the specimen top block through vertically oriented HP steel sections. The HP section closest to the specimen was connected to the top block with a pair of hollow structural steel (HSS) sections for transmitting compression and six 2.26-in. (57-mm) diameter high-strength threaded rods for transmitting tension (Figure 3.4). Additional steel fixtures were used to brace the HP section against out-of-plane motion (Figure 3.4). Steel plates with a mirror finish (attached to the HP section) and nylon pads (attached to the bracing) were used to minimize frictional forces.

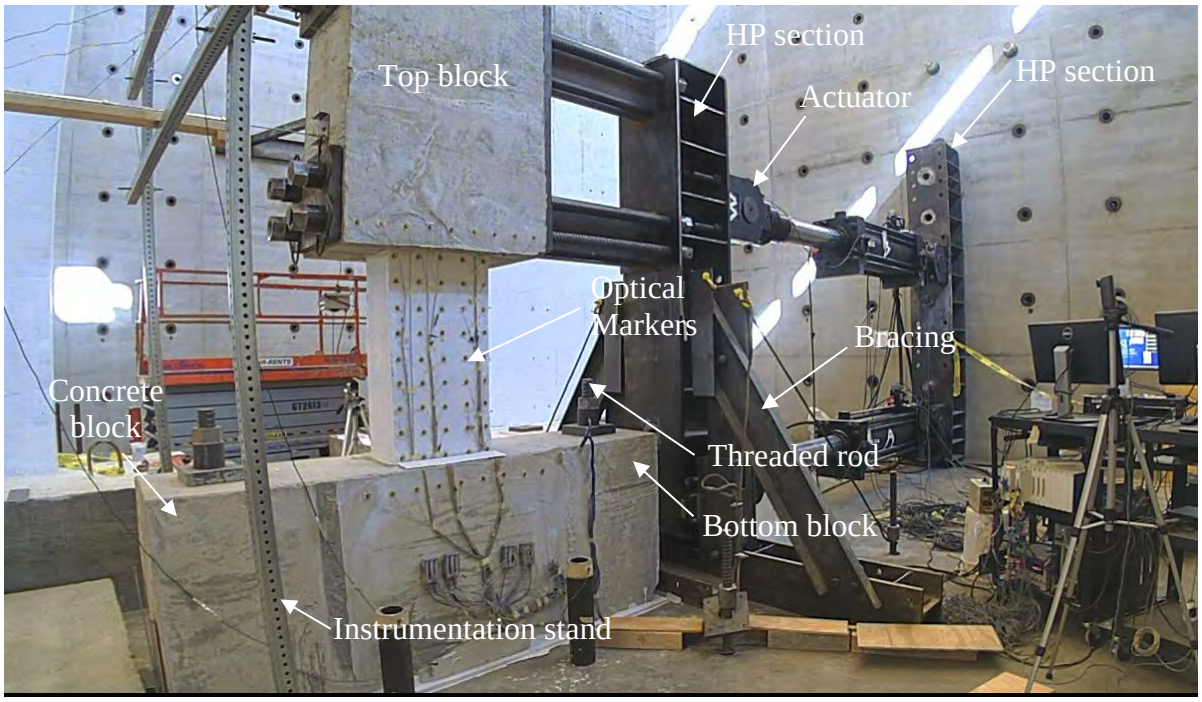

Figure 3.4 – General test setup

To minimize sliding of the bottom block relative to the strong floor in the positive loading direction, a 100 by 68 by 10-in. (2540 by 1730 by 250-mm) concrete block was bolted to the strong floor next to the specimen using six 1.75-in. (44-mm) diameter high-strength threaded rods. Shim plates were inserted between this block and the specimen bottom block prior to testing. A wide-flanged section (that was also part of the bracing) was used in a similar manner to reduce sliding in the negative loading direction.

In addition to these, the test setup for CB2AD had two 3.0-in. (75-mm) diameter high-strength threaded rods connecting the top and bottom blocks on both sides to restrain any axial growth (Figures 3.5 and 3.6). Two steel pipes with outer diameters of 6.63 in. (170 mm) and inner diameters of 6.07 in. (155 mm) were placed within the top and bottom blocks during casting. Before testing, two 5.0-in. (125-mm) diameter Gr. 50 solid steel rods were passed through those steel pipes. The two 3.0-in. (75-mm) diameter high-strength threaded rods were attached at both

ends to steel fixtures that rotated freely around the 5.0-in. (125-mm) diameter steel rods while maintaining restraint against axial growth. Figure 3.7 shows the details of the steel fixtures.

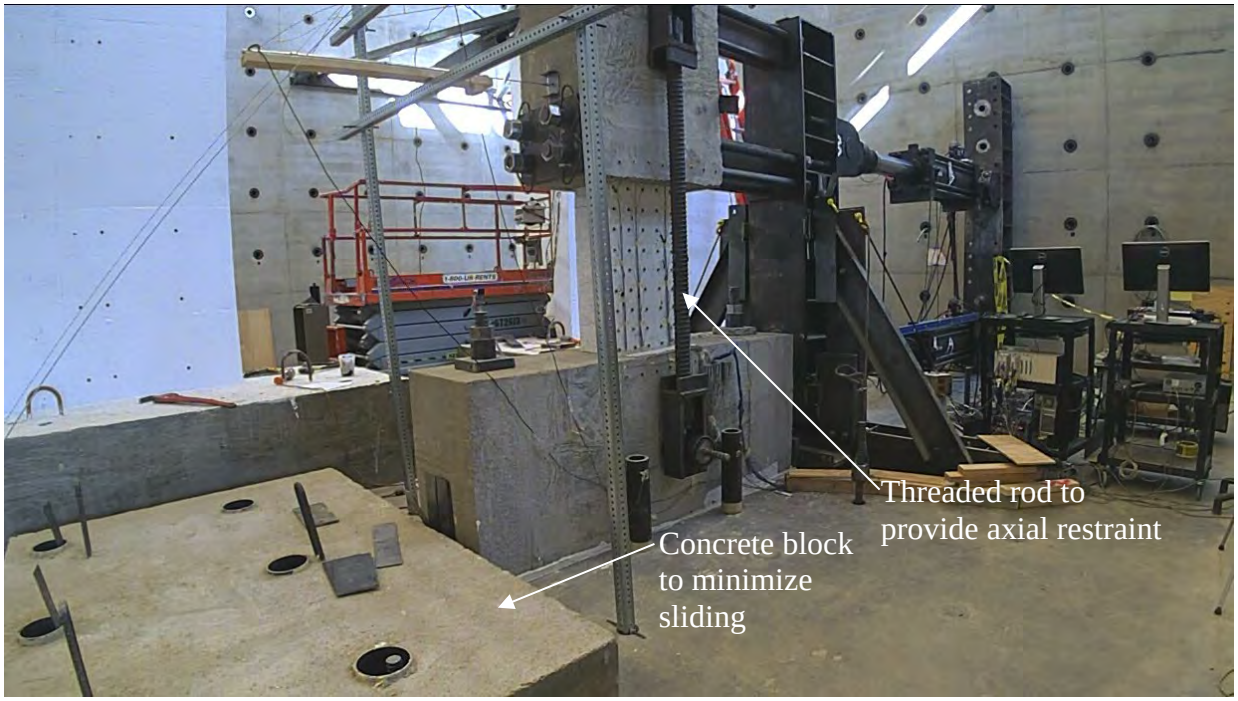

Figure 3.5 – Axially-restrained test setup for CB2AD

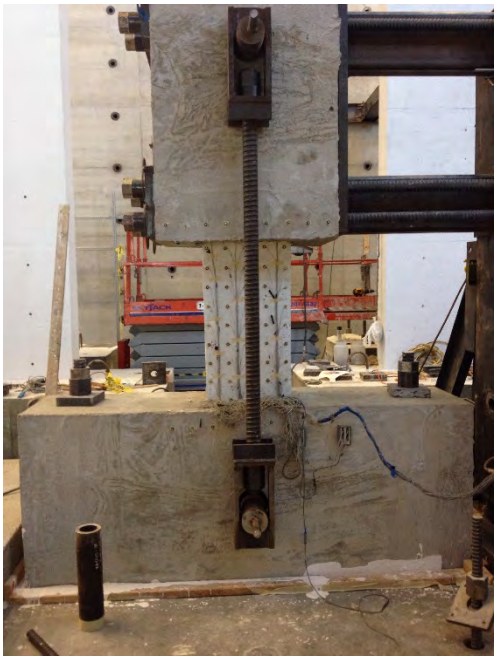

Figure 3.6 – Fixture for axial restraint of CB2AD

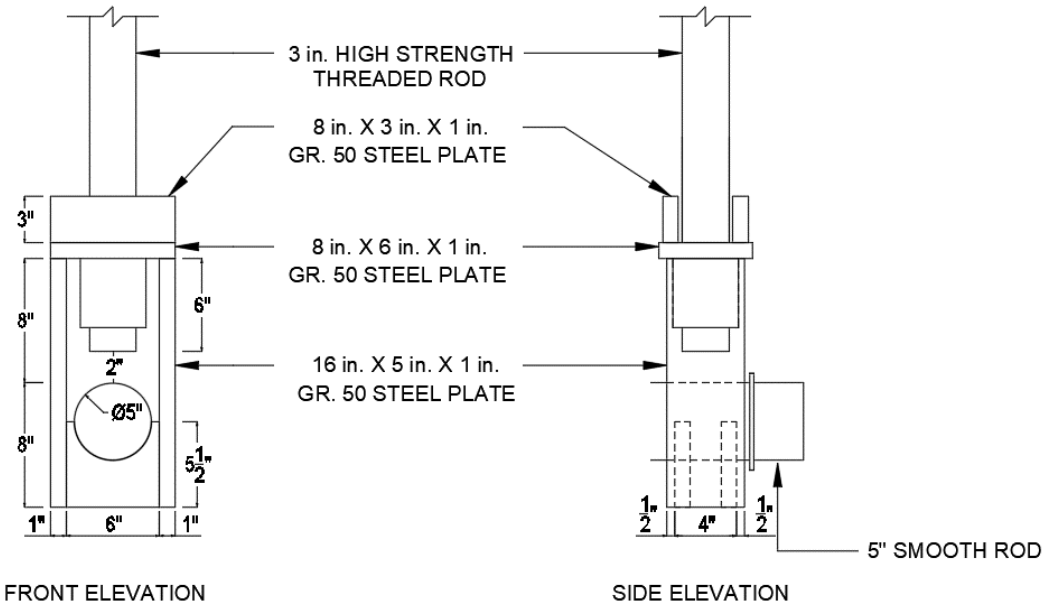

Figure 3.7 – Details of fixture for axial restraint of CB2AD (1 in. = 25.4 mm)

3.3 INSTRUMENTATION

Several instruments were used to record deformations of the specimens. An infrared-based non-contact position measurement system was used to record the position of 59 markers, attached to the surface of the specimens, which emit infrared light pulses that are detected by cameras. The spatial coordinates of the markers were triangulated and recorded throughout the tests at a selected frequency. The markers were arranged in a 4-in. (100-mm) square grid on one face of the coupling beam and part of the top and bottom blocks (Figure 3.8). Data from this system were analyzed to determine the distribution of deformations.

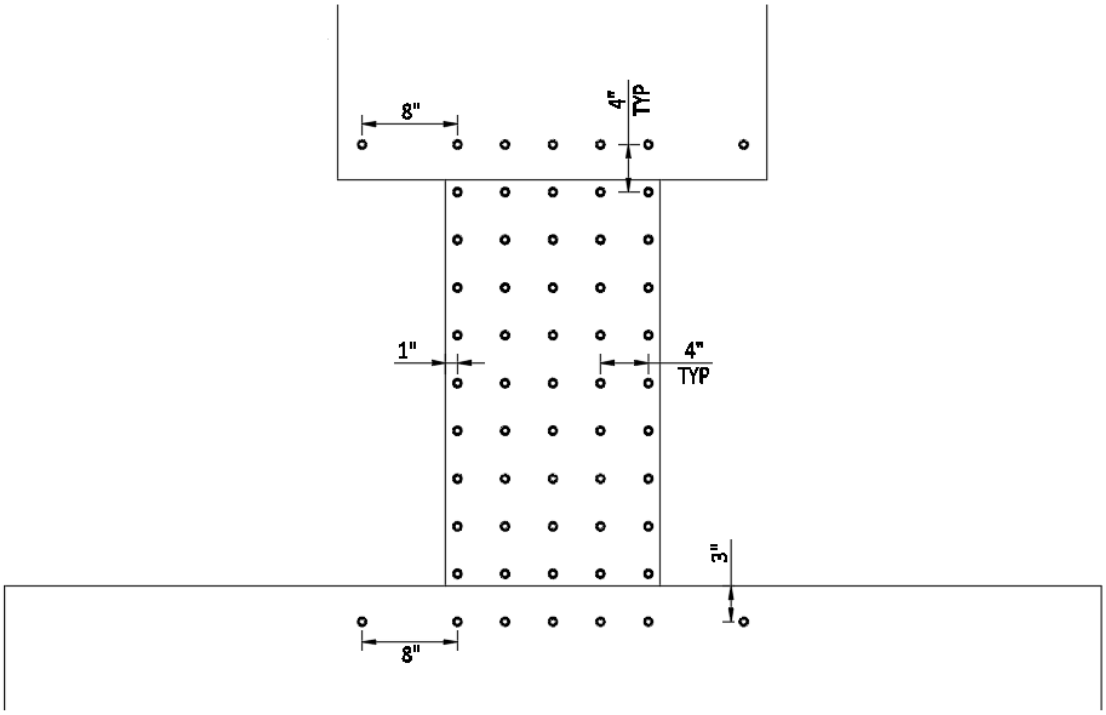

Figure 3.8 – Optical marker positions (1 in. = 25.4 mm)

In addition to the infrared markers, seven potentiometers were used during the test of CB2 (which was constructed and tested before the other four) as a redundant measuring system. Throughout the tests, lateral deflection of the top block was measured with two potentiometers installed horizontally on opposite sides. To measure the rotation of the top block with respect to the bottom block, two potentiometers were positioned vertically connecting the top and bottom blocks. Three potentiometers (two vertical and one horizontal) were used to monitor rotation and sliding of the bottom block relative to the strong floor. The readings from these potentiometers were found to be less precise than measurements based on the infrared marker positions. As a result, these potentiometers were not used in the later tests. Instead, two LVDTs (linear variable differential transformers) were attached to the end of the top block to measure lateral deflection

and rotation along with the infrared optical system for the other four tests (CB1, CB2D, CB2AD, and CB3D). The location of the external instrumentation is shown in Figure 3.9.

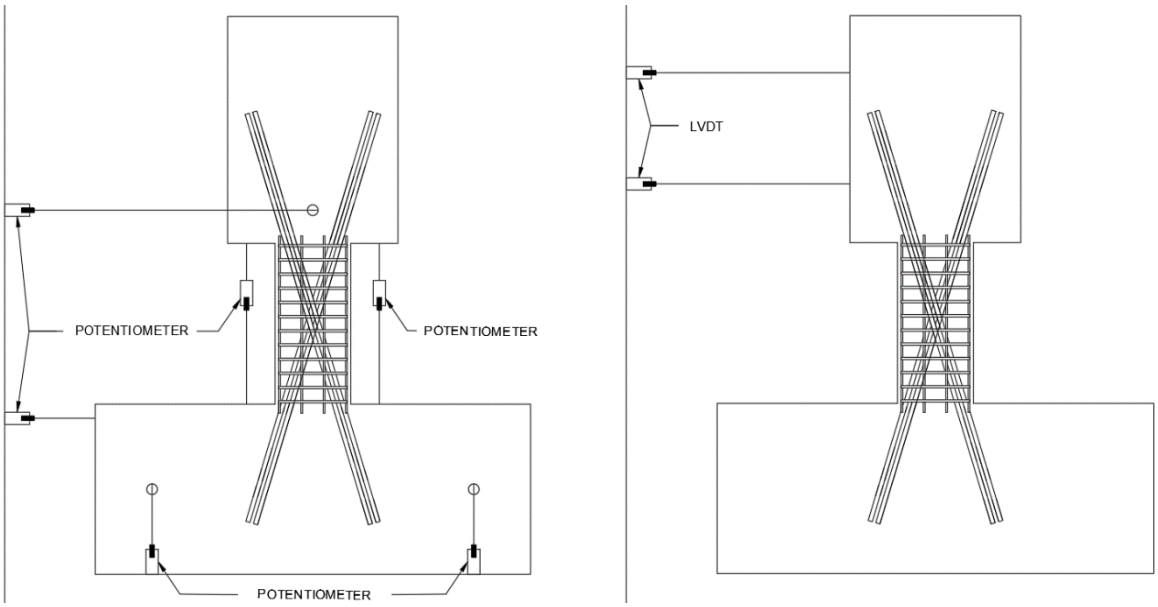

(a) CB2 (b) CB1, CB2D, CB2AD, CB3D

Figure 3.9 – Instrumentation

Diagonal, transverse, and longitudinal reinforcing bars were instrumented with 28 120-ohm electrical resistance strain gauges placed at the locations shown in Figure 3.10 (also shown in Figure D.1, Figure D.62 and Figure D.88). In each specimen, two diagonal bars were instrumented with six strain gauges each, eleven strain gauges were attached to the outside perimeter of hoops and on crossties, and two of the No. 3 (10) longitudinal bars were instrumented with five strain gauges (three to one, and two to the other. The strain gauges were rated for 15% strain to allow measurements throughout the test.

For the test of CB2AD, two strain gauges were attached to each of the two 3-in. (75-mm) diameter threaded rods for calculation of the restraining force.

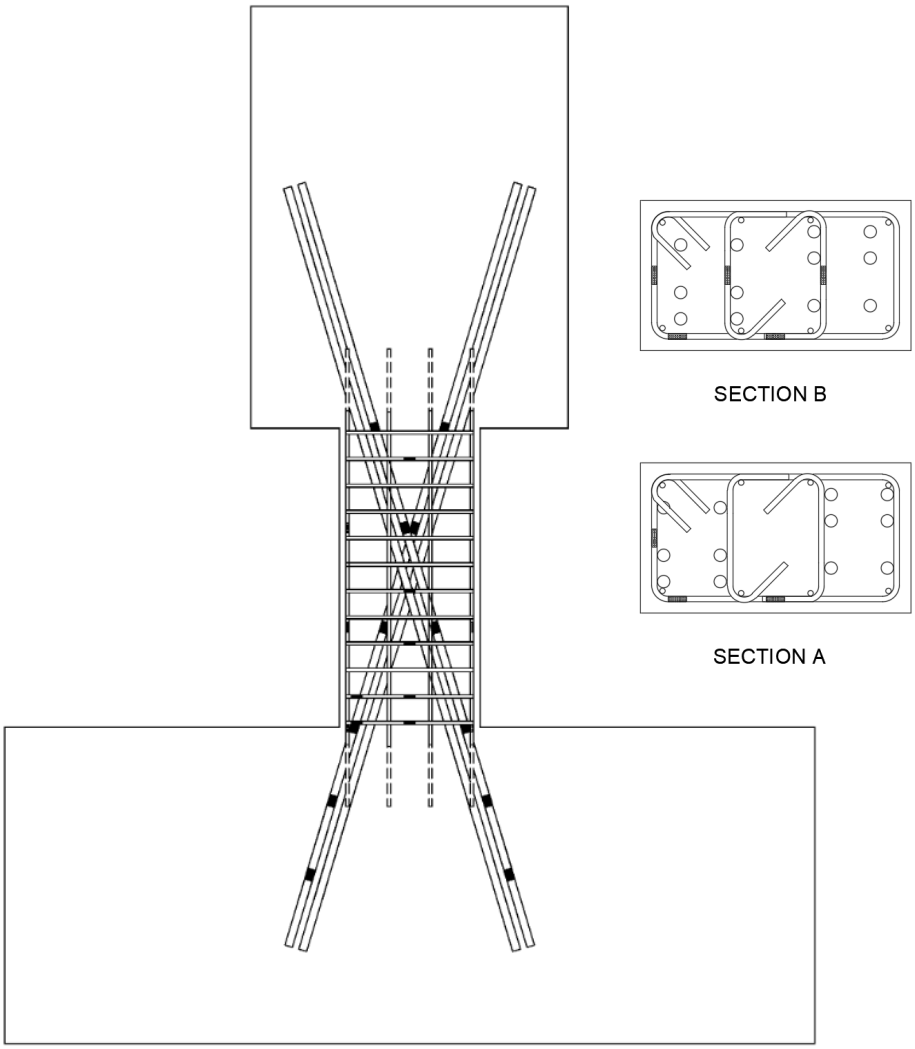

Figure 3.10 – Strain gauge layout

3.4 LOADING PROTOCOL

Specimens were subjected to a series of reversed cyclic displacements following the protocol shown in Table 3.5 and Figure 3.11, which is patterned after the protocol recommended in FEMA 461 (2007). To overcome imprecision of relatively small displacement measurements, force-based control was used prior to yielding of the diagonal reinforcement; force was increased until the chord rotation was approximately equal to the target values in Table 3.5 and the loading direction

was then reversed. The remaining cycles were imposed using displacement control. The ratio between forces or displacements applied by the two actuators was selected such that an inflection point remained near mid-span of the coupling beam throughout the tests (beams were bent in double-curvature).

Table 3.5 – Loading protocol

Step [a]	1	2	3	4	5	6	7	8	9	10	11	12	13
CR [b] %	0.2	0.3	0.5	0.75	1.0	1.5	2.0	3.0	4.0	5.0	6.0	8.0	10.0

[a] Two cycles of loading in each step, following recommendations in FEMA 461.

[b] Chord rotation, defined as the relative lateral displacement between end blocks divided by the beam clear span and accounting for relative rotation between the bottom and top blocks as described in Section 4.1.1.

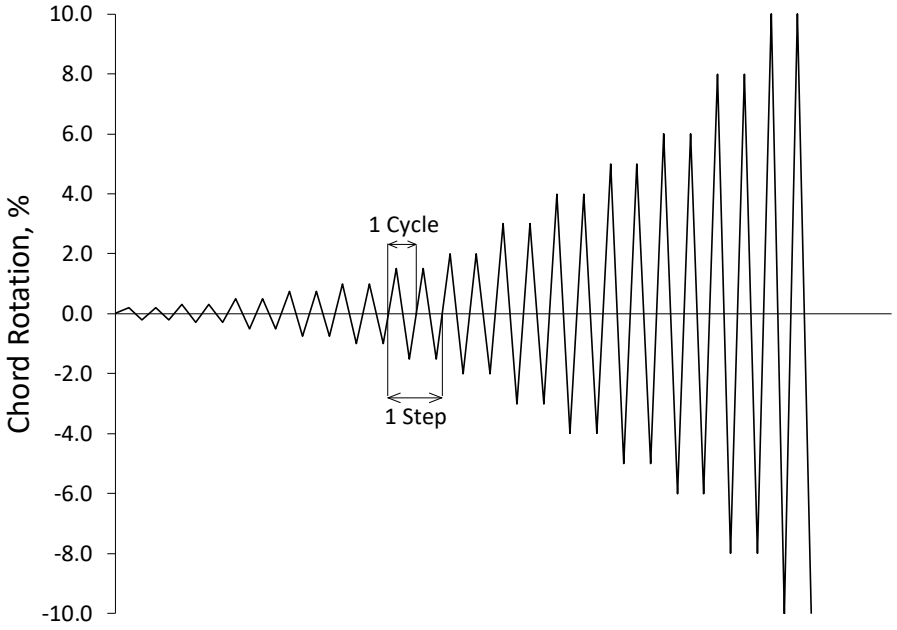

Figure 3.11 – Loading protocol

As can be seen in Figure 3.4, the weight of all the fixtures (HP, HSS, and actuators) hung off one side of the specimen, causing a uniform moment in the beam of approximately 42 ft-kips (57 m-kN) prior to loading. To counteract this moment and start from a neutral point, an approximately equal and opposite moment was applied using the actuators before the start of the test.

The loading rate for chord rotations up to 1% was approximately 0.01 in./sec (0.25 mm/sec); the rate was increased to 0.02 in./sec (0.51 mm/sec) for larger chord rotations. Prior to testing, several small cycles were imposed (with forces below the cracking load) to facilitate tightening of the threaded rods connecting the bottom block to the strong floor and the top block to the actuators.

CHAPTER 4 RESULTS AND OBSERVATIONS

4.1 SHEAR VERSUS CHORD ROTATION

4.1.1 CHORD ROTATION

Beam chord rotation, CR, is defined as the relative displacement between top and bottom blocks, corrected for rotation of both top and bottom blocks, divided by the clear span of the beam (Eq. 4.1).

$$CR = \frac{\delta_{top} - \delta_{bottom}}{\ell_n} - \frac{\theta_{z,TB} + \theta_{z,BB}}{2} \quad \text{Eq. 4.1}$$

In Figure 4.1, θ_{top} is negative and all other values are positive. Displacements and rotations were calculated using data from the infrared-based non-contact position measurement system (Section 3.3).

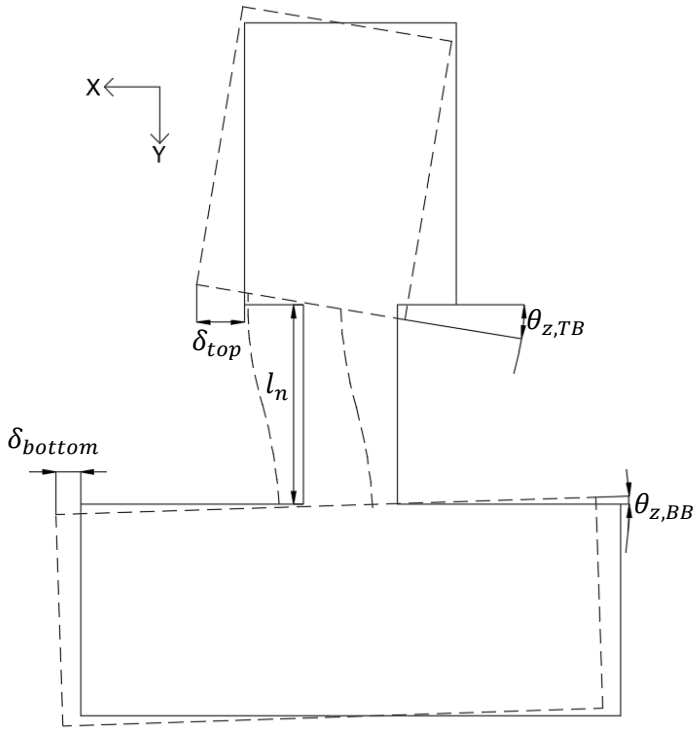

Figure 4.1 – Deformed shape of coupling beam

However, top and bottom block displacements were not measured at the beam-wall interface. They were measured 3 in. (75 mm) above the bottom of the top block and 3 in. (75 mm) below the top of the bottom block. To correct for the effects of the instrumentation placement, δ_{top} was replaced with $\left(\delta_{top,m} - (3\text{ in.})\theta_{z,TB}\right)$, where the *m* subscript refers to the measured value, and δ_{bottom} was replaced with $\left(\delta_{bottom,m} + (3\text{ in.})\theta_{z,BB}\right)$. With these substitutions, and inserting 34 in. (860 mm) in place of ℓ_n, Eq. 4.1 becomes Eq. 4.2.

$$CR = \frac{\delta_{top,m} - \delta_{bottom,m} - (20\ in.)\theta_{z,TB} - (20\ in.)\theta_{z,BB}}{34\ in.} \qquad \text{Eq. 4.2}$$

4.1.2 SPECIMEN RESPONSE AND OBSERVATIONS

Each of the five coupling beam specimens described in Chapter 3 was subjected to the loading history shown in Figure 3.11. The measured shear force versus chord rotation is plotted in Figures 4.2 through 4.6 for each specimen. Photos of the specimens during and after testing are shown in Appendix B. The progression of damage will be discussed in more detail in Section 4.2.

4.1.2.1 CB1

The control specimen, CB1, completed two cycles at 6% chord rotation while retaining more than 80% of its peak strength (Figure 4.2). One of the 12 No. 7 (22 mm) diagonal bars and several longitudinal bars fractured during the first excursion to 8% chord rotation at approximately 6% chord rotation (Figure B.23, Figure B.24). The specimen completed two cycles at a target chord rotation of 8% but the force dropped below 40% of the peak load in the second cycle due to bar fracture and severe damage to the concrete core. The test was stopped during the first excursion to 10% chord rotation due to limitations of the testing apparatus.

Reinforcement buckling preceded bar fracture. Buckling of the longitudinal bars was first observed during the first cycle to -5% chord rotation (Figure B.21). This buckled bar never fractured. Buckling of a diagonal bar was first observed during the first cycle to -6% chord rotation (Figure B.22). That same diagonal bar fractured during the first excursion to 8% chord rotation.

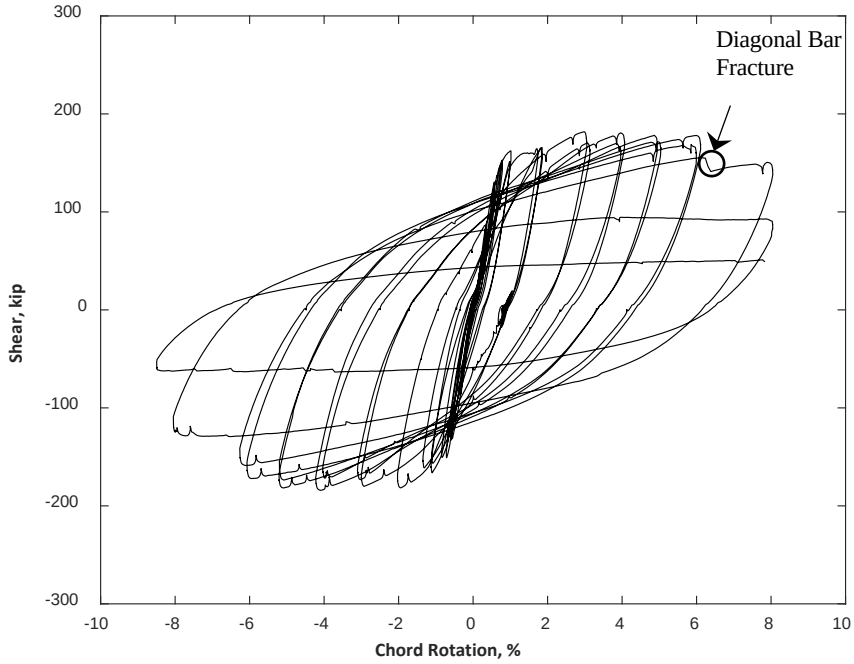

Figure 4.2 – Shear versus chord rotation for CB1 (1 kip = 4.45 kN)

The maximum shear forces resisted by the specimen were 182 and -184 kips (810 and -820 kN) at chord rotations of +3.0 and -4.1%, respectively. The maximum shear force resisted by the specimen corresponds to a shear stress of $13.2\sqrt{f_{cm}}$ [psi] ($1.10\sqrt{f_{cm}}$ [MPa]).

4.1.2.2 CB2

The measured shear versus chord rotation response for CB2 is shown in Figure 4.3. The specimen retained more than 80% of its peak strength in both loading directions until the final push towards +6% chord rotation. Failure of the specimen was sudden and dominated by fracture of two of the 8 No. 6 (19 mm) diagonal bars (Figure B.25). Though the shape of the fractured and adjacent bars observed after testing indicated that bar fracture was preceded by bar buckling, no buckling was observed during testing.

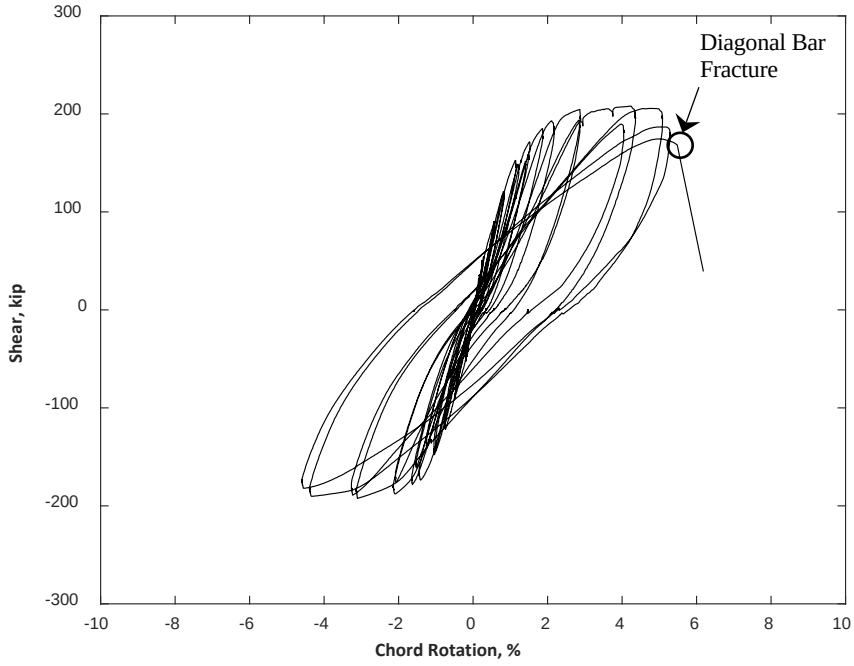

Figure 4.3– Shear versus chord rotation for CB2 (1 kip = 4.45 kN)

The maximum shear forces resisted by the specimen were 207 and -192 kips (920 and -850 kN) in the positive and negative loading directions, respectively. The maximum shear corresponds to a shear stress of $13.6\sqrt{f_{cm}}$ [psi] ($1.13\sqrt{f_{cm}}$ [MPa]). The peak forces occurred at chord rotations of +4.2 and -3.1%.

4.1.2.3 CB2D

The measured shear versus chord rotation plot for CB2D is shown in Figure 4.4. The specimen completed one cycle at 5% chord rotation with while retaining more than 80% of its peak strength. Strength dropped below 80% of peak strength during the second excursion to -5% chord rotation due to the buckling of diagonal bars (Figure B.27). The secondary (non-diagonal) longitudinal bars first fractured during the second excursion to +5% chord rotation (Figure B.26).

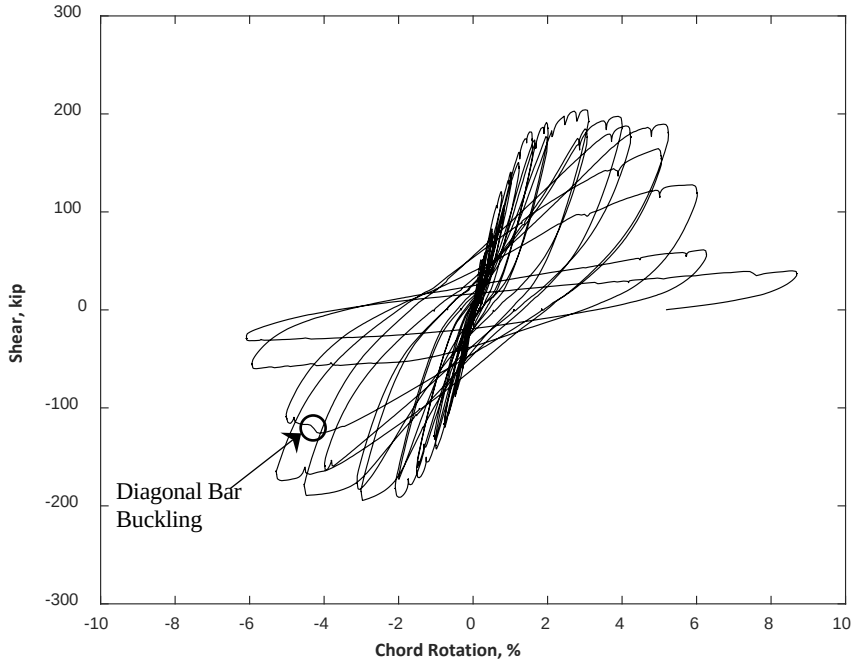

Figure 4.4 – Shear versus chord rotation for CB2D (1 kip = 4.45 kN)

During the cycles to 6% chord rotation, CB2D exhibited a large reduction in strength, with peak strengths in the second cycle to 6% chord rotation reaching approximately 30% of the maximum strength. During these cycles, most of the secondary (non-diagonal) longitudinal bars fractured. All the diagonal bars exhibited buckling, but none of them fractured. The failure mechanism of CB2D was thus different from that of CB1 and CB2, which had a similar target shear stress but terminated secondary (non-diagonal) longitudinal bars. CB2D exhibited less concentrated damage at the face of the wall but damage to the concrete core was more extensive (Figure 4.7). The test was stopped after passing 8% chord rotation as the force dropped below 20% of the peak load.

The maximum shear forces resisted by the specimen were 204 and -194 kips (910 and -860 kN) in the positive and negative loading directions, respectively. In both directions, the corresponding chord rotation was 3.0%. The maximum shear force resisted by the specimen

corresponds to a shear stress of $14.3\sqrt{f_{cm}}$ [psi] ($1.20\sqrt{f_{cm}}$ [MPa]), 5% higher than that of CB2, which was identical to CB2D except the secondary (non-diagonal) longitudinal bars were terminated 2 in. (50 mm) from the beam-wall interface.

4.1.2.4 CB2AD

The measured shear is plotted versus chord rotation for CB2AD in Figure 4.5. Strength dropped below 80% of the peak during the second excursion to +5% chord rotation due to buckling of most of the longitudinal (Figure B.28) and diagonal bars (Figure B.29). The failure mechanism of the beam was similar to that of CB2D, where most of the secondary (non-diagonal) longitudinal bars fractured but none of the diagonal bars fractured. The test was stopped when the force dropped to approximately 20% of the peak load after passing 6% chord rotation.

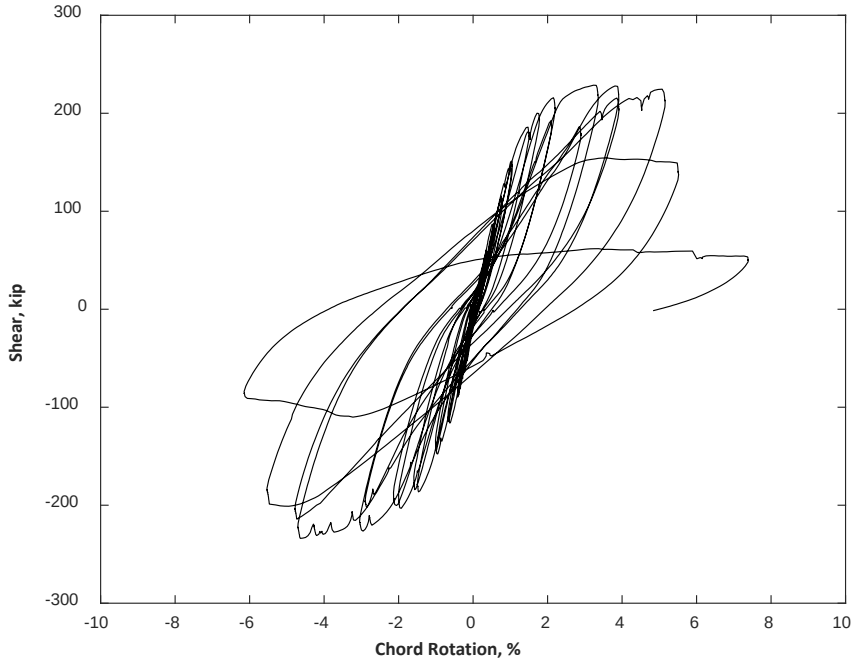

Figure 4.5 – Shear versus chord rotation for CB2AD (1 kip = 4.45 kN)

The maximum shear forces resisted by the specimen were 228 and -234 kips (1010 and -1040 kN) at chord rotations of +3.2 and -4.7%, respectively. The maximum shear force resisted by the specimen corresponds to a shear stress of $17.4\sqrt{f_{cm}}$ [psi] ($1.50\sqrt{f_{cm}}$ [MPa]), which is 28 and 22% higher than that of CB2 and CB2D, respectively. This high shear stress resulted from the axial restraint.

4.1.2.5 CB3D

A plot of measured shear versus chord rotation is shown in Figure 4.6 for CB3D. The specimen completed two cycles at 5% chord rotation while retaining more than 80% of its peak strength. During the first excursion to -6% chord rotation, strength suddenly dropped below 80% due to simultaneous buckling of three of the 12 No. 6 (19 mm) diagonal bars (Figure B.31). The secondary (non-diagonal) longitudinal bars had previously buckled during the second cycle to -4% chord rotation (Figure B.30), which was at a smaller chord rotation than in any of the other tests. Though, like CB2D and CB2AD, the specimen had secondary (non-diagonal) longitudinal bars developed satisfying the ACI 318-14 code requirement for development length, strength loss was not as gradual as observed in those two specimens.

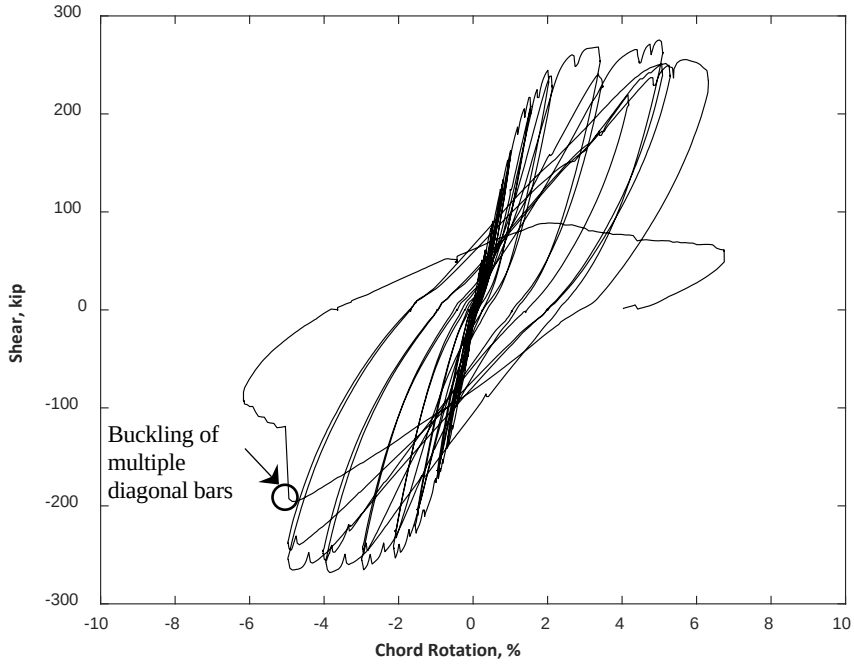

Figure 4.6 – Shear versus chord rotation for CB3D (1 kip = 4.45 kN)

The maximum shear forces resisted by the specimen were 275 and -268 kips (1220 and -1190 kN) at chord rotations of +5.0 and -3.8%, respectively. The maximum shear force resisted by the specimen corresponds to a shear stress of $19.4\sqrt{f_{cm}}$ [psi] ($1.63\sqrt{f_{cm}}$ [MPa]).

4.1.3 BEAM STRENGTH AND CHORD ROTATION CAPACITY

Table 4.1 shows the maximum measured shear force and the chord rotation capacity for each specimen. The chord rotation capacity of a specimen is defined herein as the average of the maximum chord rotations imposed in each loading direction without more than a 20% reduction in shear strength. According to this definition, CB1 had a chord rotation capacity of 7.1% (8.0% in one direction and 6.3% in the other). CB2, CB2D, and CB2AD exhibited chord rotation capacities of 5.1% (5.6% and 4.5%), 5.3% (same in both directions), and 5.3% (5.1% and 5.5%)

respectively. For CB3D, the chord rotation capacity was calculated as 5.6% (6.3% in one direction and 5.0% in the other).

Table 4.1 – Maximum measured shear force and chord rotation

Specimen ID	V_{max} [a] kips (kN)		$v_{max}/\sqrt{f_{cm}}$ [b] psi (MPa)		CR_{max} [c] %		CR_{cap} [d] %
	−	+	−	+	−	+	
CB1	184 (820)	182 (810)	13.2 (1.10)	13.1 (1.10)	6.3	8.0	7.1
CB2	192 (920)	207 (920)	12.6 (1.05)	13.6 (1.13)	4.5	5.6	5.1
CB2D	194 (860)	204 (910)	13.6 (1.13)	14.3 (1.20)	5.3	5.3	5.3
CB2AD	234 (1040)	228 (1010)	17.4 (1.50)	17.0 (1.42)	5.5	5.1	5.3
CB3D	268 (1190)	275 (1220)	18.9 (1.58)	19.4 (1.63)	5.0	6.3	5.6

[a] Maximum measured shear force per loading direction.
[b] Shear stress calculated as $V_{max}/(bh)$ divided by $\sqrt{f_{cm}}$, where $b = 10$ in. (250 mm), $h = 18$ in. (460 mm), and f_{cm} is taken from Table 3.3.
[c] Maximum chord rotation attained in a loading direction while maintaining a shear force not less than $0.8V_{max}$.
[d] Chord rotation capacity obtained from the average of CR_{max}.

Another definition of chord rotation capacity was used that is based on the envelope drawn to the point of maximum chord rotation reached in the first cycle to each target chord rotation. This manner of constructing a backbone curve is consistent with procedures in Section 7.6 of ASCE-SEI 41-17. Chord rotation capacity was then taken as the average chord rotation at which the backbone curve first dropped below 80% of the peak force in each loading direction. Using this second definition, CB1 had a chord rotation capacity of 7.4%, and CB2, CB2D, CB2AD, and CB3D had chord rotation capacities of 5.1%, 5.4%, 5.4%, and 5.6%, respectively. Chord rotation capacities determined according to this definition were either equal to or slightly larger than the values obtained using the prior definition. Trends among specimens were similar regardless.

According to both definitions, chord rotation capacities exhibited by specimens with Grade 120 (830) diagonal reinforcement were between 5.1 and 5.6%. These were smaller than that exhibited by the control specimen with Grade 60 (420) diagonal reinforcement (7.1% and 7.4% by two definitions). This reduction in chord rotation capacity of specimens with Grade 120 (830) diagonal reinforcement may be due to the larger transverse reinforcement spacing in terms of d_b ($4d_b$ versus $3.4d_b$). For the Grade 60 and 120 (420 and 830) bars to be similarly prone to buckling, the transverse reinforcement spacing would have needed to be $6d_b$ and $4d_b$, respectively.

4.2 PROGRESSION OF DAMAGE

Photographs in Figure B.1 through Figure B.20 in Appendix B show the condition of the specimens at peak chord rotations during the second cycle to target chord rotations of 2, 3, 4 and 5% (actual chord rotations are provided below each figure). Horizontal cracking associated with flexure was observed on the two 10-in. (250-mm) sides of the beams at both ends of the specimens. Inclined cracks were observed on the 18-in. (460-mm) faces that, in most cases, connected to horizontal cracks on the 10-in. (250-mm) sides. The first cracks occurred at a chord rotation of approximately 0.2%. New cracks developed through chord rotations of approximately 4%, after which existing cracks continued to widen, but new cracks were not observed.

Figure 4.7 shows all the specimens at a chord rotation of approximately 5%. It is evident in Figure 4.7 that in CB1 and CB2, deformations concentrated near the beam-to-wall interface where the diagonal bars buckled and then ultimately fractured. In CB2D, CB2AD, and CB3D, damage was more distributed throughout the span of the beam. This difference is attributed to the choice of whether to terminate or continue the secondary (non-diagonal) longitudinal reinforcing

bars beyond the beam-wall interface. Where secondary longitudinal bars were terminated near the beam-wall interface, deformations concentrated near the interface.

As the chord rotation demands increased in accordance with the loading protocol (Figure 3.11), each of the specimens exhibited buckling and/or fracture of reinforcement. Table 4.2 identifies the target chord rotation cycles where bar buckling or bar fracture was first observed during the test of each coupling beam specimen. Buckling and/or fracture of diagonal and longitudinal bars are treated independently in Table 4.2. Figure B.21 through Figure B.31 show most of the events (bar buckling and bar fracture) identified in Table 4.2.

Buckling of diagonal reinforcement was first observed during the second cycle to a chord rotation of +5% for CB2AD, second cycle to a chord rotation of -5% for CB2D, and first cycle to a chord rotation of -6% for CB1 and CB3D. No visible buckling of diagonal reinforcement was observed for CB2, though the shape of the bars near the fractured bar, observed after testing, indicates that buckling occurred. Fracture of diagonal reinforcement was first observed during the first cycle to +6% chord rotation for CB2 and +8% chord rotation for CB1. The other three specimens (CB2D, CB2AD, and CB3D) clearly exhibited buckling of the diagonal bars, but none of them fractured. Because of the embedment length of the secondary (non-diagonal) longitudinal reinforcing bars, these specimens exhibited more extensive damage within the beam span and less fracture of bars at the wall connection.

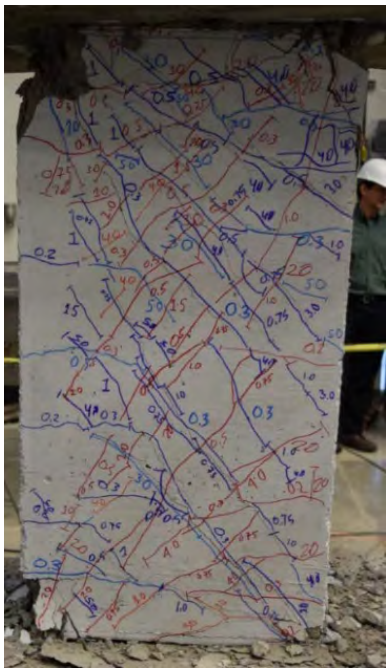

CB1 (5.0%)

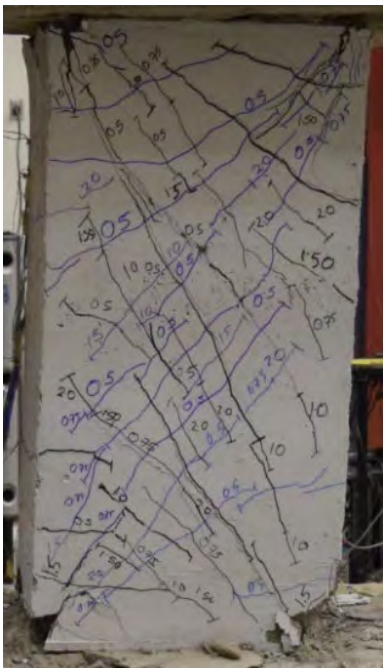

CB2 (5.2%)

CB2D (5.2%)

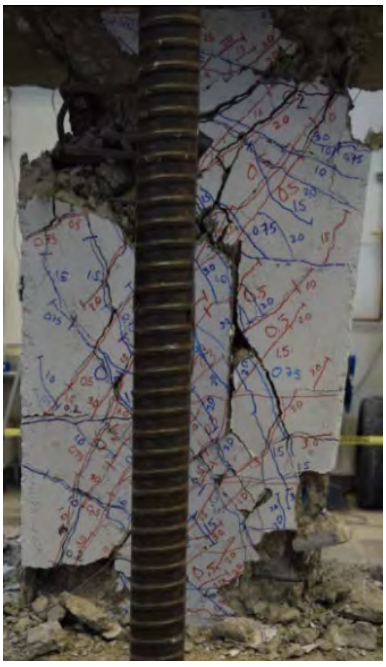

CB2AD (5.5%)

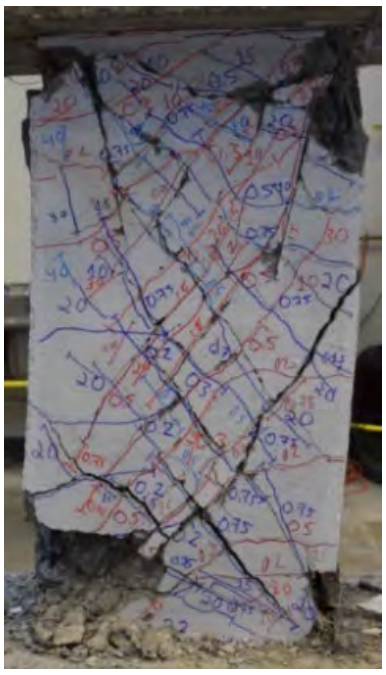

CB3D (5.4%)

Figure 4.7 – Specimens at approximately 5% chord rotation

Table 4.2 – Target chord rotation of the cycle when bar buckling or bar fracture was first observed

Specimen ID	Bar Type	Target Chord Rotation Cycle [a]													
		4%				5%				6%				8%	
		i+	i–	ii+	ii–	i+	i–	ii+	ii–	i+	i–	ii+	ii–	i+	i–
CB1	Diagonal										B			F	
	Longitudinal						B							F	
CB2	Diagonal					F									
	Longitudinal														
CB2D	Diagonal								B						
	Longitudinal					F									
CB2AD	Diagonal							B							
	Longitudinal							B							
CB3D	Diagonal										B				
	Longitudinal				B	F									

[a] Notation:
i+: first cycle in positive loading direction;
i–: first cycle in negative loading direction;
ii+: second cycle in positive loading direction;
ii–: second cycle in negative loading direction;
B: bar buckling;
F: bar fracture.

4.3 CALCULATED AND MEASURED STRENGTHS

Table 4.3 shows the measured shear strength of each specimen and the measured strength divided by the strength calculated using three methods. Strength was calculated using three methods. Method 1 was the nominal shear strength determined in accordance with ACI 318-14 Eq. 18.10.7.4, Method 2 was the shear force corresponding to development of the nominal flexural strength, M_n, at both ends of the beam, and Method 3 was the shear force corresponding to development of the probable flexural strength, M_{pr}, at both ends of the beam (calculated assuming

a tensile reinforcement stress of $1.25f_y$). To calculate the flexural strength (Methods 2 and 3), the beams were assumed to be doubly reinforced and the longitudinal component of the diagonal bar group area was used. In CB1 and CB2, the contribution of the secondary (non-diagonal) longitudinal bars was neglected as the bars were cut off near the beam-wall interface. In each of the three cases, measured-to-calculated strength ratios are provided assuming specified and measured yield stresses and concrete strengths. Except for CB2AD, axial force was neglected in Methods 2 and 3.

Table 4.3 – Measured strength divided by calculated strength

ID	Measured Shear Strength	Method 1 [a]		Method 2 [b]		Method 3 [c]	
	kips (kN)	(a)	(b)	(a)	(b)	(a)	(b)
CB1	184 (820)	1.38	1.31	1.06	1.02	0.90	0.86
CB2	207 (920)	1.45	1.47	1.29	1.19	1.15	1.07
CB2D	204 (910)	1.52	1.46	1.15	1.10	1.05	1.01
CB2AD	234 (1040)	1.85	1.67	1.32	1.31	1.21	1.20
		-	-	1.24 [d]	1.24 [d]	1.18 [d]	1.23 [d]
CB3D	275 (1220)	1.38	1.31	1.21	1.17	1.12	1.10

[a] Calculated nominal shear strength based on ACI 318-14 Eq. 18.10.7.4; (a) using specified material properties, (b) using measured material properties.
[b] Calculated nominal shear strength based on M_n; (a) using specified material properties, (b) using measured material properties.
[c] Calculated nominal shear strength based on M_{pr}; (a) using specified material properties, (b) using measured material properties.
[d] Includes axial force equal to 100 kips (445 kN) based on results in Section 4.7.

For all specimens constructed with Grade 120 (830) diagonal reinforcement, measured shear strengths were larger than all six calculated strengths. The maximum difference was between the strength of CB2AD and the nominal strength calculated using ACI provisions and specified

material properties, where measured strength was 85% larger than the calculated value. This overstrength is due to many factors including reinforcement overstrength, reinforcement strain hardening, development of secondary reinforcement, and axial restraint. The other two specimens (CB2 and CB2D), designed to have a nominal shear strength of $10\sqrt{f_c'}$ [psi] ($0.83\sqrt{f_c'}$ [MPa]) exceeded the nominal strength based on ACI by approximately 50%, while CB3D, the one designed for $15\sqrt{f_c'}$ [psi] ($1.25\sqrt{f_c'}$ [MPa]), exceeded the nominal strength by more than 30%. For the specimens with developed secondary (non-diagonal) longitudinal bars (CB2D, CB2AD, and CB3D), the contribution of the secondary longitudinal bars to flexural strength was on the order of 10% of the flexural strength. Among specimens with Grade 120 (830) diagonal reinforcement, Method 3 resulted in the most accurate estimation of strength, although it still provided an estimate that was consistently less than the measured value. Perhaps alpha, the factor used to increase bar stress when calculating probable moment strength, should be taken to be larger than its typical value of 1.25 when steel with round-house behavior is used and an accurate estimate of strength is required.

For control specimen CB1, the only specimen with Grade 60 (420) diagonal reinforcement, strength calculated using Method 3 overestimated the measured strength by more than 10%. For CB1, the most accurate estimation of strength was based on Method 2b (the shear force corresponding to development of beam nominal flexural strength, M_n, at both ends of the beam using measured material properties). The measured strength exceeded this value by only 2%.

4.4 CHORD ROTATION COMPONENTS

Data from the optical markers attached to the surface of each specimen were analyzed to quantify the specimen deformations attributable to flexural rotation, strain penetration, shear, and

sliding at the beam ends. As shown in Figure 4.8, the markers were arranged in a 4-in. (100-mm) square grid pattern over one face of each specimen and part of the top and bottom blocks. The term 'layer' refers to the space between two marker rows (e.g., Layer 1 is between marker Rows 1 and 2 as shown in Figure 4.8) and the term 'station' (the shaded area in Figure 4.8) refers to the region surrounded by four corner markers (A, B, C, and D, in Figure 4.9).

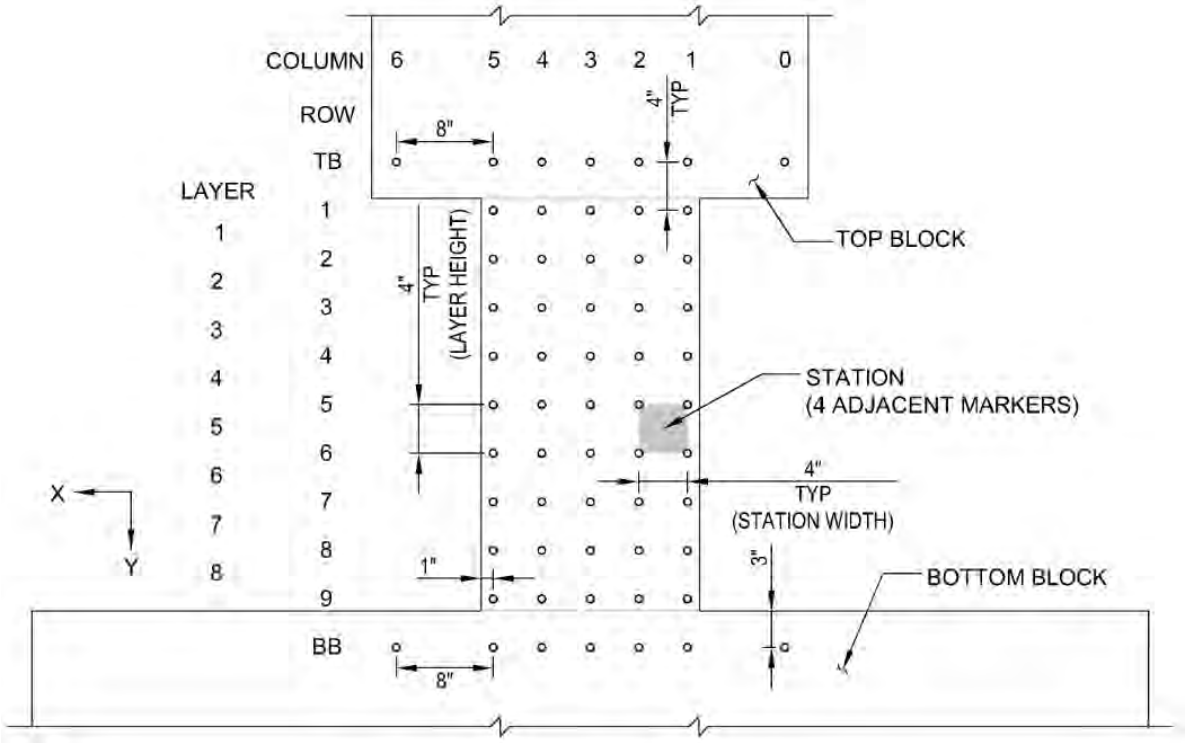

Figure 4.8 – Locations of optical markers on coupling beam specimens (1 in. = 25.4 mm)

4.4.1 FLEXURAL ROTATION AND STRAIN PENETRATION

Flexural rotations were calculated for each of the coupling beam specimens using data from the optical position tracking system. Flexural rotation was calculated for each layer throughout the test as the difference between the rotations of the marker rows above and below the layer. For a given row of markers, rotation was calculated using the vertical displacements of the two

outermost markers in the row (Eq. 4.3, where θ_i is the flexural rotation in layer i, y is the change in vertical position of the marker identified by the subscript, and $\ell_{i,C1C5}$ is the initial horizontal distance between Columns 1 and 5 (Figure 4.8) in Row i). In the case of marker malfunction, markers from Column 2 were used instead of Column 1 and markers from Column 4 were used instead of Column 5. In a few occasions (later in the test), markers from Column 3 needed to be used instead of either Column 4 or Column 2. Cases where the markers in either Column 1 or 5 were replaced are identified in plots with solid shapes.

$$\theta_i = \frac{\left(y_{R_i C_5} - y_{R_i C_1}\right)}{\ell_{i,C_1C_5}} - \frac{\left(y_{R_{i+1} C_5} - y_{R_{i+1} C_1}\right)}{\ell_{i+1,C_1C_5}} \qquad \text{Eq. 4.3}$$

Figure C.1 through Figure C.10 in Appendix C show the distribution of flexural rotations over the beam span for all specimens. The flexural rotation calculated for each layer is plotted at the mid-height of the layer. The plotted values are taken at the peak chord rotation in the second cycle to each target chord rotation. Rotations occurring at the beam ends, referred to herein as strain penetration, are not included.

The plots show that during cycles to both positive and negative chord rotations, flexural rotations of all the specimens were small and somewhat uniform near the midspan throughout the tests. Near the ends of the beams, flexural rotations increased with increases in chord rotation. For CB3D, flexural rotations remained small and nearly constant throughout the beam span up to a chord rotation of about 2.1%, after which data was not available.

Strain penetration refers to the relative rotation between the beam ends and the adjacent top or bottom blocks. It was calculated using Eq. 4.3 as the relative rotation between the top row (Row 1 in Figure 4.8) or bottom row (Row 9 in Figure 4.8) of markers on the beam and those

located on the top block or bottom block, respectively. This definition of strain penetration therefore includes beam end rotation due to straining and slip of bars anchored into the end blocks and flexural rotations occurring within the first 1 in. (25.4 mm) of the beam span, which were assumed to be small relative to the beam-end rotations. Figure C.11 through Figure C.20 show plots of flexural rotations along the beam length that include strain penetration.

Up to about 1% chord rotation, rotations due to strain penetration were slightly larger than rotations due to flexure for all specimens. Beyond 1%, rotation due to strain penetration increased significantly for CB1 and CB2. The other three specimens (CB2D, CB2AD, and CB3D) exhibited much less rotation due to strain penetration. This difference is attributable to the continuation of the secondary (non-diagonal) longitudinal reinforcing bars beyond the beam-wall interface in CB2D, CB2AD, and CB3D. This detailing reduced the concentration of rotations at the beam ends.

4.4.2 SHEAR DEFORMATIONS

Shear deformations were calculated throughout the beam span using optical marker data (Figure 4.8). Shear distortion of each station was calculated throughout the tests using the positions of the four corner markers (A, B, C, and D, in Figure 4.9) and then averaged across each horizontal layer.

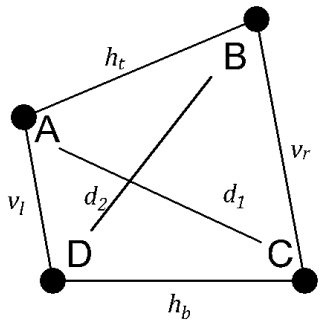

Figure 4.9 – General deformed shape of a station

The distorted shape of a station (Figure 4.9) can be decomposed into three distinct deformation components that cause changes in the angles formed by each corner of the station: flexural rotation θ, shear distortion γ, and expansion ψ (Figure 4.10).

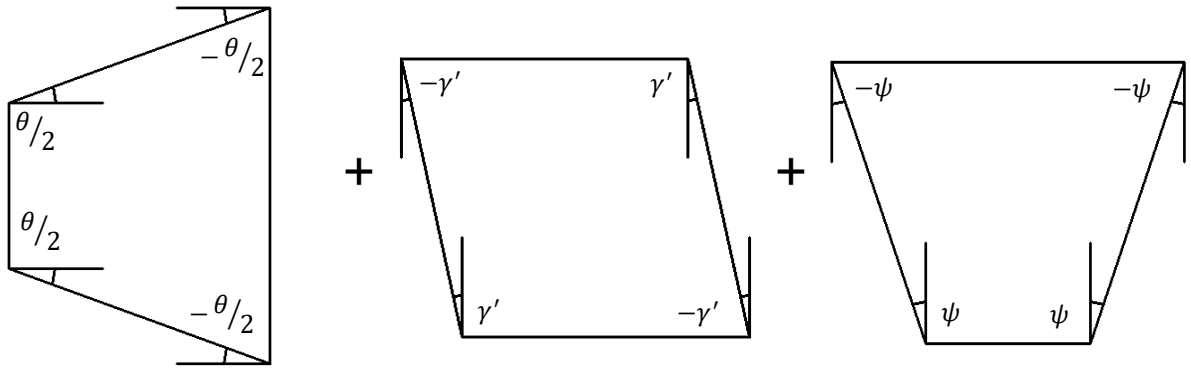

Bending Shear Expansion

Figure 4.10 – Components of angular change of a station

The change in angle of each corner of a station was set equal to the sum of the three components of angular change, as shown in Eq. 4.4 through Eq. 4.7, where $\Delta A, \Delta B, C$, and ΔD are the change in angle of each of the four corners of a distorted station (Figure 4.9).

$$\Delta A = +\theta/_2 - \gamma' - \psi \quad \text{Eq. 4.4}$$

$$\Delta B = -\theta/_2 + \gamma' - \psi \quad \text{Eq. 4.5}$$

$$\Delta C = -\theta/_2 - \gamma' + \psi \quad \text{Eq. 4.6}$$

$$\Delta D = +\theta/_2 + \gamma' + \psi \quad \text{Eq. 4.7}$$

The shear distortion of the station was then calculated with Eq. 4.8.

$$\gamma' = -\frac{1}{4}(\Delta A - \Delta B + \Delta C - \Delta D) \quad \text{Eq. 4.8}$$

This approach assumes uniform curvature within the element, which is believed to be a reasonable assumption given that the layer height is only 4 in. (100 mm). Angles A, B, C and D were calculated using Eq. 4.9 through Eq. 4.12, where the variables represent the distances between station corners as illustrated in Figure 4.9.

$$A = cos^{-1}\left\{\frac{h_t^2 + v_l^2 - d_2^2}{2\ h_t\ v_l}\right\} \quad \text{Eq. 4.9}$$

$$B = cos^{-1}\left\{\frac{h_t^2 + v_r^2 - d_1^2}{2\ h_t\ v_r}\right\} \quad \text{Eq. 4.10}$$

$$C = cos^{-1}\left\{\frac{h_b^2 + v_r^2 - d_2^2}{2\ h_b\ v_r}\right\} \quad \text{Eq. 4.11}$$

$$D = cos^{-1}\left\{\frac{h_b^2 + v_l^2 - d_1^2}{2\ h_b\ v_l}\right\} \quad \text{Eq. 4.12}$$

The shear distortion of a layer was calculated using Eq. 4.13, a weighted average of the shear distortions calculated for the four stations comprising one layer. In Eq. 4.13 subscript i

indicates the layer number, subscript j indicates the station number, n_s is the number of stations (four), and ℓ_j is the width of the station (nominally 4 in. (100 mm)). When a marker stopped functioning, as often occurred late in a test as damage accumulated, the stations associated with that marker were omitted from the weighted average. Instances where this occurred are identified in plots of results by shading points so they are solid.

$$\gamma_i = \frac{\sum_{j=1}^{n_s} \gamma'_{i,j}\, \ell_j}{\sum_{j=1}^{n_s} \ell_j} \qquad \text{Eq. 4.13}$$

Figure C.21 through Figure C.30 show the distribution of shear distortion per layer, γ_i, over the height of the specimens both for positive and negative loading directions. The shear distortion for a given layer is plotted at the distance from midspan associated with the mid-height of the layer, with positive and negative values of distance indicating layers located above and below midspan. In each figure, shear distortions are plotted for different chord rotations. The plotted values are from the second cycle to a target chord rotation. Shearing at the joint with the top and bottom blocks is not included in these figures.

The plots show that shear distortions of all specimens were small and somewhat uniform throughout the beam span in both loading directions up to a chord rotation of approximately 1%. For larger chord rotations, shear distortions of CB1 were largest in the topmost layer with values of 0.0085 and -0.0088 rad at 3% chord rotation in positive and negative loading directions, respectively. These values were similar for CB2. CB2D and CB3D exhibited larger shear distortions at lower chord rotations (0.012 rad at 2% chord rotation for CB2D and -0.014 rad at -2.1% chord rotation for CB3D). This is attributed to the continuation of the secondary (non-

diagonal) longitudinal reinforcing bars beyond the beam-wall interface, which caused a decrease in rotations concentrated at the beam ends.

CB1 exhibited its largest shear distortions in the top and bottommost layers, with a midpoint located 14 in. (360 mm) away from midspan. In CB2, CB2D, and CB3D, shear distortions were largest in a layer having its midpoint located 10 in. (250 mm) from midspan. For CB1, shear distortion at midspan was nearly zero throughout the test, while the other specimens (CB2, CB2D, CB2AD, and CB3D) exhibited larger shear distortions near midspan. It is not known why CB2 had larger shear distortions within the beam span than CB1.

Shear distortions of CB2AD, the only specimen tested with axial restraint, were small up to a chord rotation of 1% like the other specimens. Unlike other specimens, for larger chord rotations, maximum shear distortion was found near the midspan of the beam, in a layer with its midpoint located 6 in. (150 mm) above midspan for positive chord rotations and in a layer with its midpoint located 2 in. (50 mm) below midspan for negative chord rotation. This is consistent with the extensive damage observed throughout the span of this beam (Figure B.19).

4.4.3 SLIDING

Sliding is defined herein as the relative movement between the beam ends and the adjacent end blocks (both top and bottom), measured parallel to the face of the blocks and corrected for twisting (if any) of both top and bottom blocks. Sliding was calculated as the difference between horizontal displacements of the rows located on the top and bottom blocks and the rows closest to the top and bottom blocks, respectively (Figure 4.8). Sliding was calculated using Eq. 4.14 and Eq. 4.15, where $\Delta_{sl,top}$ and $\Delta_{sl,bot}$ are referred to as sliding at the beam-top block and beam-bottom block interfaces, respectively; δ, θ_y, and θ_z are displacement, rotation about the y-axis, and

rotation about the z-axis, respectively; and subscripts BB, TB, 1, and 9 refer to the row numbers shown in Figure 4.8. Eq. 4.14 and Eq. 4.15 were derived assuming that all flexural rotation in the 1 in. of beam closest to the wall faces was concentrated at the wall face.

$$\Delta_{sl,top} = \delta_{TB} - \delta_1 - (3\ in.)\theta_{z,TB} - (1\ in.)\theta_1 - (5\ in.)\theta_{y,TB} \quad \text{Eq. 4.14}$$

$$\Delta_{sl,bot} = \delta_9 - \delta_{BB} - (1\ in.)\theta_9 - (3\ in.)\theta_{z,BB} + (5\ in.)\theta_{y,BB} \quad \text{Eq. 4.15}$$

Figure C.31 through Figure C.40 show the sliding at beam ends for all specimens plotted against chord rotation. The figures indicate that in most cases and in both directions, the value of sliding increased with increases in chord rotation. Up to a chord rotation of 3%, in both positive and negative loading directions, none of the specimens experienced sliding larger than ±0.06 in. (±1.5 mm) at the bottom and ±0.08 in. (±2.0 mm) at the top, except CB2AD, which had about +0.18 in. (±4.6 mm) top sliding at approximately +3% chord rotation (Figure C.37). The reason for this difference is not evident. At larger chord rotations, the maximum sliding calculated was for CB2 with approximately -0.23 in. (±5.8 mm) of top sliding at -4% chord rotation (Figure C.33).

4.4.4 CONTRIBUTION/COMPARISON

Based on the calculated deformation components described previously, the relative contributions of the four mechanisms to the total beam chord rotation were calculated for the second cycle of loading to each target chord rotation from 0.75% until data was available. The four deformation components considered were flexural rotation, strain penetration evident at the beam ends, shear deformation, and sliding at the connections with the top and bottom blocks. Figures

4.11 through 4.15 show the calculated cumulative relative contributions to chord rotation of the four mechanisms plotted versus chord rotation for each coupling beam.

The total chord rotation due to flexure, θ_f, was calculated with Eq. 4.16, where θ_i is the flexural rotation in layer *i* and d_i is the distance between midspan and midheight of layer *i*. The distance from beam midspan to midheight of a layer was negative for layers above the middle of the beam (*i* = 1 to 4). This approach assumes curvature is uniformly distributed within each layer, which is approximately true because of the small layer dimension.

$$\theta_f = \frac{\sum_{i=1}^{n_l} \theta_i \, d_i}{l_n} \qquad \text{Eq. 4.16}$$

The total chord rotation due to strain penetration, θ_{sp}, into the top and bottom blocks was calculated with Eq. 4.17.

$$\theta_{sp} = \frac{\theta_{sp,bot} - \theta_{sp,top}}{2} \qquad \text{Eq. 4.17}$$

The total chord rotation due to shear distortion, θ_v, was calculated with Eq. 4.18, the sum over n_l layers of the product of average shear distortion for a given layer, γ_i, and the height of the layer, h_i, divided by l_n.

$$\theta_v = \frac{\sum_{i=1}^{n_l} \gamma_i \, h_i}{l_n} \qquad \text{Eq. 4.18}$$

The total chord rotation due to sliding at the face of the blocks, θ_{sl}, was calculated using Eq. 4.19.

$$\theta_{sl} = \frac{\Delta_{sl,top} + \Delta_{sl,bot}}{l_n} \quad \text{Eq. 4.19}$$

CB1 and CB2, the two specimens with secondary (non-diagonal) longitudinal bars terminated near the beam-wall interface (as recommended by the ACI 318-14 commentary), experienced similar contributions from different components to the total chord rotation (Figures 4.11 and 4.12). In both loading directions, strain penetration accounted for most of the total chord rotation, as expected for coupling beams with secondary (non-diagonal) longitudinal bars terminated near the beam-wall interface. When the specimens were loaded in the positive direction, the contribution of flexure was small, remaining less than 20% throughout the tests. Rotation due to strain penetration accounted for the major part (45 to 90%) of the total chord rotation. The contribution of shear ranged between 10 and 25%. Finally, the contribution of sliding at the beam ends was between 5 and 10% of the total chord rotation. In the negative loading direction, the contributions to total chord rotation of flexure, strain penetration, shear, and sliding were about 5 to 35%, 35 to 70%, 10 to 25%, and 5 to 15%, respectively. In both loading directions, the sum of all calculated contributions accounted for 85 to 100% of the total chord rotation of CB1 and CB2.

Secondary (non-diagonal) longitudinal bars were not terminated near the beam-wall interface in CB2D, CB2AD, and CB3D. This difference in detailing caused a change in the relative contributions to total chord rotation, compared to those of CB1 and CB2 (Figures 4.13 to 4.15). The contributions to total chord rotation of flexure, strain penetration, shear, and sliding were about 10 to 25%, 30 to 50%, 20 to 50%, and 5 to 10%, respectively. In the negative loading direction, the sum of calculated contributions accounted for between 85 to 95% of total chord rotation. The contributions to total chord rotation of flexure, strain penetration, shear, and sliding were about 10 to 35%, 25 to 50%, 25 to 30%, and 0 to 10%, respectively. Unlike CB1 and CB2, strain penetration

did not account for the majority of chord rotation in CB2D, CB2AD, and CB3D. The developed secondary (non-diagonal) longitudinal bars resulted in less concentration of rotations near the beam-wall interface (less strain penetration), and more damage spread throughout the beam span. The relative importance of both flexural and shear deformations therefore increased in specimens with developed secondary reinforcement. The contribution of sliding was similar (and small) for all specimens.

Overall, neither diagonal reinforcement grade nor axial restraint were associated with notable changes in the relative importance of deformation mechanisms.

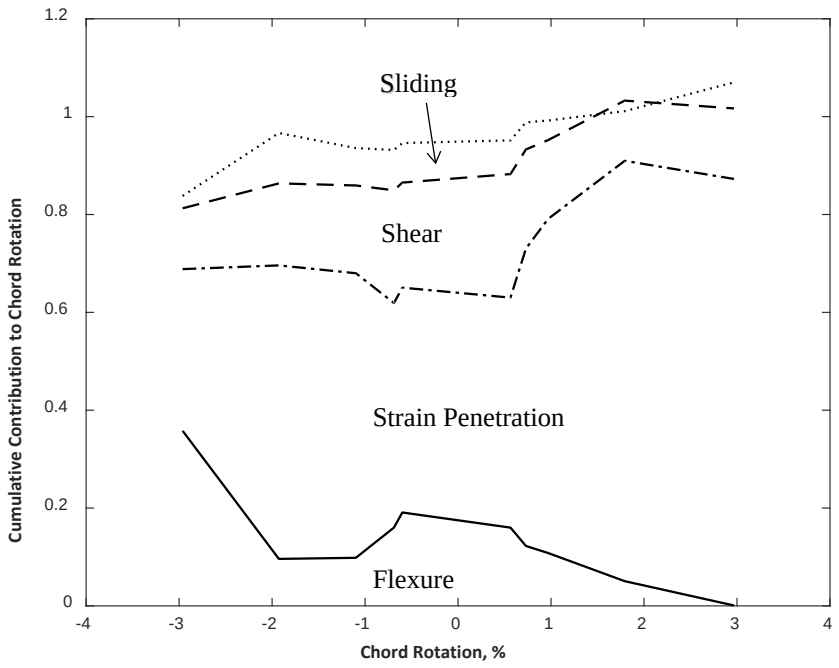

Figure 4.11 – Cumulative relative contribution of chord rotation components for CB1

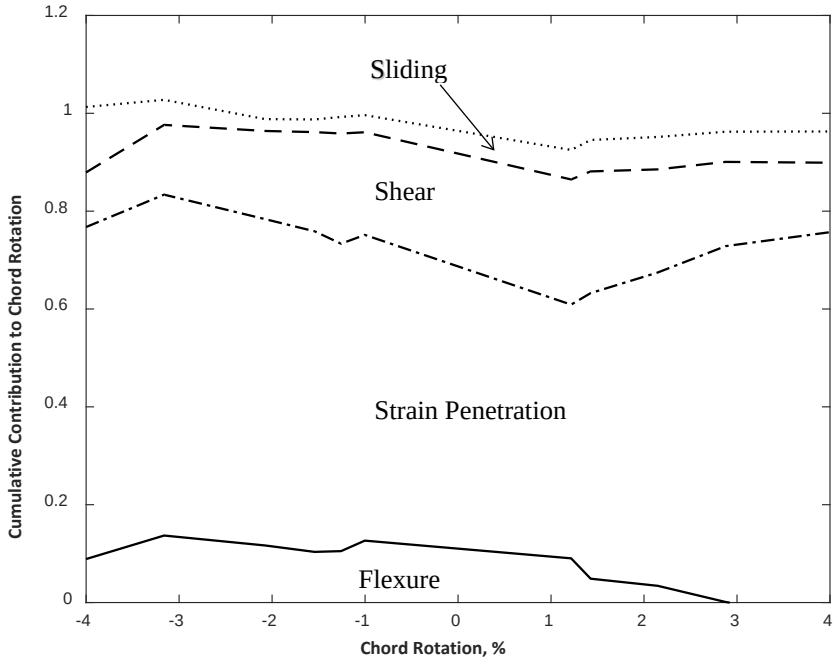

Figure 4.12 – Cumulative relative contribution of chord rotation components for CB2

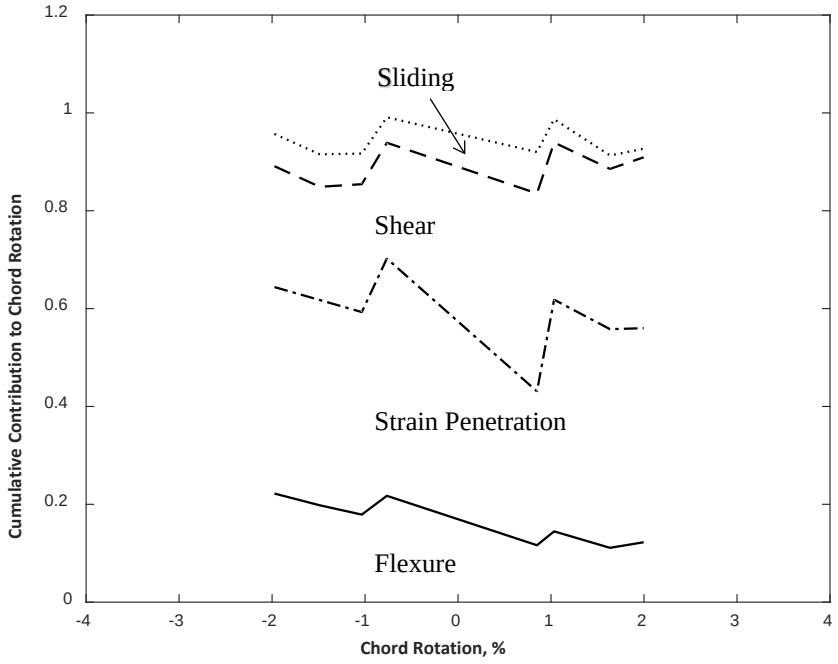

Figure 4.13 – Cumulative relative contribution of chord rotation components for CB2D

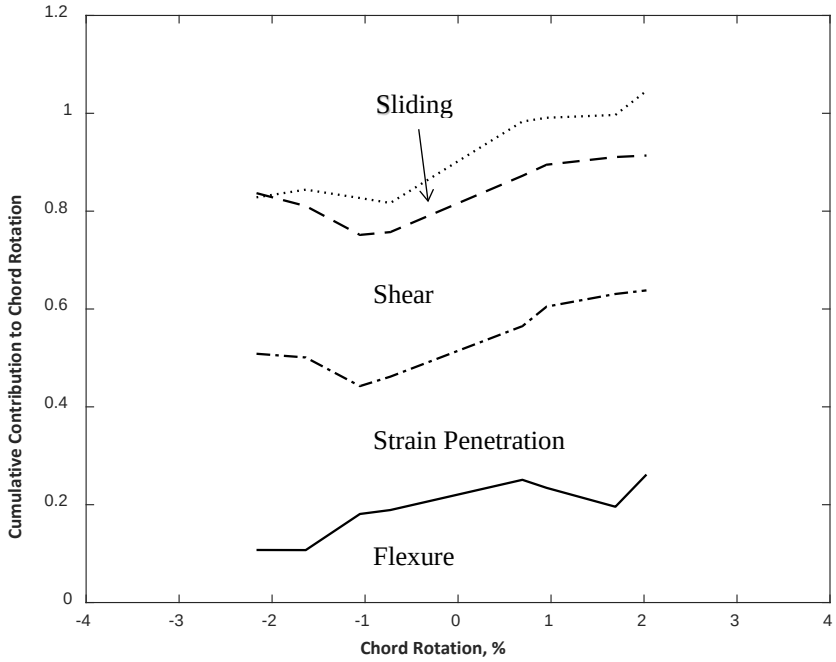

Figure 4.14 – Cumulative relative contribution of chord rotation components for CB2AD

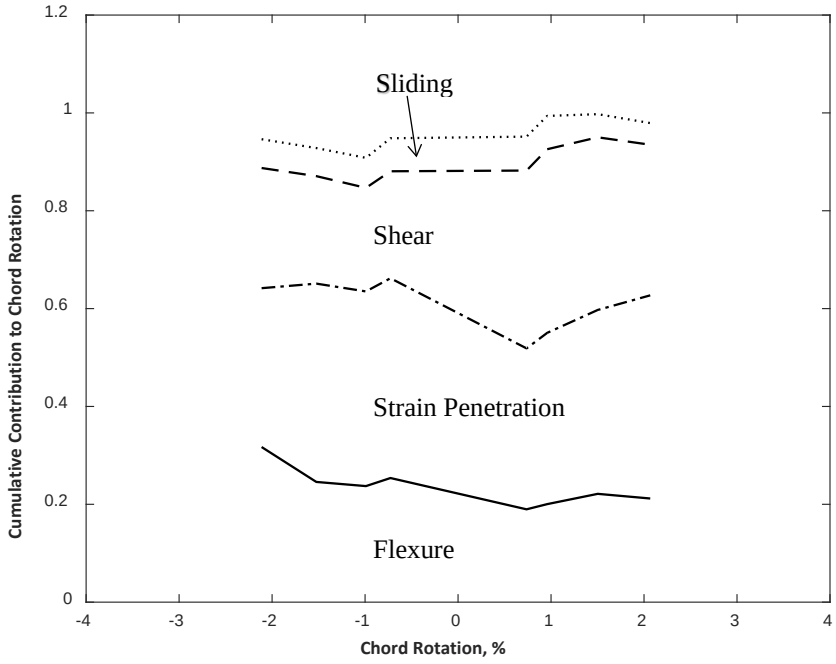

Figure 4.15 – Cumulative relative contribution of chord rotation components for CB3D

4.5 MEASURED REINFORCEMENT STRAINS

Diagonal, transverse, and secondary longitudinal reinforcing bars were instrumented with 28 electrical resistance strain gauges attached at the locations shown in Figure 3.10. In each specimen, two diagonal bars were instrumented with six strain gauges each, five strain gauges were attached to the No. 3 (10 mm) secondary (non-diagonal) longitudinal bars, and the hoops and crossties were instrumented with eleven strain gauges. The strain gauges were rated for 15% strain to allow measurements throughout the tests. The locations of strain gauges and the measured strain data are shown in Figure D.1 through Figure D.143 in Appendix D. All strain gauge data are reported assuming zero strain in the reinforcement at the start of the tests.

4.5.1 DIAGONAL REINFORCEMENT

Figure D.2 through Figure D.61 show the strains measured with gauges on two diagonal bars in each specimen. The measured strains indicate that for all specimens, the strains in the diagonal bars were less than 1% at locations within the bottom block (gauges D1 through D4 in Figure D.1, plots shown in Figure D.2 through Figure D.21). Strains recorded with gauges D1 and D2, located a distance of two thirds of the embedment length from the wall face ($20d_b$ for CB1 and $32d_b$ for other specimens), were lower in all specimens than the strains corresponding to measured yield stress, 0.22% for Grade 60 (420) and 0.67% for Grade 120 (830). Strains recorded with gauges D3 and D4, located a distance of one third of the embedment length from the wall face ($10d_b$ for CB1 and $16d_b$ for others), were larger than the strain associated with yield stress for all specimens with Grade 120 (830) diagonal bars. This yielding of reinforcement occurred at a chord rotation of approximately 1.5%. In CB1, the only specimen with Grade 60 (420) diagonal reinforcement, gauges D3 and D4 were not functional.

Figure D.22 through Figure D.31 show the strains measured with gauges on the diagonal bars at the beam–bottom block interface (D5 and D6). The measured strains indicate that yielding of the diagonal reinforcement at this interface generally occurred while loading to a chord rotation of 1.5% or 2.0% in specimens with Grade 120 (830) diagonal reinforcement, and at a target chord rotation of 0.75% for CB1, which had Grade 60 (420) diagonal reinforcement. The difference in strains measured with D5 for CB1 and other specimens is clearly visible in Figure 4.16, which shows the strains measured with D5 for all specimens at peak chord rotations up to 5%. The figure indicates that for CB1, the maximum strain recorded with D5 was almost 4.0% at a chord rotation of +2%, while for other specimens, recorded strain did not exceed 1.5% at the same chord rotation. Figure 4.16 also shows an effect of bar constitutive properties on strain demands. Because the Grade 60 (420) bars had a yield plateau, a large increase in strain occurred for CB1 when the bar yielded that was not associated with a large increase in chord rotation. Because the Grade 120 (830) bars had a roundhouse-shaped constitutive behavior (Figure 3.3), increases in strain were more closely associated with increases in chord rotation. Strains recorded with D6 could not be compared as D6 was not functional for all specimens. The range of strains recorded with D6 for some specimens, such as CB3D, was large. For CB3D, which was designed to have a 50% higher nominal shear strength than the ACI Building Code limit, strains varied between -2.0 and +5% at chord rotations of 4 and 5%.

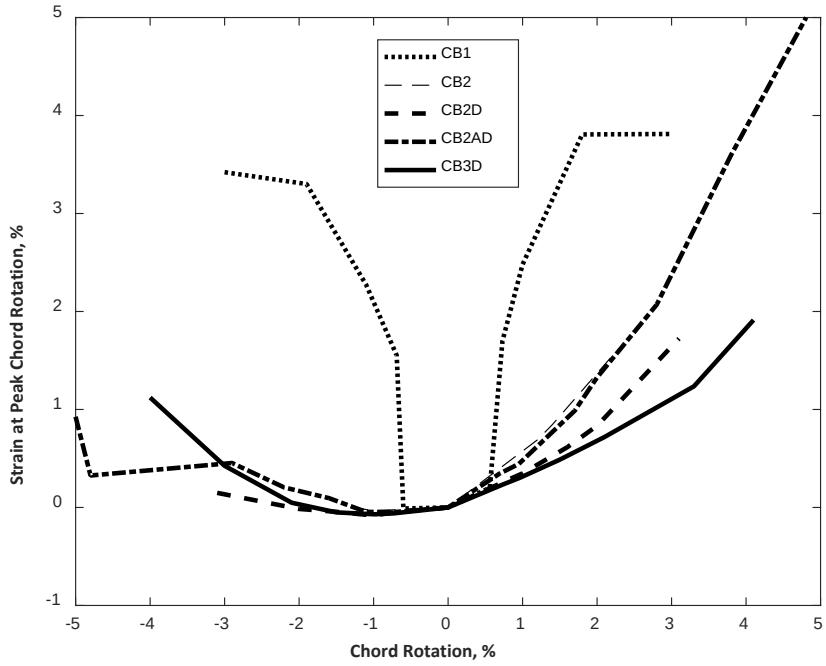

Figure 4.16 – Strains measured with gauge D5 at peak chord rotations

For CB1, measured diagonal bar strains (from gauges D7, D8, D9, and D10) indicate that the diagonal bars reached values larger than the yield strain at every instrumented location within the beam span. Yielding of the bar generally occurred at a chord rotation of 1.5% to 3.0%. The maximum strain recorded for CB1 (with D9) was 5.0% at a chord rotation of 7.5% (Figure D.42). For CB2, the maximum measured diagonal bar strain (D8) was only 1.0% at a chord rotation of -5%, much lower than that for CB1 (Figure D.38). For CB2D, the maximum recorded diagonal bar strain (D7) was 2.5% at a chord rotation of 5% (Figure D.34), a higher value than for CB2, but not as high as for CB1. The maximum measured diagonal bar strains (D10) for CB2AD and CB3D were almost 3.0% (Figure D.50 and Figure D.51, respectively).

Figures 4.17 and 4.18 show the strains measured with gauges D7 and D8, respectively, for all specimens at peak chord rotations up to 5%. The higher values of strain recorded with D7 in

CB1 than in other specimens are evident in Figure 4.17, especially between 1% and 4% chord rotation. However, there was no clear difference in strains measured with D8 in CB1 and other specimens. The difference in length of secondary (non-diagonal) longitudinal bars (whether they are terminated near the wall face or developed) does not seem to have a notable effect on diagonal bar strains.

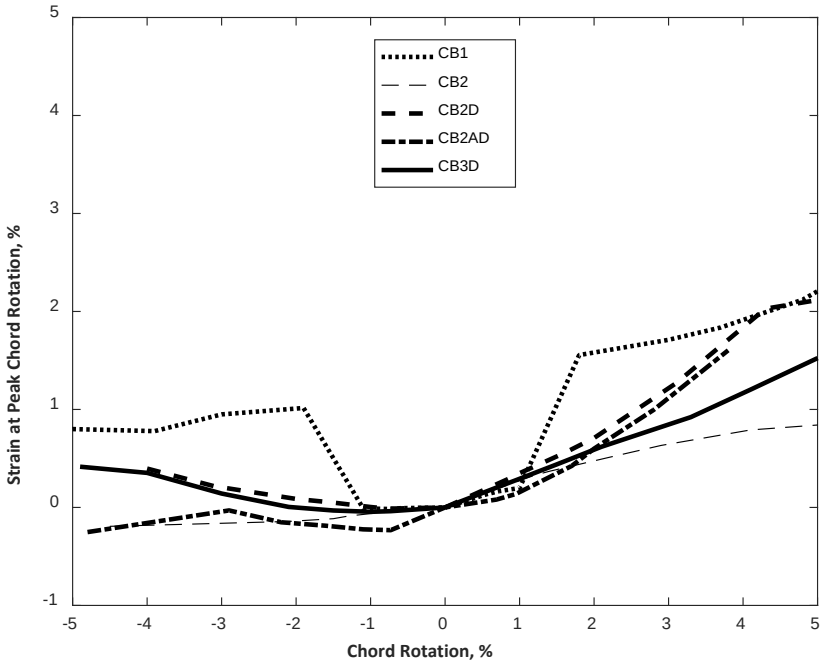

Figure 4.17 – Strains measured with gauge D7 at peak chord rotations

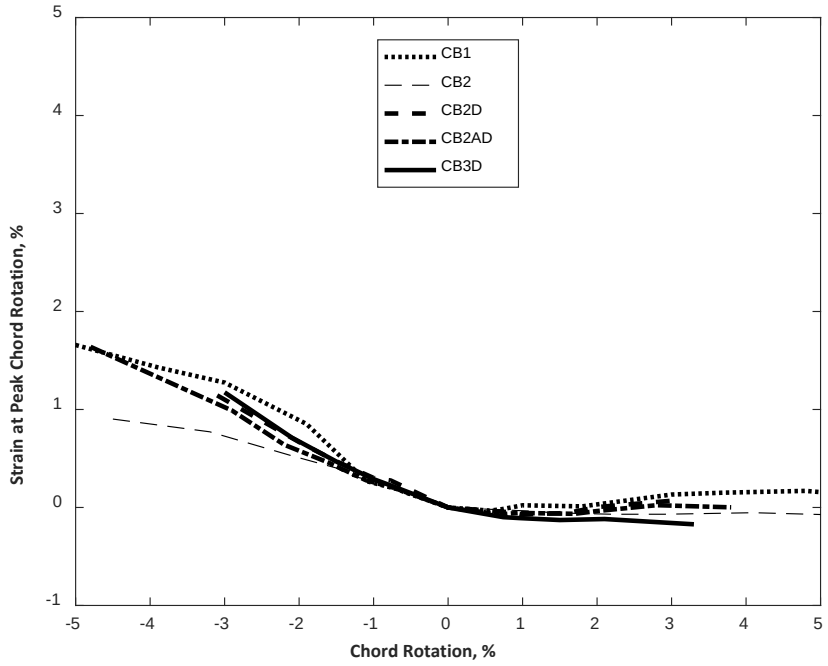

Figure 4.18 – Strains measured with gauge D8 at peak chord rotations

Strain gauges located on diagonal bars at the beam-top block interface recorded similar values as those located at the beam-bottom block interface. According to the measured strains shown in Figure D.52 through Figure D.61 for gauges D11 and D12, yielding of diagonal reinforcement at the beam-top block interface generally occurred while loading to a chord rotation of 1.5% except for CB1, for which yielding occurred at 1% chord rotation. For CB1, the maximum strain recorded on the diagonal bars at the beam–top block interface (with D12) was more than 5.0% at a target chord rotation of 6% (Figure D.57), while for other specimens, recorded strains did not exceed 2.0%. Figure 4.19 shows the strains measured with D11 for four specimens (except CB2) at peak chord rotations. The figure indicates that at 2% chord rotation, in both the positive and negative loading directions, strains recorded for CB1 were much higher than those recorded for the other specimens.

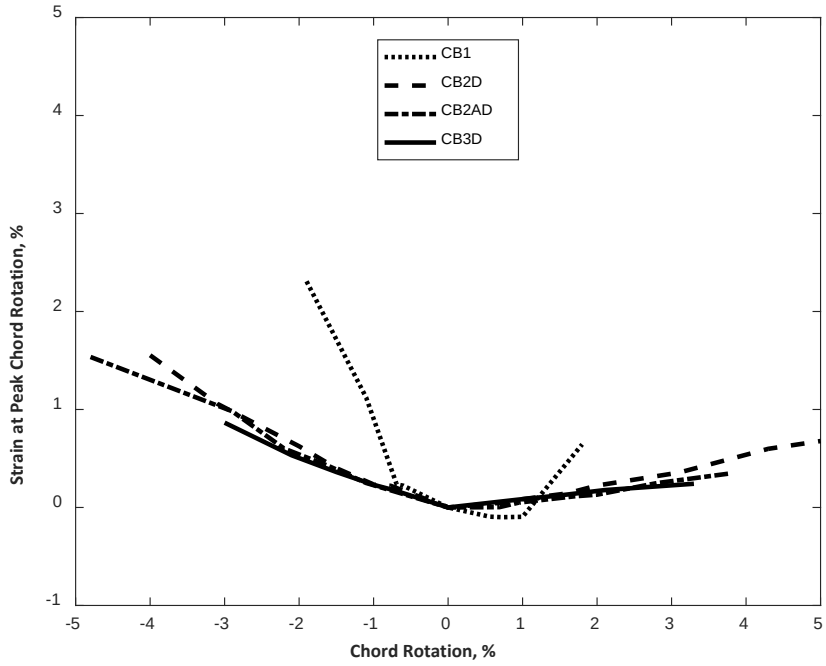

Figure 4.19 – Strains measured with gauge D11 at peak chord rotations

4.5.2 SECONDARY (NON-DIAGONAL) LONGITUDINAL REINFORCEMENT

Figure D.63 through Figure D.87 show the strains measured on the secondary (non-diagonal) longitudinal reinforcement. As expected, in most cases (except for H2), strains measured in the longitudinal bars were larger in CB2D, CB2AD, and CB3D than those in CB1 and CB2. In CB2D, CB2AD, and CB3D, the secondary (non-diagonal) longitudinal bars were extended 9 in. (230 mm) (i.e. $24d_b$, where d_b is the diameter of longitudinal bars) into the walls, a length equal to the development length calculated per ACI 318-14 Eq. 25.4.2.3a with $1.25f_y$ substituted for f_y and ignoring the minimum length of 12 in. (305 mm) (the extension is shown with dotted lines in Figure D.62). In CB1 and CB2, the secondary (non-diagonal) longitudinal reinforcement was terminated 2 in. (50 mm) into the top and bottom blocks as recommended in the ACI Building

Code commentary and common in current design practice. Figures 4.20 and 4.21 show the strains measured with H3 and H4, respectively, for all the specimens at the peak chord rotation of each loading cycle. The figures also indicate the higher strain values recorded for CB2D, CB2AD, and CB3D relative to those in CB1 and CB2.

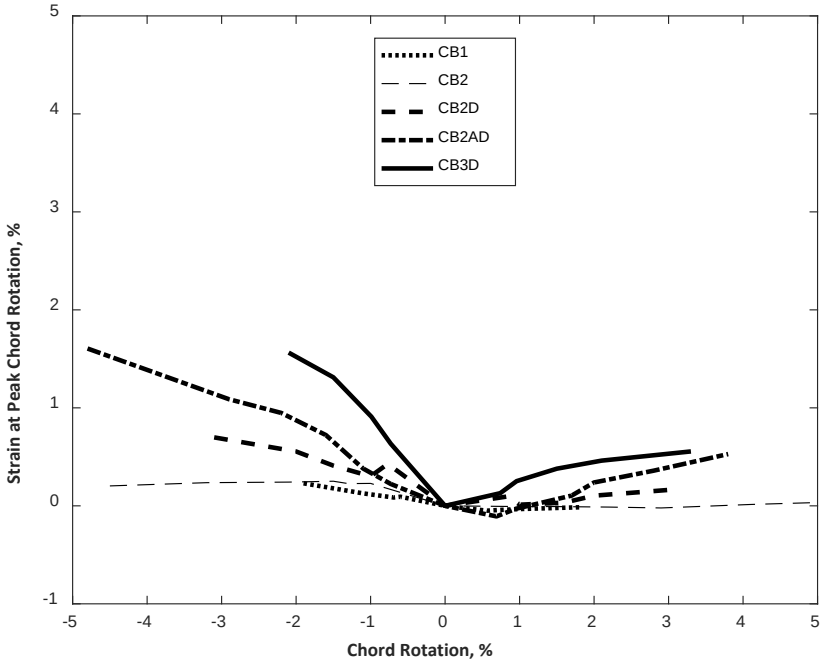

Figure 4.20 – Strains measured with gauge H3 at peak chord rotations

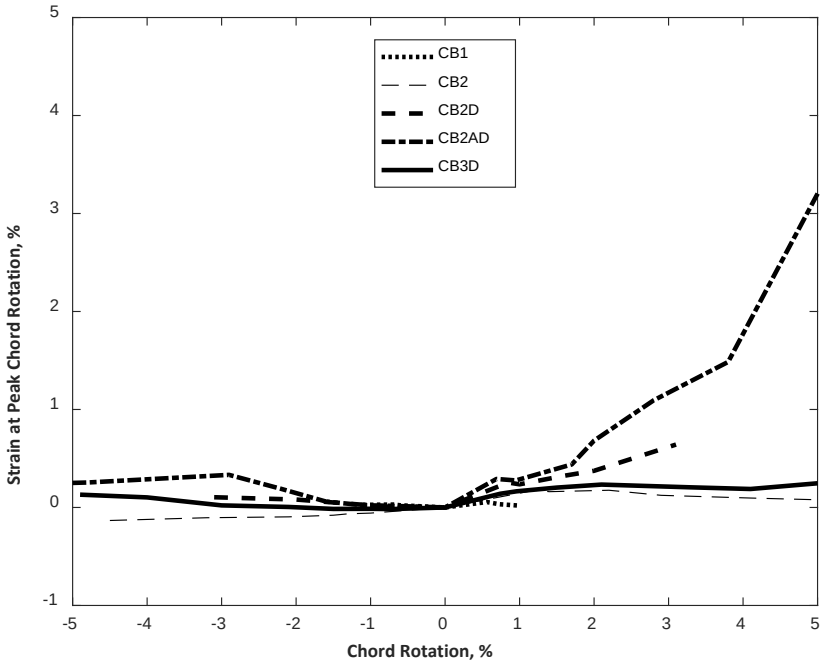

Figure 4.21 – Strains measured with gauge H4 at peak chord rotations

4.5.3 TRANSVERSE REINFORCEMENT

Figure D.89 through Figure D.143 show the strains recorded with gauges on the hoops and crossties of the specimens. The first hoop, located 2 in. (50 mm) from the bottom block, was instrumented with three strain gauges – one at the middle of the longer leg (S1), one near the end of the longer leg (S2), and one at the middle of the shorter leg (S3), as shown in Figure D.88. Gauges were attached on the outside perimeter of the hoops. In no case did either gauge attached to the longer leg (S1 and S2) record strains larger than 0.2% (Figure D.89 through Figure D.98). The strains measured with the gauge attached to the shorter leg (S3) were similar to those measured with the other two (S1 and S2) for CB1 and CB2 (less than 0.2%). In CB2D and CB2AD, the maximum strain recorded with S3 was 0.4%, and in CB3D the maximum strain recorded was

0.3%. Figure 4.22 shows the strains measured with S3 at peak chord rotations for each specimen. The largest values occurred at chord rotations exceeding 2%, when the shorter hoop leg may have been engaged and working to restrain buckling of diagonal and secondary longitudinal bars.

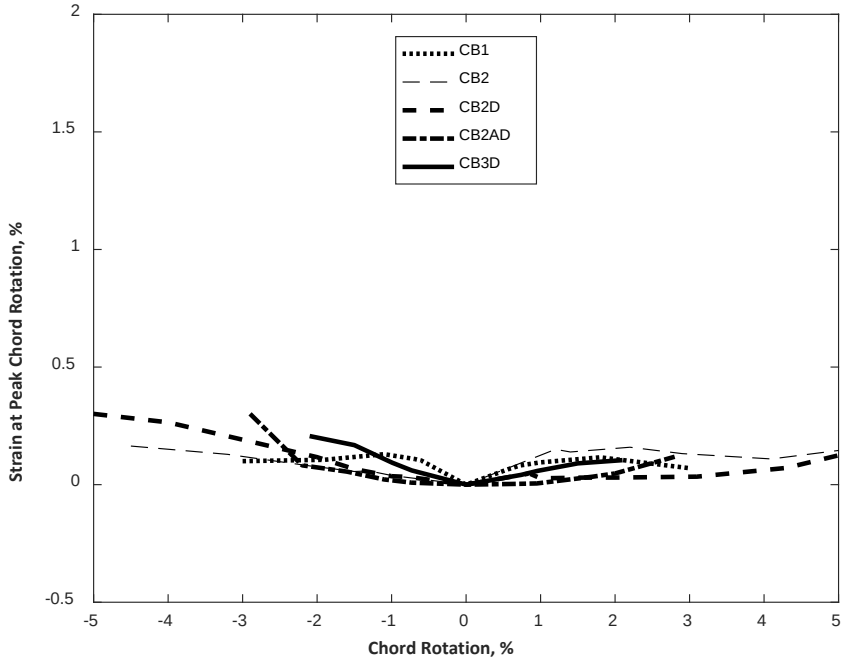

Figure 4.22 – Strains measured with gauge S3 at peak chord rotations

The second hoop, located 3 in. (75 mm) from the first, was also instrumented with three strain gauges (S4, S5 and S6) at the same locations as the first hoop. In most cases, the maximum strain recorded was not larger than 0.3%, except for CB2AD, which exhibited a maximum strain of 0.6% on its shorter leg (S6) while loading to a chord rotation of 6%.

Gauges S7 and S8 were located at the middle of the longer legs of the fourth and sixth hoops from the bottom block, respectively (the sixth hoop was at midspan). Figures 4.23 and 4.24 show the strains measured with S7 and S8, respectively, at the peak chord rotation of each loading direction. Strains recorded with these two gauges indicate large differences between CB1, the

specimen with conventional Grade 60 (420) diagonal reinforcement, and the other specimens with high strength Grade 120 (830) diagonal reinforcement. In CB1, both gauges measured strains less than 0.2% (strains measured with S7 were close to 0.1% at peak chord rotations). Strains measured with S7 and S8 in CB2, which was nominally identical to CB1 but with Grade 120 (830) diagonal bars), exceeded the yield strain at chord rotations larger than approximately 1%. The strains recorded for CB2D, CB2AD, and CB3D were even larger, which should be expected in specimens with developed secondary reinforcement. In these specimens, shear damage was spread throughout the beam instead of concentrating near the beam-wall interface. An explanation for these differences is not readily apparent. Additional research is necessary to replicate and explain these observations.

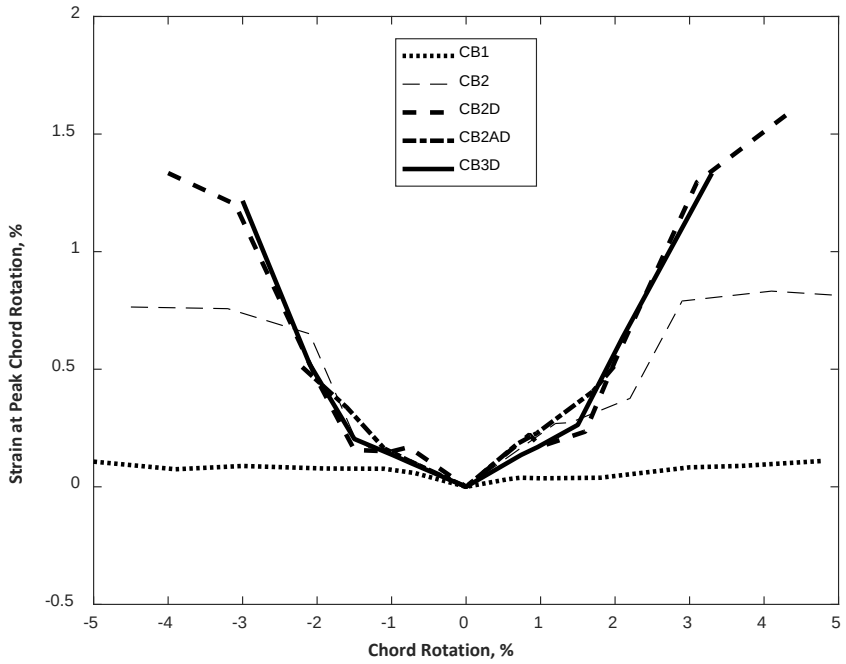

Figure 4.23 – Strains measured with gauge S7 at peak chord rotations

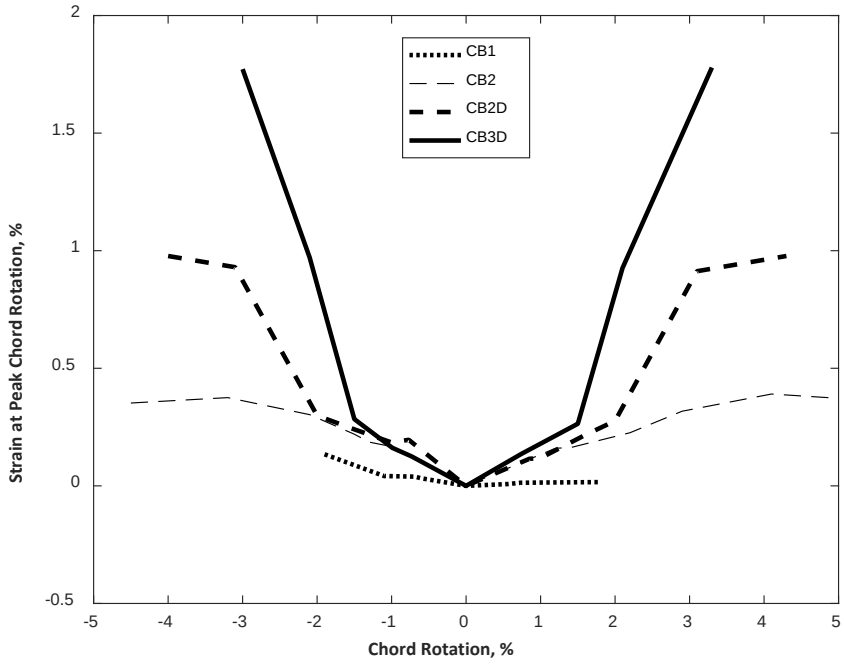

Figure 4.24 – Strains measured with gauge S8 at peak chord rotations

For specimens with Grade 120 (830) diagonal reinforcement, strains measured with gauges S7 and S8 were larger than those measured with S1, S4, and S9, which were attached to the longer legs of the hoops near the beam ends. This was expected because the end blocks tend to provide confinement near the ends of the beams. In addition, beam shear strength tends to be less dependent on hoops near a compression support than that at midspan.

Figure D.134 through Figure D.143 show the strains recorded for each specimen with gauges T1 and T2 located on the two through-thickness crossties located 5 in. (125 mm) from the bottom block. Only one of the gauges in one of the specimens (T1 in CB3D) recorded strains larger than 0.3%. This gauge recorded a maximum value of almost 0.9% at a chord rotation of -5%. Figure 4.25 shows the strains measured with T1 at peak chord rotations for all specimens. Though not observed in Figure 4.23, Figures 4.24 and 4.25 clearly show higher strains in CB3D, the

specimen designed to have a higher nominal shear strength (50% more than the ACI Building Code limit). This, once again, may indicate a need for more confinement in beams designed for larger shear stresses. Relative to other specimens, no clear difference in strains was observed for CB2AD, the specimen tested with axial restraint.

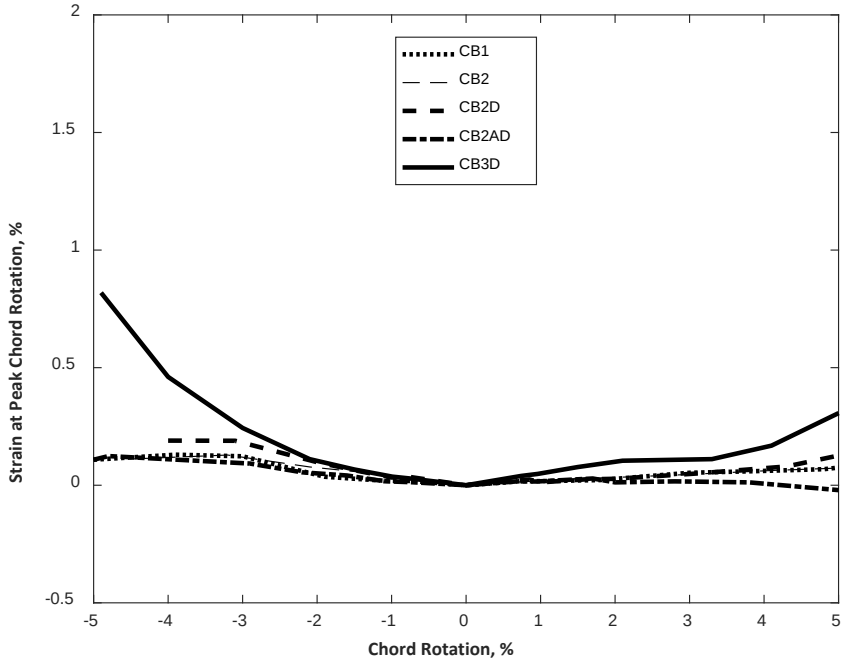

Figure 4.25 – Strains measured with gauge T1 at peak chord rotations

4.6 CRACK WIDTHS

Although small crack widths are not an important design aim for earthquake-resisting members like coupling beams, crack widths can be an approximate external measure of damage. Understanding how crack widths measured at zero force (after unloading) relate to crack widths at peak chord rotation and damage states may be useful to those conducting post-earthquake damage assessments. Also, because use of high strength steel instead of conventional Grade 60 (420) steel

results in smaller amounts of reinforcement, it is worth documenting how steel grade affects maximum crack widths and the crack widths after unloading.

Crack widths were measured using crack comparators on three sides of the beam (the other side of the beam was reserved for instrumentation) at four instances during the second cycle to each target chord rotation: peak positive chord rotation, zero force during the excursion from positive peak to negative peak, peak negative chord rotation, and again zero force during the excursion from negative peak to the next positive peak. Measurements were taken at zero force to know the extent to which cracks close after unloading.

Figures 4.26 and 4.27 show the largest crack widths measured at peak chord rotations and at zero shear force following peak chord rotations, respectively, plotted against peak chord rotation of each cycle. Crack widths measured at peak chord rotation (Figure 4.26) remained below 0.06 in. (1.5 mm) up to 2% chord rotation and 0.10 in. (2.5 mm) up to 5% chord rotation. At zero shear force following peak chord rotations, cracks tended to close somewhat in both the positive and negative loading directions (Figure 4.27). There was no clear difference in behavior between specimens with conventional Grade 60 (420) diagonal reinforcement and those with high strength Grade 120 (830) diagonal reinforcement in terms of both crack widths at peak chord rotation (Figure 4.26) and after unloading (Figure 4.27). Also, neither the length of secondary (non-diagonal) longitudinal bars, nor the design shear stress, nor the presence of axial restraint seemed to have a measurable effect on the size of the cracks at peak chord rotations (Figure 4.26) or after unloading (Figure 4.27). These observations appear to contradict observations made regarding Figure 4.7, where specimens with developed secondary (non-diagonal) longitudinal bars (CB2D, CB2AD, and CB3D) were seen to have larger crack widths than CB1 and CB2, the specimens with secondary longitudinal bars terminated near the beam-wall interface. The reason behind this

inconsistency is that in CB1 and CB2, a small number of wide flexural cracks occurred on the 10-in. (250-mm) sides of the beam near the beam-bottom block interface, whereas the large cracks in CB2D, CB2AD, and CB3D occurred nearer to midspan on the 18-in. (460-mm) side of the beam.

To quantify the extent to which cracks closed after loading, a crack width ratio defined as crack width at zero shear force (w_{zero}) over crack width at the preceding peak displacement (w_{peak}) was calculated. Crack width ratio is plotted against chord rotation in Figure 4.28. Due to the large variability, there is no clear difference between specimens with different grades of diagonal reinforcement, lengths of longitudinal reinforcement, design shear stresses, or axial restraint.

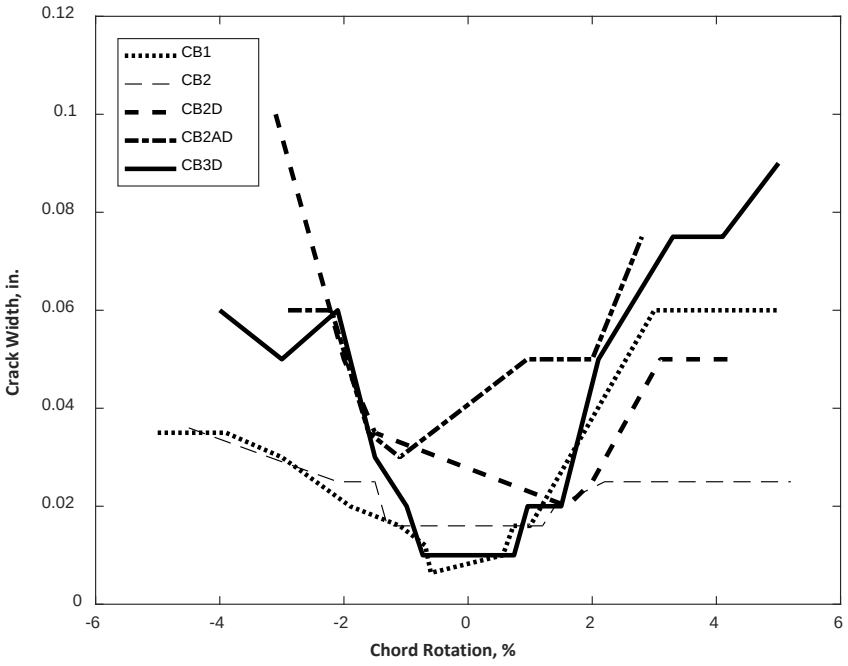

Figure 4.26 – Measured crack width at peak chord rotations (1 in. = 25.4 mm)

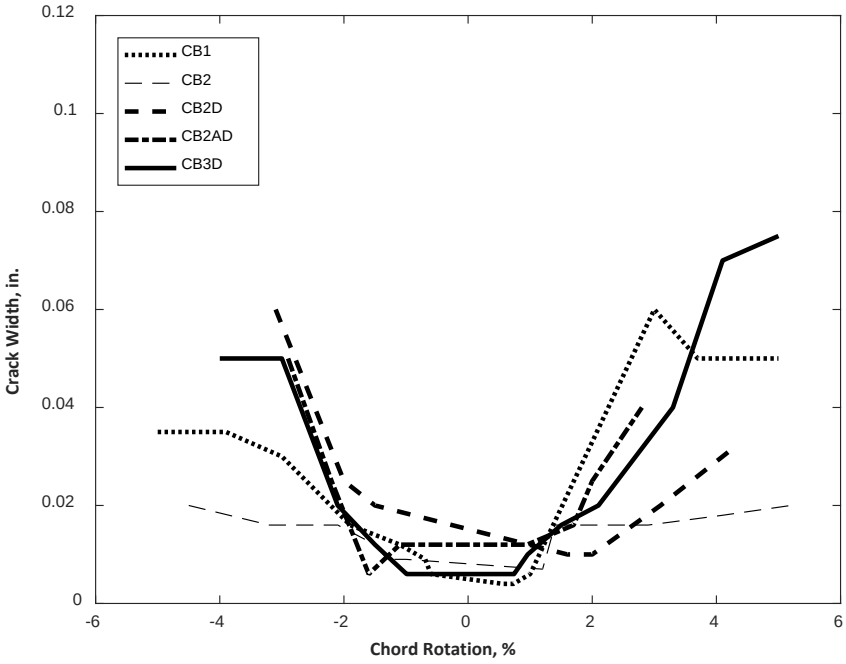

Figure 4.27 – Measured crack width at zero shear versus peak chord rotation attained (1 in. = 25.4 mm)

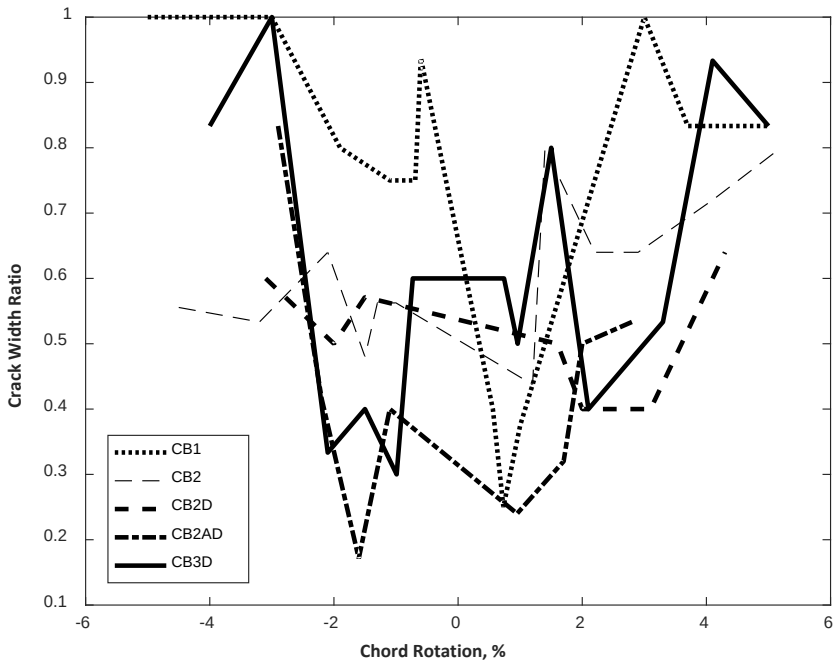

Figure 4.28 – Crack width ratio versus chord rotation

4.7 BEAM ELONGATION

The elongations of the coupling beam specimens are plotted in Figures 4.29 through 4.33 in terms of normalized beam length (the ratio of beam length at any time to the original beam length) versus chord rotation. Elongation of a beam was calculated as the difference between the vertical position of the middle marker on the top block (3 in. [75 mm] above the bottom of the top block) and the vertical position of the middle marker on the bottom block (3 in. [75 mm] below the top of the bottom block). If the middle marker was not functioning, the average vertical position of the two adjacent markers was used. The original beam length was taken as the clear length of each beam specimen measured prior to testing.

From Figure 4.29, CB1 elongated more than 2.5% while loading to a chord rotation of -6%, after which the beam shortened. This shortening coincided with the buckling of diagonal bars. While loading to a target chord rotation of +10%, the target that could not be reached due to limitations of the test setup, the beam shortened more than 2% relative to its original length at a chord rotation of +8%.

Figure 4.30 shows the elongation of CB2. While loading to a chord rotation of more than 5% in the positive loading direction, the specimen elongated more than 1.5%. Unlike CB1, CB2 did not shorten. This is consistent with the observation that in CB2, no visible buckling or associated loss of strength occurred.

Figures 4.31 and 4.32 show the elongations of CB2D and CB2AD. Both the beams exhibited less elongation than CB1 and CB2. This difference in elongations may be due to the increased length of the secondary (non-diagonal) longitudinal reinforcement in CB2D and CB2AD. The presence of axial restraint in the test of CB2AD resulted in less elongation than in

CB2D, with maximum elongations of 1% and 0.6% for CB2D and CB2AD, respectively. After reaching 5% chord rotation in both positive and negative loading directions, both specimens shortened, coinciding with buckling of diagonal bars.

The elongation of CB3D is shown in Figure 4.33. Though CB3D had its secondary (non-diagonal) longitudinal bars extended in to the blocks like CB2D and CB2AD, elongation was larger than for CB2D and CB2AD. While loading to a chord rotation of -5%, the beam elongated more than 1.5%. After the first excursion to -6% chord rotation, the beam started to shorten due to simultaneous buckling of several of the No. 6 (19 mm) diagonal bars.

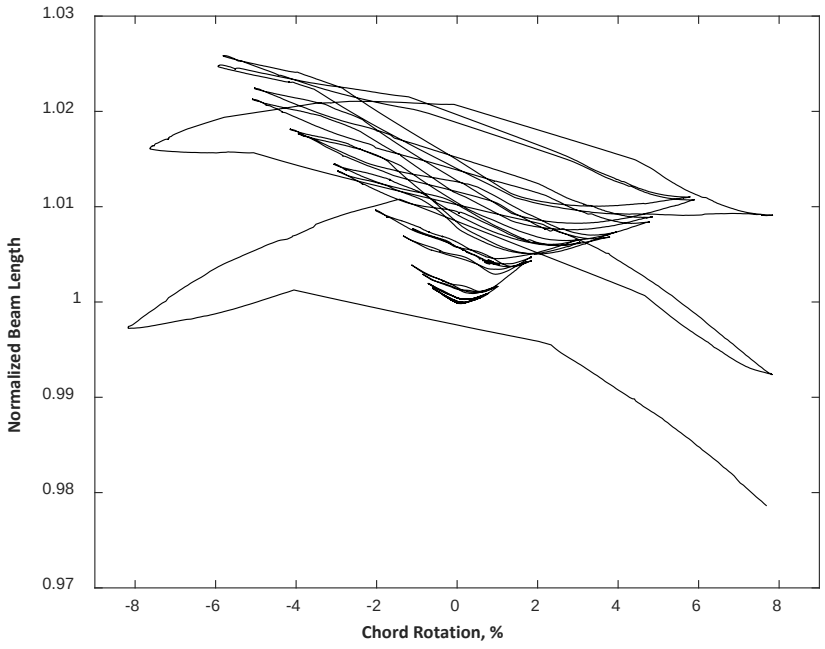

Figure 4.29 – Beam elongation for CB1

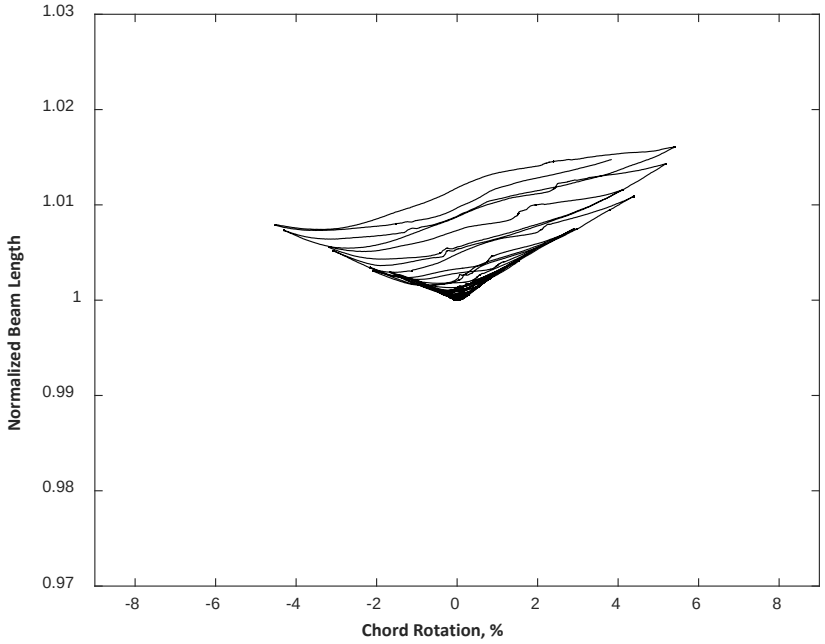

Figure 4.30 – Beam elongation for CB2

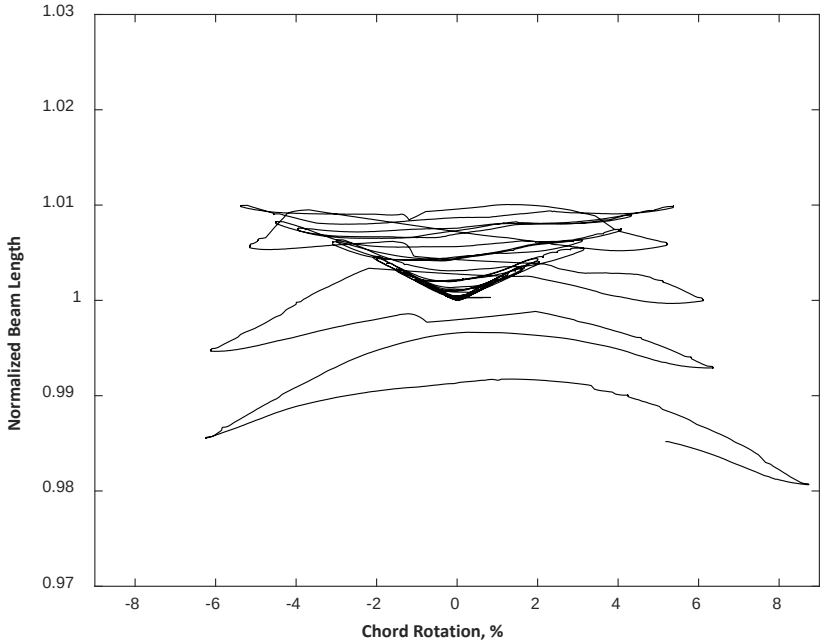

Figure 4.31 – Beam elongation for CB2D

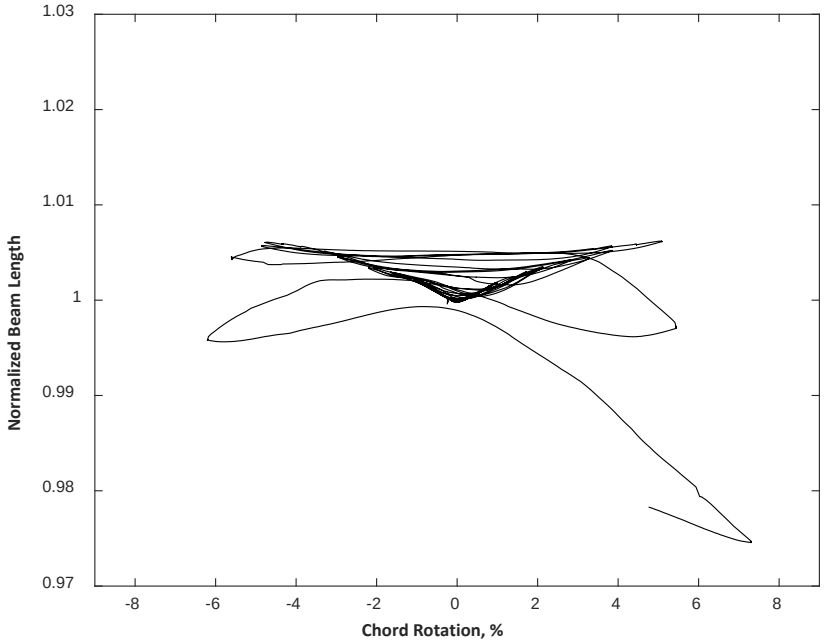

Figure 4.32 – Beam elongation for CB2AD

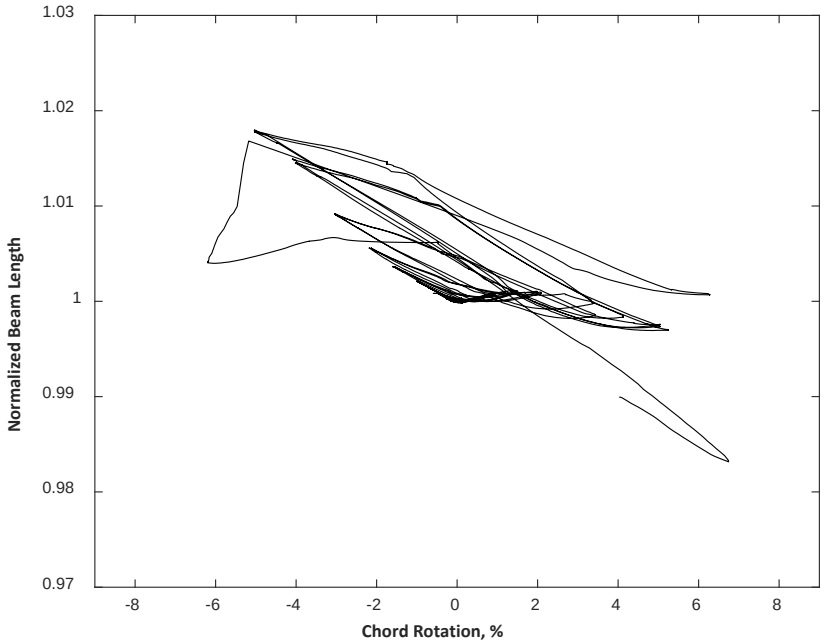

Figure 4.33 – Beam elongation for CB3D

To calculate the axial restraining force generated while testing CB2AD, two strain gauges were attached to each of the two 3-in. (75-mm) diameter high-strength threaded rods used to link the top and bottom blocks and restrain axial growth (Figures 3.5 and 3.6). As discussed earlier in this section, elongation of CB2AD was smaller than that of other specimens because of the axial restraint. Due to the restraint, the beam experienced an axial force that increased with chord rotation up to approximately 5% chord rotation. The axial force was estimated using the strain data recorded with the gauges on the threaded rods assuming an elastic modulus of 29,000 ksi (200 GPa) and nominal area of 6.8 in.^{2} (4400 mm^2). Total beam axial force is plotted against chord rotation in Figure 4.34.

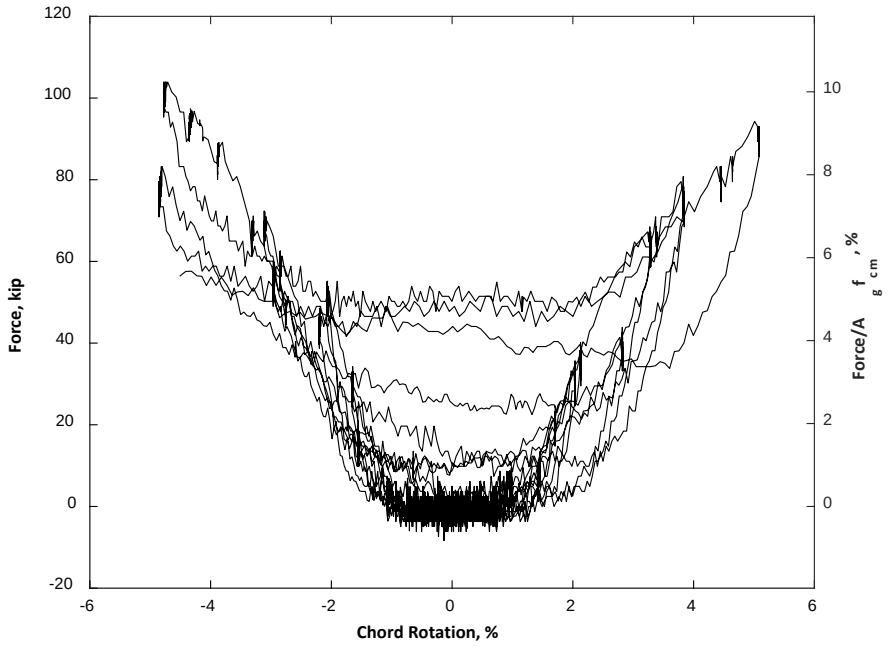

Figure 4.34 – Restraining force measured in CB2AD (1 kip = 4.45 kN)

Up to 2% chord rotation, the peak axial force was approximately 60 kips (260 kN). This increased with further increases in chord rotation up to a maximum axial force of 110 kips (480

kN) at a chord rotation of 5%. This maximum axial force is approximately 50% of the longitudinal component of $A_s f_y$ for one diagonal group based on an area of 1.76 in.^{2} (1140 mm^2) and a yield stress of 128 ksi (883 MPa). Figure 4.34 also shows the axial restraining force as a percentage of $A_g f_{cm}$. The figure indicates that axial force just exceeded 10% of $A_g f_{cm}$.

Axial restraint of CB2AD did not result in reduced chord rotation capacity compared to CB2D. This is not consistent with findings reported by Poudel (2018) from the test of a specimen with conventional Grade 60 (420) diagonal reinforcement (specimen was named CB1A). In that test, the maximum axial restraining force developed was nearly 19% of $A_g f_{cm}$. Also, the chord rotation capacity exhibited by CB1A was approximately 10% less than CB1, the control specimen reported herein with Grade 60 (420) diagonal reinforcement and tested without axial restraint.

To try to understand the different effects of axial restraint observed in the tests of CB1A (Poudel, 2018) and CB2AD, the stiffness of the entire restraining assemblies, including connections with the top and bottom blocks, was estimated. Figure 4.35 is a plot of axial force versus elongation of CB2AD. If beam axial force and elongation were linearly related, the slope of the relationship could be taken as the effective stiffness of the axial restraint mechanism present during the test. However, this was not the case. There was very little axial force up to approximately 0.08 in. (2 mm), after which axial force began to increase with elongation. From the figure, the effective stiffness of the axial restraint system when loading was found to be approximately 900 kips/in. (157 kN/mm). When unloading, the stiffness was estimated to be 1200 kips/in. (210 kN/mm). This difference in loading and unloading stiffness led to a sort of ratcheting effect, shown in Figure 4.35. Restraint system stiffness accounting for this ratcheting was approximated as the slope of a line drawn through the peaks of each cycle (Figure 4.35). The slope of this line is 650 kips/in. (114 kN/mm).

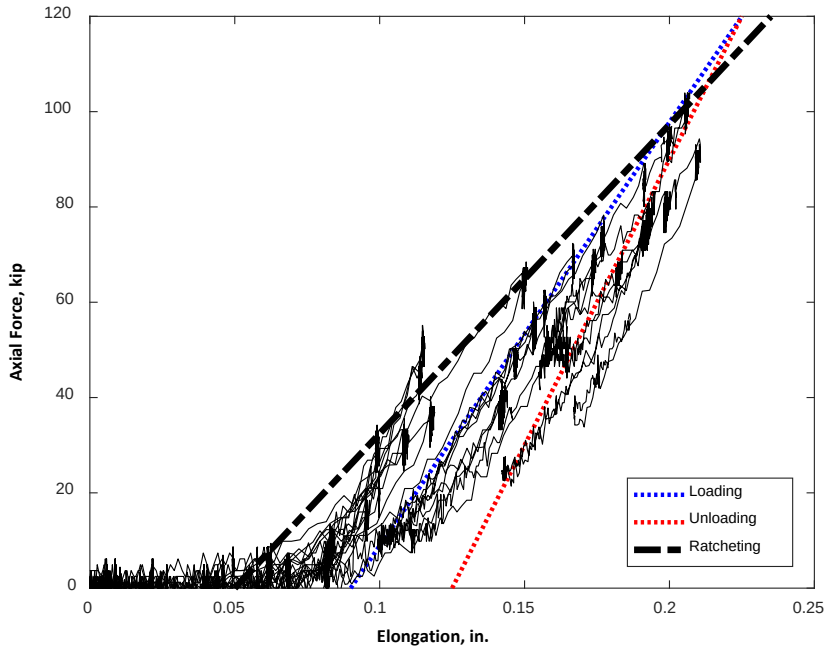

Figure 4.35 – Axial force versus elongation in CB2AD (1 kip = 4.45 kN)

The restraint system stiffness of CB1A, was reported by Poudel (2018) to be 1200 kips/in. (210 kN/mm) using the same definition (the slope of a line drawn through the peaks of the cycles). This is approximately double the stiffness observed for CB2AD. This difference in restraining system stiffness is probably the reason for the difference in maximum axial force developed in CB2AD and CB1A (about 10% of $A_g f_{cm}$ versus 19% of $A_g f_{cm}$). This is also believed to explain the differences observed in terms of the effect of axial restraint on beam chord rotation capacity.

4.8 CHANGES IN BEAM DEPTH

Normalized beam depth is plotted in Figures 4.36 through 4.45 for both positive and negative loading directions. Normalized beam depth was calculated as the change in relative distance between the two outermost markers in a row, divided by the initial distance between the markers. It was calculated at the peak chord rotation in the second cycle to each target chord

rotation. Typically, the outermost markers were those located in Columns 1 and 5 (Figure 4.8). In the case of marker malfunction, markers from Column 2 were used instead of Column 1 and Column 4 were used instead of Column 5. In a few occasions (later in the test), markers from Column 3 needed to be used instead of either Column 4 or Column 2. Values calculated using markers from Columns 2, 3, or 4 are identified with a solid symbol in Figures 4.36 to 4.45.

Changes in the depth of CB1 and CB2, the specimens with the secondary (non-diagonal) longitudinal reinforcement terminated near the beam-block interface, were small ($\leq$0.6%) near midspan and larger near the beam-block interface (up to 1.0%). CB2 exhibited slightly larger changes in depth than CB1, especially near midspan (Figures 4.36, 4.37, 4.38, and 4.39).

Changes in the depth of CB2D and CB2AD, the two specimens with the secondary (non-diagonal) longitudinal reinforcement extended into the blocks, did not vary much from midspan to end and were larger than those of CB1 and CB2 after a chord rotation of 2% (Figures 4.40, 4.41, 4.42, and 4.43). The depth of CB2D was more than 2% larger than its original depth at a chord rotation of 3%, indicating that shear related damage was becoming extensive at that stage of loading as a result of deformations moving away from the joint and into the span due to the extended secondary reinforcement. CB2AD, most probably due to the presence of axial restraint, exhibited the largest change in depth among all the specimens (Figures 4.42 and 4.43), exceeding 1% expansion at a chord rotation of 2% and 3% expansion at a chord rotation of about 3%. This may indicate that axial restraint increased the shear-related damage beginning at a chord rotation of only 2% (also evident in Figure C.27 and Figure C.28).

CB3D, the other specimen with secondary (non-diagonal) longitudinal reinforcement extended into the blocks, exhibited changes in depth similar to CB2D up to 2% chord rotation,

after which change in beam depth could not be calculated (Figures 4.44 and 4.45). The higher design shear stress therefore did not cause a marked change in damage up to 2% chord rotation.

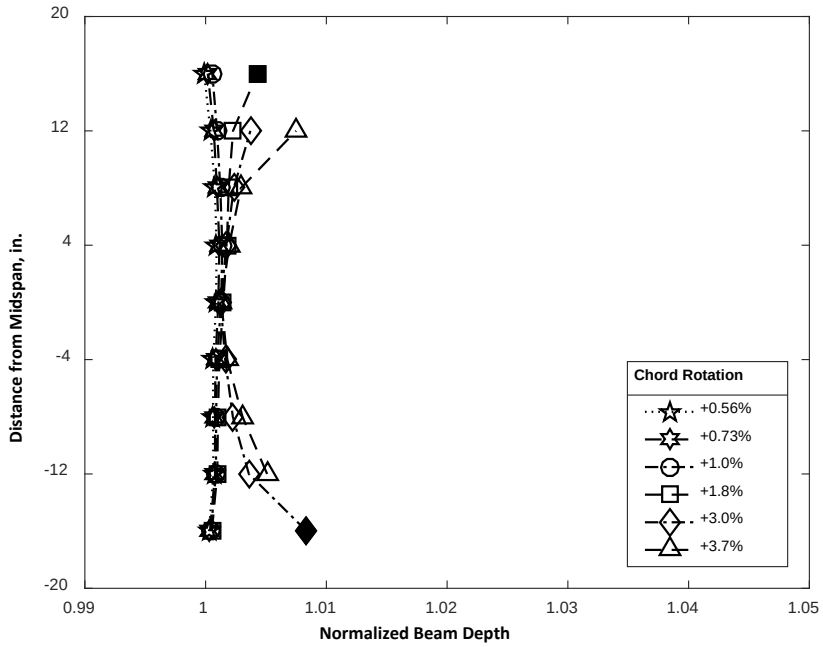

Figure 4.36 – Normalized beam depth for CB1 at positive chord rotations, solid symbols indicate use of markers that are not in the outermost columns (1 in. = 25.4 mm)

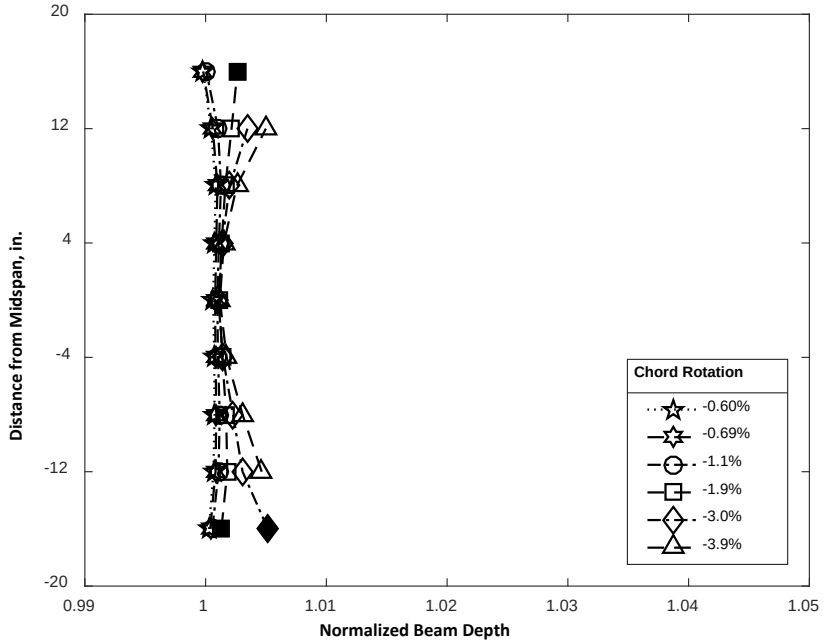

Figure 4.37 – Normalized beam depth for CB1 at negative chord rotations, solid symbols indicate use of markers that are not in the outermost columns (1 in. = 25.4 mm)

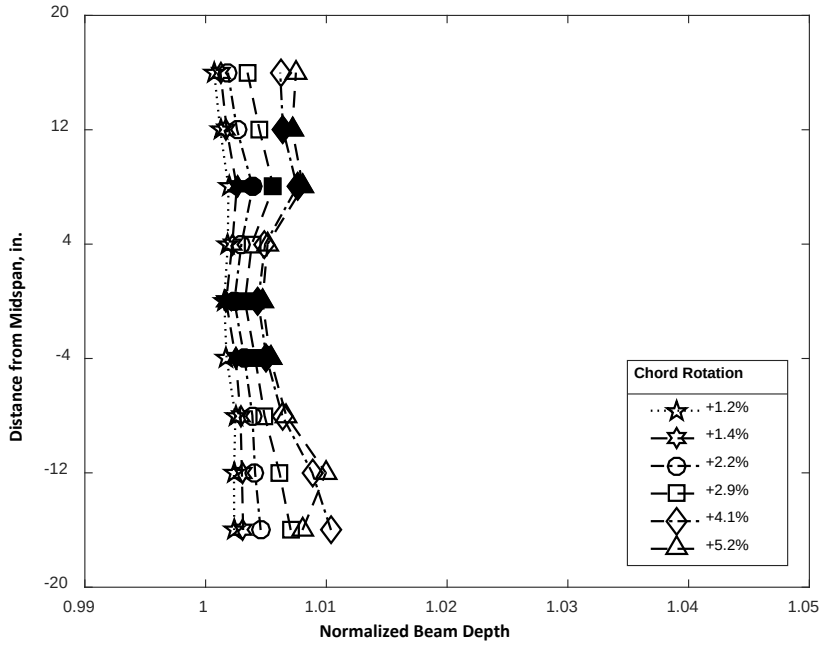

Figure 4.38 – Normalized beam depth for CB2 at positive chord rotations, solid symbols indicate use of markers that are not in the outermost columns (1 in. = 25.4 mm)

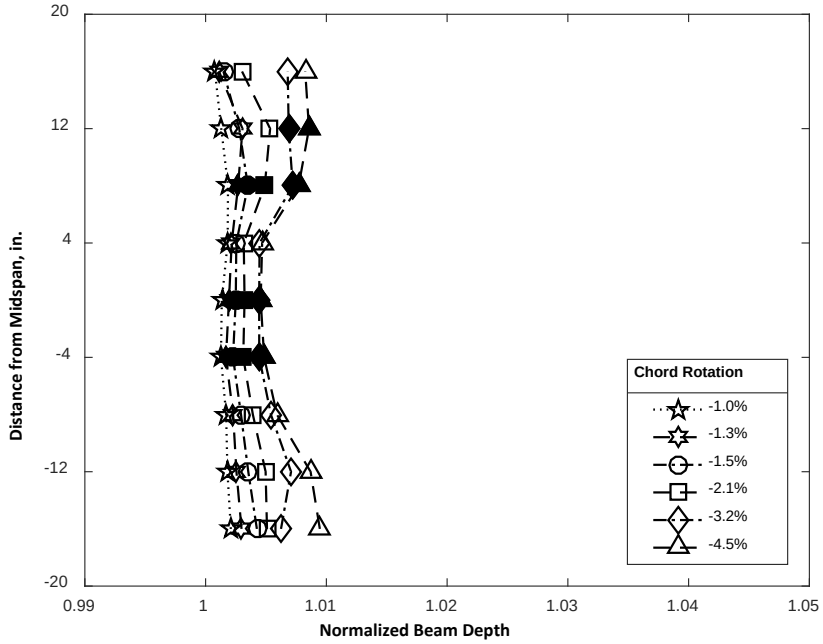

Figure 4.39 – Normalized beam depth for CB2 at negative chord rotations, solid symbols indicate use of markers that are not in the outermost columns (1 in. = 25.4 mm)

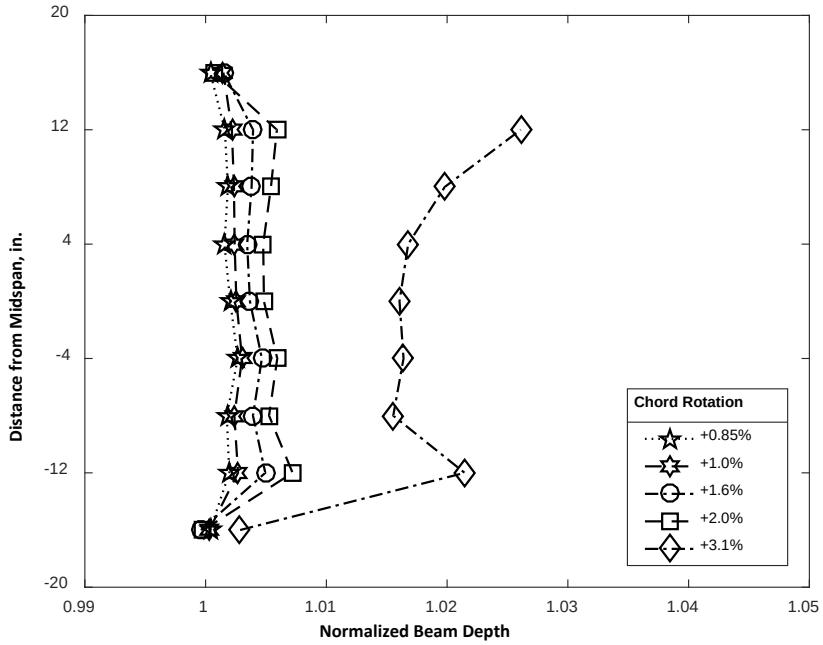

Figure 4.40 – Normalized beam depth for CB2D at positive chord rotations (1 in. = 25.4 mm)

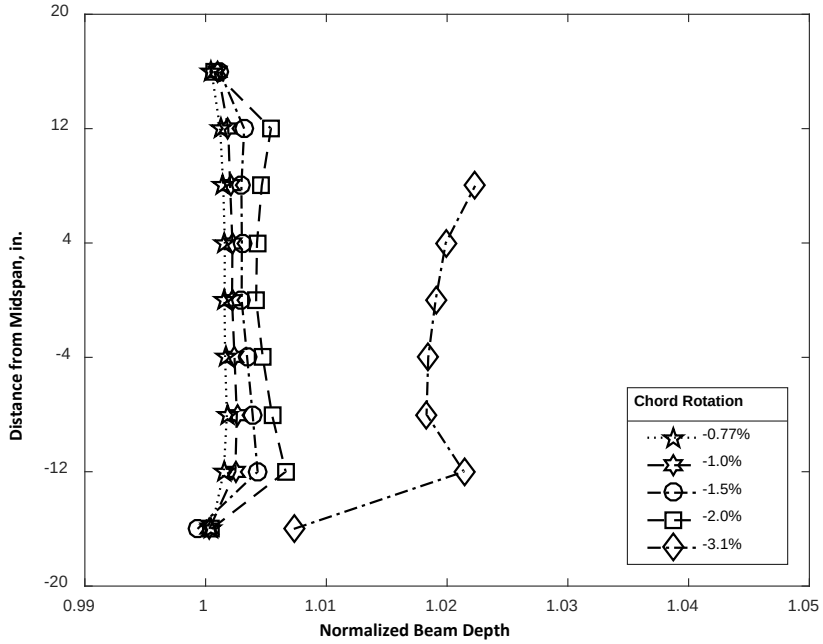

Figure 4.41 – Normalized beam depth for CB2D at negative chord rotations (1 in. = 25.4 mm)

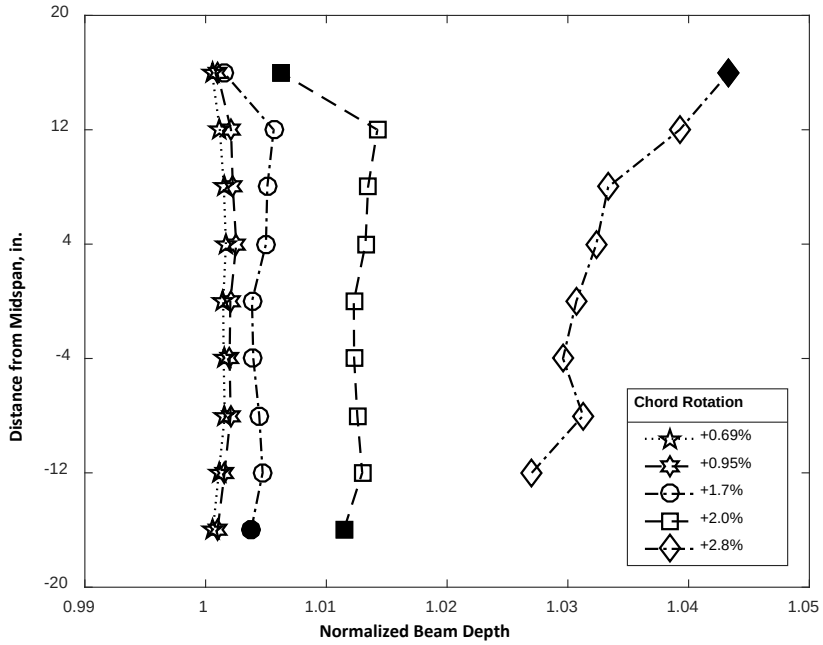

Figure 4.42 – Normalized beam depth for CB2AD at positive chord rotations, solid symbols indicate use of markers that are not in the outermost columns (1 in. = 25.4 mm)

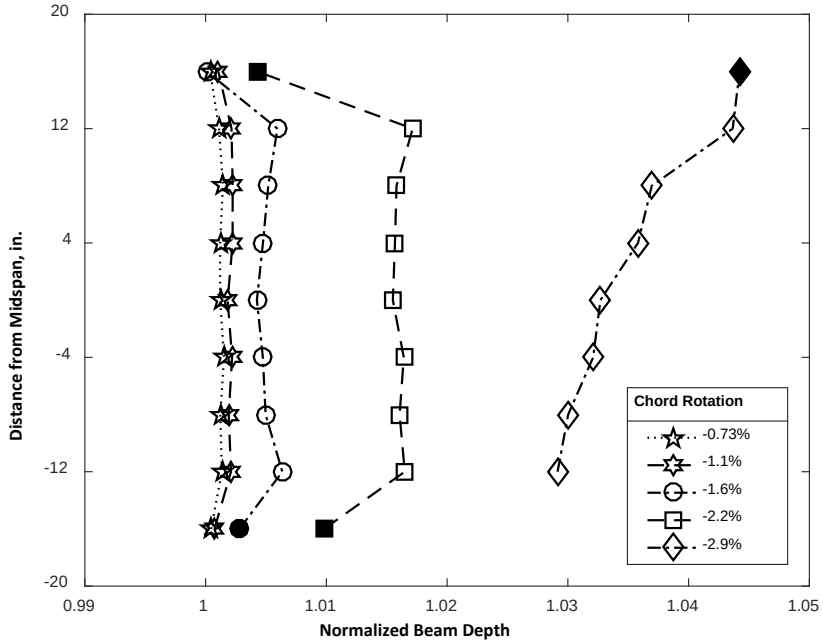

Figure 4.43 – Normalized beam depth for CB2AD at negative chord rotations, solid symbols indicate use of markers that are not in the outermost columns (1 in. = 25.4 mm)

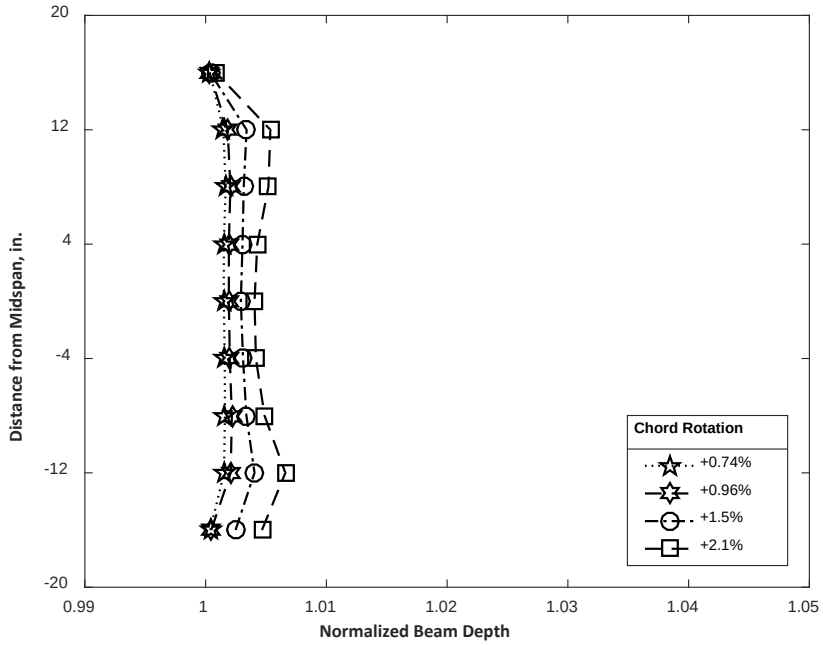

Figure 4.44 – Normalized beam depth for CB3D at positive chord rotations (1 in. = 25.4 mm)

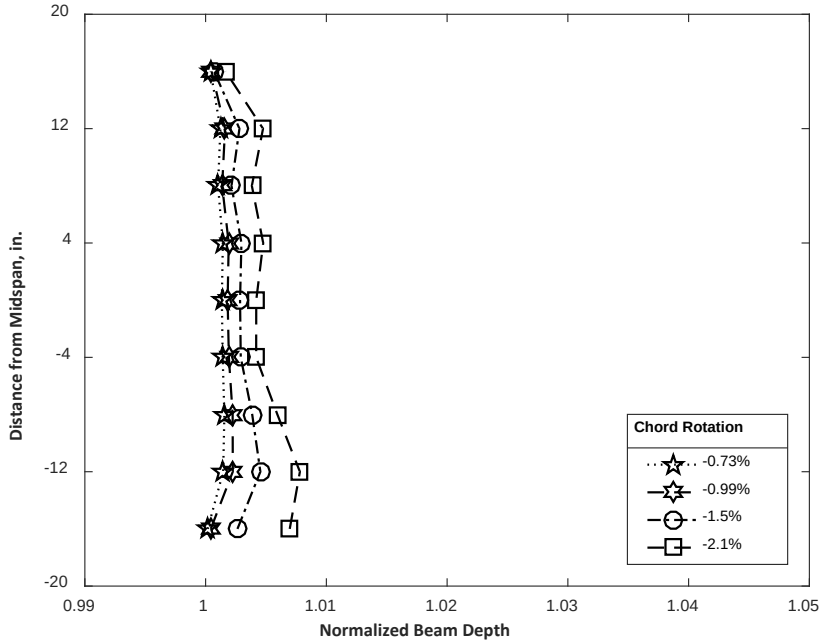

Figure 4.45 – Normalized beam depth for CB3D at negative chord rotations (1 in. = 25.4 mm)

4.9 STIFFNESS

Stiffness is the force required to cause a unit displacement. In this section, stiffness is defined as the shear force required to cause the top of a coupling beam to travel a unit distance with respect to the bottom of the beam, assuming zero relative rotation between beam ends. Data from the measured shear versus chord rotation results of all the specimens (Figures 4.2 through 4.6) were used to calculate stiffness. Displacement was taken as the product of chord rotation (Eq. 4.2) and clear span length (34 in. [860 mm]).

Figure 4.46 represents an idealized force-displacement curve used by Otani in 1981 to propose different measures of stiffness and energy dissipation. As shown in the figure, effective initial stiffness K_e is defined as the secant stiffness to the notional yield point and unloading

stiffness K_u represents the secant stiffness from the maximum displacement of a loading cycle to the point of zero lateral force.

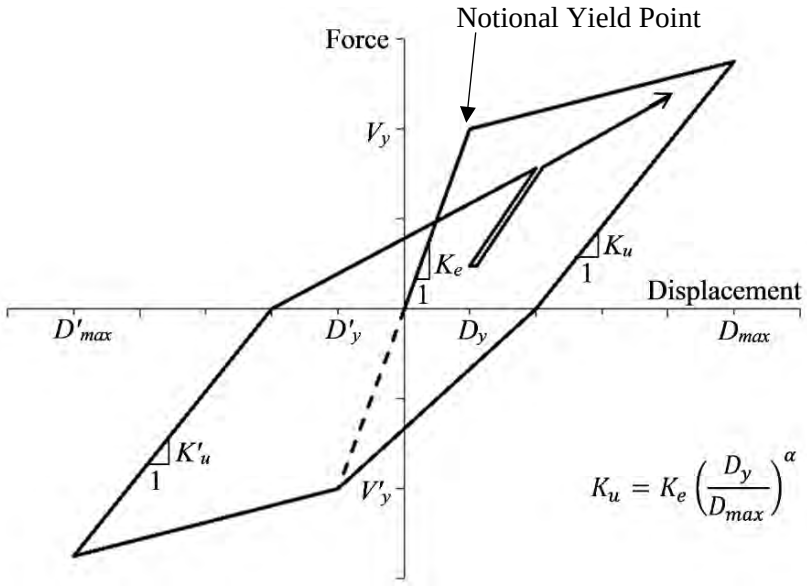

Figure 4.46 – Idealized force-displacement curve and hysteresis model (Otani, 1981)

4.9.1 EFFECTIVE INITIAL STIFFNESS

Envelopes of the measured shear force-chord rotation responses for the coupling beam specimens are shown in Figures 4.47 through 4.51. The coordinates of each data point defining the envelopes are presented in Table E.1 through Table E.10 in Appendix E. The envelope was determined by identifying the chord rotation (for each loading direction) associated with the peak shear attained for each step of the loading protocol (Table 3.5).

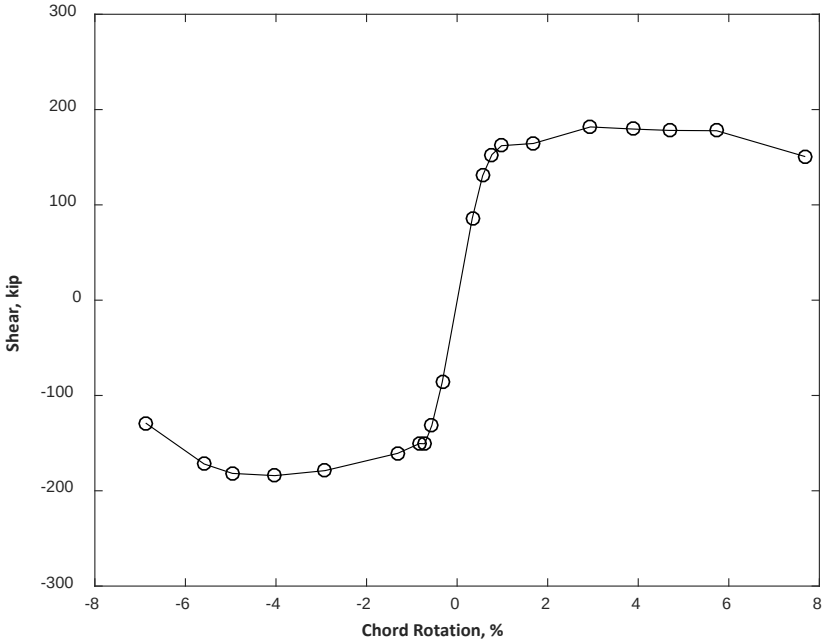

Figure 4.47 – Envelope of shear versus chord rotation for CB1 (1 kip = 4.45 kN)

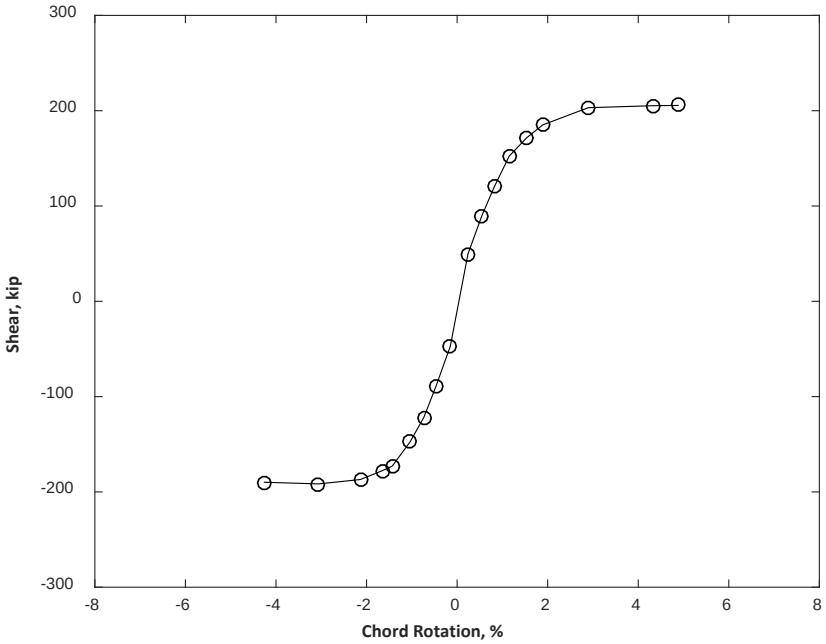

Figure 4.48 – Envelope of shear versus chord rotation for CB2 (1 kip = 4.45 kN)

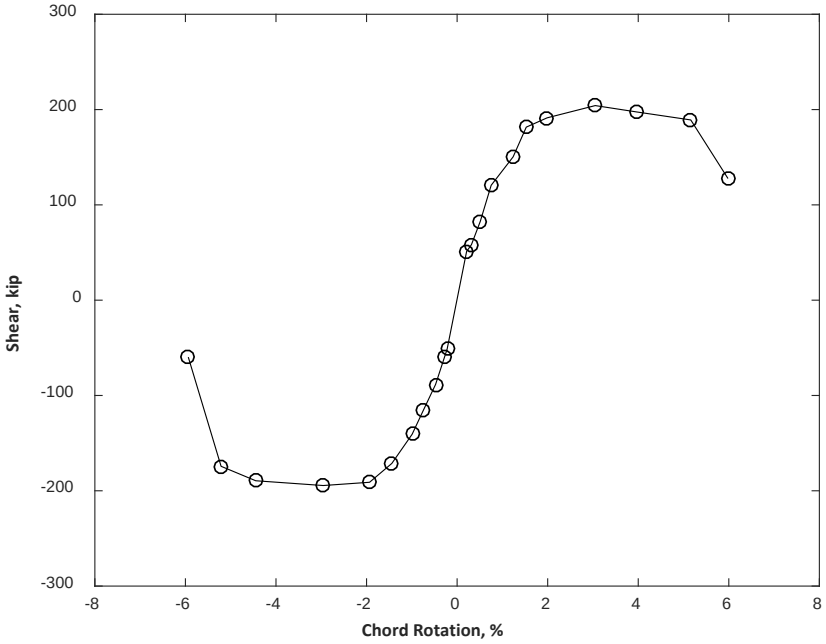

Figure 4.49 – Envelope of shear versus chord rotation for CB2D (1 kip = 4.45 kN)

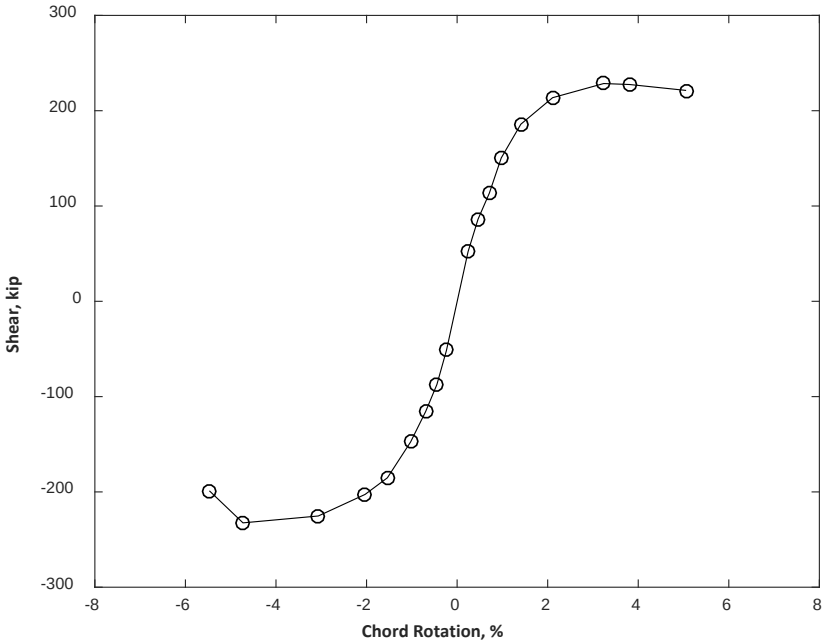

Figure 4.50 – Envelope of shear versus chord rotation for CB2AD (1 kip = 4.45 kN)

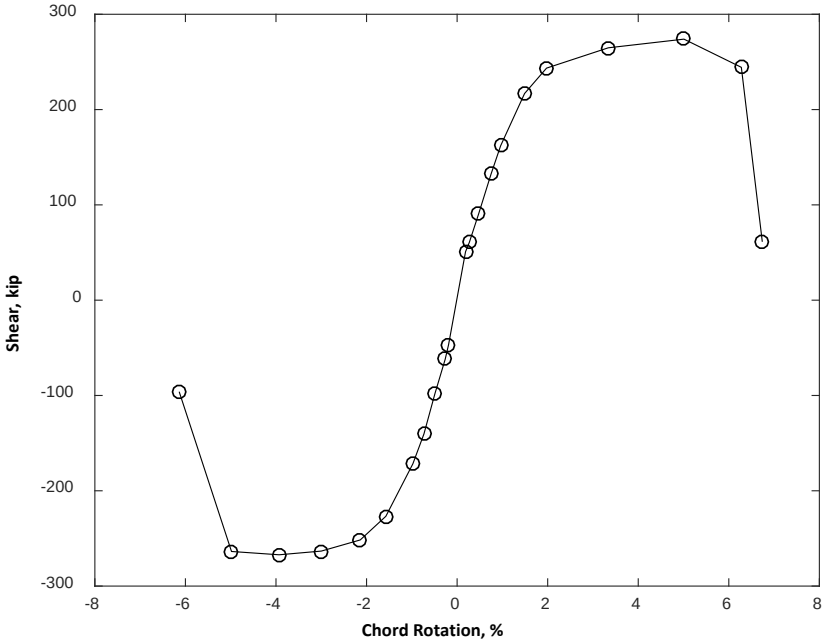

Figure 4.51 – Envelope of shear versus chord rotation for CB3D (1 kip = 4.45 kN)

To allow for a direct comparison of the coupling beam envelopes, the data from Figures 4.47 through 4.51 are combined in Figure 4.52. The peak force imposed on CB3D exceeded that of the other four specimens because it was designed to have larger strength. The figure also shows that the stiffnesses of the specimens are similar, with the stiffness of CB1 being slightly larger than that of the others, especially at shear forces between 100 and 150 kips. This small but consistent difference in stiffness was correlated with the smaller amount of high-strength diagonal reinforcement in specimens constructed with Grade 120 (830) steel. Specimen CB1 had 12 No. 7 (22 mm) diagonal bars, while the other specimens had 8 No. 6 (19 mm) (CB2, CB2D and CB2AD) and 12 No. 6 (19 mm) (CB3D) diagonal bars (Table 1.1).

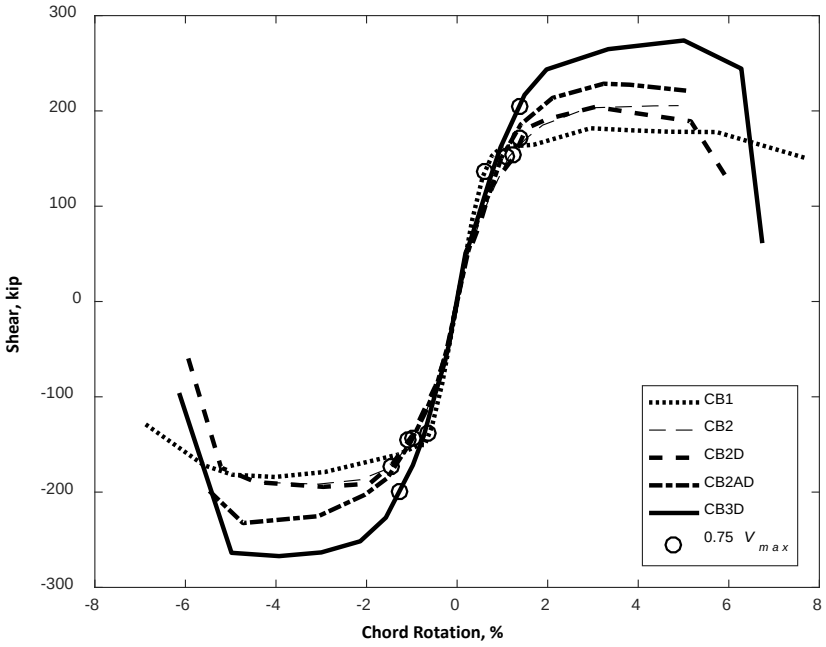

Figure 4.52 – Envelopes of shear versus chord rotation (1 kip = 4.45 kN)

The envelopes of the measured shear force-chord rotation data were used to determine the effective initial stiffness K_e based on the secant to 75% of the maximum force resisted by the coupling beam specimens in each loading direction. This definition was used because it is simple and the because tangent stiffness of the shear force-chord rotation curve started to decrease after this point (Figure 4.52). The value of the shear force associated with 75% of the maximum and the corresponding secant stiffness, K_e, are shown in Table E.1 through Table E.10 in Appendix E. The chord rotation at 75% of the maximum force is also listed in Table E.1 through Table E.10 in Appendix E. For this definition of K_e, the chord rotation at yield increased approximately in proportion with yield stress.

The values of K_e obtained for CB1 are 660 and 670 kips/in. (115 and 117 kN/mm) in the positive and negative directions, respectively. The values of K_e obtained for CB2, CB2D and CB2AD in both positive and negative directions range from 360 to 420 kips/in. (63 to 73 kN/mm).

The values of K_e obtained for CB3D are in between the previous two – ranging from 440 to 470 kips/in. (77 to 82 kN/mm). In summary, the average value of K_e obtained for CB1 was 660 kips/in. (116 kN/mm), about 68% higher than 390 kips/in. (69 kN/mm), the average value of K_e obtained for CB2, CB2D, and CB2AD, and more than 45% higher than 460 kips/in. (80 kN/mm), the average value of K_e obtained for CB3D in both the positive and negative loading directions.

Neglecting shear deformations, an effective moment of inertia (I_{eff}) was calculated based on the shear force-chord rotation data by setting the chord rotation at $0.75V_{max}$ equal to $0.75V_{max}{l_n}^2/12E_cI_{I_{eff}}$. Values of I_{eff}/I_g are shown in Figure 4.53 for each specimen and loading direction. The ratios were approximately 0.1 for CB1 and 0.06 for all other specimens. Values of I_{eff} were approximately 40% lower for specimens with high strength Grade 120 (830) reinforcement than for the specimen with conventional Grade 60 (420) reinforcement. A similar plot is shown in Figure 4.54 with transformed moment of inertia (I_{tr}) instead of gross moment of inertia (I_g). The ratios reduced to approximately 0.08 for CB1 and 0.055 for all other specimens.

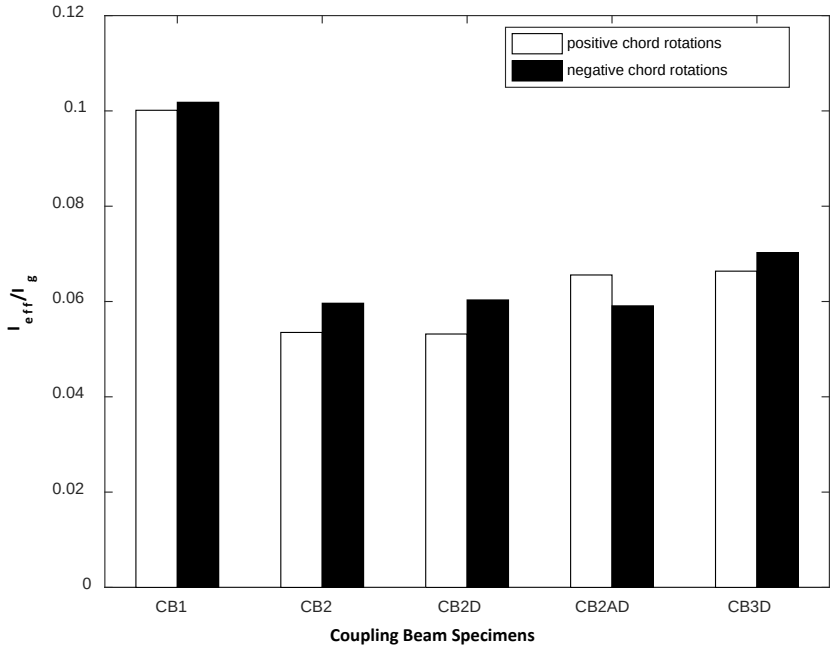

Figure 4.53 – Effective moment of inertia I_{eff} normalized by gross moment of inertia I_g

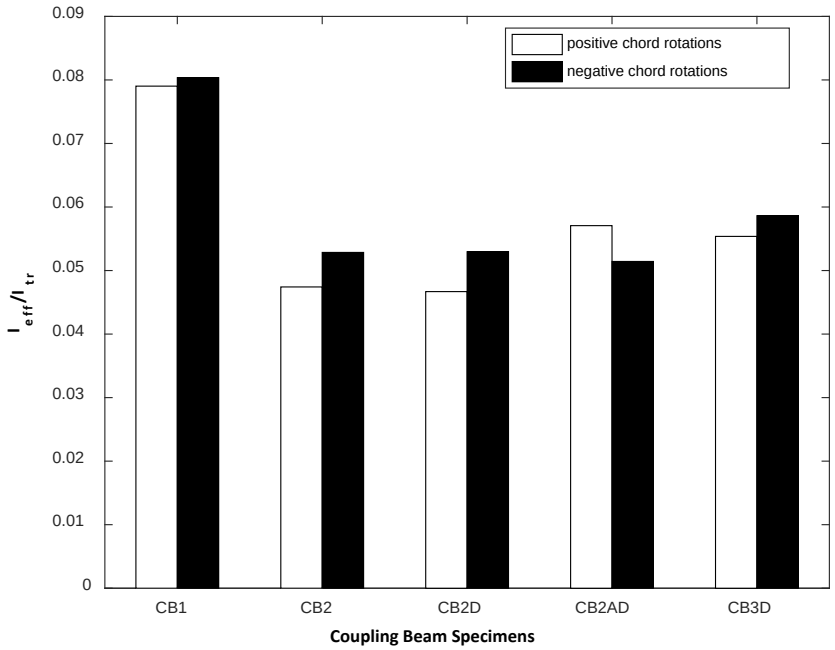

Figure 4.54 – Effective moment of inertia I_{eff} normalized by transformed moment of inertia I_{tr}

4.9.2 UNLOADING STIFFNESS

The unloading stiffness K_u, as discussed earlier, is the secant stiffness from the maximum chord rotation of a loading cycle to the point of zero shear force (Figure 4.46). Table E.11 through Table E.20 contain the measured shear versus chord rotation data used to calculate K_u. The data correspond to the peak chord rotation (and the associated shear force) during the second cycle to each target chord rotation. Values of K_u in Table E.11 through Table E.20 are plotted in Figures 4.55 through 4.59 as a function of chord rotation. To allow for a direct comparison among specimens, the data from Figures 4.55 through 4.59 are combined in Figure 4.60. This shows K_u is somewhat similar for the specimens with high strength Grade 120 (830) diagonal reinforcement (CB2, CB2D, CB2AD, CB3D) and larger for CB1, the control specimen with conventional Grade 60 (420) diagonal reinforcement.

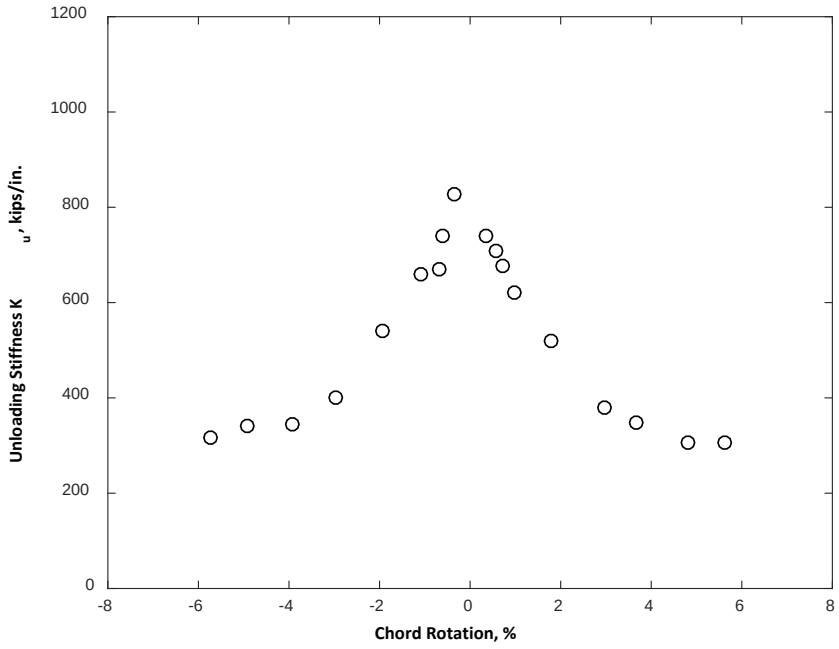

Figure 4.55 – Unloading stiffness K_u versus chord rotation for CB1 (1 kip/in. = 0.175 kN/mm)

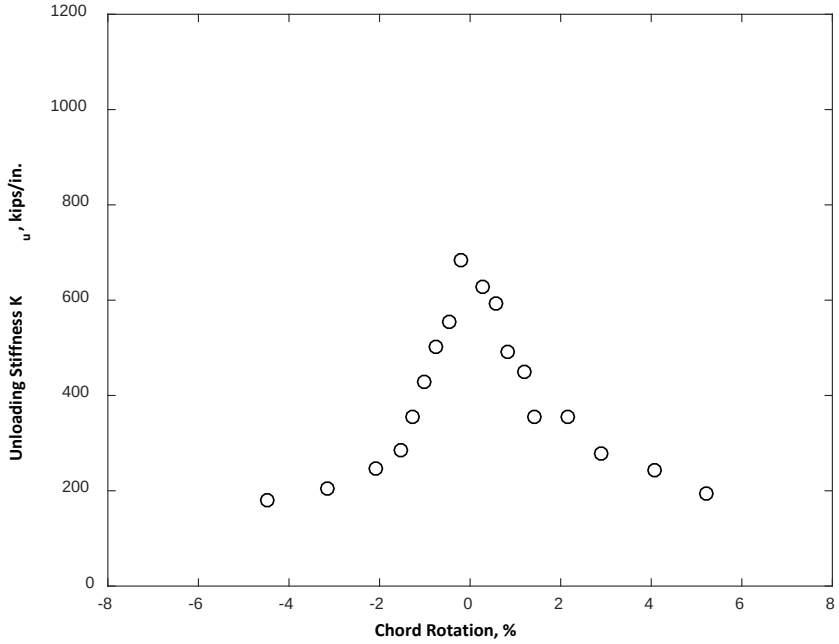

Figure 4.56 – Unloading stiffness K_u versus chord rotation for CB2 (1 kip/in. = 0.175 kN/mm)

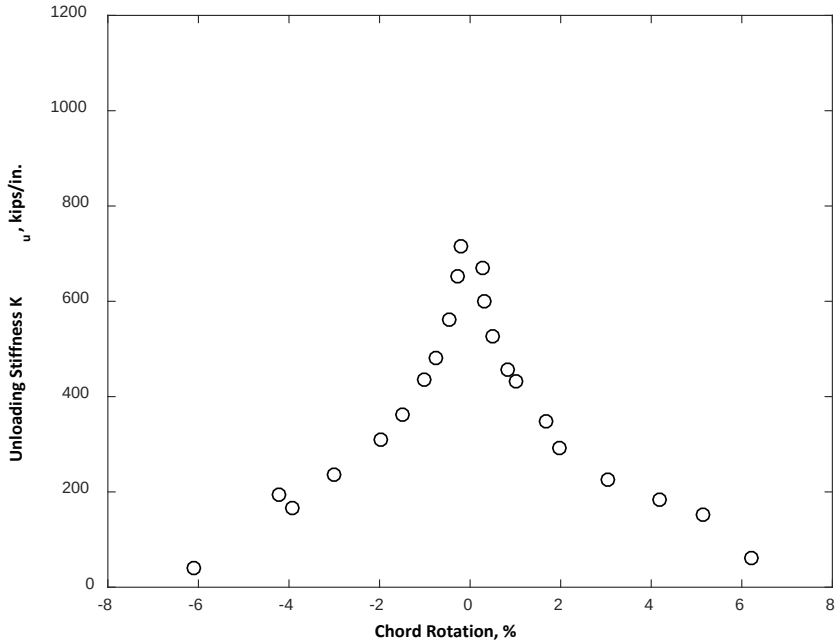

Figure 4.57 – Unloading stiffness K_u versus chord rotation for CB2D (1 kip/in. = 0.175 kN/mm)

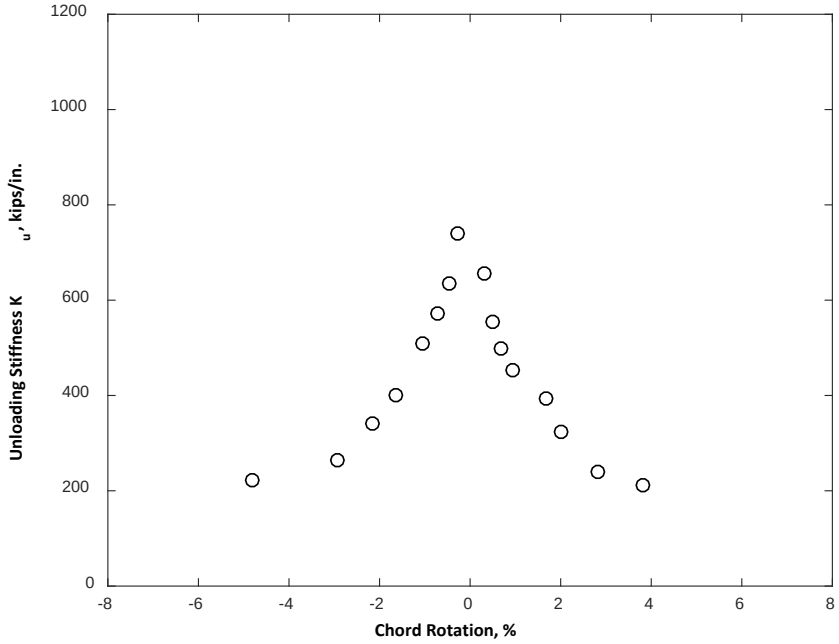

Figure 4.58 – Unloading stiffness K_u versus chord rotation for CB2AD (1 kip/in. = 0.175 kN/mm)

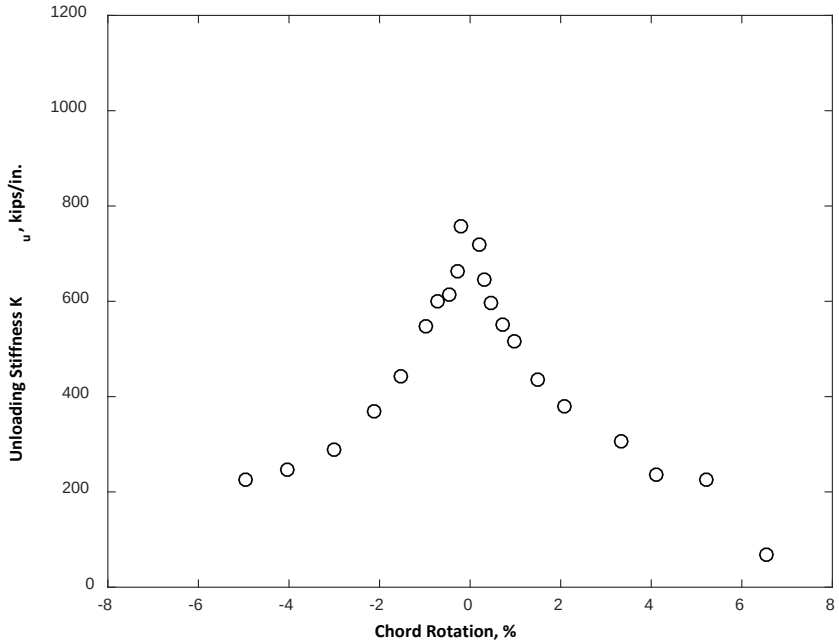

Figure 4.59 – Unloading stiffness K_u versus chord rotation for CB3D (1 kip/in. = 0.175 kN/mm)

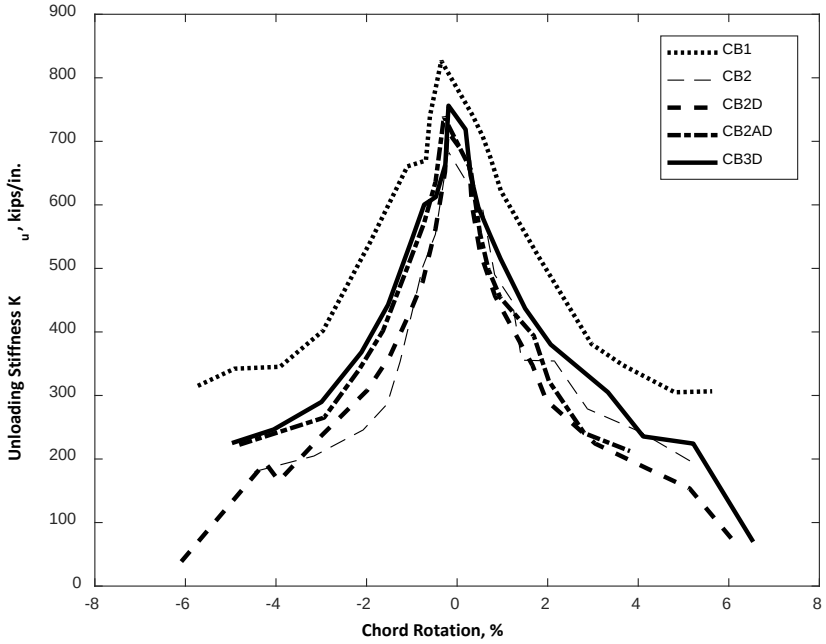

Figure 4.60 – Unloading stiffness K_u versus chord rotation (1 kip/in. = 0.175 kN/mm)

4.10 HYSTERETIC ENERGY DISSIPATION

The shear versus chord rotation data obtained during the second cycle of each loading step were used to calculate a hysteretic energy dissipation index, E_h to examine how reinforcement grade and detailing (cutoff versus developed) affected the hysteretic energy dissipated by the coupling beams. The index E_h was calculated with Eq. 4.20 (Otani 1981), where W is the area enclosed by the shear versus chord rotation curve during the second cycle of each loading step, divided by $2\pi D_m V_m$, where D_m and V_m are the peak chord rotation and shear imposed in that cycle. The index represents the equivalent viscous damping factor of a linear-elastic system capable of dissipating energy W in one cycle under steady-state oscillation.

$$E_h = \frac{W}{2\pi D_m V_m} \qquad \text{Eq. 4.20}$$

Figure 4.61 shows E_h versus chord rotations for all five specimens. The figure shows that for chord rotations between 3 and 5%, E_h for CB1, the control specimen with conventional Grade 60 (420) diagonal reinforcement, was approximately two times larger than E_h for specimens with high-strength Grade 120 (830) diagonal reinforcement. The value of E_h therefore changed in approximately inverse proportion to the yield stress. The chord rotations plotted in Figure 4.61 can be adjusted by multiplying chord rotation by $60/f_y$ in ksi ($420/f_y$ in MPa). Figure 4.62, a plot of E_h versus chord rotations adjusted for the yield stress of the diagonal bars, shows that E_h is a function of plastic deformation, which for a given chord rotation is smaller for a beam having higher grade of reinforcement with higher yield stress.

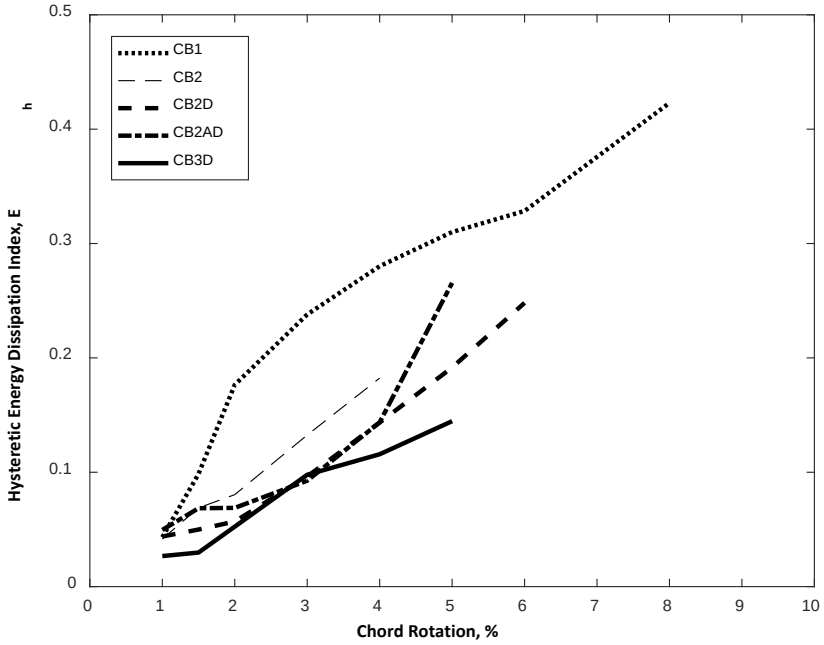

Figure 4.61 – Hysteretic energy dissipation index E_h versus chord rotation

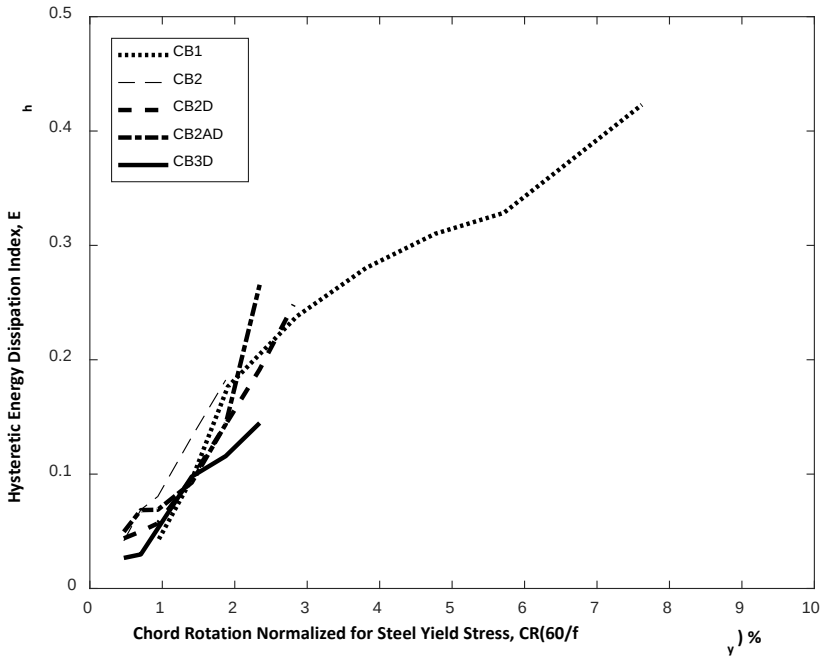

Figure 4.62 – Hysteretic energy dissipation index E_h versus chord rotation normalized for yield stress of diagonal bars

4.11 RESIDUAL CHORD ROTATIONS WHEN UNLOADED

Residual chord rotation after unloading (at zero shear force) is important as an indicator of potential repair needs after an earthquake. Figure 4.63 shows the residual chord rotation divided by peak chord rotation of the same loading cycle plotted versus chord rotation. For this plot, residual chord rotation was calculated for the second cycle of loading to each target drift. Starting from 1% chord rotation, large differences were evident between CB1, the control specimen with conventional Grade 60 (420) diagonal reinforcement, and the other specimens. For instance, at 4% chord rotation, residual chord rotations were below 40% of the prior peak in both loading directions for CB2, CB2D, CB2AD, and CB3D. At the same target chord rotation, the residual chord rotation was more than 60% of the previous peak for CB1.

Similar to hysteretic energy dissipation, residual chord rotations are related to the extent of yielding. Figure 4.64 is a replica of Figure 4.63 except the horizontal axis is multiplied by $60/f_y$ in ksi ($420/f_y$ in MPa). When chord rotation is adjusted in this manner, residual chord rotations are similar among the specimens. It therefore appears that residual displacements of isolated members decrease in approximately inverse proportion to reinforcement yield stress.

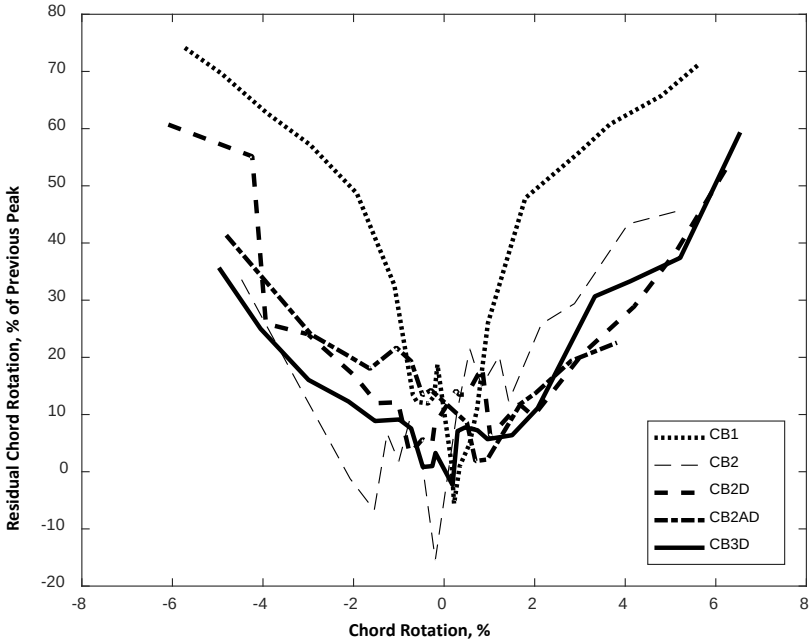

Figure 4.63 – Residual chord rotation versus chord rotation

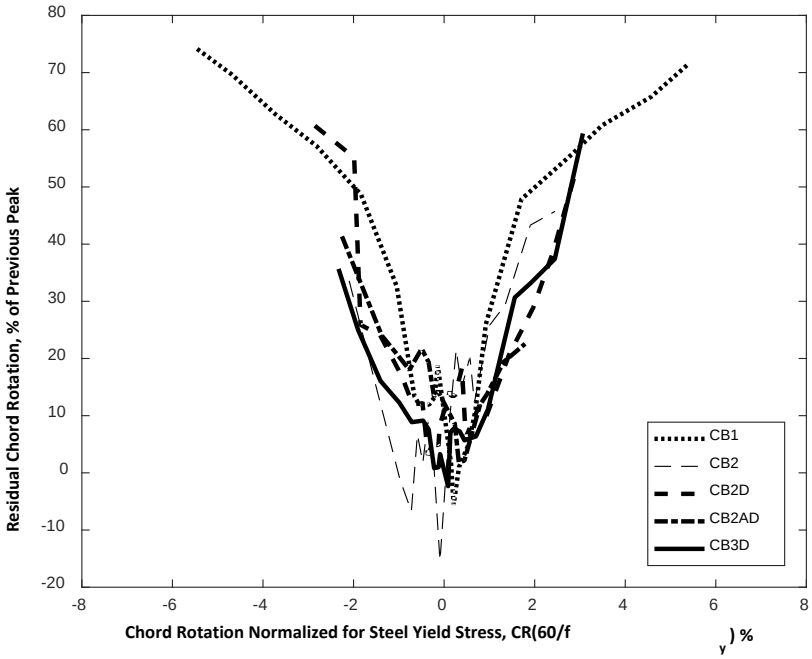

Figure 4.64 – Residual chord rotation versus chord rotation normalized for yield stress of diagonal bars

CHAPTER 5 ESTIMATION OF CHORD ROTATION CAPACITY AND MODELING RECOMMENDATIONS

5.1 ESTIMATION OF CHORD ROTATION CAPACITY

5.1.1 DATABASE DESCRIPTION

A database of results from 33 diagonally reinforced coupling beam tests (including the 5 beams reported herein) was compiled from the literature (Appendix F). The criteria for inclusion in this database were that: 1) the specimen was diagonally reinforced, 2) sufficient information was available describing the specimens, and 3) the concrete contained no fiber reinforcement. Details are provided for each specimen in Appendix F including specimen geometry, material properties, reinforcement, measured strength, and chord rotation capacity. The chord rotation capacity of a specimen was defined as the average of the maximum chord rotations imposed in each loading direction while maintaining 80% of the peak force in each loading direction. Exceptions to this definition were made for a few cases as identified in Appendix F. Several specimens that are listed in Appendix F were not included in subsequent analyses; reasons justifying the exclusions are provided.

The database includes 18 diagonally reinforced coupling beams with all longitudinal reinforcement terminated near the beam-wall interface and 15 diagonally reinforced coupling beams with all longitudinal reinforcement fully developed into the adjacent walls. Twenty of the 33 specimens were confined with hoops around the entire coupling beam cross section (designated as ‘full section confinement’). The other 13 specimens had hoops confining each diagonal cage (designated as ‘diagonal confinement’). The database includes beams with aspect ratios ranging from 1.0 to 5.0, with most specimens having aspect ratios between 1.0 and 3.5. The specimens in

the database were of reasonably large scale, with a mean clear span length of 36 in. (910 mm). Concrete strengths of the specimens varied from 2600 to 8000 psi (18 to 55 MPa), while the yield stress of the diagonal bars ranged from 40 to 128 ksi (276 to 883 MPa).

The 17 specimens in Table 5.1 were selected from the database in Appendix F for analysis. The criteria for including a specimen in the analysis database were that it had: 1) no slab, 2) a ratio of transverse reinforcement spacing to diagonal bar diameter (s/d_b) less than or equal to 6, 3) an axial force not larger than approximately 10% of $A_g f_{cm}$, 4) dimensions reasonably representative of full scale (h > 10 in. or 250 mm), and 5) a systematic loading protocol. These limits were imposed so specimens in the analysis database would represent, to some extent, beams conforming to requirements of ACI 318-14. The small number of specimens with slabs were omitted from the analysis database to remove a variable that could not be easily evaluated due to the limited number of data. It will be shown later that these specimens tended to have larger chord rotation capacities than expected for specimens with similar proportions and no slab. The three specimens with axial forces larger than 10% of $A_g f_{cm}$ were also excluded for this reason.

Table 5.1 lists key variables for each specimen in the analysis database, including: length of beam (l_n), aspect ratio (clear span-to-overall depth, l_n/h), length of secondary (non-diagonal) reinforcement (whether terminated near the beam-wall interface or developed into the wall), type of confinement (full-section confinement or diagonal-bar-group confinement), ratio of transverse reinforcement spacing to diagonal bar diameter (s/d_b) normalized by yield stress (f_y) of diagonal bars ($(s/d_b) \times \sqrt{f_y/60}$), ratio of transverse reinforcement area provided to transverse reinforcement area required in ACI 318-14 Section 18.10.7.4d(i) ($A_{\text{sh,provided}}/A_{\text{sh,calculated}}$) parallel to both beam width and depth, measured maximum shear force and shear stress, and chord

rotation capacity. It was decided to multiply s/d_b by $\sqrt{f_y/60}$ because transverse reinforcement spacing is approximately equal to the unbraced length required to restrain bar buckling and bar stress at buckling is inversely proportional to the square of that length.

Table 5.1 – Database of diagonally reinforced coupling beam specimens used for analysis

Reference	Specimen ID (as stated)	l_n in. (mm)	$\frac{l_n}{h}$	Non-diag. Reinf. Type	Conf. Type	$\frac{s}{d_b}\sqrt{\frac{f_y}{60}}$	$\frac{A_{sh,\text{provided}}}{A_{sh,\text{calculated}}}$		$V_{\text{experiment}}$ kips (kN)	$\frac{v_{\text{experiment}}}{\sqrt{f_{cm}}}$, [psi (MPa)]	Chord Rotation Capacity [a]
							Parallel to beam width	Parallel to beam depth			
Tassios, Moretti and Bezas (1996)	CB-2A	19.7 (500)	1.00	Developed	Diagonal	5.8	1.54	1.54	64 (285)	9.8 (0.82)	4.4
	CB-2B	19.7 (500)	1.67	Developed	Diagonal	5.8	1.66	1.66	38 (169)	10.2 (0.86)	5.0
Gonzalez (2001)	K	48.0 (1220)	2.74	Developed	Diagonal	3.6	1.12	2.25	221 (983)	14.6 (1.23)	7.4 [b1]
Canbolat, Parra and Wight (2005)	Specimen 1	23.6 (600)	1.00	Developed	Diagonal	6.2	1.03	1.03	106 (472)	7.4 (0.63)	3.8 [b2]
Fortney, Rassati, and Shahrooz (2008)	DCB-2	36.0 (914)	3.00	Cutoff	Diagonal	2.5	0.93	1.09	93 (414)	8.7 (0.73)	10
Naish, Fry, Klemencic, and Wallace (2013)	CB24D	36.0 (914)	2.40	Cutoff	Diagonal	3.1	1.84	2.50	159 (708)	10.7 (0.90)	8.0
	CB24F	36.0 (914)	2.40	Cutoff	Full	3.7	1.31	1.23	171 (761)	11.5 (0.97)	9.0
	CB33F	60.0 (1520)	3.33	Cutoff	Full	3.7	1.31	1.26	124 (552)	6.9 (0.58)	8.0

Reference	Specimen ID (as stated)	l_n in. (mm)	$\frac{l_n}{h}$	Non-diag. Reinf. Length	Conf. Type	$\frac{s}{d_b}\sqrt{\frac{f_y}{60}}$	$\frac{A_{sh,provided}}{A_{sh,calculated}}$		$V_{experiment}$ kips (kN)	$\frac{v_{experiment}}{\sqrt{f'_c}}$, [psi (MPa)]	Chord Rotation Capacity [a]
							Parallel to beam width	Parallel to beam depth			
Lim, Hwang, Cheng, and Lin (2016)	CB30-DA	59.1 (1500)	3.0	Developed	Diagonal	4.9	0.70	0.70	151 (672)	8.6 (0.72)	7.8
	CB30-DB	59.1 (1500)	3.0	Developed	Full	3.3	1.13	0.85	164 (730)	9.4 (0.78)	7.7
Lim, Hwang, Wang, and Chang (2016)	CB10-1	19.7 (500)	1.0	Developed	Full	4.3	2.69	1.66	325 (1450)	23.8 (1.98)	5.8
	CB20-1	39.4 (1000)	2.0	Developed	Full	3.7	1.55	1.18	241 (1070)	11.9 (1.00)	7.3
Current study	CB1	34.0 (864)	1.89	Cutoff	Full	3.5	1.09	1.12	184 (819)	13.2 (1.10)	7.1
	CB2	34.0 (864)	1.89	Cutoff	Full	5.8	0.91	0.93	207 (921)	13.6 (1.13)	5.1
	CB2D	34.0 (864)	1.89	Developed	Full	5.8	1.03	1.07	204 (908)	14.3 (1.20)	5.3
	CB2AD	34.0 (864)	1.89	Developed	Full	5.8	1.16	1.20	234 (1040)	17.4 (1.50)	5.3
	CB3D	34.0 (864)	1.89	Developed	Full	5.8	1.05	1.08	275 (1220)	19.4 (1.63)	5.6

[a] Chord rotation capacity obtained from the average of maximum chord rotations attained in both loading directions while maintaining a shear force not less than 80% of the maximum measured shear force in that loading direction.

[b] Exception from the definition of chord rotation capacity stated in 'a'.

[b1] Average of chord rotation attained in one loading direction and chord rotation corresponding to peak shear force in the other loading direction.

[b2] Average of maximum chord rotations attained in two loading directions, though in one the shear force was less than 80% of the maximum.

5.1.1.1 ANALYSIS OF TRENDS

In Figures 5.1 through 5.6, beam chord rotation capacity is plotted against l_n/h, maximum shear stress (in terms of $\sqrt{f_{cm}}$), s/d_b, $(s/d_b) \times \sqrt{f_y/60}$, and transverse reinforcement area provided parallel to beam width or depth (separate plots) divided by transverse reinforcement area required in ACI 318-14 Section 18.10.7.4d(i) ($A_{sh,\text{provided}}/A_{sh,\text{calculated}}$). Beams with cutoff longitudinal bars and beams with developed longitudinal bars are distinguished with different marker shapes. Beams with aspect ratios of 2.0 or more are identified with a cross within the markers. Solid markers identify the specimens reported herein.

Figure 5.1 shows a positive correlation between chord rotation capacity and aspect ratio, with beams with higher aspect ratios withstanding larger chord rotations. No difference was observed between the trends for beams with cutoff longitudinal reinforcement and for beams with developed longitudinal reinforcement.

The plot of chord rotation capacity versus shear stress (Figure 5.2) did not exhibit a trend. The lack of clear trend is consistent with the observation in Chapter 4 that designing CB3D for a nominal shear strength near $15\sqrt{f_c'}$ [psi] ($1.25\sqrt{f_c'}$ [MPa]), 50% more than the ACI Building Code limit, did not lead to a smaller chord rotation capacity. Shear stress may therefore not have a strong influence on the chord rotation capacity of well detailed diagonally reinforced coupling beams.

Figures 5.3 and 5.4 show negative correlations between chord rotation capacity and both s/d_b and $s/d_b\sqrt{f_y/60}$. These trends were similar for beams with cut off longitudinal bars and beams with developed longitudinal bars. Although data from tests with Grade 120 (830) are limited, the plot against $s/d_b\sqrt{f_y/60}$ is believed to be the more appropriate comparison because:

1) an important function of transverse reinforcement is restraint of bar buckling and 2) the Euler buckling equation indicates that bar stress at buckling is inversely proportional to the square of unbraced length, which can be taken approximately equal to transverse reinforcement spacing. This may also explain the lower chord rotation capacities exhibited by the specimens with Grade 120 (830) diagonal reinforcement compared to the control specimen with Grade 60 (420) diagonal reinforcement (Section 4.1.3) in this study.

No correlation was observed in Figures 5.5 and 5.6 between chord rotations and $A_{sh,\text{provided}}/A_{sh,\text{calculated}}$ in either direction (parallel to both beam width and beam depth). From measured strains in the transverse reinforcement (Section 4.5.3), it was observed that most of the hoops and crossties did not yield. The lack of trend may be because transverse reinforcement is not fully engaged.

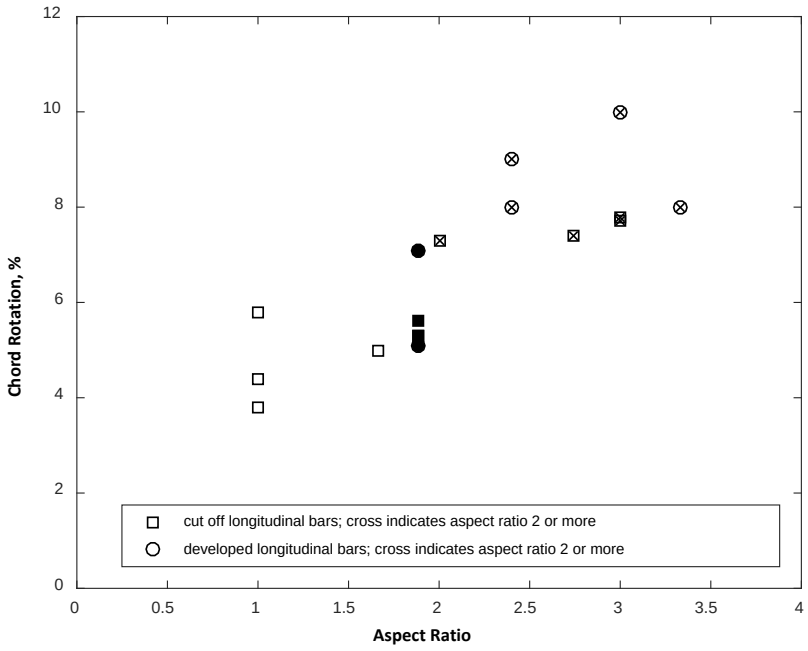

Figure 5.1 – Chord rotation versus aspect ratio (l_n/h); specimens with $l_n/h \geq 2$ have an "x"

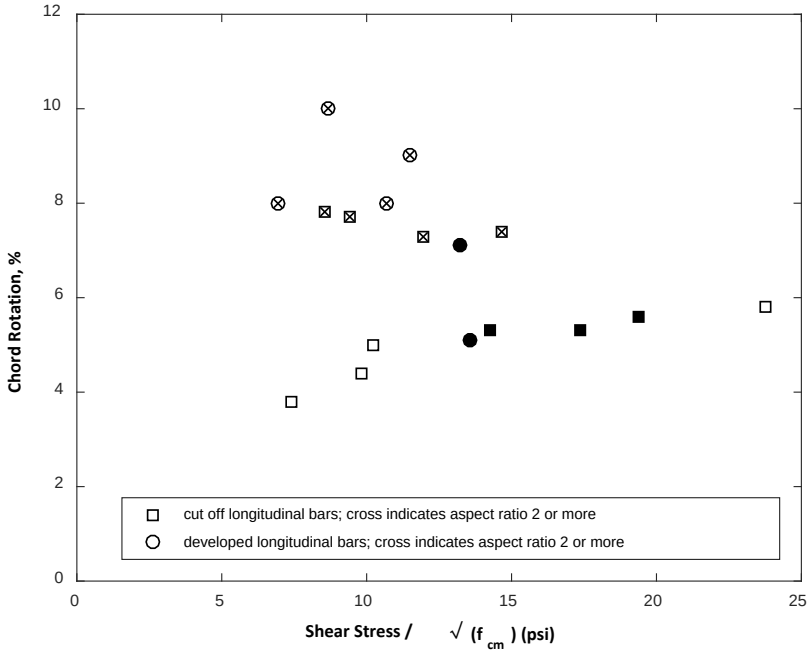

Figure 5.2 – Chord rotation versus shear stress; specimens with $l_n/h \geq 2$ have an "x"

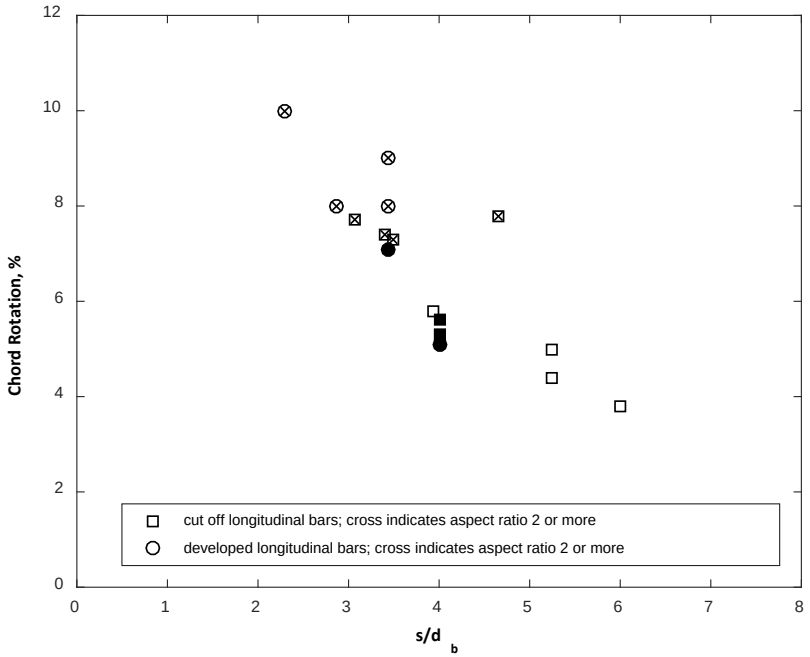

Figure 5.3 – Chord rotation versus s/d_b; specimens with $l_n/h \geq 2$ have an "x"

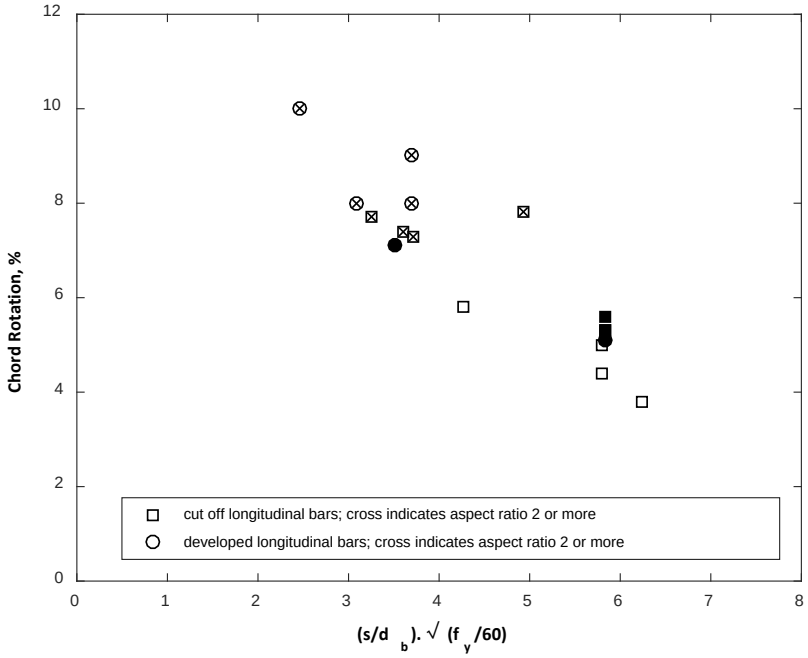

Figure 5.4 – Chord rotation versus s/d_b normalized by diagonal bar yield stress; specimens with $l_n/h \geq 2$ have an "x"

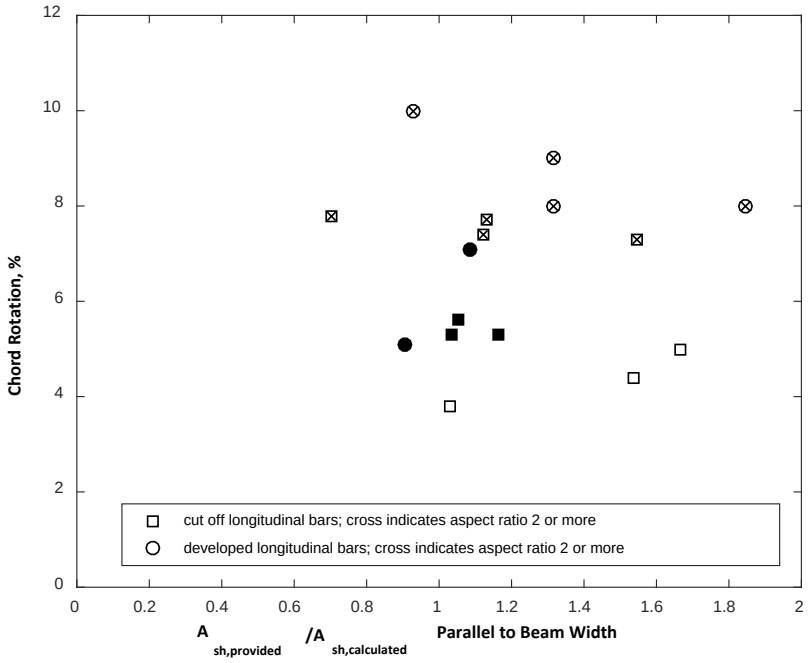

Figure 5.5 – Chord rotation versus $A_{sh,\text{provided}}/A_{sh,\text{calculated}}$ parallel to beam width; specimens with $l_n/h \geq 2$ have an "x"

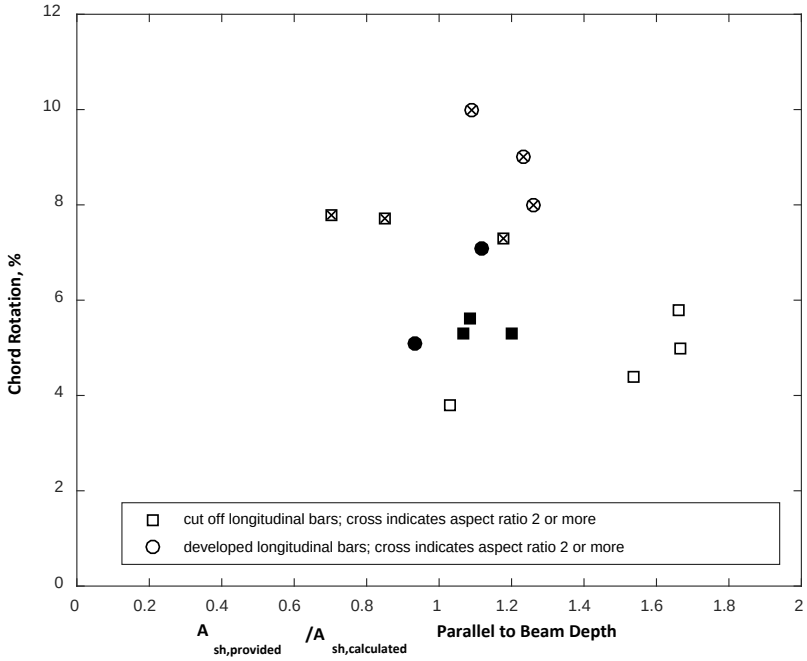

Figure 5.6 – Chord rotation versus $A_{sh,\text{provided}}/A_{sh,\text{calculated}}$ parallel to beam depth; specimens with $l_n/h \geq 2$ have an "x"

5.1.2 BEST-FIT EQUATION FOR CHORD ROTATION CAPACITY

A least squares multiple regression analysis was done on test results from the 17 specimens described in Section 5.1.1 to develop Eq. 5.1 (simplified to Eq. 5.2). The result was an equation for chord rotation capacity that accounts for the two most important variables, l_n/h and $(s/d_b) \times \sqrt{f_y/60}$. These two variables were selected based on the trends observed in Figures 5.1 through 5.6. A lower limit of 3.0 is proposed for the simplified Eq. 5.2 because it is unlikely that a diagonally reinforced concrete coupling beam would exhibit a chord rotation capacity less than 3%. All of the 33 specimens listed in Appendix F exhibited a chord rotation capacity larger than 3%.

$$CR = 8.553 + 0.970\frac{l_n}{h} - 0.874\frac{s}{d_b} \times \sqrt{\frac{f_y}{60}} \quad \text{Eq. 5.1}$$

$$CR = 8.5 + \frac{l_n}{h} - 0.9\frac{s}{d_b} \times \sqrt{\frac{f_y}{60}} \geq 3.0 \quad \text{Eq. 5.2}$$

Figure 5.7 shows the chord rotation capacities calculated with Eq. 5.2 using reported values of l_n/h and $(s/d_b) \times \sqrt{f_y/60}$ plotted against the measured chord rotation capacities. The figure shows a close fit between calculated and measured chord rotation capacities and that most of the measured values are within ±1 standard deviation. The standard deviation in Figure 5.7 was obtained by multiplying the coefficient of variation calculated for the ratios of measured-to-calculated chord rotation capacities by the trendline values. The closeness of fit indicates that Eq. 5.2 includes the most relevant parameters for estimating chord rotation capacity. It is noted that use of the same database for development and evaluation of an equation is not a rigorous approach, but the analysis is limited by the number of available data. In Figure 5.7, filled square markers identify three specimens with slabs (Naish et al., 2013); these beams were excluded from the analysis database but are shown here for comparison. All three specimens with slabs exhibited chord rotation capacities equal to or larger than calculated with Eq. 5.2 for otherwise similar specimens. It is possible slabs improve beam chord rotation capacity by confining the section.

Figure 5.8 shows the same plot as Figure 5.7, with filled triangular markers identifying the specimens with a ratio of transverse reinforcement spacing to diagonal bar diameter (s/d_b) more than 6. These specimens were excluded from the analysis database because the amount or spacing of transverse reinforcement were beyond the range considered. All these specimens were calculated to have chord rotation capacities of 3.0, the lower limit with Eq. 5.2. Similarly, Figure

5.9 shows the same plot as Figure 5.7 with filled circular markers identifying the specimens with stiff axial restraint. Although Poudel (2018) observed an approximately 10% reduction in chord rotation capacity correlated with stiff axial restraint, that trend is not evident in Figure 5.9.

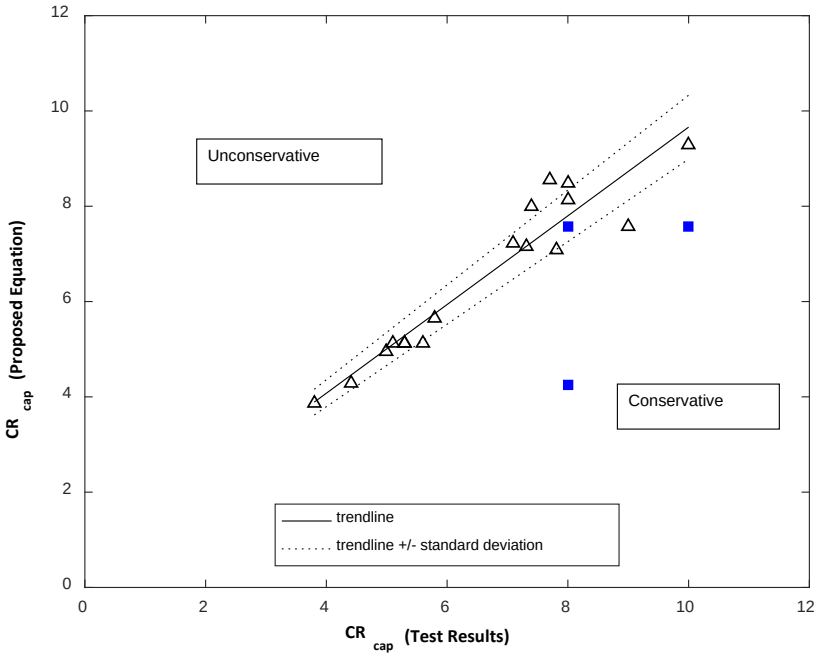

Figure 5.7 – Chord rotations calculated with Eq. 5.2 versus measured chord rotation capacity; solid squares represent specimens with slabs that were not in the analysis database

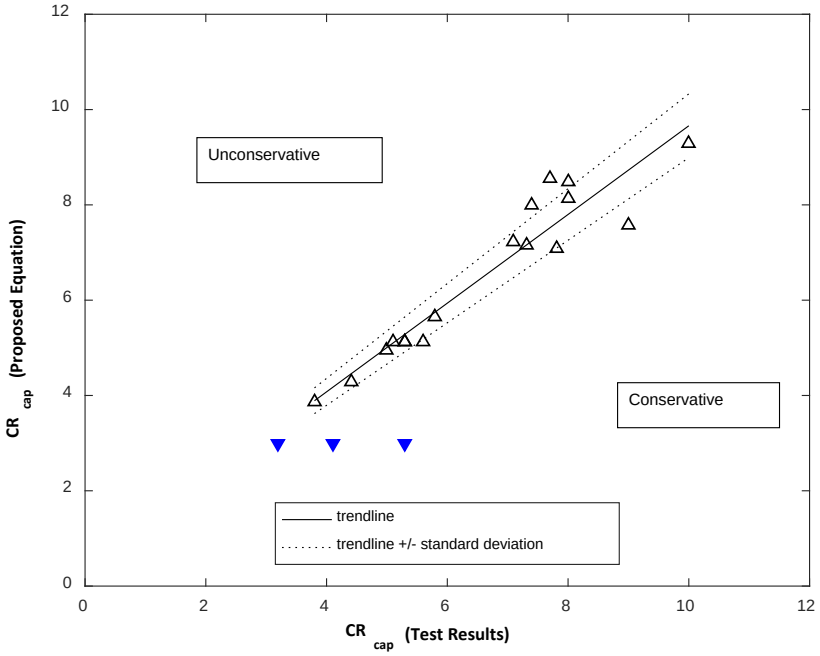

Figure 5.8 – Chord rotations calculated with Eq. 5.2 versus measured chord rotation capacity; solid triangles represent specimens with (s/d_b) more than 6 that were not in the analysis database

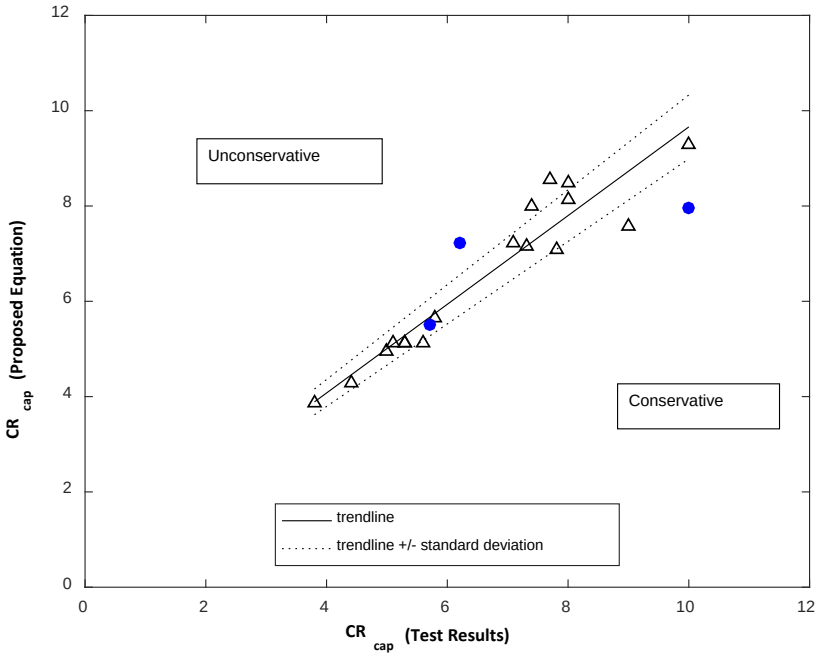

Figure 5.9 – Chord rotations calculated with Eq. 5.2 versus measured chord rotation capacity; solid circles represent specimens with stiff axial restraint that were not in the analysis database

Figures 5.10 and 5.11 show the ratios of measured-to-calculated chord rotation capacities plotted against l_n/h and $(s/d_b) \times \sqrt{f_y/60}$, respectively. The dotted lines in the figures indicate ±1 standard deviation. Both figures show the ratios are near 1.0 and relatively independent of the values on the abscissa. This shows that Eq. 5.2 captures the effect of these variables on chord rotation capacity. This also shows that values calculated with Eq. 5.2 approximately represent a median chord rotation. If a version of Eq. 5.2 were to be used as a basis for design, calculated values should be adjusted to produce the appropriate conservatism.

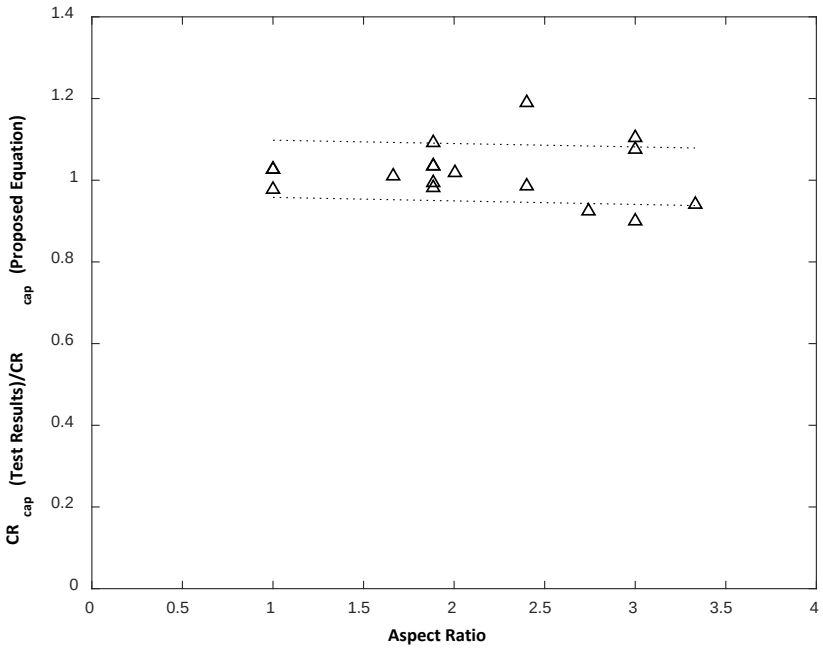

Figure 5.10 – Measured chord rotation capacity divided by the chord rotation capacity calculated with Eq. 5.2 versus aspect ratio

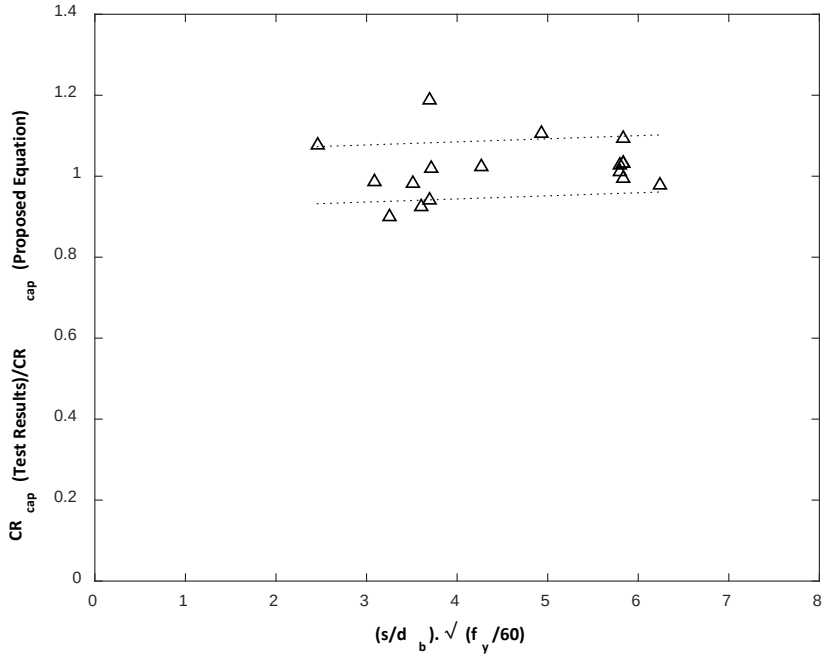

Figure 5.11 – Measured chord rotation capacity divided by the chord rotation capacity calculated with Eq. 5.2 versus s/d_b normalized by diagonal bar yield stress

5.2 RECOMMENDED FORCE-DEFORMATION ENVELOPE FOR MODELING

Figure 5.12 shows the generalized force-deformation relation recommended in ASCE 41 (2017) and ACI 369.1 (2017) for reinforced concrete coupling beams (earlier versions of ASCE 41 used Figure 10.1(a) (not reproduced here) for coupling beams, but conversations with members of ACI Committee 369 have confirmed that Figure 10.1(b) (reproduced as Figure 5.12) is the preferred option, as indicated in ASCE 41-17). The envelope is defined by points A through E, where B is the notional yield point, C the strength or peak force, D the post-peak strength, and E the point where strength is lost. These points are defined for diagonally reinforced coupling beams using the values in Table 5.2, which contains the relevant parameters from Tables 10-5 and 10-19 of ASCE 41 (2017) under the "Envelope A" heading. Table 5.2 also includes modifications to the

ASCE 41 (2017) parameters recommended in TBI (2017) ("Envelope B") and Naish et al. (2013) ("Envelope C"). The modifications proposed by Naish et al. (2013) included corrections intended to account for the scale of the test specimens because, they argued, deformations due to strain penetration do not scale in proportion to deformations attributed to other mechanisms.

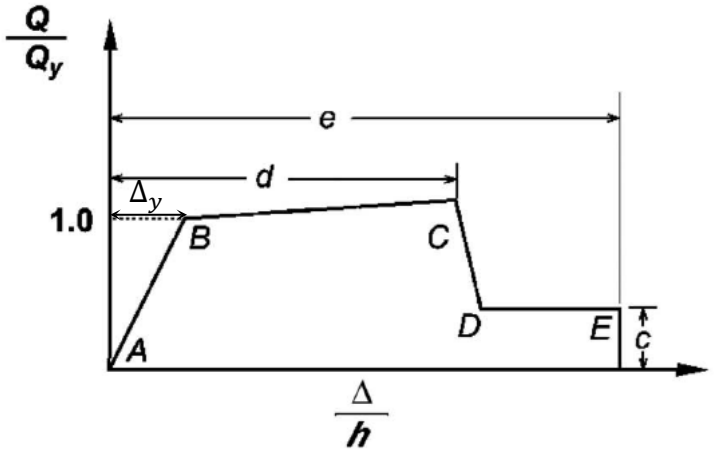

Figure 5.12 – Generalized force-deformation relationship as defined in ASCE 41 (2017) and ACI 369.1 (2017)

Figures 5.13 through 5.17 show the backbone curves (envelopes) for the five specimens described herein. The backbone curves connect the points where peak shear was attained for each step of the loading protocol (Table 3.5). Figures 5.13 through 5.17 also show Envelopes A through C based on the parameters listed in Table 5.2. For calculation of the coordinates of Point B, a stress of 1.1 times the specified f_y was assumed in the diagonal reinforcement and a concrete compressive strength of f_{cm} was used. These were used as an estimate of expected material properties for reinforcing bars and concrete respectively. Although ASCE 41 (2017) and ACI 369.1 (2017) recommend using an expected concrete compressive strength of $1.5f_c'$, this value was not appropriate for use on specimens tested within a few months of casting. For calculation of the

force at Point C, a stress of 1.25 times the specified f_y was assumed in the diagonal reinforcement (which is the stress ACI 318 recommends for calculation of probable flexural strength) and a concrete compressive strength of f_{cm} was used. The figures show the specimens attained larger strength and deformation than the envelopes defined in Table 5.2.

Table 5.2 – Envelopes used for nonlinear seismic analysis

Parameters	Envelope A ASCE 41 (2017) and ACI 369.1 (2017)	Envelope B TBI (2017)	Envelope C Naish et al. (2013)
c	0.8	0.8	0.3
d	0.03	0.03	$0.035 + \Delta_y$
e	0.05	0.05	$0.055 + \Delta_y$
I_{eff}/I_g	0.3 [a]	0.07 (l_n/h) [b]	0.15 to 0.20 [c]
Q_B [d]	V_n [e]	V_n [e]	V_n [e]
Q_C [f]	V_{pr} [g]	V_{pr} [g]	V_{pr} [g]

[a] Based on Table 10-5 of ASCE 41-17 (2017).
[b] Based on Table 4-3 of TBI (2017).
[c] 0.15 was used in Figures 5.13 through 5.17.
[d] Force at yielding point B.
[e] Based on Eq. 2.1 (without an upper limit on shear stress), using measured (or expected) material properties and α = 18 degrees. Figures 5.13 through 5.22 are based on f_{cm} and $1.1f_y$.
[f] Force at capping point C.
[g] Based on Eq. 2.1 (without an upper limit on shear stress) and using 1.25 times the specified f_y.

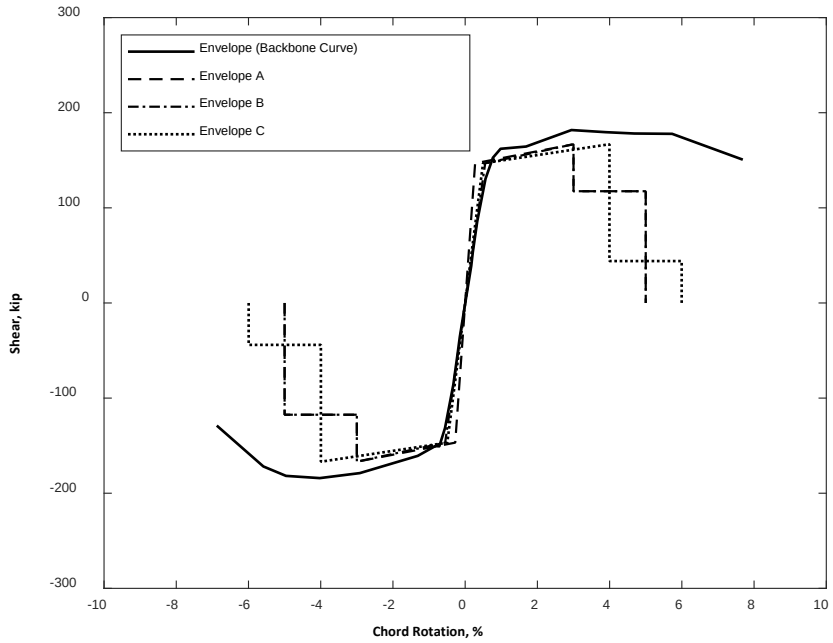

Figure 5.13 – Envelope of shear versus chord rotation for CB1 compared with other modeling parameters (1 kip = 4.45 kN)

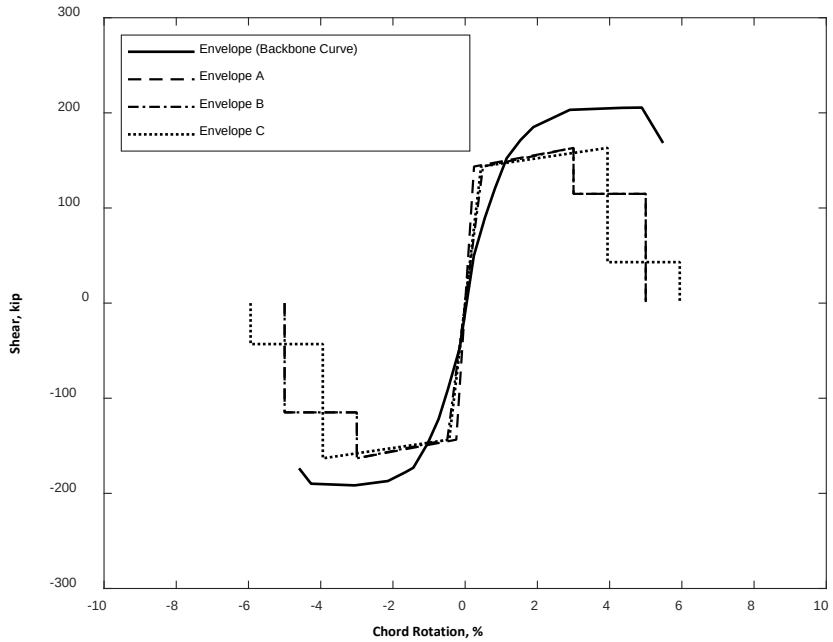

Figure 5.14 – Envelope of shear versus chord rotation for CB2 compared with other modeling parameters (1 kip = 4.45 kN)

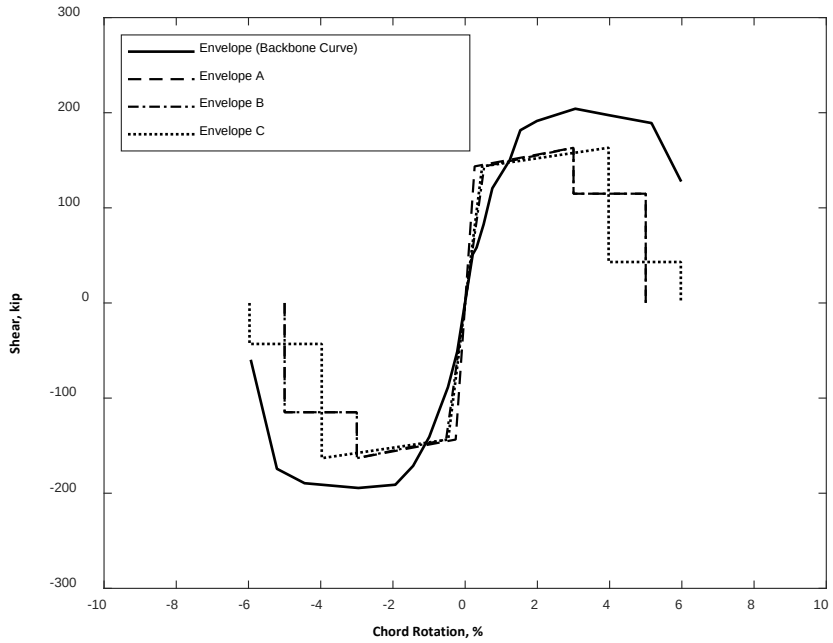

Figure 5.15 – Envelope of shear versus chord rotation for CB2D compared with other modeling parameters (1 kip = 4.45 kN)

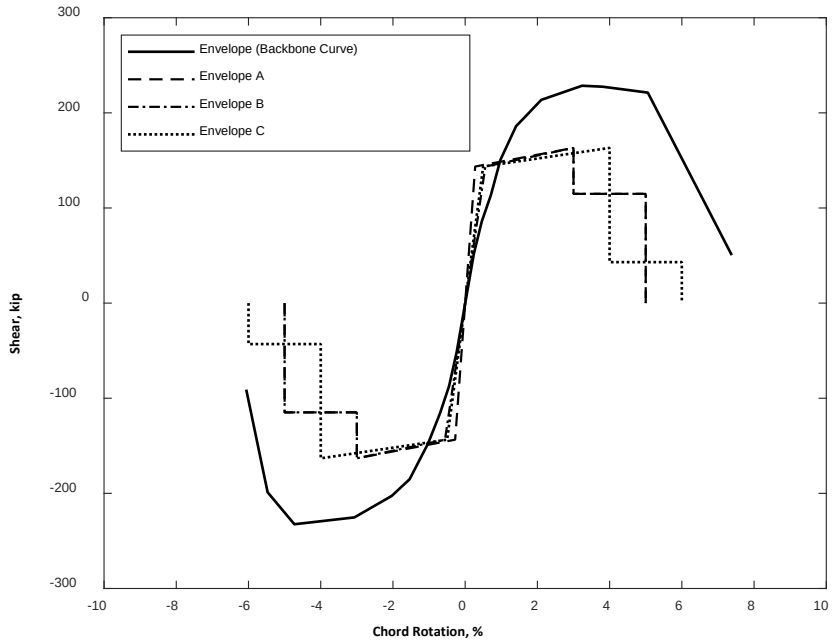

Figure 5.16 – Envelope of shear versus chord rotation for CB2AD compared with other modeling parameters (1 kip = 4.45 kN)

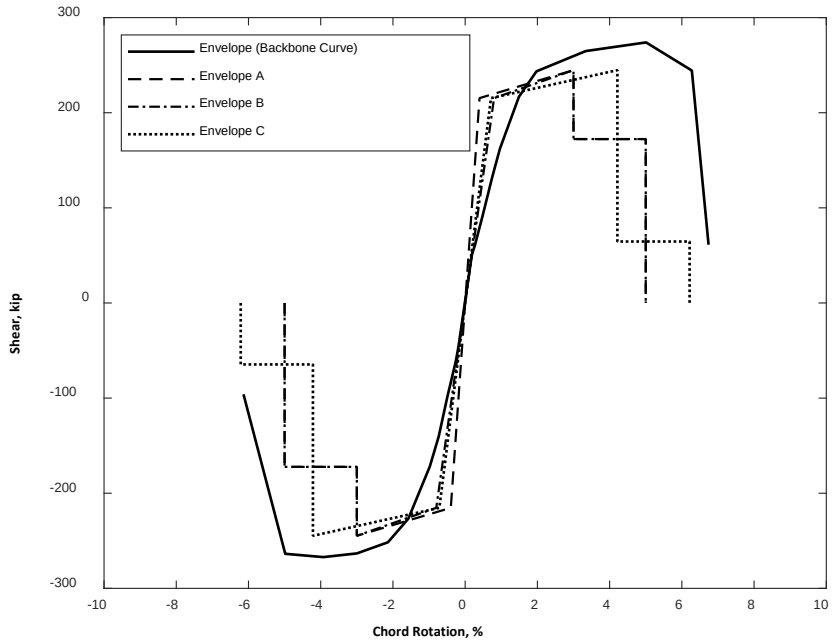

Figure 5.17 – Envelope of shear versus chord rotation for CB3D compared with other modeling parameters (1 kip = 4.45 kN)

5.2.1 MODIFICATIONS TO ACCOUNT FOR YIELD STRESS

Figure 5.13 shows that Envelope A overestimates the initial stiffness of CB1, but Envelopes B and C closely match the initial stiffness of the specimen. Figures 5.14 through 5.17 show that none of the Envelopes A through C have an initial stiffness consistent with that of the other specimens. These specimens had reduced initial stiffnesses because they were constructed with smaller amounts of Grade 120 (830) reinforcement. Although there is some disagreement about whether this apparent difference in stiffness is relevant when calculating drift of a structure under dynamic excitation (NIST 2014, Laughery 2016, To and Moehle 2017, Zhong and Deierlein 2018), the following is an effort to quantify the differences observed in the tests described herein.

To better fit the test results, the modeling parameters listed in Table 5.2 need to be modified to account for the correlation between reinforcement yield stress and initial stiffness. It was shown

in Chapter 4 that the initial stiffness of specimens with Grade 120 (830) diagonal bars was approximately 60% of the initial stiffness of CB1, constructed with Grade 60 (420) reinforcement. For simplicity, and given the few data available, it is recommended to multiply the initial stiffness by $60/f_y$ (ksi) ($420/f_y$ MPa) as shown in the last row of Table 5.3. Furthermore, the parameters *d* and *e* of Envelope C should not vary with bar grade because the total deformation capacity does not vary with reinforcement grade as long as $0.9(s/d_b)\sqrt{f_y/60}$ is constant (Section 5.1.2). This is achieved in the "Modified C" recommendations listed in Table 5.3 by setting Δ_y = 1%.

Table 5.3 – Envelopes used for nonlinear seismic analysis and proposed modifications to account for yield stress (f_y in ksi)

Parameters	Envelope A	Envelope B	Envelope C	Modified B	Modified C
c	0.8	0.8	0.3	0.8	0.3
d	0.03	0.03	$0.035 + \Delta_y$	0.03	0.045
e	0.05	0.05	$0.055 + \Delta_y$	0.05	0.065
I_{eff}/I_g	0.3	$0.07\ (l_n/h)$	0.15	$0.07\ (l_n/h)(60/f_y)$	$0.15\ (60/f_y)$

Table 5.3 lists the values for envelopes A, B, and C from Table 5.2 alongside proposed modifications. Figures 5.18 through 5.22 compare the measured backbone curves (envelopes) of the five beams in this study with the envelopes defined by the proposed modeling parameters. The figures indicate that both Modified B and C have an initial stiffness that closely matches the initial stiffness of CB2 through CB3D, the specimens with Grade 120 (830) diagonal reinforcement. Also, deformation at peak strength as well as the ultimate deformation capacities obtained from Modified B and C are equivalent to those of Envelopes B and C based on the parameters listed in Table 5.2.

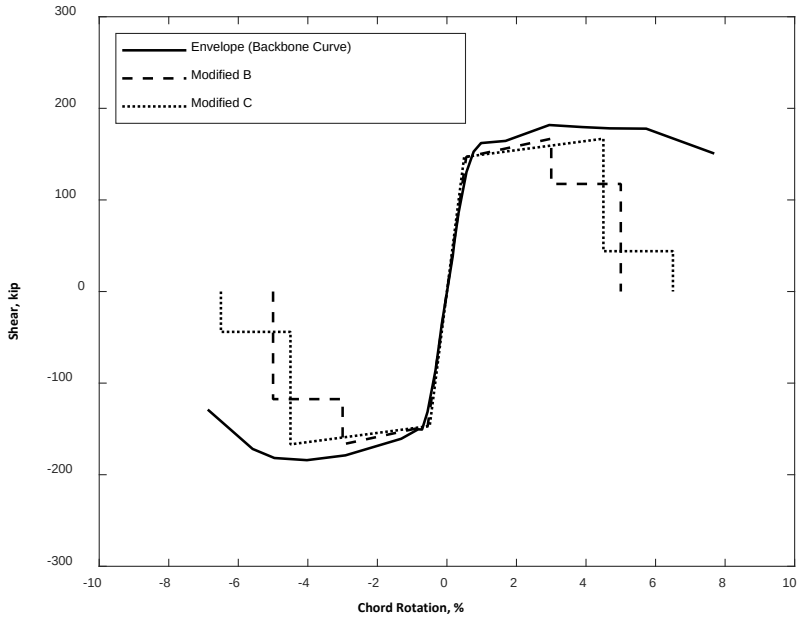

Figure 5.18 – Envelope of shear versus chord rotation for CB1 compared with proposed modeling parameters (1 kip = 4.45 kN)

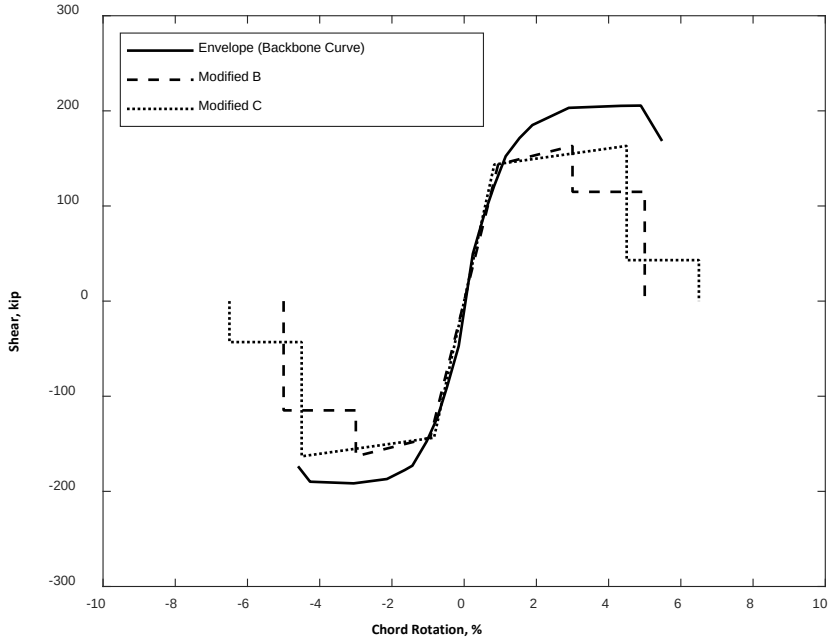

Figure 5.19 – Envelope of shear versus chord rotation for CB2 compared with proposed modeling parameters (1 kip = 4.45 kN)

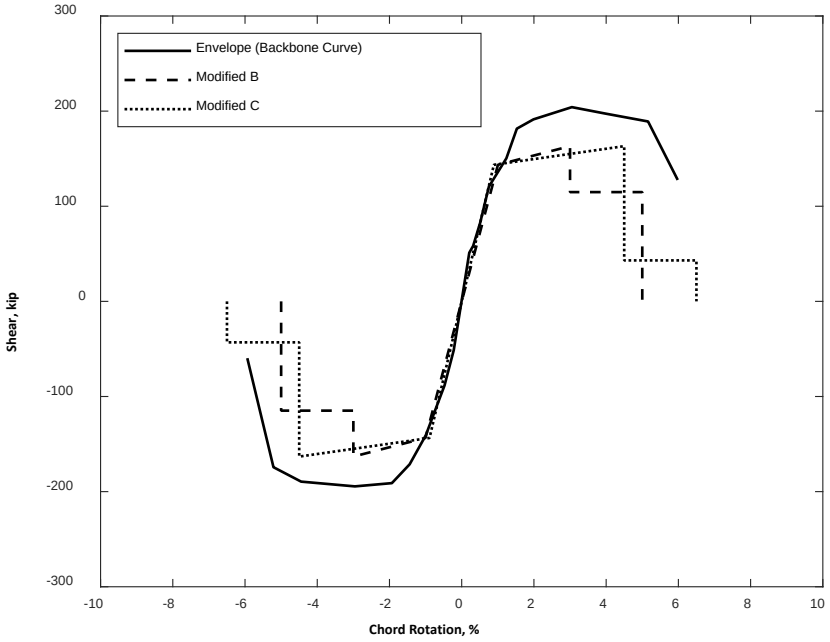

Figure 5.20 – Envelope of shear versus chord rotation for CB2D compared with proposed modeling parameters (1 kip = 4.45 kN)

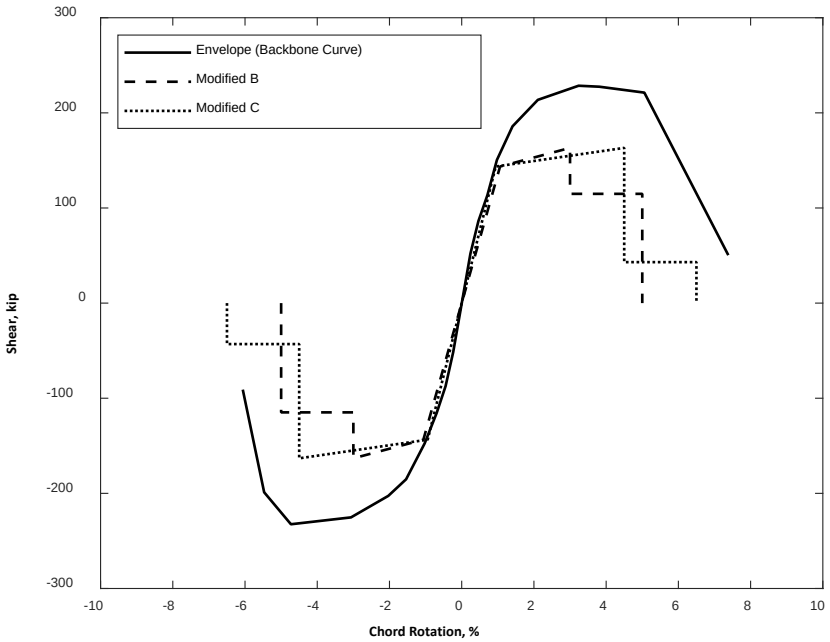

Figure 5.21 – Envelope of shear versus chord rotation for CB2AD compared with proposed modeling parameters (1 kip = 4.45 kN)

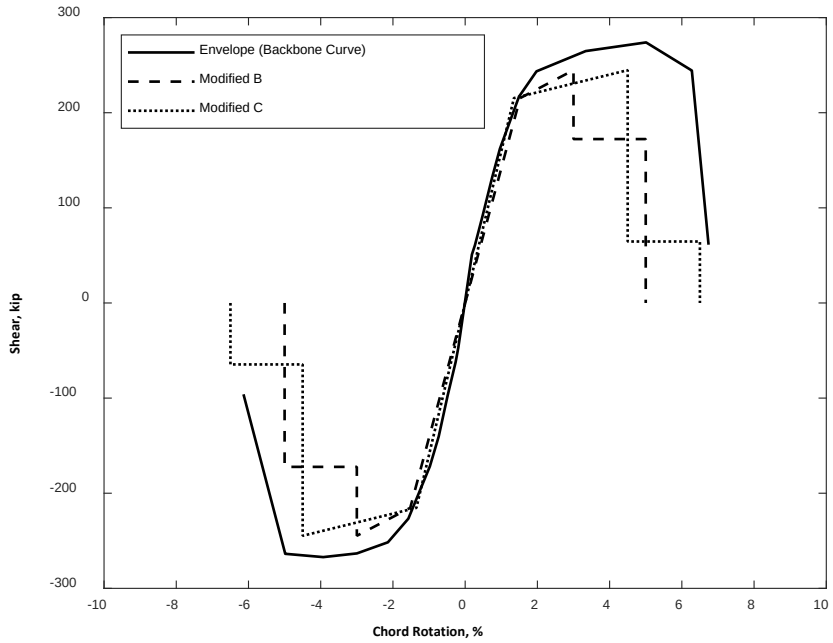

Figure 5.22 – Envelope of shear versus chord rotation for CB3D compared with proposed modeling parameters (1 kip = 4.45 kN)

5.2.2 MODIFICATIONS BASED ON DATABASE ANALYSIS

The modelling recommendations provided in Section 5.2.1 were based on the chord rotation limits recommended by others (parameter *e* in Table 5.3). The appropriateness of these limits can be evaluated using the database results described in Section 5.1.2. A normal cumulative distribution curve is plotted in Figure 5.23 for the ratios of measured-to-calculated chord rotation capacities, where chord rotation capacity was calculated using Eq. 5.2. The cumulative distribution plot is derived from the normal distribution of the ratios of measured-to-calculated chord rotation capacities with a mean ratio of 1.02 and a coefficient of variation of 7%. Only the specimens in the analysis database are included in this figure.

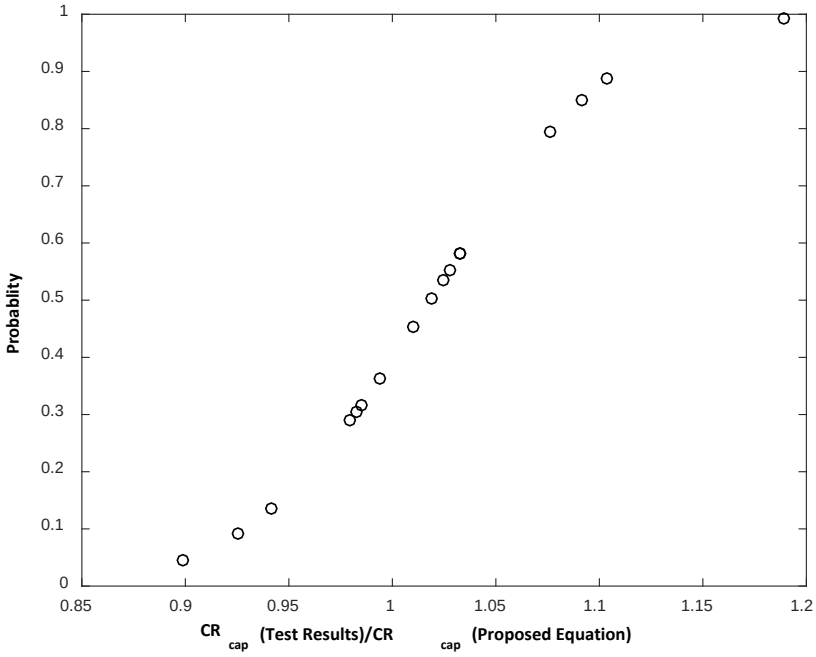

Figure 5.23 – Normal cumulative distribution for measured chord rotation capacity divided by the chord rotation capacity calculated with Eq. 5.2

Further modifications to parameters *d* and *e* are proposed in Table 5.4. It is assumed here that parameter *e* equals Eq. 5.2. Chord rotation capacity is therefore made a function of the two most important variables obtained from Section 5.1.1.1, l_n/h and $(s/d_b) \times \sqrt{f_y/60}$. A recommendation is also provided for parameter *d* that is simply equal to parameter *e* minus 0.02, similar to the definition of Envelopes A through C.

Table 5.4 – Envelopes used for nonlinear seismic analysis and proposed modifications based on database analysis

Parameters	Envelope A	Envelope B	Envelope C	Modified Envelope
a	0.03	0.03	0.035	$6.5 + \frac{l_n}{h} - 0.9\frac{s}{d_b} \times \sqrt{\frac{f_y}{60}}$
b	0.05	0.05	0.055	$8.5 + \frac{l_n}{h} - 0.9\frac{s}{d_b} \times \sqrt{\frac{f_y}{60}}$
c	0.8	0.8	0.3	0.8
I_{eff}/I_g [a]	0.3	0.07 (l_n/h)	0.15	0.07 $(l_n/h)(60/f_y)$

[a] Effective section property expressed as a fraction of gross section property.

CHAPTER 6 SUMMARY AND CONCLUSIONS

An experimental program was conducted to investigate the deformation capacity of coupling beams reinforced with high-strength steel under reversed cyclic displacements. Results were reported from tests of five diagonally reinforced concrete coupling beams (CB1, CB2, CB2D, CB2AD, and CB3D). The main variables were yield stress of the diagonal reinforcement, target beam shear stress, length of the secondary (non-diagonal) longitudinal reinforcement, and axial restraint. All specimens had the same nominal concrete compressive strength and beam dimensions. In addition to analyzing the test results, a database of 17 specimens, selected from among 33 diagonally reinforced coupling beam tests reported in the literature, was analyzed to determine which specimen parameters most strongly influence deformation capacity. Chord rotation capacity was defined as the average of the largest chord rotations in each loading direction at which the force exceeded 80% of the peak force. The following conclusions were drawn on the basis of these tests and analyses:

1) Chord rotation capacities exhibited by specimens with Grade 120 (830) diagonal reinforcement were between 5.1 and 5.6%. These were smaller than that exhibited by the control specimen with Grade 60 (420) diagonal reinforcement (7.1%). This difference may be partly attributable to the wider transverse reinforcement spacing in terms of d_b ($4d_b$ versus $3.4d_b$ for specimens constructed with Grade 120 and 60 (830 and 420) bars).
2) Higher diagonal bar grade was correlated with large and consistent changes in beam stiffness, hysteretic energy dissipation, and residual chord rotation at zero force. A change from Grade 60 to 120 (420 to 830) resulted in an approximately 40% reduction in stiffness, 50% reduction in hysteretic energy dissipation, and 50% reduction in residual chord rotation. The extent to

which these differences would affect the drift of a full-scale structure under dynamic excitation was outside the project scope.

3) The 2017 Tall Building Initiative Report recommends using an effective moment of inertia of 0.07 $(l_n/h)I_g$ for diagonally reinforced coupling beams. When multiplied by $(60/f_y)$, this closely represented the stiffness of all specimens tested in this study, regardless of grade.

4) A simple equation, reproduced as Eq. 6.1, was proposed to represent the mean coupling beam chord rotation capacity for a database of 17 specimens. The equation is based on a database of diagonally reinforced concrete coupling beams with aspect ratios between 1.0 and 4.0, transverse reinforcement spacing not more than $6d_b$, and reinforcement yield stress between 60 and 130 ksi (420 and 900 MPa). The equation is not a function of shear stress because it was found to not have a strong correlation with the chord rotation capacity of well detailed diagonally reinforced coupling beams.

$$CR = 8.5 + \frac{l_n}{h} - 0.9\frac{s}{d_b} \times \sqrt{\frac{f_y}{60}} \qquad \text{Eq. 6.1}$$

5) It may be appropriate to calculate probable flexural strength assuming bar stresses larger than 1.25 times the yield stress when steel without a yield plateau is used and an accurate estimate of strength is required. For specimens with Grade 120 (830) diagonal reinforcement, beam strength estimated on the basis of the beam attaining its probable flexural strength at both ends was closer to measured strength than estimates obtained with other simple methods, although it still provided an estimate that was frequently less than the measured value.

6) Design for shear stresses larger than $10\sqrt{f_c'}$ [psi] ($0.83\sqrt{f_c'}$ [MPa]) may be feasible in well detailed diagonally reinforced coupling beams. The specimen designed for a nominal shear

stress near $15\sqrt{f_c'}$ [psi] ($1.25\sqrt{f_c'}$ [MPa]), 50% more than the ACI Building Code limit, exhibited a chord rotation capacity and mode of damage similar to other specimens. There also was no trend between deformation capacity and shear stress among database specimens. Furthermore, shear damage (in terms of shear deformations) did not increase with shear stress.

7) Axial restraint resulted in a maximum beam axial force of approximately 10% of $A_g f_{cm}$. The result was large beam overstrength, with the maximum specimen strength exceeding the nominal strength by 85%. There was evidence that the axially restrained specimen exhibited larger shear-related damage than a similar unrestrained specimen beginning at 2% chord rotation (based on increases in beam depth). Axial restraint did not, however, result in reduced chord rotation capacity or changes in the relative contribution from different deformation mechanisms. This was counter to findings reported by Poudel 2018. The difference may be due to the difference in restraining system stiffness which caused a higher axial force to develop in the specimen tested by Poudel (2018).
8) Specimens with secondary longitudinal reinforcement cutoff near the wall face exhibited a localization of damage at the beam-wall interface. Specimens with secondary longitudinal reinforcement extended into the wall had damage that was more distributed throughout the span. Despite this difference in damage, deformation capacities exhibited by the specimens were similar.

REFERENCES

1. ACI Committee 318 (1999). *Building Code Requirements for Structural Concrete (ACI 318-99) and Commentary*. American Concrete Institute, Farmington Hills, Michigan.
2. ACI Committee 318 (2002). *Building Code Requirements for Structural Concrete (ACI 318-02) and Commentary*. American Concrete Institute, Farmington Hills, Michigan.
3. ACI Committee 318 (2005). *Building Code Requirements for Structural Concrete (ACI 318-05) and Commentary*. American Concrete Institute, Farmington Hills, Michigan.
4. ACI Committee 318 (2008). *Building Code Requirements for Structural Concrete (ACI 318-08) and Commentary*. American Concrete Institute, Farmington Hills, Michigan.
5. ACI Committee 318 (2014). *Building Code Requirements for Structural Concrete (ACI 318-14) and Commentary*. American Concrete Institute, Farmington Hills, Michigan.
6. ACI Committee 318 (2014). B*uilding Code Requirements for Structural Concrete (ACI 318-14) and Commentary*. American Concrete Institute, Farmington Hills, Michigan.
7. ACI Committee 369 (2017). *Standard Requirements for Seismic Evaluation and Retrofit of Existing Concrete Buildings (ACI 369.1-17) and Commentary*. American Concrete Institute, Farmington Hills, Michigan.
8. Ameen, S., Weber-Kamin, A. S., Lequesne, R. D., and Lepage, A. (2018). "Diagonally-Reinforced Concrete Coupling Beams with High-strength Steel Bars". *The 11th National Conference on Earthquake Engineering*, Los Angeles, California.
9. ASCE 41 (2017). *Seismic Evaluation and Retrofit of Existing Buildings (ASCE/SEI 41-17)*. American Society of Civil Engineers, Reston, Virginia.
10. ASTM A370 (2017). *Standard Test Methods and Definitions for Mechanical Testing of Steel Products (ASTM A370-17)*. ASTM International, West Conshohocken, Pennsylvania.
11. ASTM A706/A706M-15, (2015), *Standard Specification for Deformed and Plain Low-Alloy Steel Bars for Concrete Reinforcement*. ASTM International, West Conshohocken, Pennsylvania.
12. ASTM A1035/A1035M-16a, (2016), *Standard Specification for Deformed and Plain, Low-Carbon, Chromium, Steel Bars for Concrete Reinforcement*. ASTM International, West Conshohocken, Pennsylvania.
13. ASTM C33/C33M-16 (2016). *Standard Specification for Concrete Aggregates*. ASTM International, West Conshohocken, Pennsylvania.
14. ASTM C39/C39M-17a (2017). *Standard Test Method for Compressive Strength of Cylindrical Concrete Specimens*. ASTM International, West Conshohocken, Pennsylvania.
15. ASTM C494/C494M-16 (2016). *Standard Specification for Chemical Admixtures for Concrete*. ASTM International, West Conshohocken, Pennsylvania.
16. ASTM E8/E8M-16a (2016). *Standard Test Methods for Tension Testing of Metallic Materials*. ASTM International, West Conshohocken, Pennsylvania.
17. Canbolat, B. A. (2004). *Seismic Behavior of High-Performance Fiber Reinforced Cementitious Composite Coupling Beams*. PhD Dissertation, The University of Michigan.
18. Canbolat, B. A., Parra-Montesinos, G. J., and Wight, J. K. (2005). "Experimental Study on Seismic Behavior of High-Performance Fiber-Reinforced Cement Composite Coupling Beams". *ACI Structural Journal*, 102(1), 159-166.
19. Chen, Y. and Lu, X. (2012). "New Replaceable Coupling Beams for Shear Wall Structures". *The 15th World Conference on Earthquake Engineering*, Lisboa, 2012.

20. Cheng, M.-Y., Hung, S.-C., Lequesne, R. D., and Lepage, A. (2016). "Earthquake-Resistant Squat Walls Reinforced with High-Strength Steel". *ACI Structural Journal*, 113(5), 1065-1076.
21. Choi, Y., Hajyalikhani, P., and Chao, S. (2018). "Seismic performance of innovative reinforced concrete coupling beam – double-beam coupling beam". *ACI Structural Journal*, 115(1), 113-125.
22. FEMA 461, (2007). *Interim Testing Protocols for Determining the Seismic Performance Characteristics of Structural and Nonstructural Components*. Applied Technology Council, Redwood City, California.
23. Fortney, P. J., Rassati, G. A., and Shahrooz, B. M. (2008). "Investigation on Effect of Transverse Reinforcement on Performance of Diagonally Reinforced Coupling Beams". *ACI Structural Journal*, 105(6), 781-788.
24. Galano, L. and Vignoli, A. (2000). "Seismic Behavior of Short Coupling Beams with Different Reinforcement Layouts". *ACI Structural Journal*, 97(6), 876-885.
25. Ghannoum, W. M. and Slavin, C. M. (2015). *Defining Structurally Acceptable Properties of High-Strength Steel Bars through Material and Column Testing – Part I: Material Testing Report*. Research Grant Agreement #05-14, Charles Pankow Foundation, Vancouver, Washington.
26. Gong, B., Shahrooz, B. M., and Gillum, A. J. (1996). "Seismic Behavior and Design of Composite Coupling Beams". *Journal of Structural Engineering*, ASCE, 258-271.
27. Gonzalez, E. (2001). *Seismic Response of Diagonally Reinforced Slender Coupling Beams*. MSc Dissertation, University of British Columbia, Vancouver.
28. Han, S. W., Lee, C. S., Shin, M., and Lee, K. (2015). "Cyclic Performance of Precast Coupling Beams with Bundled Diagonal Reinforcement". *Engineering Structures*, 93, 142-151.
29. Harries, K. A., Fortney, P. J., Shahrooz, B.M., and Brienen, P. J. (2005). "Practical Design of Diagonally Reinforced Concrete Coupling Beams – Critical Review of ACI 318 Requirements". *ACI Structural Journal*, 102(6), 876-882.
30. Harries, K. A., Mitchell, D., Cook, W. D., and Redwood, R. G. (1993). "Seismic Response of Steel Beams Coupling Concrete Walls". *Journal of Structural Engineering*, ASCE, 119(12), 3611-3629.
31. Irwin, A. W. and Ord, A. E. C. (1976). "Cyclic Load Tests on Shear Wall Coupling Beams". *Proceedings of the Institution of Civil Engineers, Part 1 – Design and Construction*, 61(2), 331-342.
32. Kuramoto, H., Minami, K., and Wakabayashi, M. (1988). "Deformation Capacity of Diagonally Reinforced Concrete Short Columns Subject to Axial Compressive Stress". *Proceedings of 9th World Conference on Earthquake Engineering*, IV, 377-382.
33. Lam, W.-Y., Su, R. K.-L., and Pam, H.-J. (2005). "Experimental Study on Embedded Steel Plate Composite Coupling Beams". *Journal of Structural Engineering*, ASCE, 131(8), 1294-1302.
34. Laughery, L. A. (2016). *Response of High-Strength Steel Reinforced Concrete Structures to Simulated Earthquakes*. PhD Dissertation, Purdue University, West Lafayette, Indiana.
35. Lequesne, R. D. (2011). *Behavior and Design of High-Performance Fiber-Reinforced Concrete Coupling Beams and Coupled-Wall Systems*. PhD Dissertation, The University of Michigan, USA.

36. Lequesne, R. D., Parra-Montesinos, G., and Wight, J. (2013). “Seismic Behavior and Detailing of High-Performance Fiber-Reinforced Concrete Coupling Beams and Coupled Wall Systems”. *Journal of Structural Engineering*, 139, Special Issue: NEES 2: Advances in Earthquake Engineering, 1362–1370.
37. Lequesne, R. D., Parra-Montesinos, G., and Wight, J. (2016). “Seismic Response of Fiber-Reinforced Concrete Coupled Walls”. *ACI Structural Journal*, 113(3), 435-445.
38. Lim, E. W., Hwang, S. J., Wang, T. W., and Chang, Y. H. (2016a). “An Investigation on the Seismic Behavior of Deep Reinforced Concrete Coupling Beams”. *ACI Structural Journal*, 113(2), 217-226.
39. Lim, E., Hwang, S.-J., Cheng, C.-H., and Lin, P.-Y. (2016). “Cyclic Tests of Reinforced Concrete Coupling Beam with Intermediate Span-Depth Ratio”. *ACI Structural Journal*, 113(3), 515-524.
40. Lim, W.-Y., Kang. T. H.-K., and Hong, S.-G. (2016). “Cyclic Testing of Bolted Steel Coupling Beams in Fast-Track Precast Concrete Construction”. *ACI Structural Journal*, 113(6), 1289-1300.
41. Motter, C. J., Fields, C. F., Hooper, J. D., Klemencic, R., and Wallace, J. W. (2017). “Steel-Reinforced Concrete Coupling Beams. I: Testing”. *Journal of Structural Engineering*, ASCE, 143(3), 04016191-1-11.
42. Naish, D., Fry, J. A., Klemencic, R., and Wallace, J. (2009). *Reinforced Concrete Link Beams: Alternative Details for Improved Constructability*. Report to Charles Pankow Foundation, UCLA-SGEL, 103 pp.
43. Naish, D., Fry, J. A., Klemencic, R., and Wallace, J. (2013). Reinforced Concrete Coupling Beams – Part I: Testing”. *ACI Structural Journal*, 110(6), 1057-1065.
44. Naish, D., Fry, J. A., Klemencic, R., and Wallace, J. (2013). Reinforced Concrete Coupling Beams – Part II: Modeling”. *ACI Structural Journal*, 110(6), 1067-1076.
45. Nielsen, N. N. and Imbeault, F. A. (1971). “Validity of Various Hysteretic Systems”. *Proceedings of Third Japan National Conference on Earthquake Engineering*, 707-14.
46. NIST (2014). *Use of High-Strength Reinforcement in Earthquake-Resistant Concrete Structures (NIST GCR 14-917-30)*. National Institute of Standards and Technology, Gaithersburg, Maryland.
47. Otani, S. (1981). “Hysteresis Models of Reinforced Concrete for Earthquake Response Analysis”. *The University of Tokyo Journal of Faculty of Engineering*. 36(2), 407-441.
48. Park, W.-S. and Yun, H.-D. (2005). “Seismic behaviour of steel coupling beams linking reinforced concrete shear walls”. *Engineering Structures*, 27, 1024-1039.
49. Parra-Montesinos, G. J., Wight, J. K., and Setkit, M. (2010). “Earthquake-Resistant Coupling Beams without Diagonal Reinforcement”. *Concrete International*, 32(12), 36-40.
50. Paulay, T. (1969). *The Coupling of Shear Walls*. PhD Dissertation, University of Canterbury, Christchurch, New Zealand.
51. Paulay, T. (1971). “Coupling Beams of Reinforced Concrete Shear Walls”. *Journal of the Structural Division*, ASCE, 97(ST3), 843-861.
52. Paulay, T. and Binney, J. R. (1974). “Diagonally Reinforced Coupling Beams of Shear Walls”. *Shear in Reinforced Concrete*, SP-42, American Concrete Institute, Detroit, MI, 2, 579-598.
53. Paulay, T. and Santhakumar, A. R. (1976). “Ductile Behavior of Coupled Shear Walls”. *Journal of the Structural Division*, ASCE, 102(ST1), 93-108.

54. Poudel, A., Lequesne, R. D., and Lepage, A. (2018). *Diagonally Reinforced Concrete Coupling Beams: Effects of Axial Restraint*. SL Report 18-3, The University of Kansas Center for Research, Inc., September 2018.
55. Rautenberg, J. M., Pujol, S., Tavallali, H., and Lepage, A., (2012). "Reconsidering the Use of High-Strength Reinforcement in Concrete Columns". *Engineering Structures*, 37, 135-142.
56. Richart, F. E. and Brown, R. L. (1934). *An Investigation of Reinforced Concrete Columns*. Engineering Experiment Station, University of Illinois.
57. Shiu, K. N., Barney, G. B., Fiorato, A. E., and Corley, W. G. (1978). "Reversing Load Tests of Reinforced Concrete Coupling Beams". *Central American Conference on Earthquake Engineering – Conferencia Centroamericana de Ingenieria Siemica*,Proceedings, 239-249.
58. Subedi, N. K. (1991). "RC-Coupled Shear Wall Structures. I: Analysis of Coupling Beams". *Journal of Structural Engineering*, ASCE, 117(3), 667-680.
59. Tassios, T. P., Moretti, M., and Bezas, A. (1996), "On the Behavior and Ductility of Reinforced Concrete Coupling Beams of Shear Walls". *ACI Structural Journal*, 93(6), 1-10.
60. Tavallali, H. (2011). *Cyclic Response of Concrete Beams Reinforced with Ultra High Strength Steel*. PhD Dissertation, Pennsylvania State University, USA.
61. Tegos, I. A. and Penelis, G. G. (1988). "Seismic Resistance of Short Columns and Coupling Beams reinforced with Inclined Bars". *ACI Structural Journal*, 85(1), 82-88.
62. To, D. V. and Moehle, J. P. (2017). *Seismic Performance Characterization of Beams with High-Strength Reinforcement*. Report to Charles Pankow Foundation, University of California, Berkeley.
63. TBI (2017). *Guidelines for Performance-Based Seismic Design of Tall Buildings (Tall Buildings Initiative).* Pacific Earthquake Engineering Research Center, Berkeley, California.
64. Weldon, B. D. and Kurama, Y. C. (2006). "Post-Tensioned Precast Concrete Coupling Beam Systems". *Proceedings of the 8th U.S. National Conference on Earthquake Engineering*, April 18-22, San Francisco, California, USA.
65. Yun, H.-D., Kim, S.-W., Jeon, E., Park, W.-S., and Lee, Y.-T. (2008), "Effects of Fiber-Reinforced Cement Composites' Ductility on the Seismic Performance of Short Coupling Beams". *Magazine of Concrete Research*, 60(3), 223-233.
66. Yotakhong, P. (2003). *Flexural Performance of MMFX Reinforcing Rebars in Concrete Structures*. MSc Dissertation, North Carolina State University, USA.
67. Zhang, H., Zhang, R., and Huang, C. (2007), "Experimental Study of Shear Resistance of Steel Fiber Reinforced High-Strength Concrete Coupling Beams". *Tumu Gongcheng Xuebao*, 40(11), 15-22.
68. Zhong, K. and Deierlein, G. G. (2018). "Assessing Seismic Safety of Concrete Moment Frames with High Strength Reinforcing Steel". *The 11th National Conference on Earthquake Engineering*, Los Angeles, California.
69. Zhu, Y., Zhou, F. L., and Su, R. K. L. (2008). "Seismic Effects on Coupled Shear Wall Structure by Coupling Beams with Side Bolted Steel Plates". *The 14th World Conference on Earthquake Engineering*, October 12-17, Beijing, China.

NOTATION

A_{cw} = coupling beam cross-sectional area (bh), in.^{2} (mm^2)

A_{sh} = total cross-sectional area of transverse reinforcement, including crossties, within spacing s and perpendicular to dimension b, in.^{2} (mm^2)

A_{vd} = total reinforcement area of each diagonal group, in.^{2} (mm^2) (Figure 2.11),

A_g = gross cross-sectional area, in.^{2} (mm^2)

b = beam width, in. (mm)

c = parameter used to represent residual strength (Figure 5.12)

d = parameter used to calculate total deformation to capping point C (Figure 5.12)

e = parameter used to calculate total deformation to point E (Figure 5.12)

CM = cementitious material, includes cement and fly ash (Table 3.2)

CR = chord rotation

CR_{cap} = chord rotation capacity obtained from the average of CR_{max}

CR_{max} = Maximum chord rotation attained in a loading direction while maintaining a shear force not less than $0.8V_{max}$.

D_m = Peak displacement during a loading cycle, in. (mm)

D_{max} = previously attained maximum displacement in the direction of loading, in. (mm)

D_y = notional yield displacement, in. (mm)

d_b = diameter of diagonal bars, in. (mm)

d_i = distance between midspan and midheight of layer *i*, in. (mm)

d_1 = distance between the top left and bottom right corners of a station, in. (mm) (Figure 4.9)

d_2 = distance between the bottom left and top right corners of a station, in. (mm) (Figure 4.9)

E_c = modulus of elasticity of concrete, ksi (MPa)

E_h = hysteretic energy dissipation index

f_c' = specified compressive strength of concrete, psi (MPa)

f_{cm} = average measured compressive strength of the concrete, psi (MPa)

f_t = tensile strength of reinforcement, ksi (MPa)

f_y = yield stress of reinforcement, ksi (MPa)

h = overall depth of beam, in. (mm)

h_b = distance between the bottom corners of a station, in. (mm) (Figure 4.9)

h_t = distance between the top corners of a station, in. (mm) (Figure 4.9)

I_{eff} = effective moment of inertia, in.^{4} (mm^4)

I_g = moment of inertia of gross concrete section about centroidal axis, neglecting reinforcement, in.^{4} (mm^4)

I_{tr} = moment of inertia of transformed concrete section about centroidal axis, typically multiplied with E_c, in.^{4} (mm^4)

K_e = effective initial stiffness, kip/in. (kN/mm)

K_u = unloading stiffness, kip/in. (kN/mm)

L = length of a fixed beam, in. (mm)

ℓ = width of a station (nominally 4 in. (100 mm)) (Figure 4.8)

$\ell_{i,C1C5}$ = initial distance between Columns 1 and 5 (Figure 4.8) in Row i

l_n = coupling beam clear span length measured from the top of the bottom block to the bottom of the top block, in. (mm)

M_n = nominal flexural strength, kip-ft (kN-m)

M_{pr} = probable flexural strength, kip-ft (kN-m)

n_s = number of stations (four)

Q_B = force at yielding point B (Figure 5.12)

Q_C = force at capping point C (Figure 5.12)

s = transverse reinforcement spacing, in. (mm)

V_m force associated with peak displacement D_m.

v_l = distance between left-most corners of a station, in. (mm) (Figure 4.9)

v_{max} = shear stress calculated as $V_{max}/(bh)$

V_{max} = maximum measured shear force, kip (kN)

V_n = nominal shear strength, kip (kN)

v_r = distance between right-most corners of a station, in. (mm) (Figure 4.9)

y = change in vertical position of the marker identified by the subscript

α = angle defining the orientation of diagonal reinforcement relative to the longitudinal beam axis

ΔA = change in angle A of a station (Figure 4.9)

ΔB = change in angle B of a station (Figure 4.9)

ΔC = change in angle C of a station (Figure 4.9)

ΔD = change in angle D of a station (Figure 4.9)

$\Delta_{sl,bot}$ = sliding at the beam-bottom block interface

$\Delta_{sl,top}$ = sliding at the beam-top block interface

Δ_y = drift ratio associated with reinforcement yielding estimated using V_n and I_{eff}

W = amount of hysteretic energy dissipated per cycle for each loading direction resisting a force V_m at the peak displacement D_m.

δ = displacement, in. (mm)

δ_{bottom} = displacement of bottom block (at its top surface) (Figure 4.1), in. (mm)

$\delta_{bottom,m}$ = displacement of bottom block measured 3 in. (75 mm) below its top surface, in. (mm)

δ_{top} = displacement of top block (at its bottom surface) (Figure 4.1), in. (mm)

$\delta_{top,m}$ = displacement of top block measured 3 in. (75 mm) above its bottom surface), in. (mm)

ε_{sf} = measured fracture elongation of reinforcement

ε_{su} = measured uniform elongation of reinforcement

θ = flexural rotation (Figure 4.10)

θ_f = chord rotation due to flexure

θ_i = flexural rotation in layer *i*

θ_{sl} = chord rotation due to sliding at the face of the blocks

θ_{sp} = chord rotation due to strain penetration into the top and bottom blocks

$\theta_{sp,bot}$ = rotation due to strain penetration into the bottom block

$\theta_{sp,top}$ = rotation due to strain penetration into the top block

θ_v = chord rotation due to shear distortion

θ_y = rotation about y-axis

θ_z = rotation about z-axis

$\theta_{z,BB}$ = rotation of bottom block in the plane of the specimen (about z-axis) (Figure 4.1)

$\theta_{z,TB}$ = rotation of the top block in the plane of the specimen (about z-axis) (Figure 4.1)

ψ = angle change due to expansion (Figure 4.10)

γ = distortion due to shear (Figure 4.10)

APPENDIX A PHOTOS DURING CONSTRUCTION

Figure A.1 - Formwork for a coupling beam specimen

Figure A.2 - Bottom block reinforcement

Figure A.3 - Bottom block reinforcement inside formwork

Figure A.4 - Top block reinforcement inside formwork

Figure A.5 - CB1 before casting

Figure A.6 - CB2 before casting

Figure A.7 – CB2D before casting

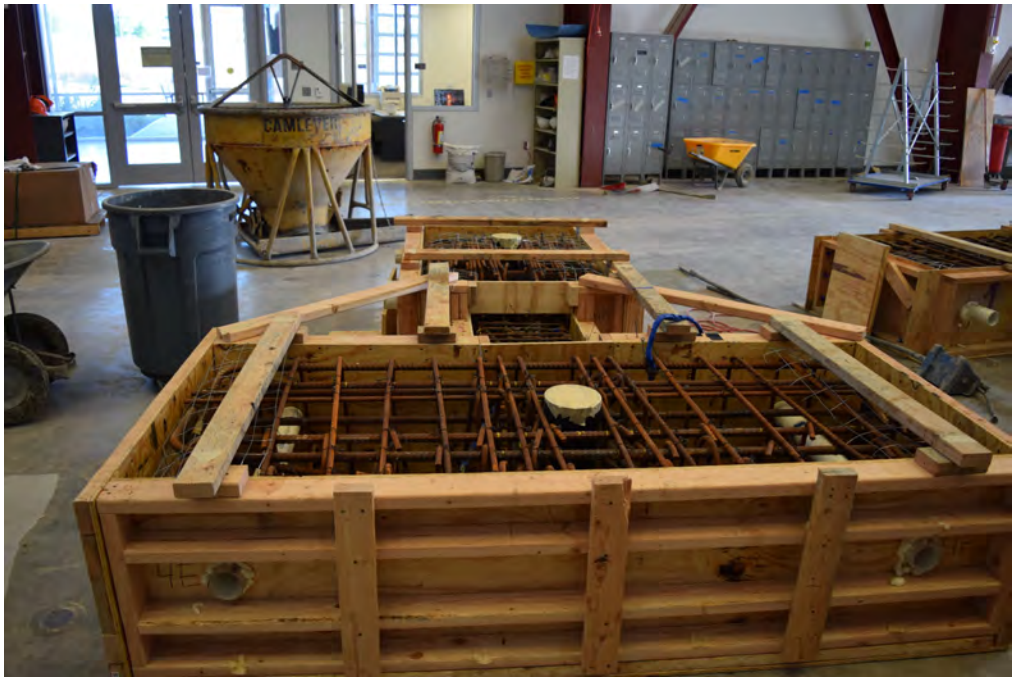

Figure A.8 – CB2AD before casting (steel pipes embedded into top and bottom blocks)

Figure A.9 – CB3D before casting

Figure A.10 – Curing of a coupling beam specimen

Figure A.11 – Coupling beam specimen after stripping formwork

APPENDIX B PHOTOS OF SPECIMENS DURING AND AFTER TESTING

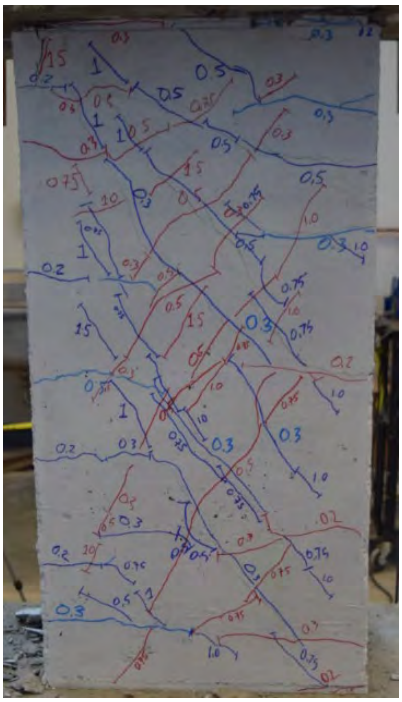

(+1.8%)

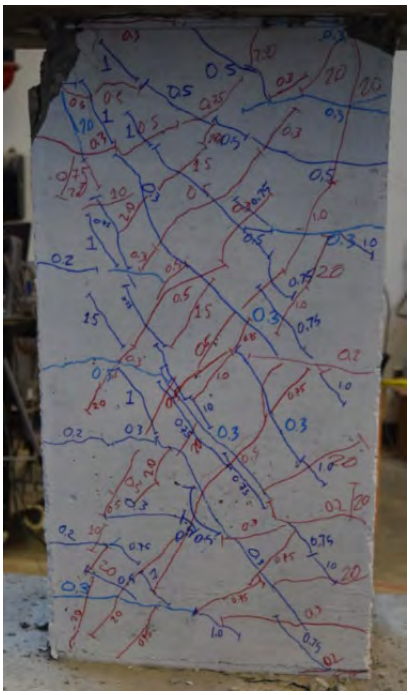

(-1.9%)

Figure B.1 – CB1 at target 2% chord rotation

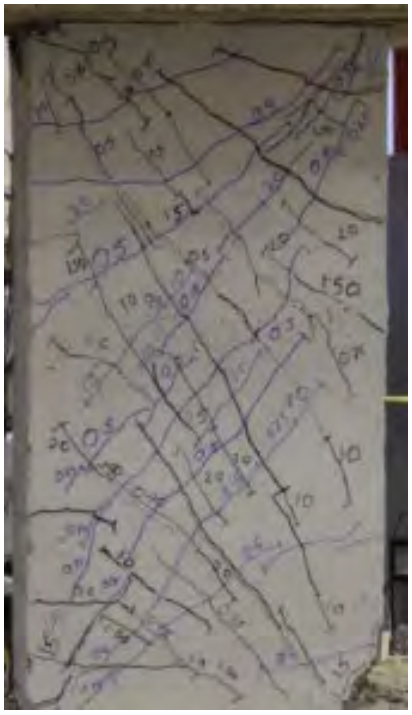

(+2.9%)

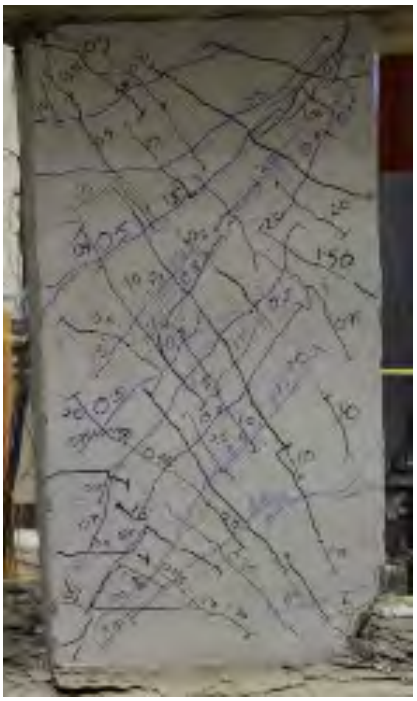

(-2.1%)

Figure B.2 – CB2 at target 2% chord rotation

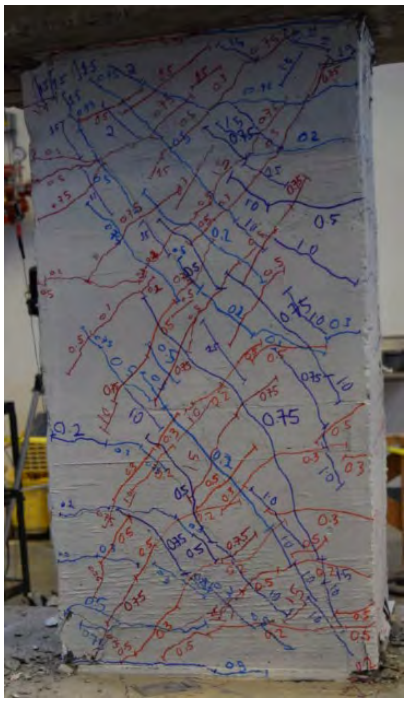

(+2.0%)

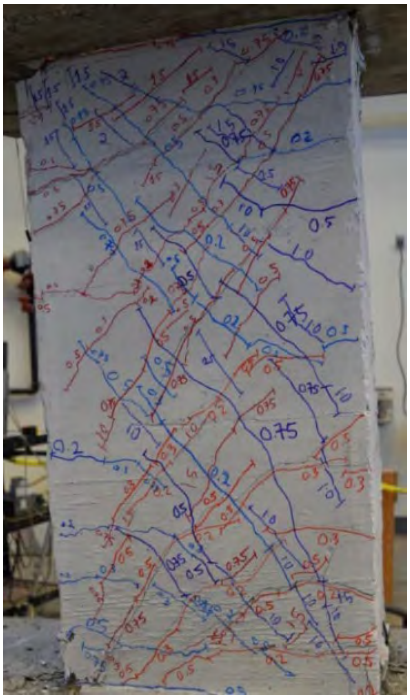

(-2.0%)

Figure B.3 – CB2D at target 2% chord rotation

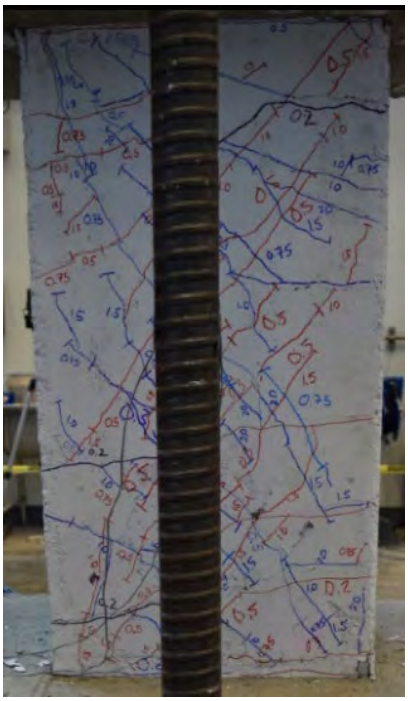

(+2.0%)

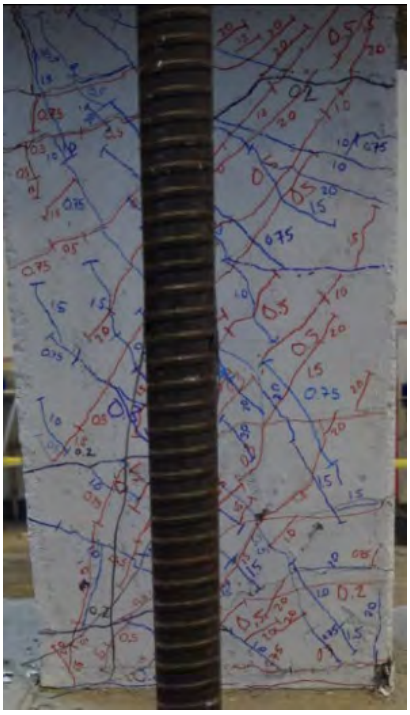

(-2.2%)

Figure B.4 – CB2AD at target 2% chord rotation

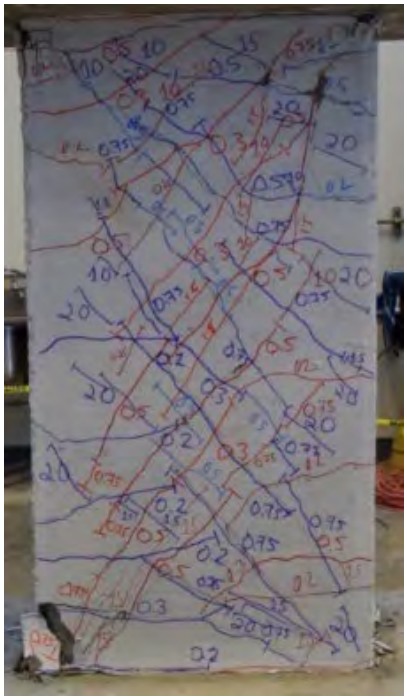

(+2.1%)

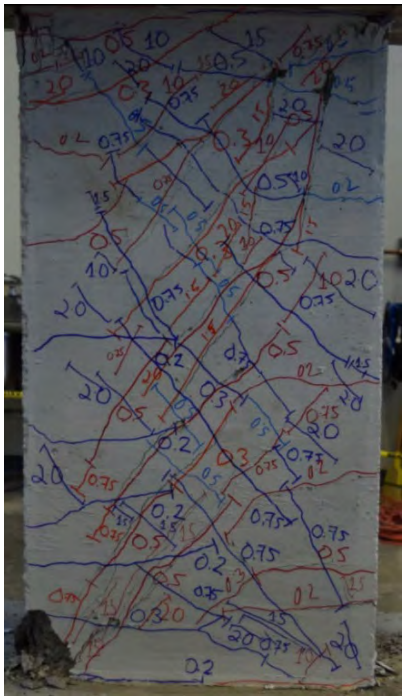

(-2.1%)

Figure B.5 – CB3D at target 2% chord rotation

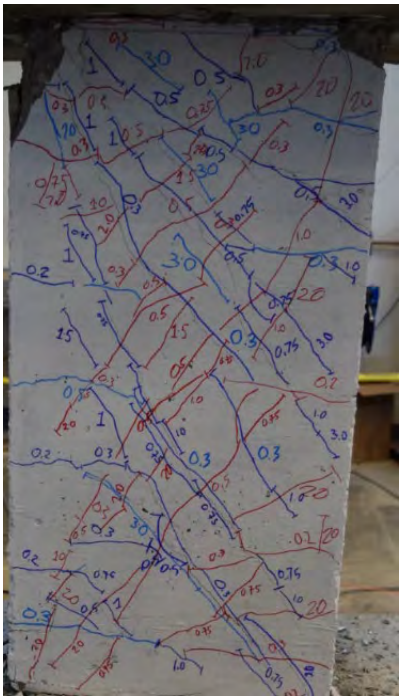

(+3.0%)

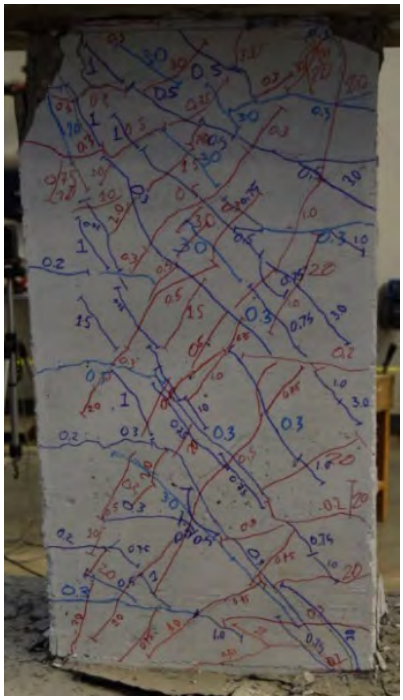

(-3.0%)

Figure B.6 – CB1 at target 3% chord rotation

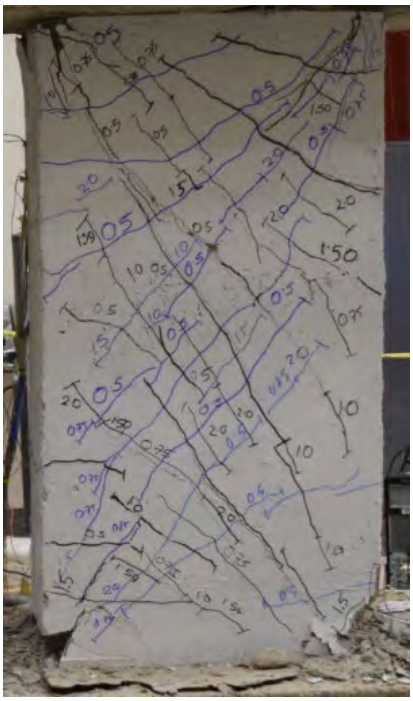

(+4.1%)

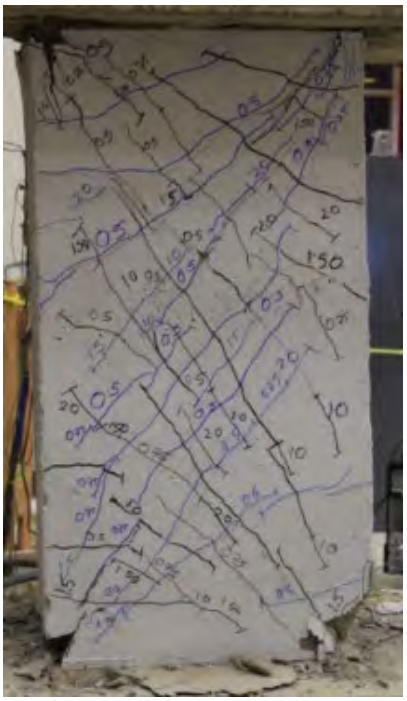

(-3.2%)

Figure B.7 – CB2 at target 3% chord rotation

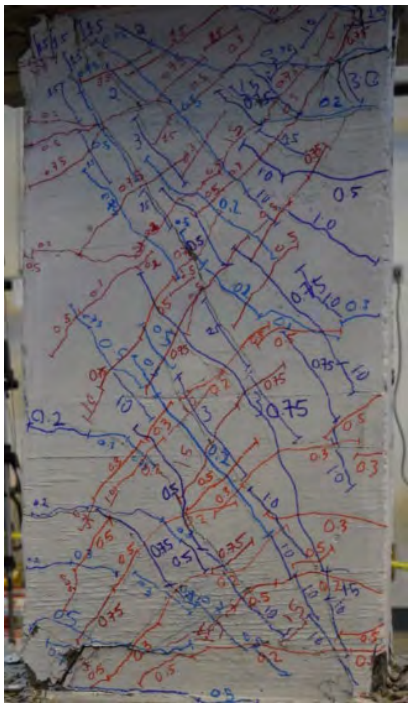

(+3.1%)

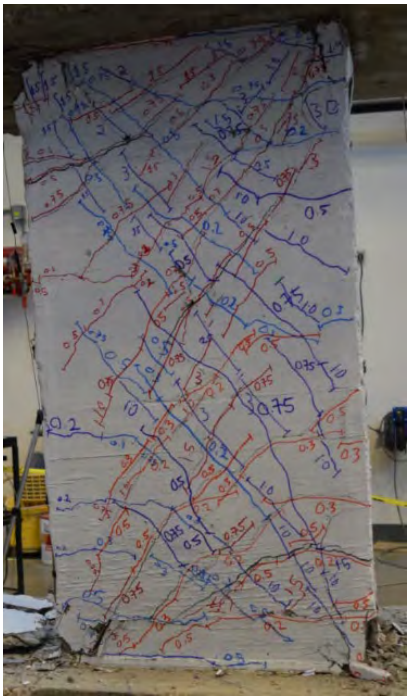

(-3.1%)

Figure B.8 – CB2D at target 3% chord rotation

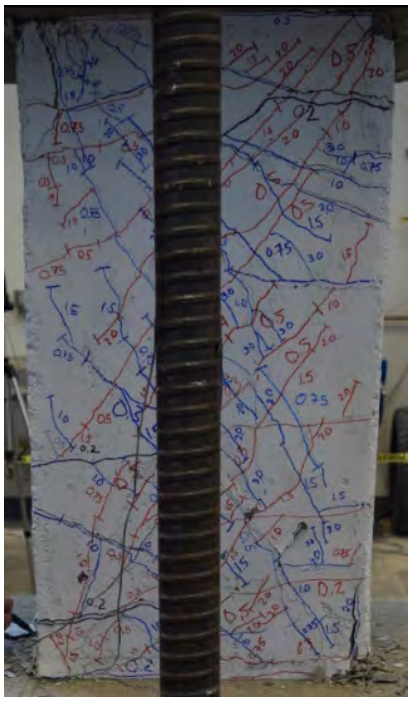

(+2.8%)

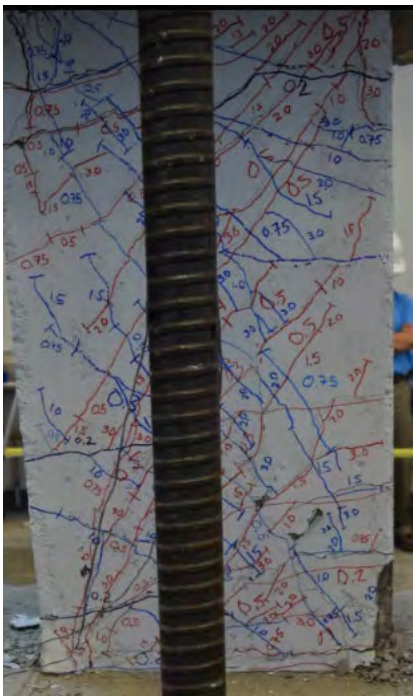

(-2.9%)

Figure B.9 – CB2AD at target 3% chord rotation

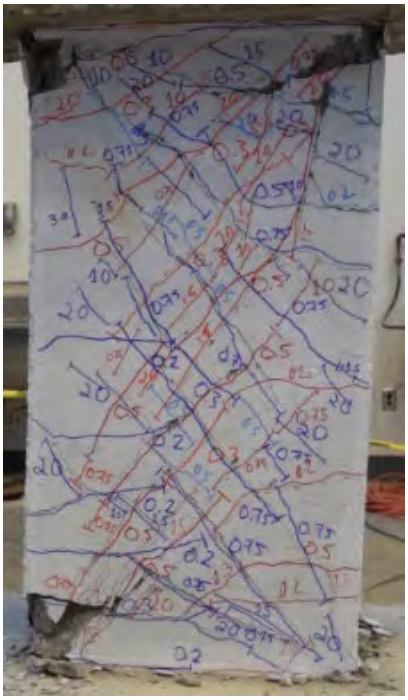

(+3.3%)

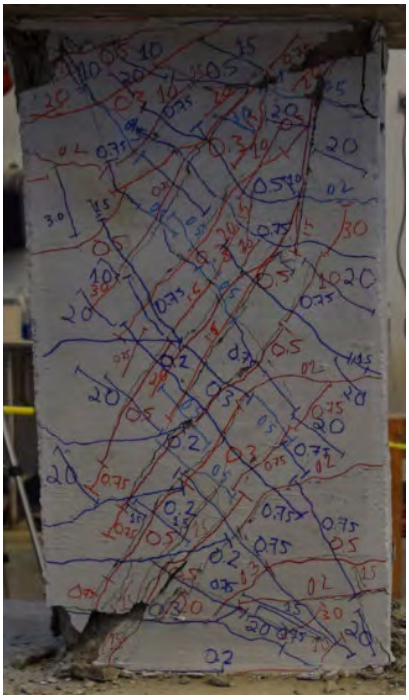

(-3.0%)

Figure B.10 – CB3D at target 3% chord rotation

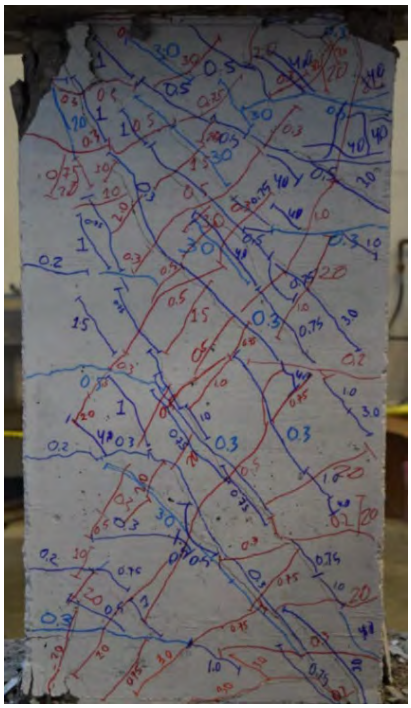

(+3.9%)

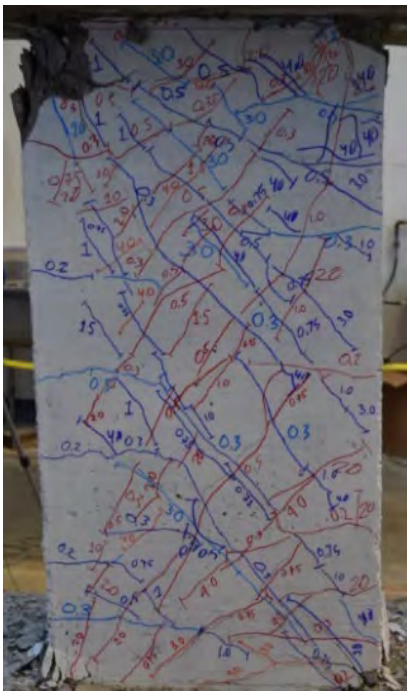

(-3.9%)

Figure B.11 – CB1 at target 4% chord rotation

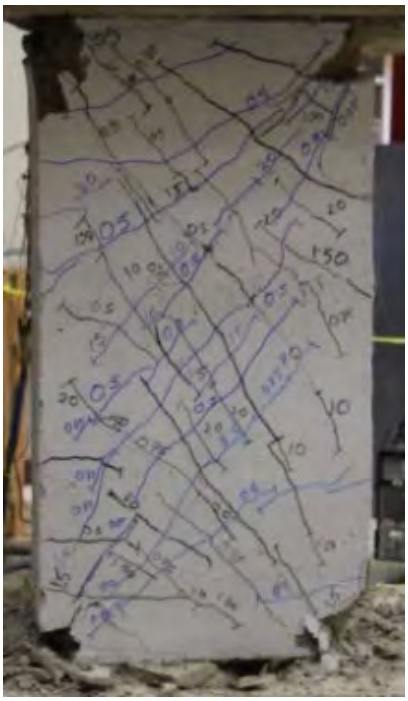

(+5.2%)

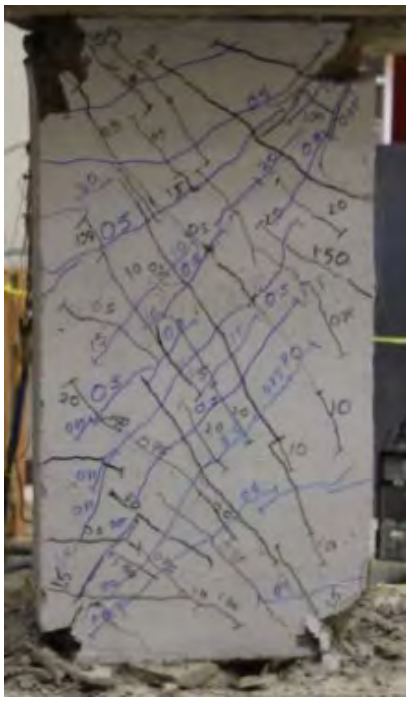

(-4.5%)

Figure B.12 – CB2 at target 4% chord rotation

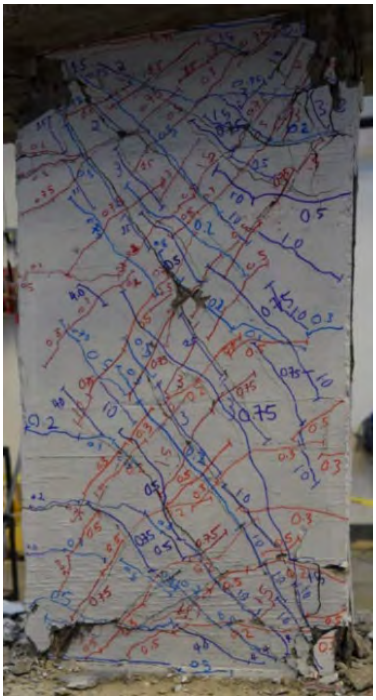

(+4.3%)

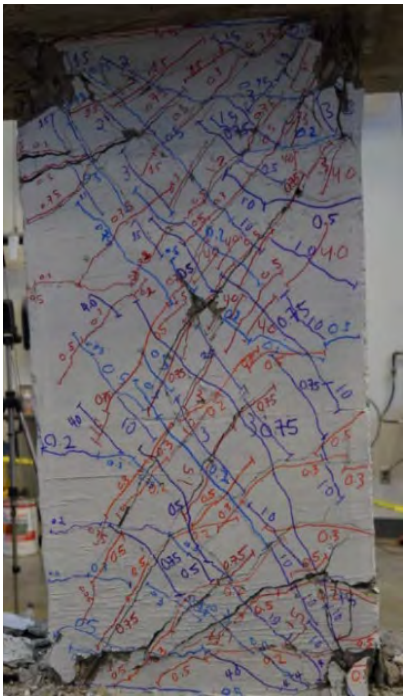

(-4.0%)

Figure B.13 – CB2D at target 4% chord rotation

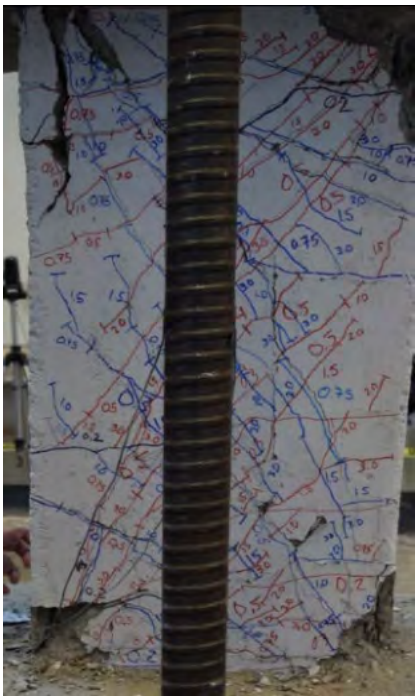

(+3.8%)

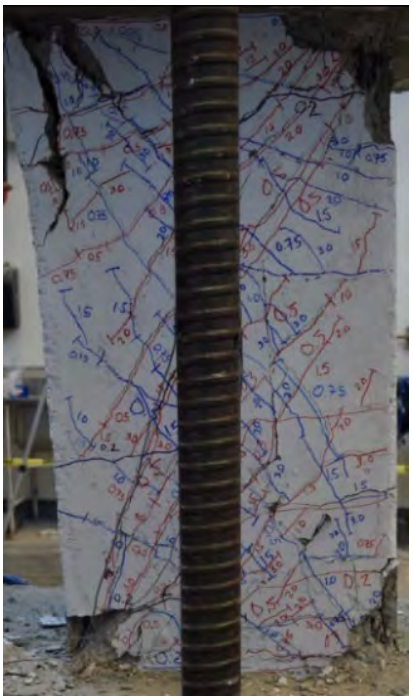

(-4.8%)

Figure B.14 – CB2AD at target 4% chord rotation

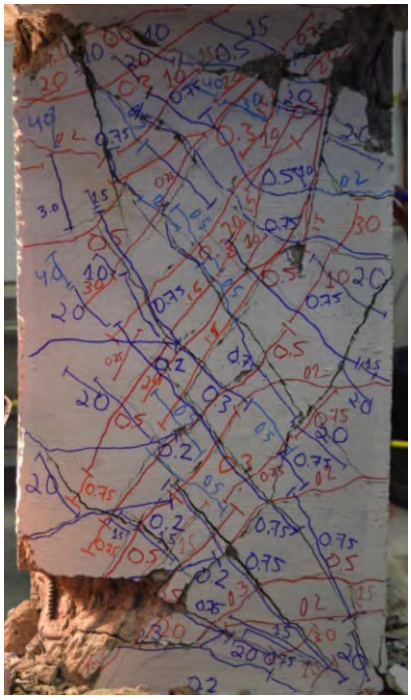

(+4.1%)

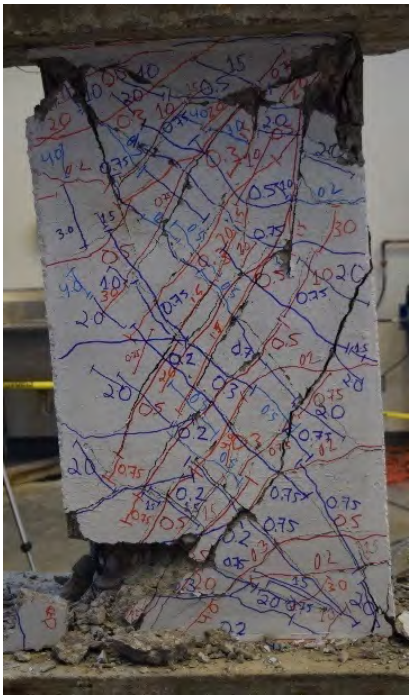

(-4.1%)

Figure B.15 – CB3D at target 4% chord rotation

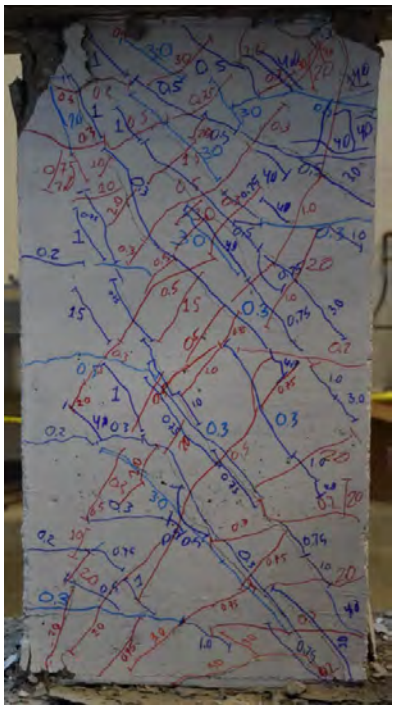

(+5.0%)

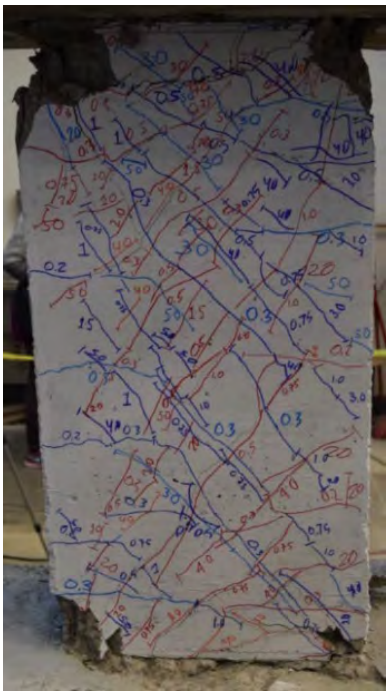

(-5.0%)

Figure B.16 – CB1 at target 5% chord rotation

Did not reach

Did not reach

Figure B.17 – CB2 at target 5% chord rotation

(+5.2%)

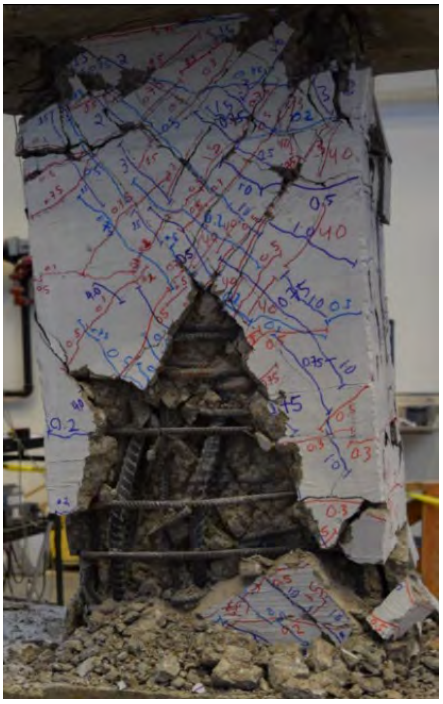

(-5.2%)

Figure B.18 – CB2D at target 5% chord rotation

(+5.5%)

(-6.2%)

Figure B.19 – CB2AD at target 5% chord rotation

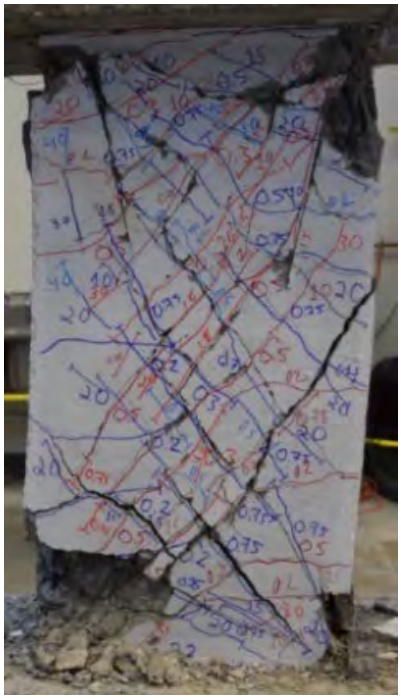

(+5.4%)

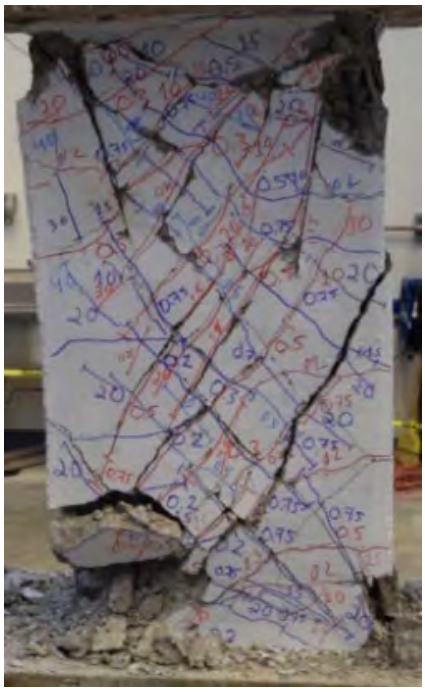

(-4.9%)

Figure B.20 – CB3D at target 5% chord rotation

Figure B.21 – CB1 with longitudinal bar buckling during first cycle to -5% chord rotation

Figure B.22 – CB1 with diagonal bar buckling during first cycle to -6% chord rotation

Figure B.23 – CB1 with diagonal bar fracture during first cycle to +8% chord rotation

Figure B.24 – CB1 with longitudinal bar fracture during first cycle to +8% chord rotation

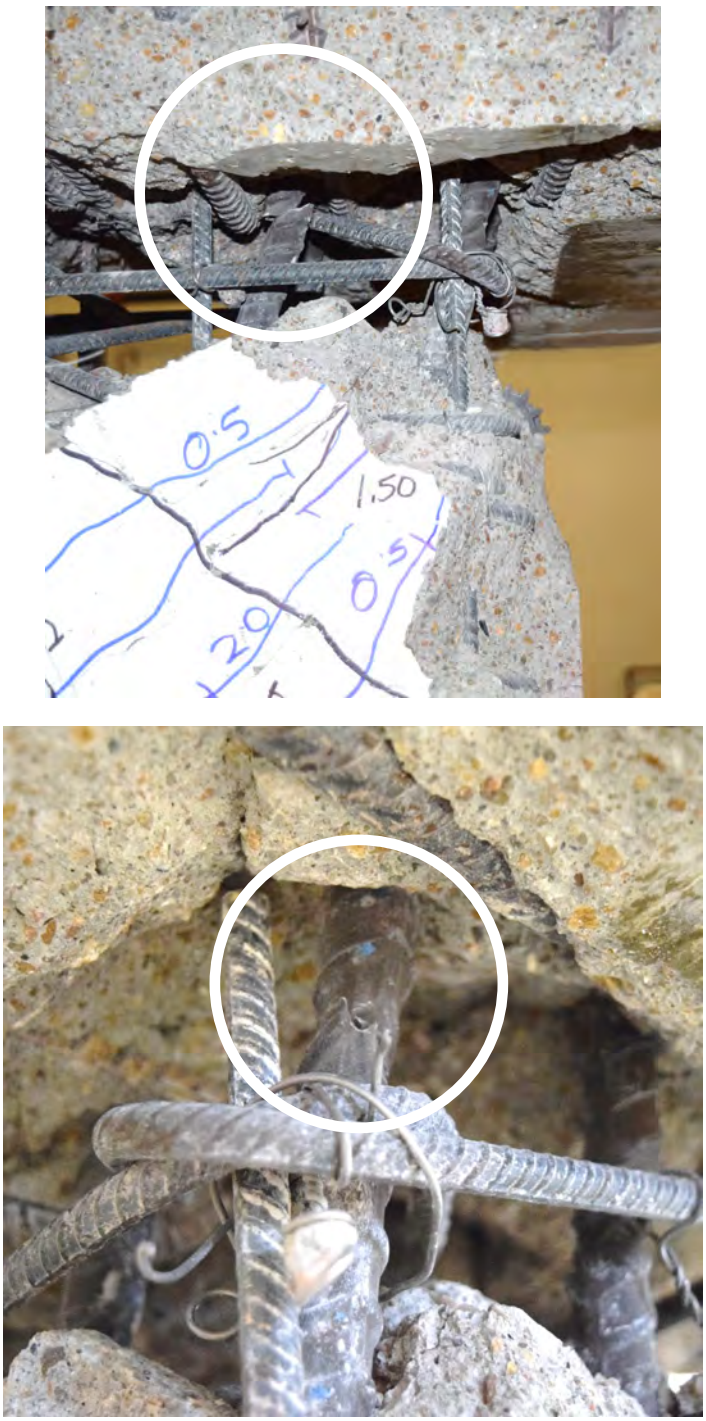

Figure B.25 – CB2 with two diagonal bar fractures during first cycle to +6% chord rotation

Figure B.26 – CB2D with longitudinal bar fracture during second cycle to +5% chord rotation

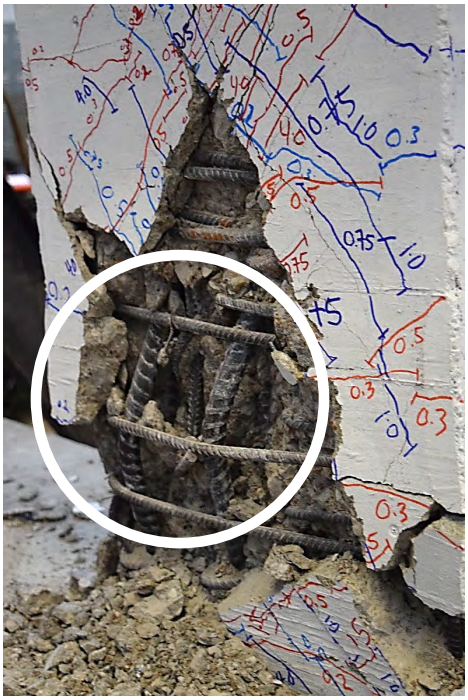

Figure B.27 – CB2D with diagonal bar buckling during second cycle to -5% chord rotation

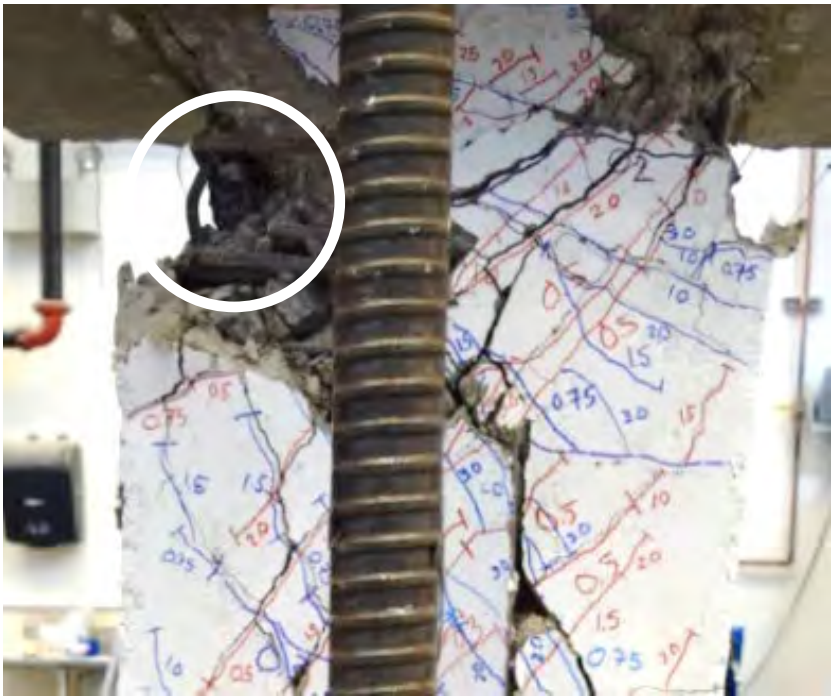

Figure B.28 – CB2AD with longitudinal bar buckling during second cycle to +5% chord rotation

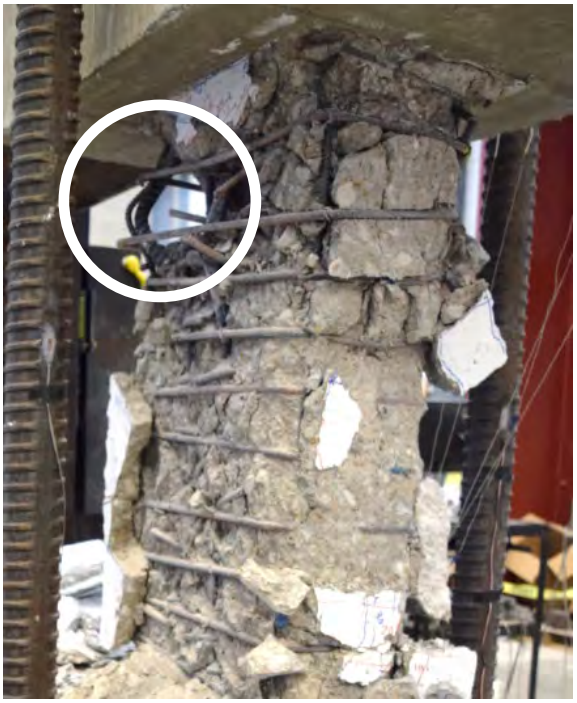

Figure B.29 – CB2AD with diagonal bar buckling during first cycle to +6% chord rotation

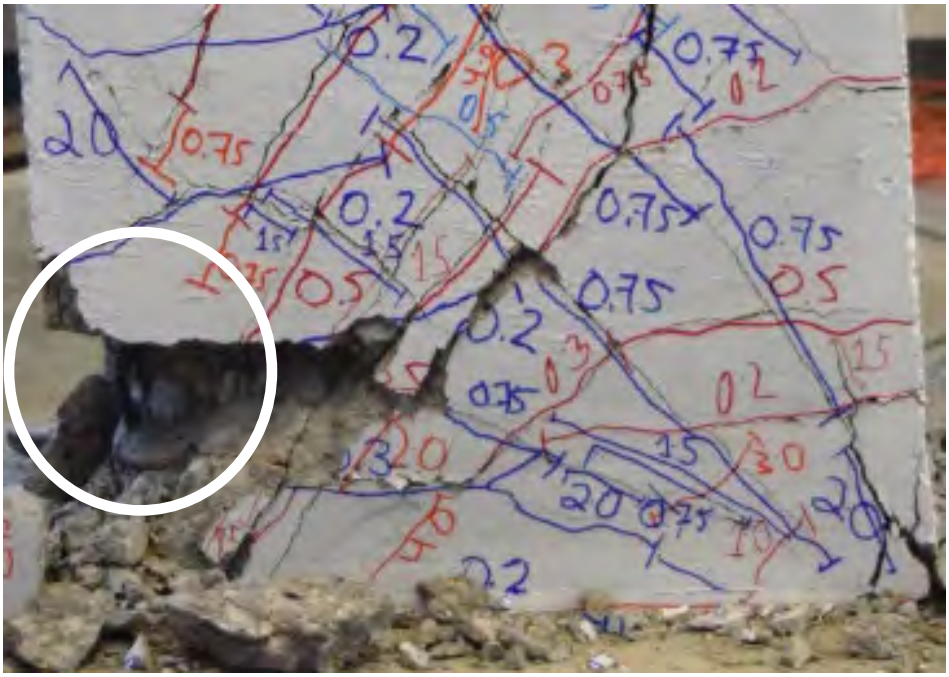

Figure B.30 – CB3D with longitudinal bar buckling during second cycle to -4% chord rotation

Figure B.31 – CB3D with diagonal bar buckling during first cycle to -6% chord rotation

APPENDIX C COMPONENTS OF CHORD ROTATION

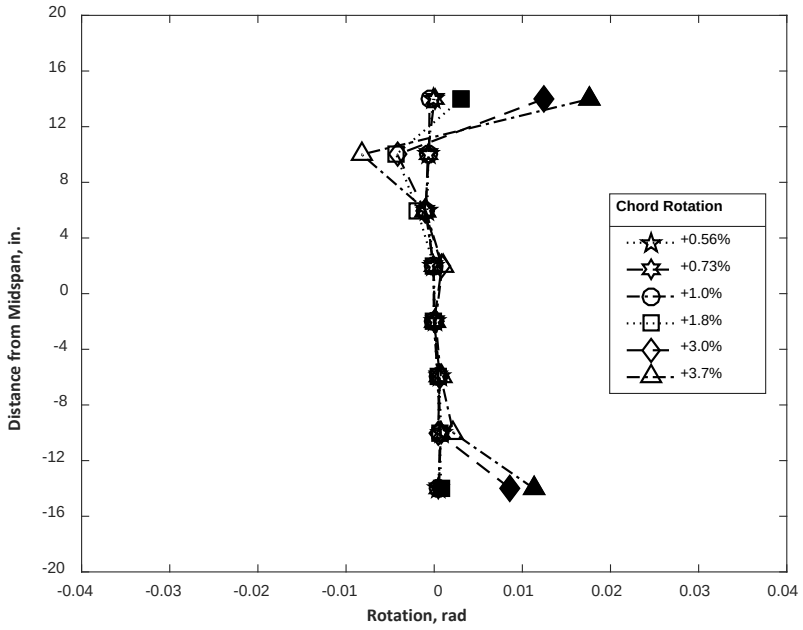

Figure C.1 – Calculated flexural rotation for CB1 at positive chord rotations (1 in. = 25.4 mm)

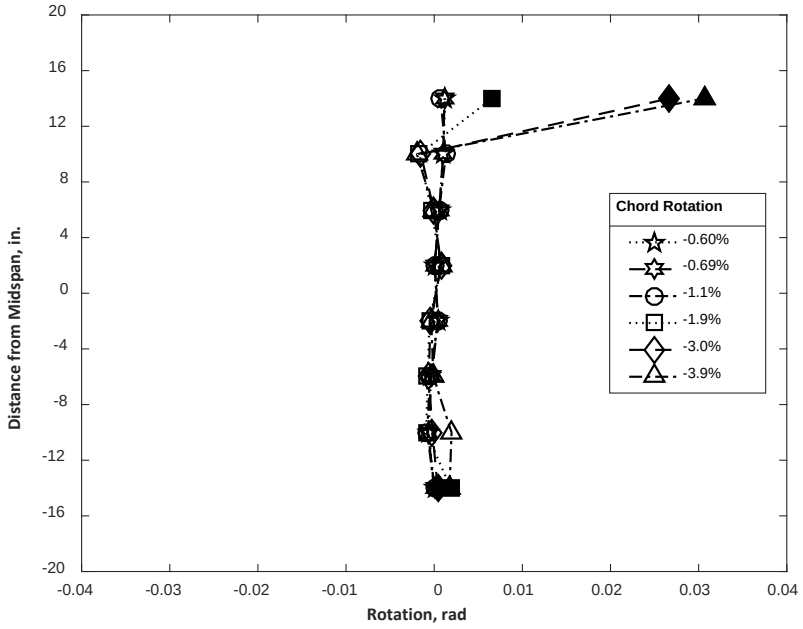

Figure C.2 – Calculated flexural rotation for CB1 at negative chord rotations (1 in. = 25.4 mm)

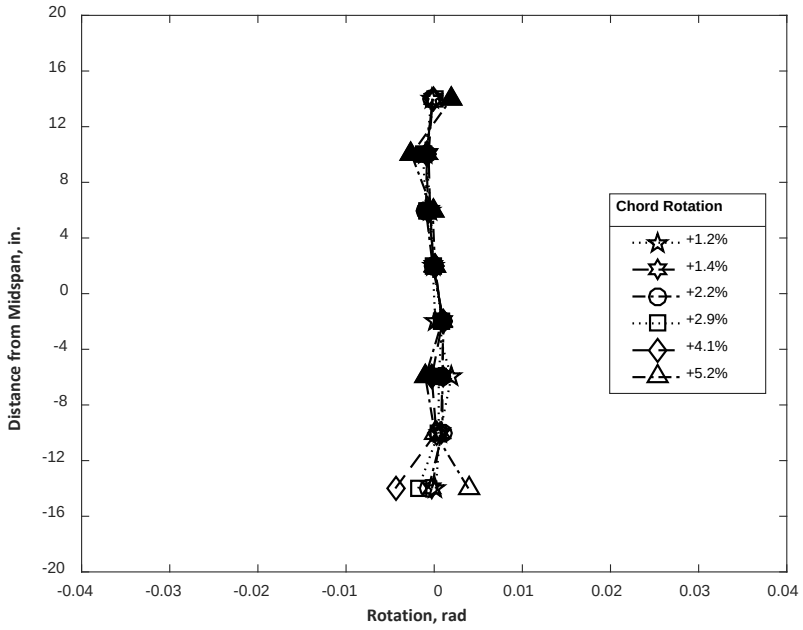

Figure C.3 – Calculated flexural rotation for CB2 at positive chord rotations (1 in. = 25.4 mm)

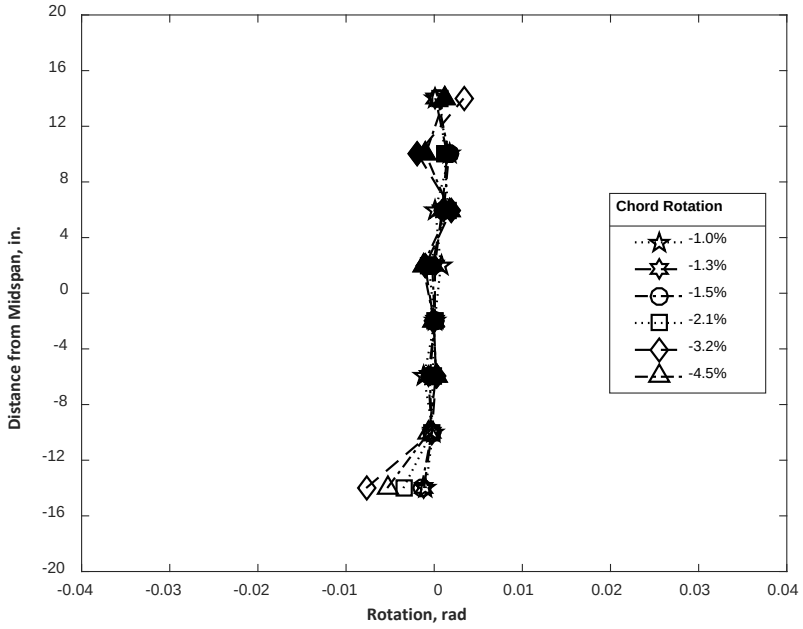

Figure C.4 – Calculated flexural rotation for CB2 at negative chord rotations (1 in. = 25.4 mm)

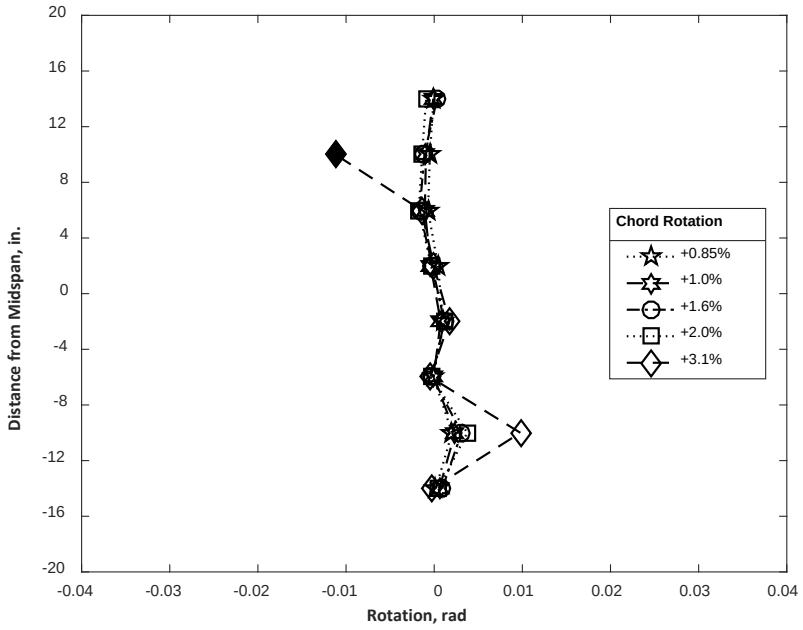

Figure C.5 – Calculated flexural rotation for CB2D at positive chord rotations (1 in. = 25.4 mm)

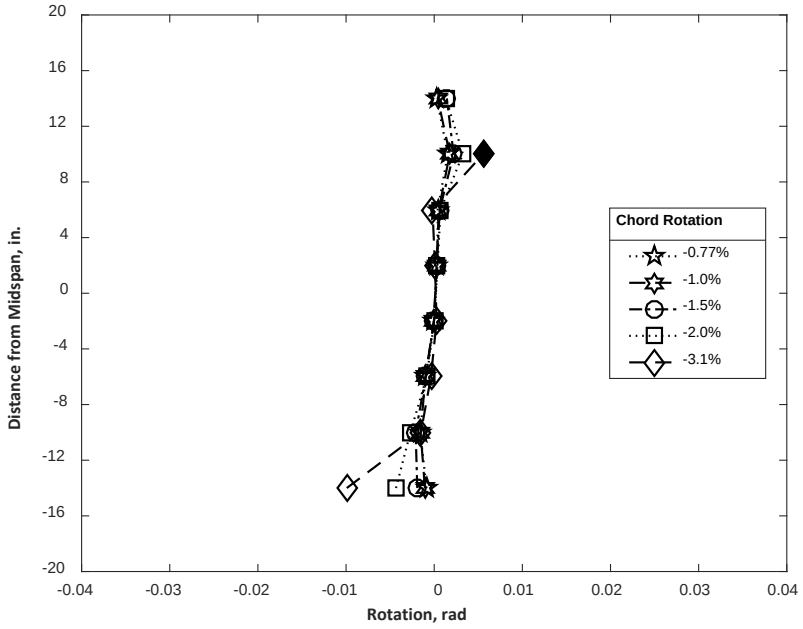

Figure C.6 – Calculated flexural rotation for CB2D at negative chord rotations (1 in. = 25.4 mm)

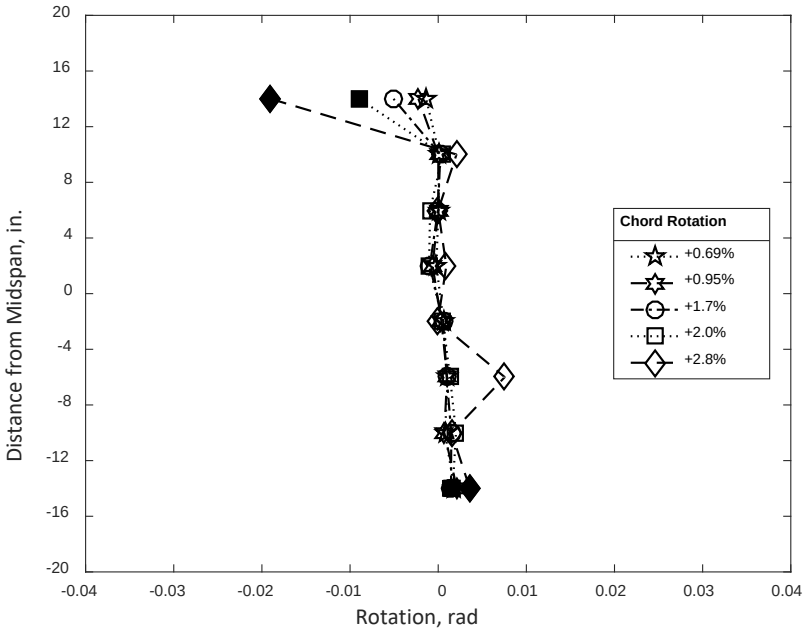

Figure C.7 – Calculated flexural rotation for CB2AD at positive chord rotations (1 in. = 25.4 mm)

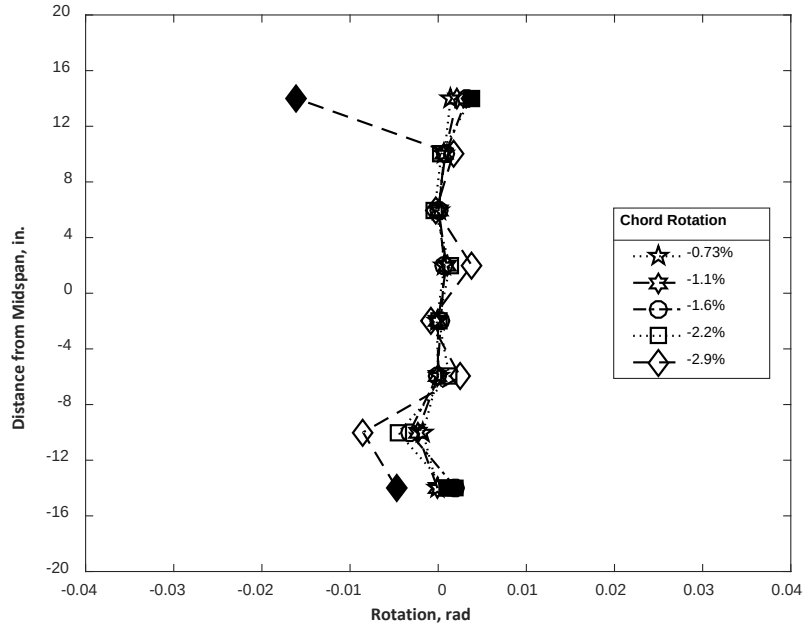

Figure C.8 – Calculated flexural rotation for CB2AD at negative chord rotations (1 in. = 25.4 mm)

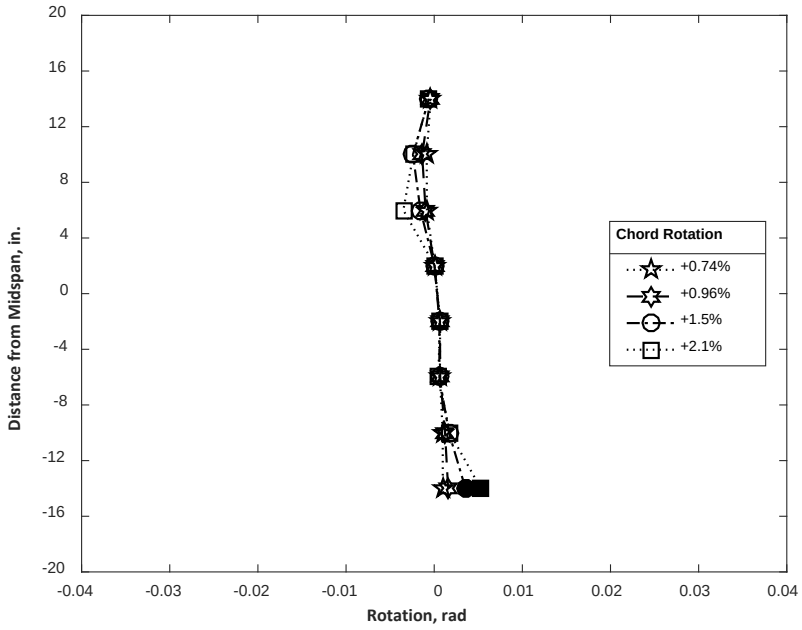

Figure C.9 – Calculated flexural rotation for CB3D at positive chord rotations (1 in. = 25.4 mm)

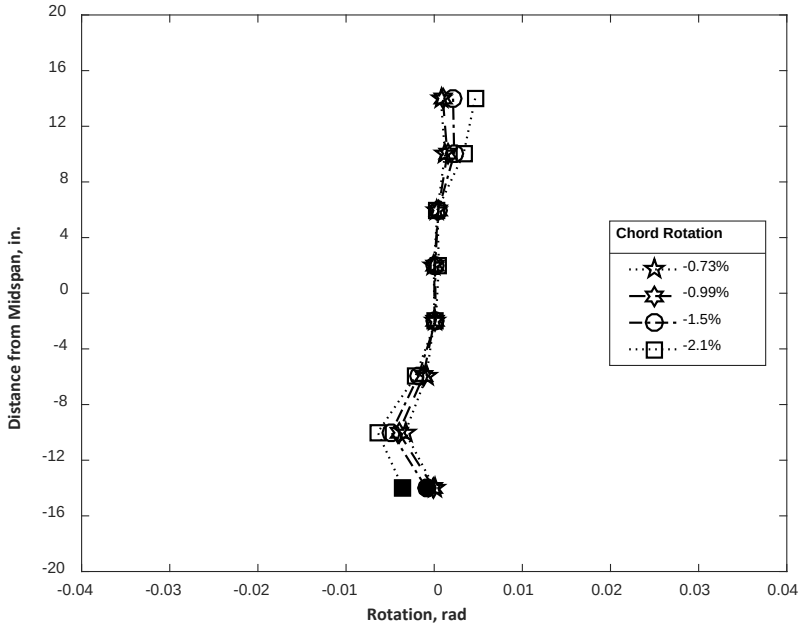

Figure C.10 – Calculated flexural rotation for CB3D at negative chord rotations (1 in. = 25.4 mm)

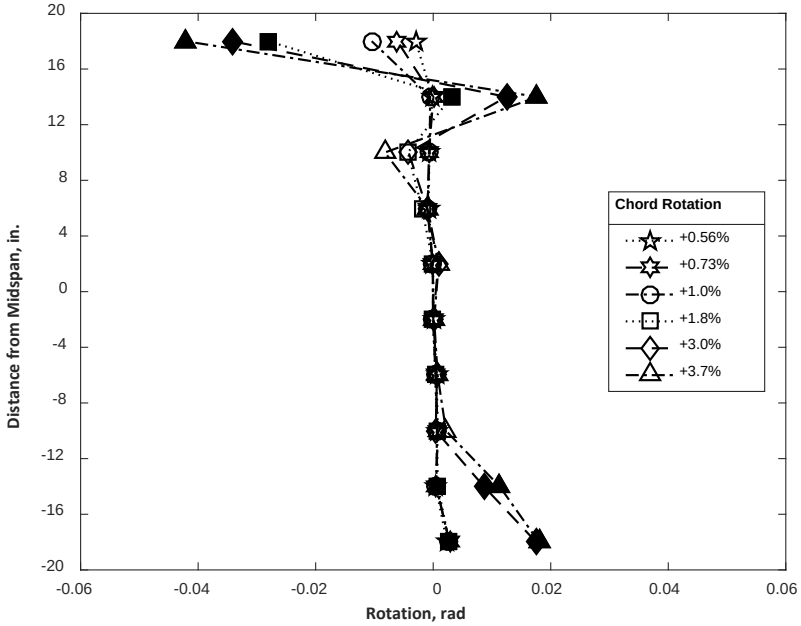

Figure C.11 – Calculated flexural rotation including strain penetration for CB1 at positive chord rotations (1 in. = 25.4 mm)

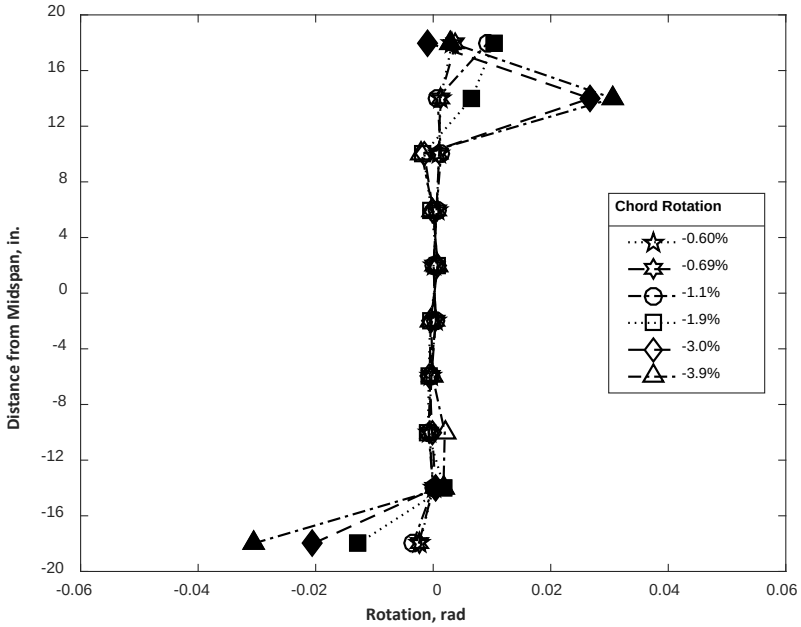

Figure C.12 – Calculated flexural rotation including strain penetration for CB1 at negative chord rotations (1 in. = 25.4 mm)

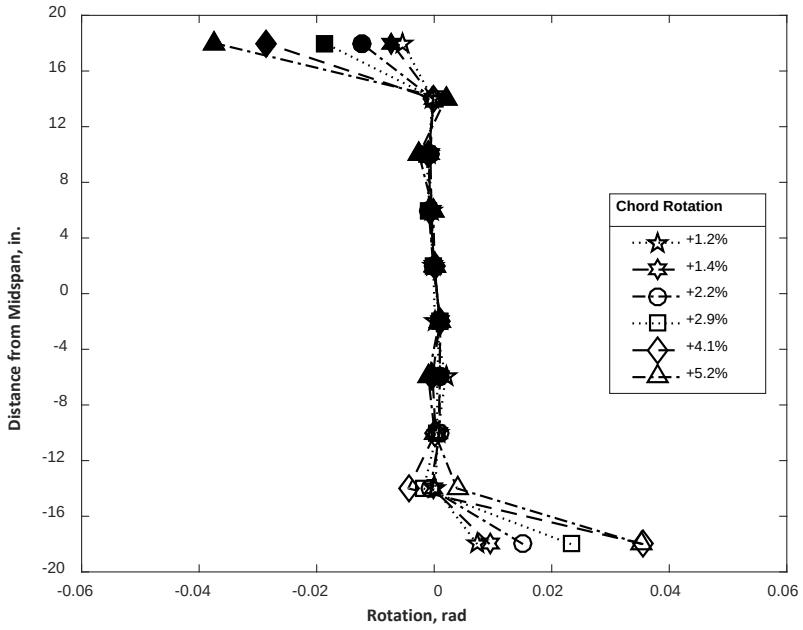

Figure C.13 – Calculated flexural rotation including strain penetration for CB2 at positive chord rotations (1 in. = 25.4 mm)

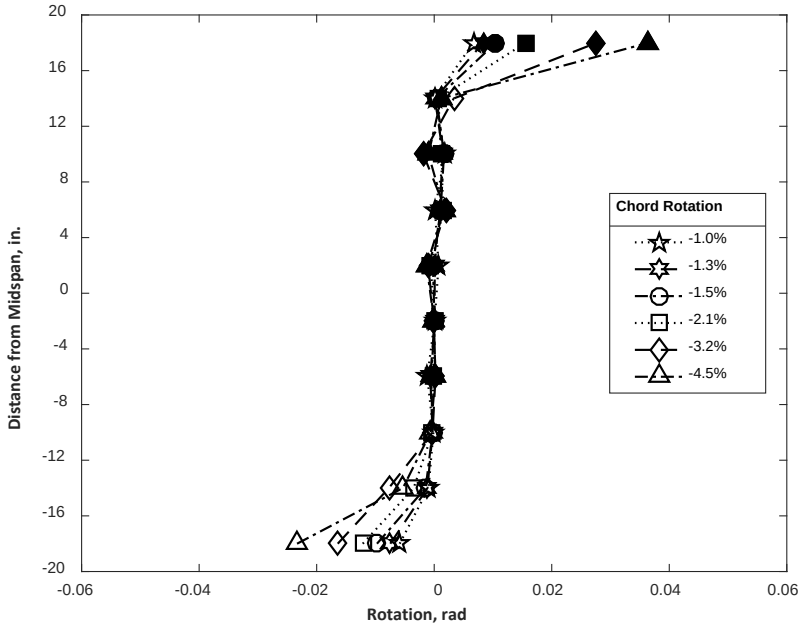

Figure C.14 – Calculated flexural rotation including strain penetration for CB2 at negative chord rotations (1 in. = 25.4 mm)

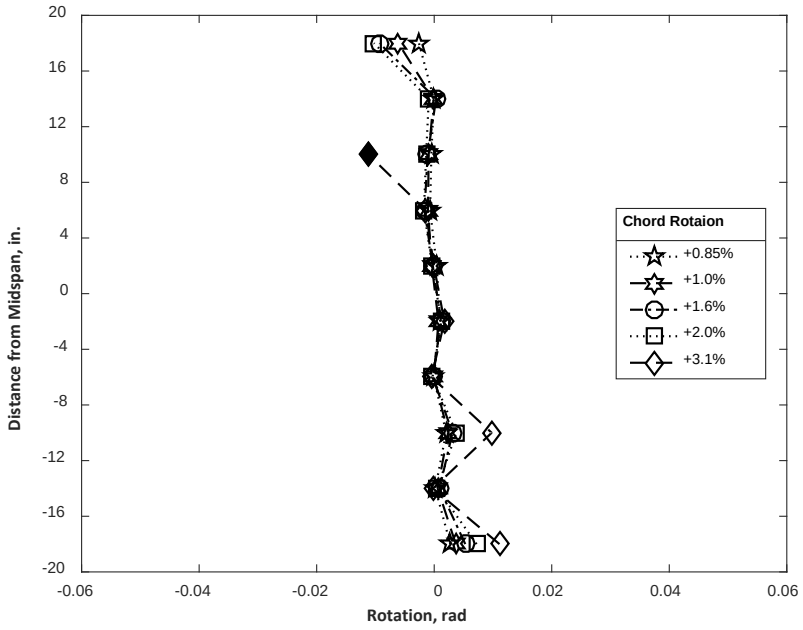

Figure C.15 – Calculated flexural rotation including strain penetration for CB2D at positive chord rotations (1 in. = 25.4 mm)

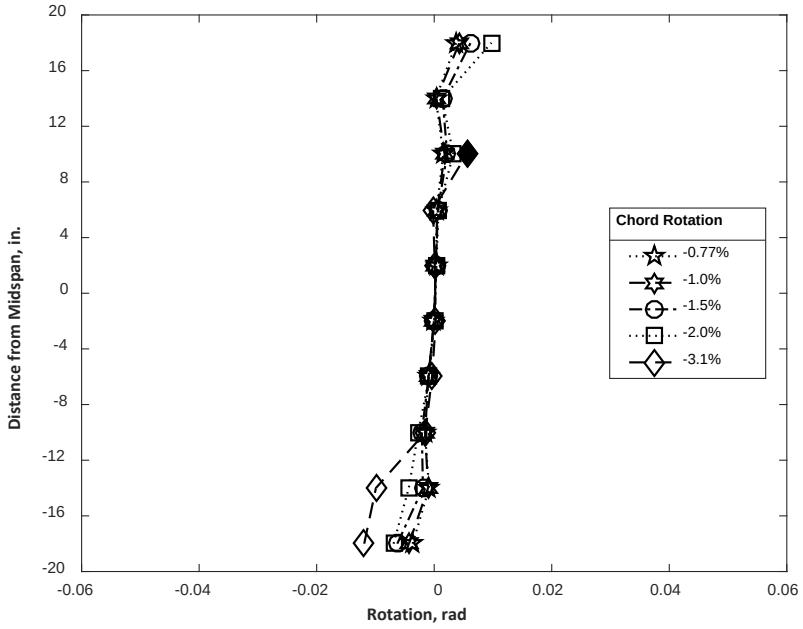

Figure C.16 – Calculated flexural rotation including strain penetration for CB2D at negative chord rotations (1 in. = 25.4 mm)

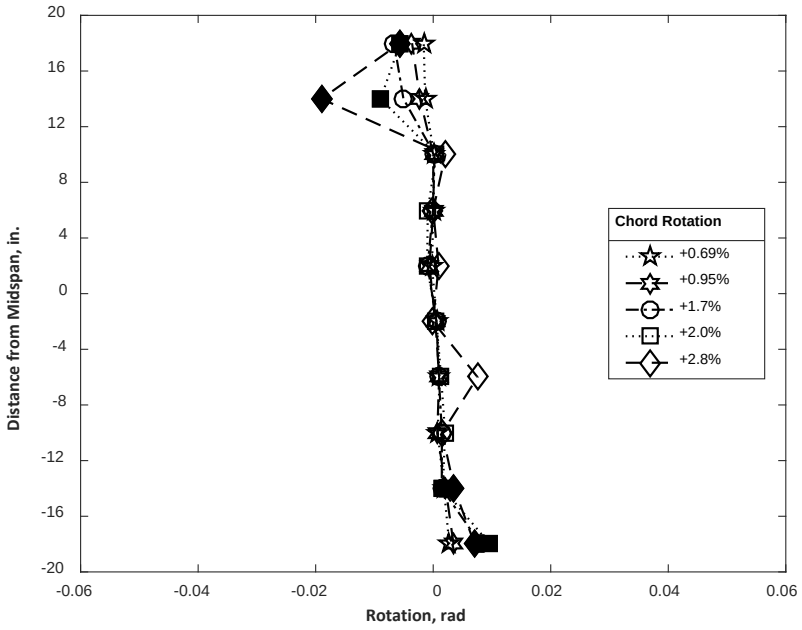

Figure C.17 – Calculated flexural rotation including strain penetration for CB2AD at positive chord rotations (1 in. = 25.4 mm)

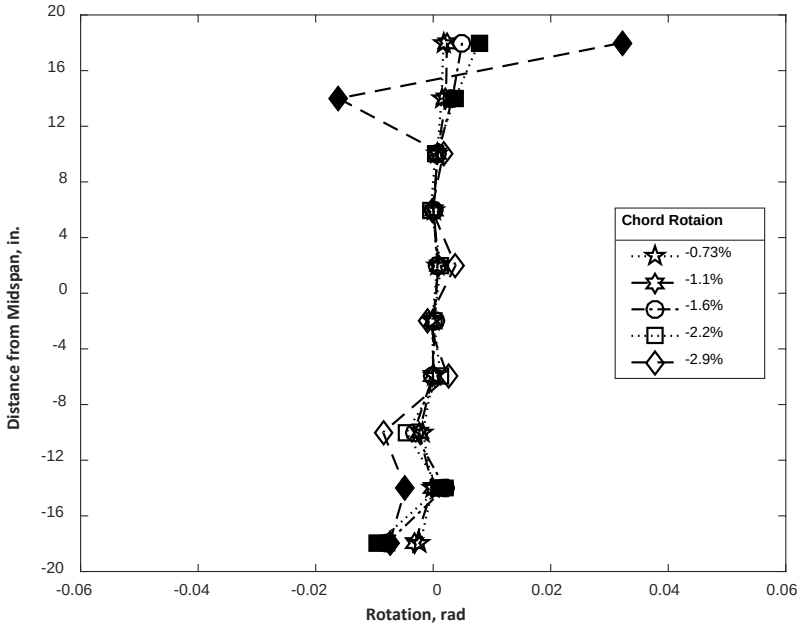

Figure C.18 – Calculated flexural rotation including strain penetration for CB2AD at negative chord rotations (1 in. = 25.4 mm)

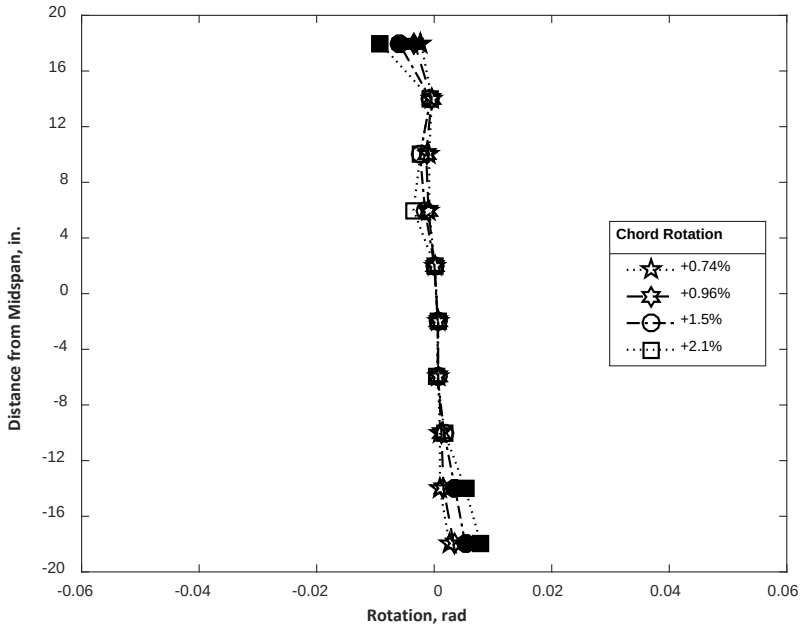

Figure C.19 – Calculated flexural rotation including strain penetration for CB3D at positive chord rotations (1 in. = 25.4 mm)

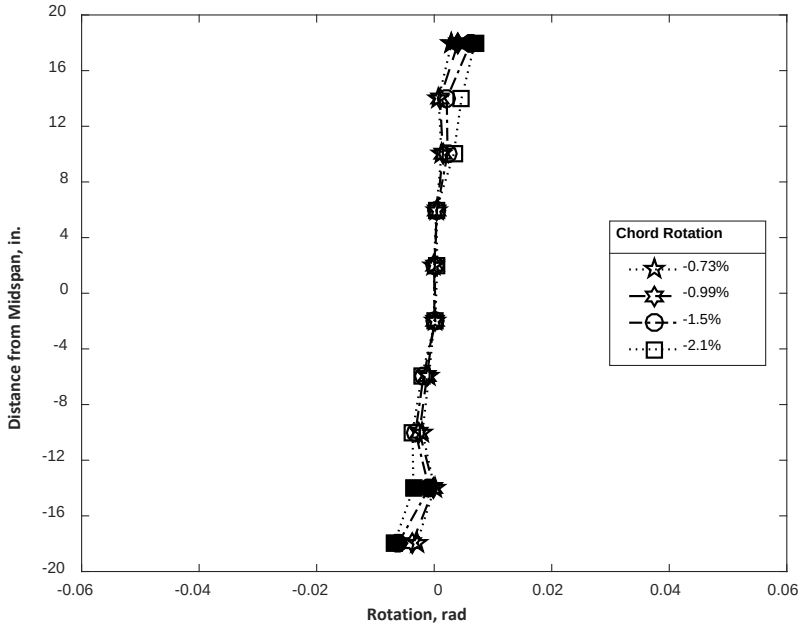

Figure C.20 – Calculated flexural rotation including strain penetration for CB3D at negative chord rotations (1 in. = 25.4 mm)

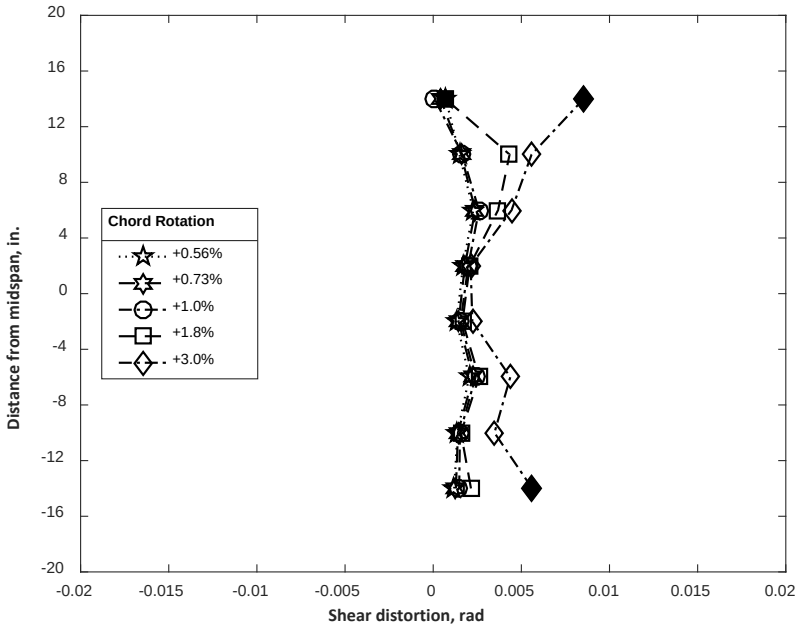

Figure C.21 – Calculated shear distortion for CB1 at positive chord rotations (1 in. = 25.4 mm)

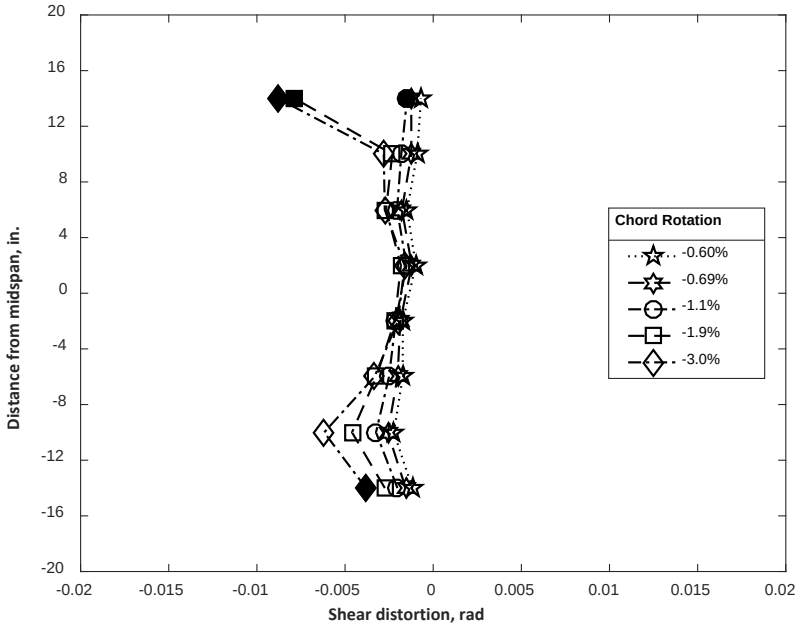

Figure C.22 – Calculated shear distortion for CB1 at negative chord rotations (1 in. = 25.4 mm)

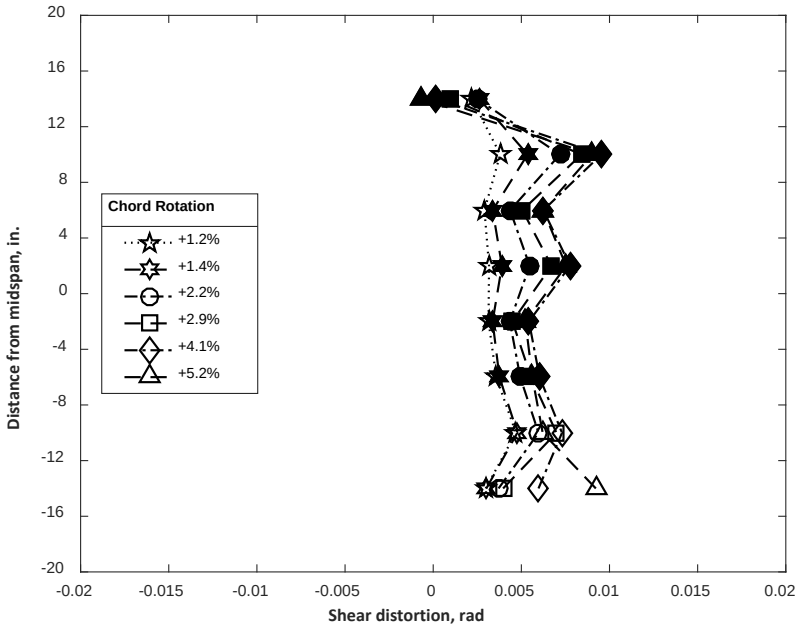

Figure C.23 – Calculated shear distortion for CB2 at positive chord rotations (1 in. = 25.4 mm)

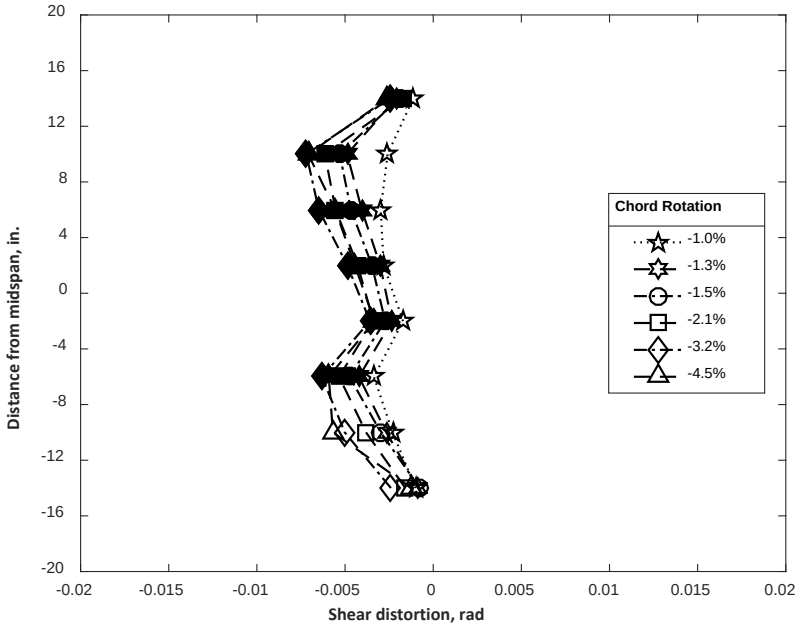

Figure C.24 – Calculated shear distortion for CB2 at negative chord rotations (1 in. = 25.4 mm)

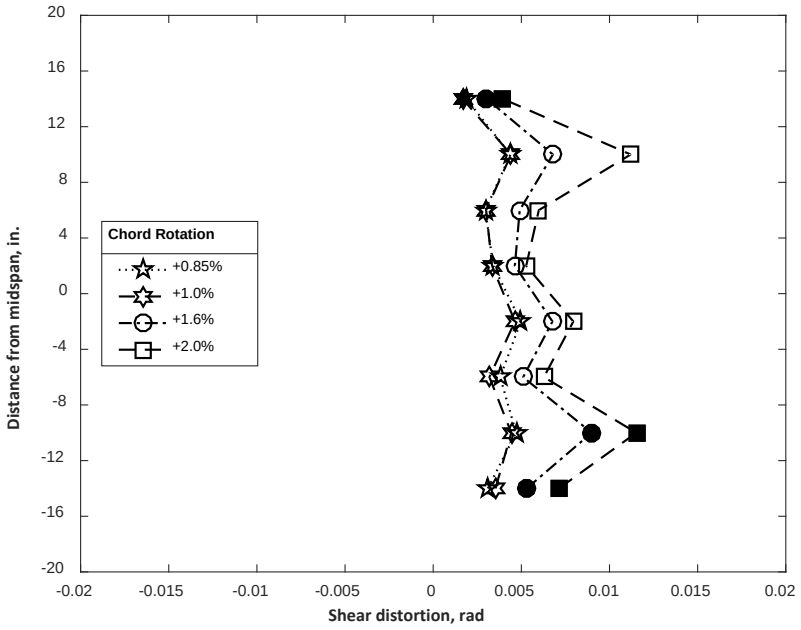

Figure C.25 – Calculated shear distortion for CB2D at positive chord rotations (1 in. = 25.4 mm)

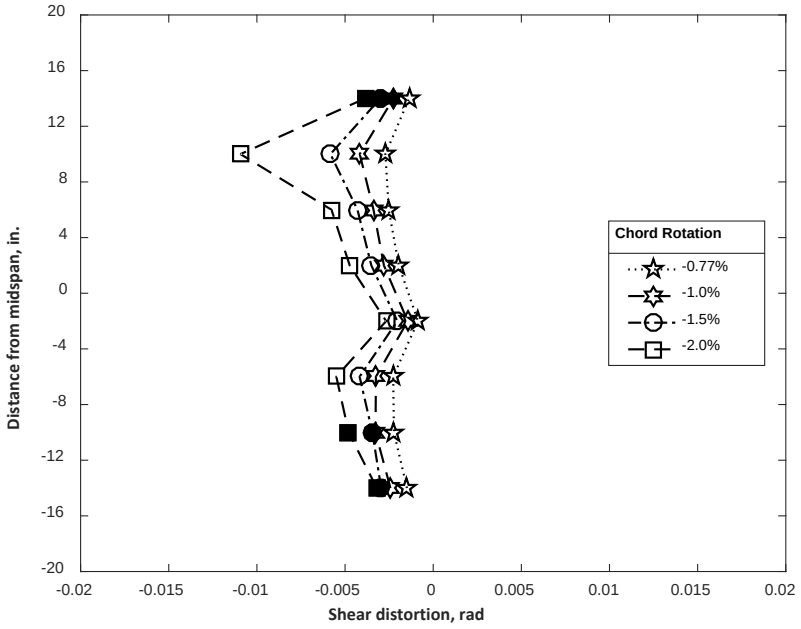

Figure C.26 – Calculated shear distortion for CB2D at negative chord rotations (1 in. = 25.4 mm)

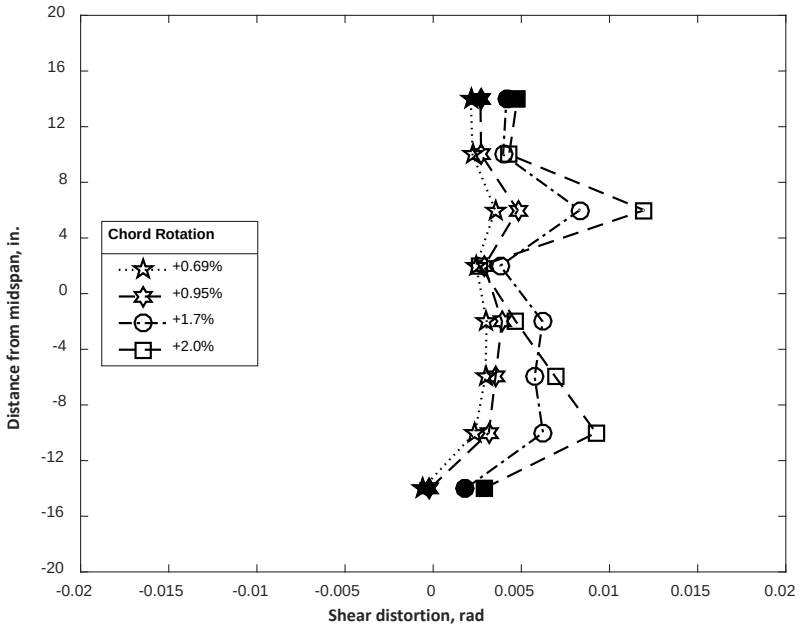

Figure C.27 – Calculated shear distortion for CB2AD at positive chord rotations (1 in. = 25.4 mm)

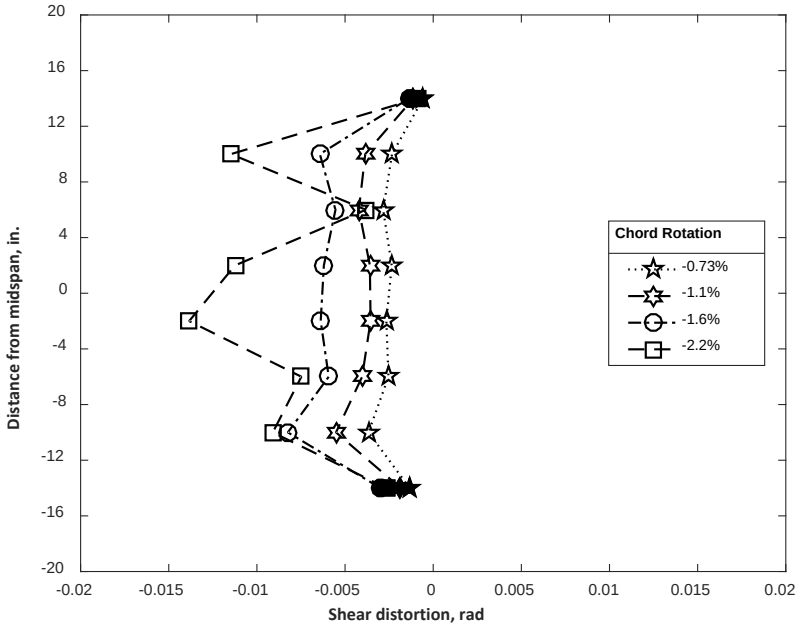

Figure C.28 – Calculated shear distortion for CB2AD at negative chord rotations (1 in. = 25.4 mm)

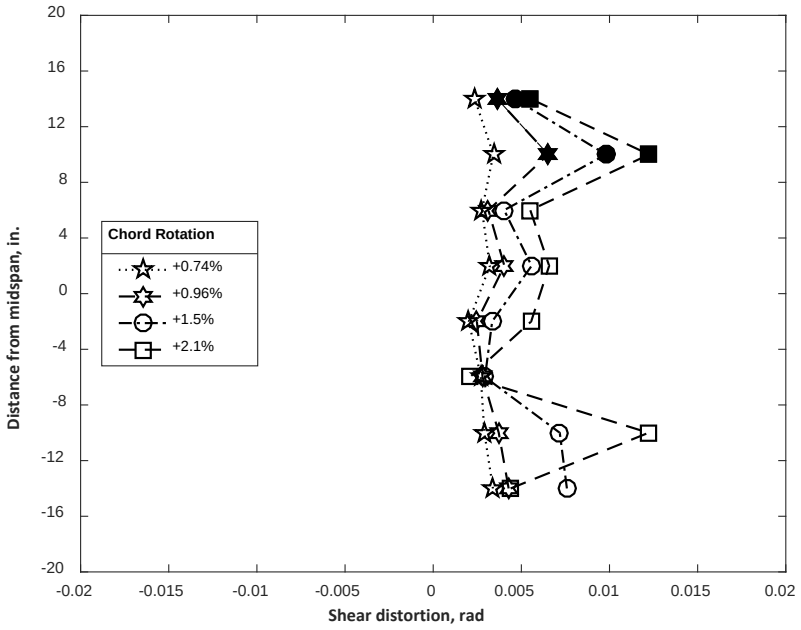

Figure C.29 – Calculated shear distortion for CB3D at positive chord rotations (1 in. = 25.4 mm)

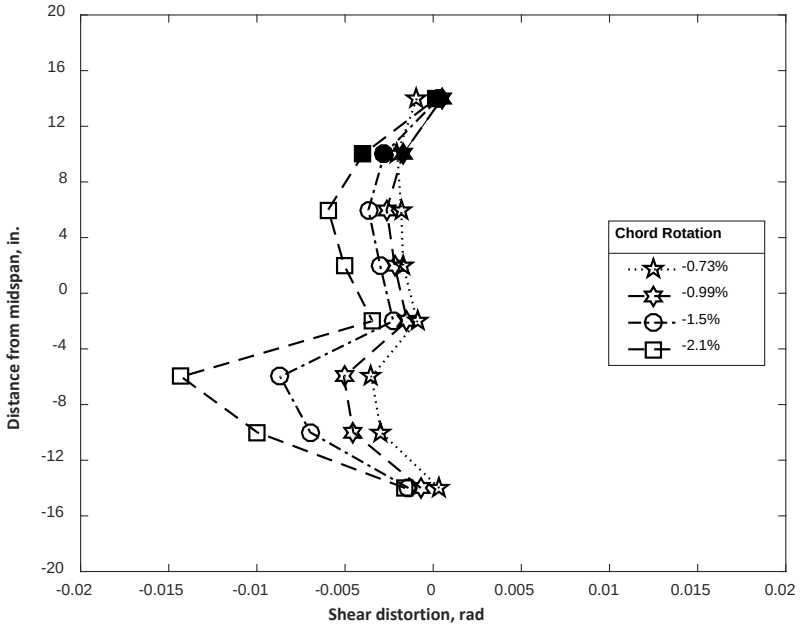

Figure C.30 – Calculated shear distortion for CB3D at negative chord rotations (1 in. = 25.4 mm)

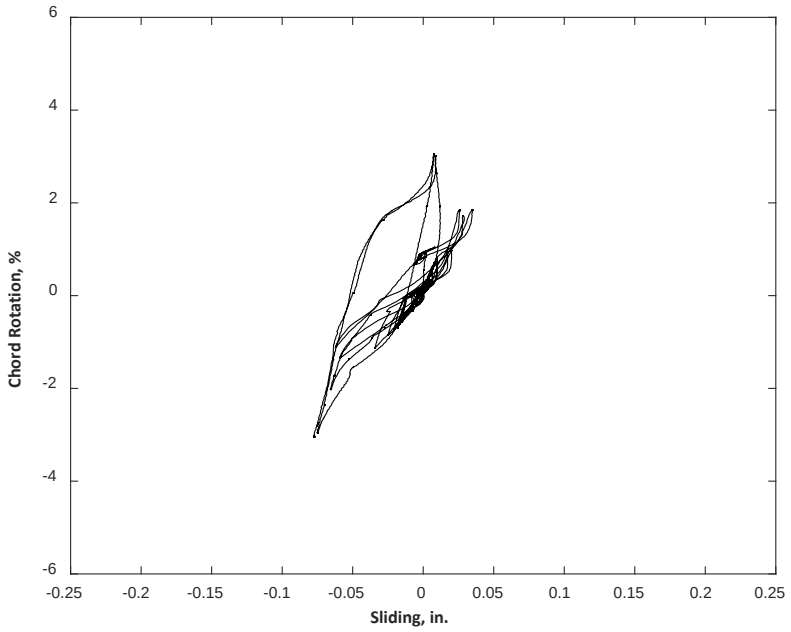

Figure C.31 – Calculated sliding at top for CB1 (1 in. = 25.4 mm)

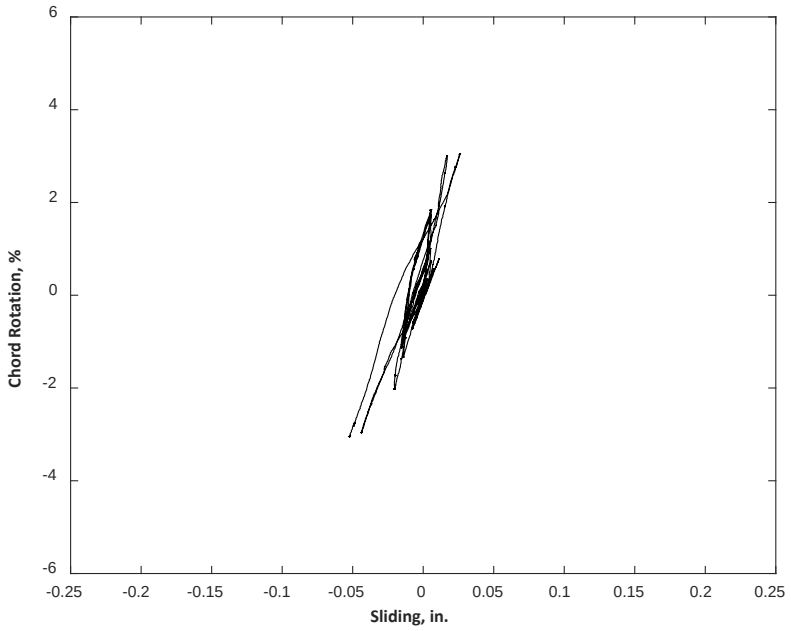

Figure C.32 – Calculated sliding at bottom for CB1 (1 in. = 25.4 mm)

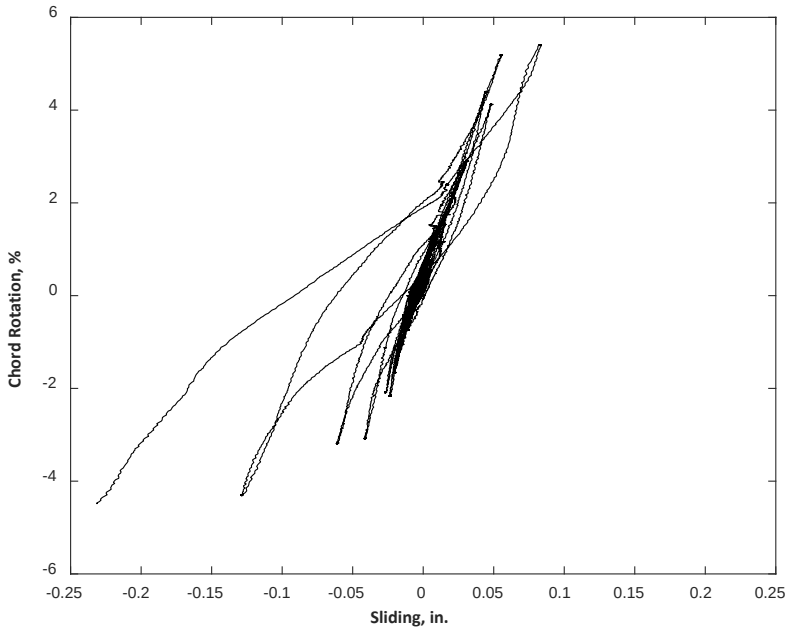

Figure C.33 – Calculated sliding at top for CB2 (1 in. = 25.4 mm)

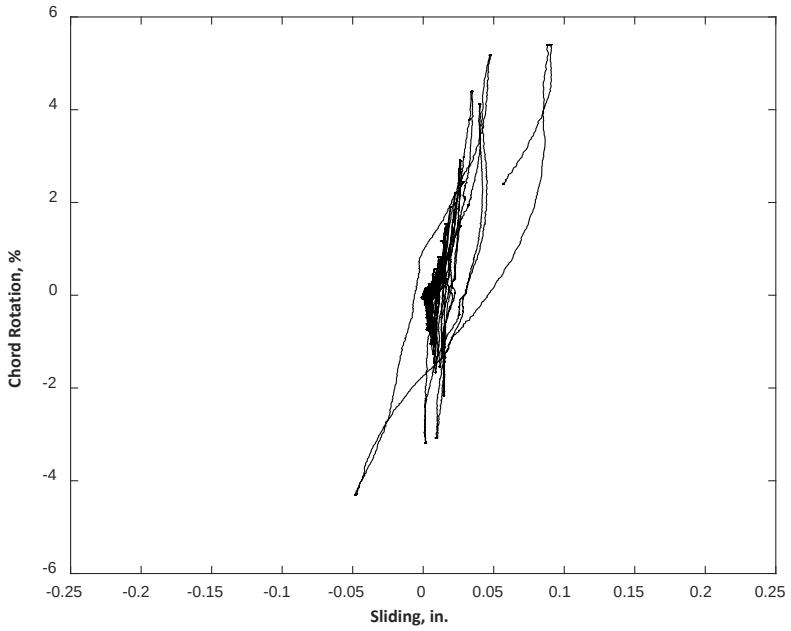

Figure C.34 – Calculated sliding at bottom for CB2 (1 in. = 25.4 mm)

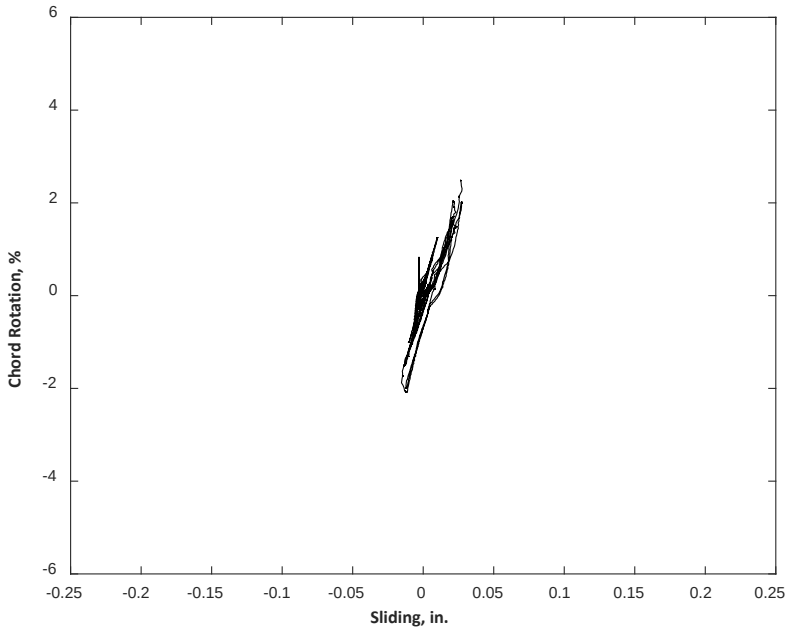

Figure C.35 – Calculated sliding at top for CB2D (1 in. = 25.4 mm)

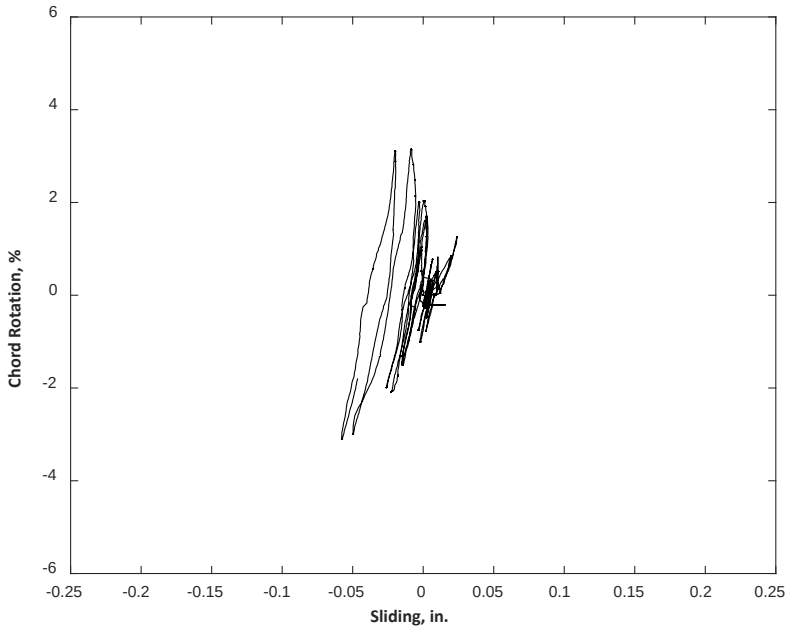

Figure C.36 – Calculated sliding at bottom for CB2D (1 in. = 25.4 mm)

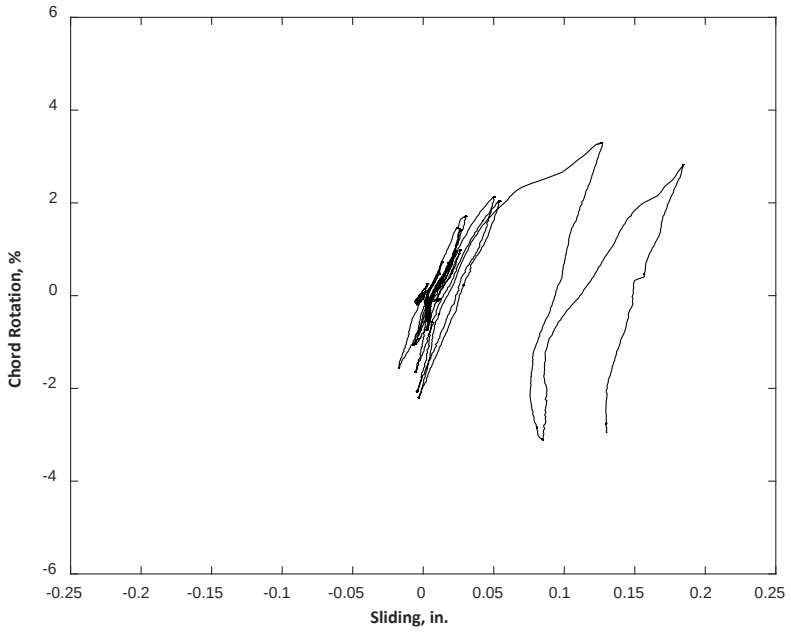

Figure C.37 – Calculated sliding at top for CB2AD (1 in. = 25.4 mm)

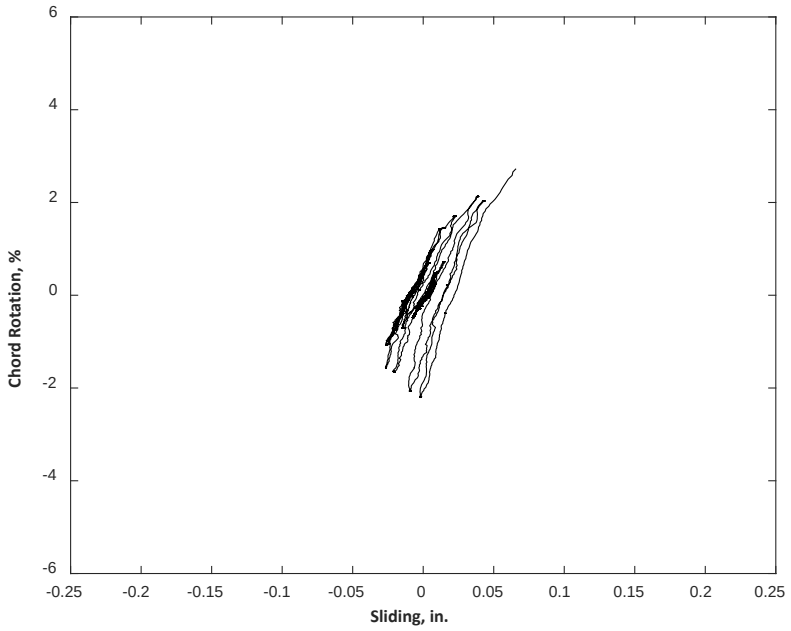

Figure C.38 – Calculated sliding at bottom for CB2AD (1 in. = 25.4 mm)

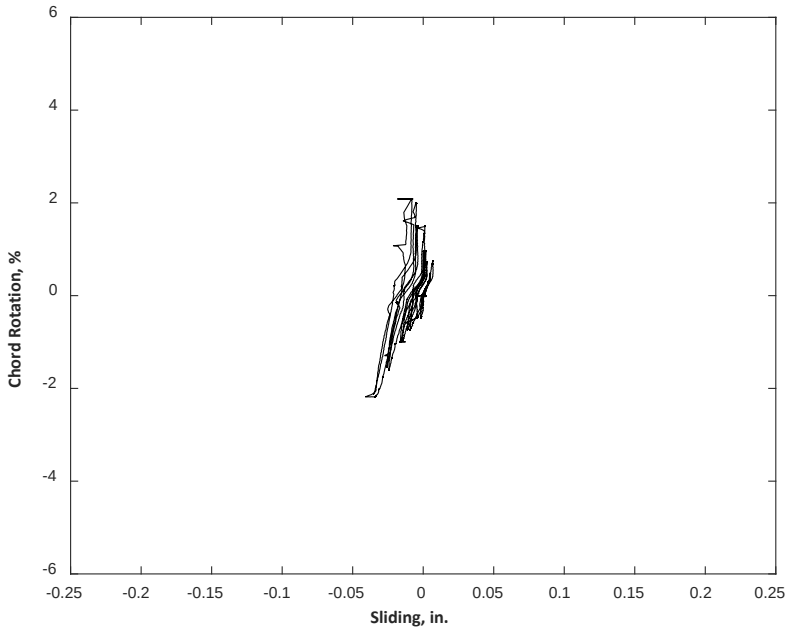

Figure C.39 – Calculated sliding at top for CB3D (1 in. = 25.4 mm)

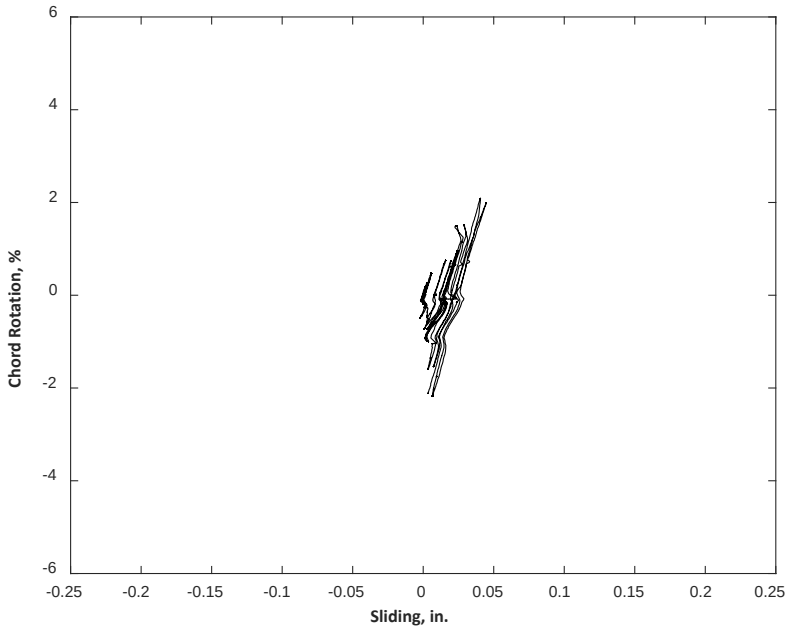

Figure C.40 – Calculated sliding at bottom for CB3D (1 in. = 25.4 mm)

APPENDIX D STRAIN MEASUREMENTS

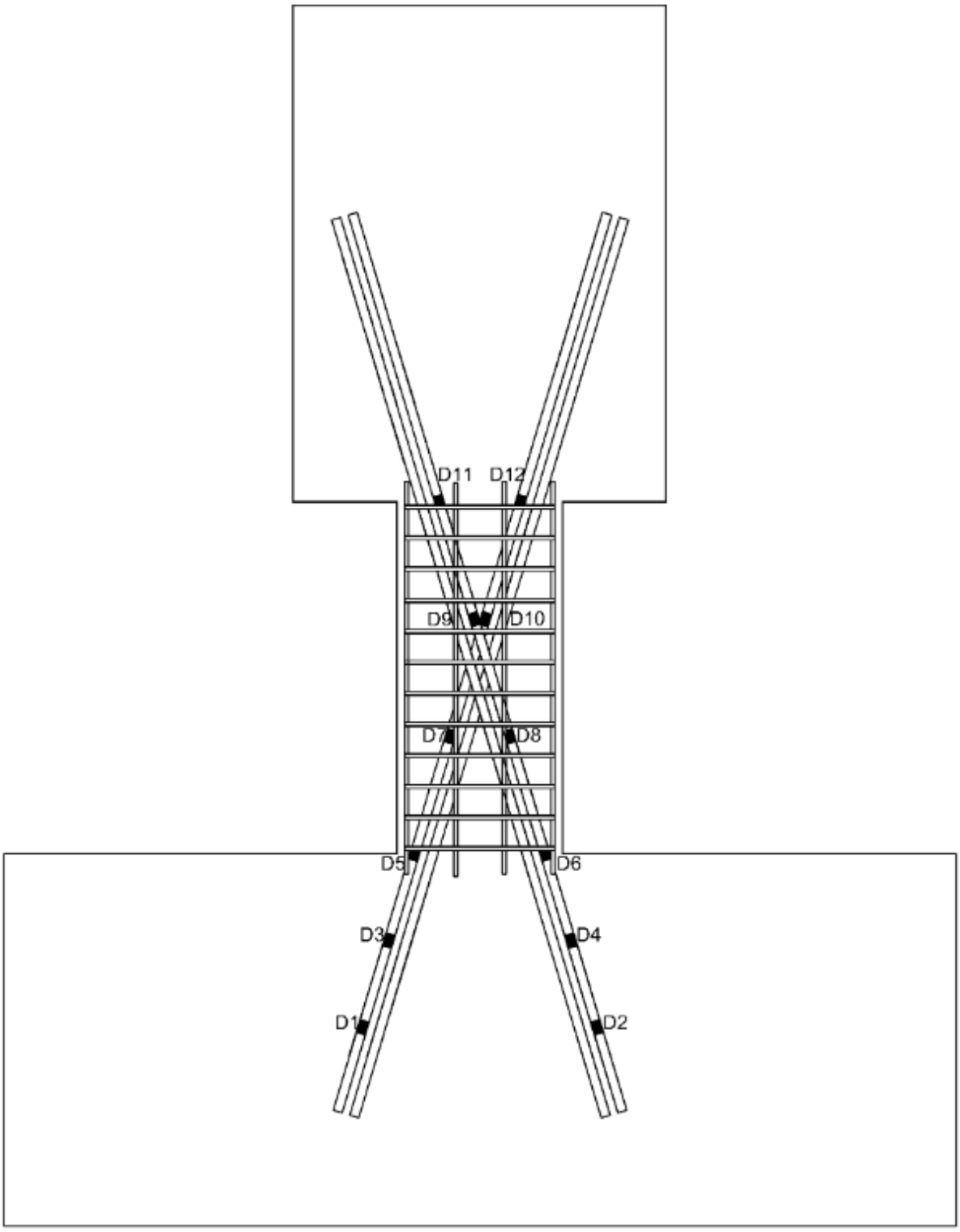

Figure D.1 – Location of strain gauges on diagonal bars

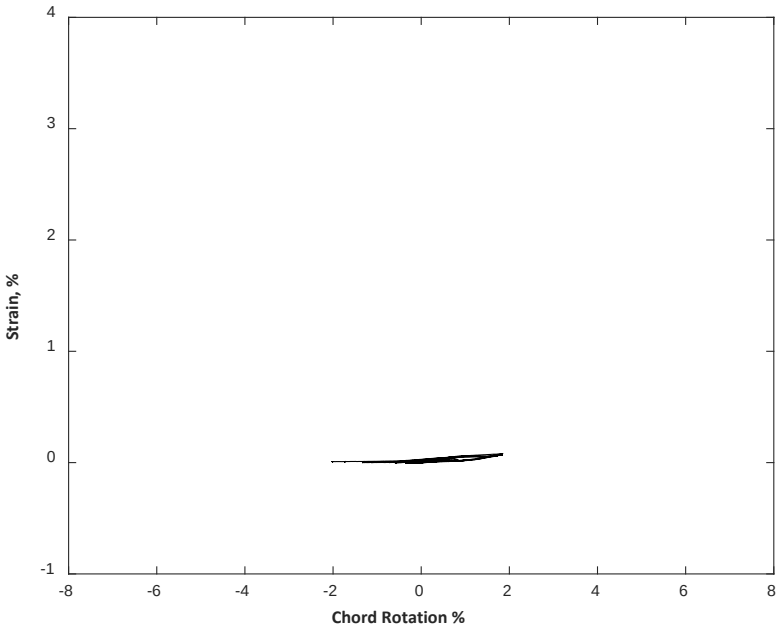

Figure D.2 – Strain measured with D1 for CB1

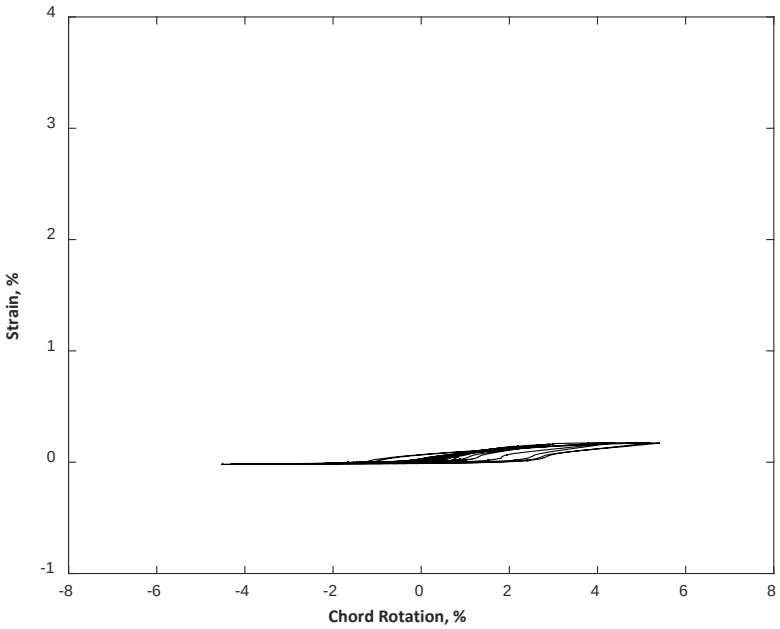

Figure D.3 – Strain measured with D1 for CB2

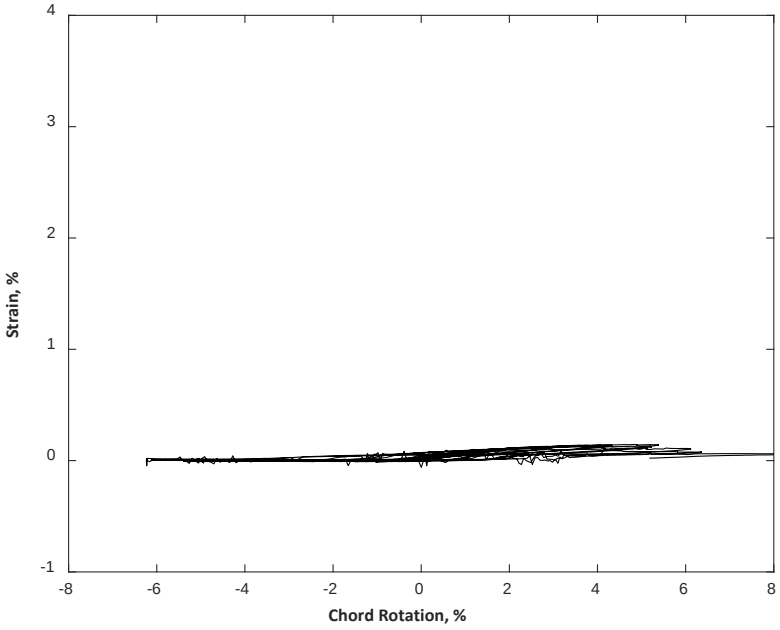

Figure D.4 – Strain measured with D1 for CB2D

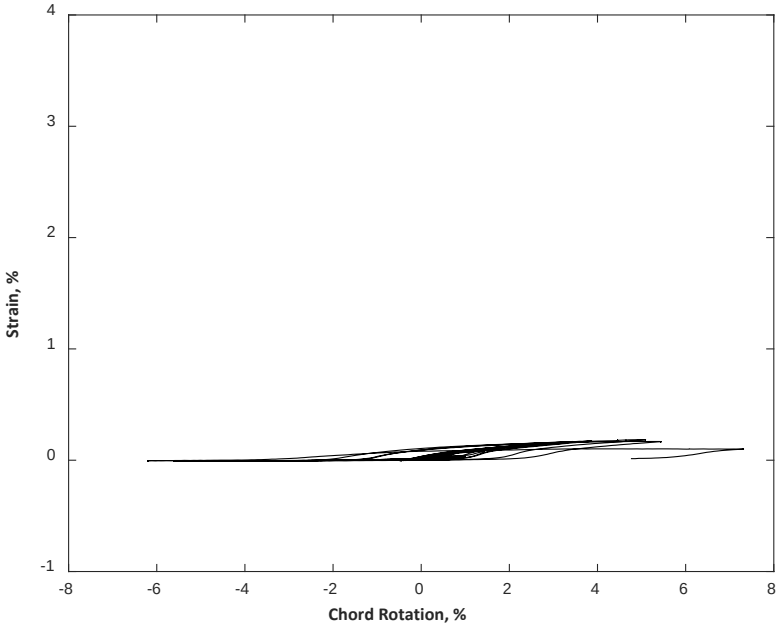

Figure D.5 – Strain measured with D1 for CB2AD

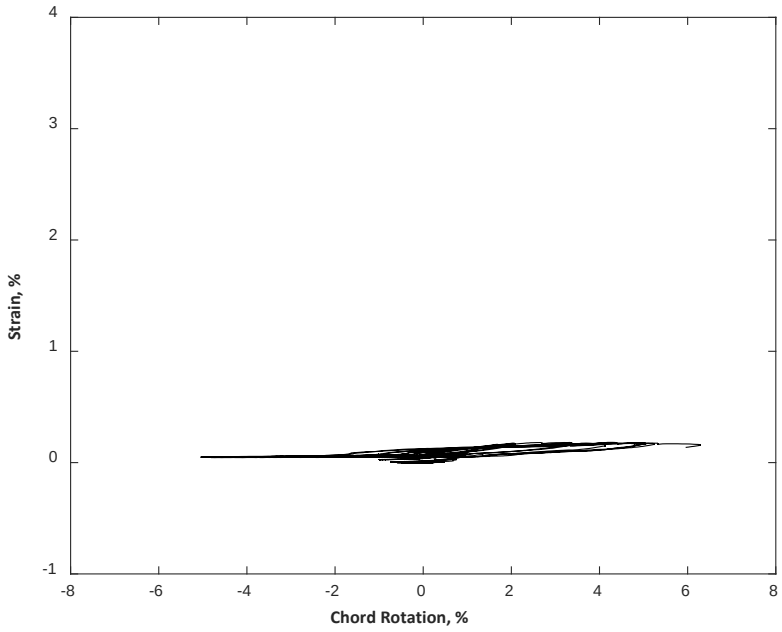

Figure D.6 – Strain measured with D1 for CB3D

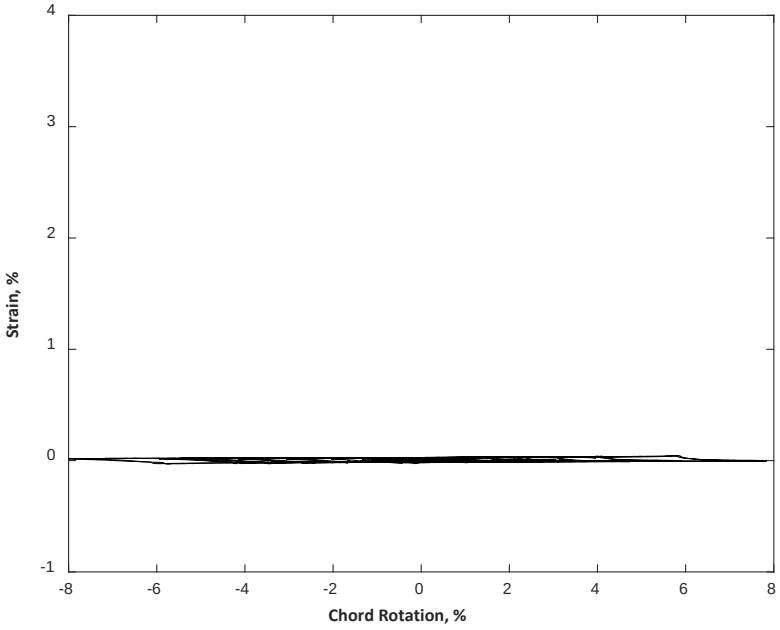

Figure D.7 – Strain measured with D2 for CB1

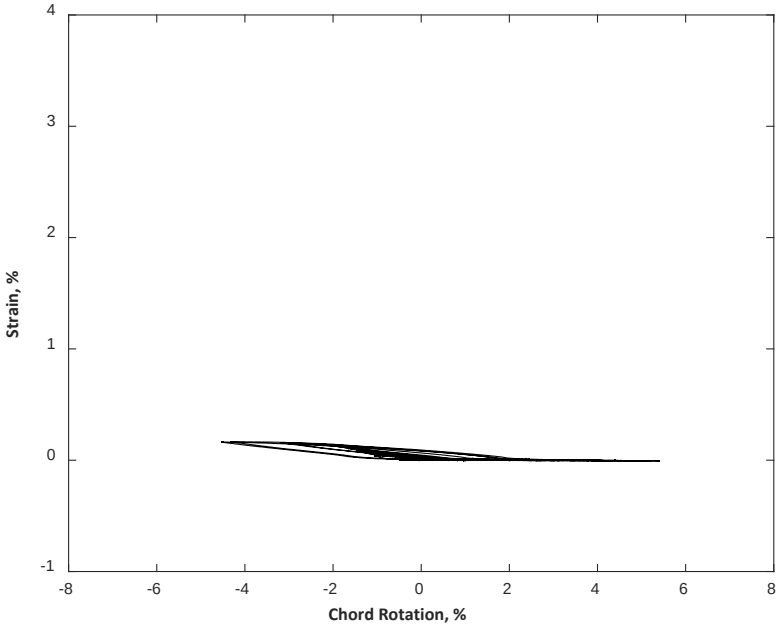

Figure D.8 – Strain measured with D2 for CB2

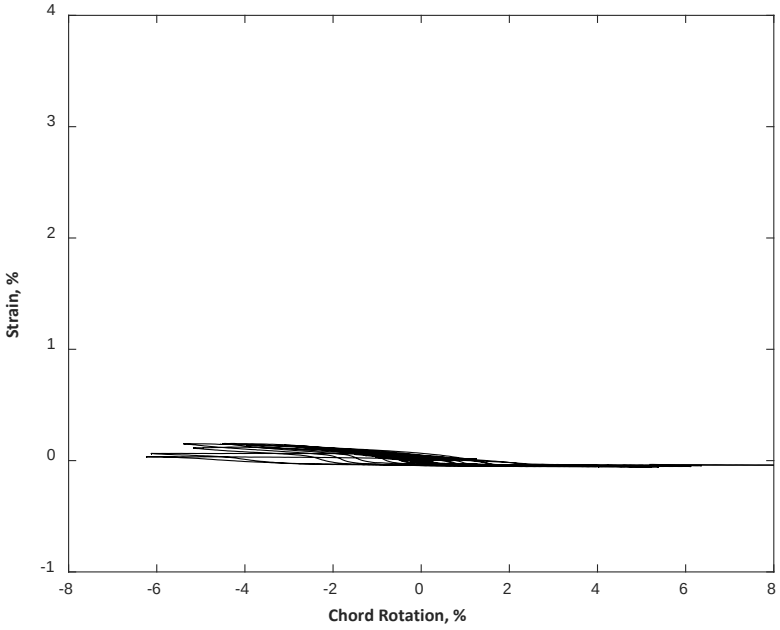

Figure D.9 – Strain measured with D2 for CB2D

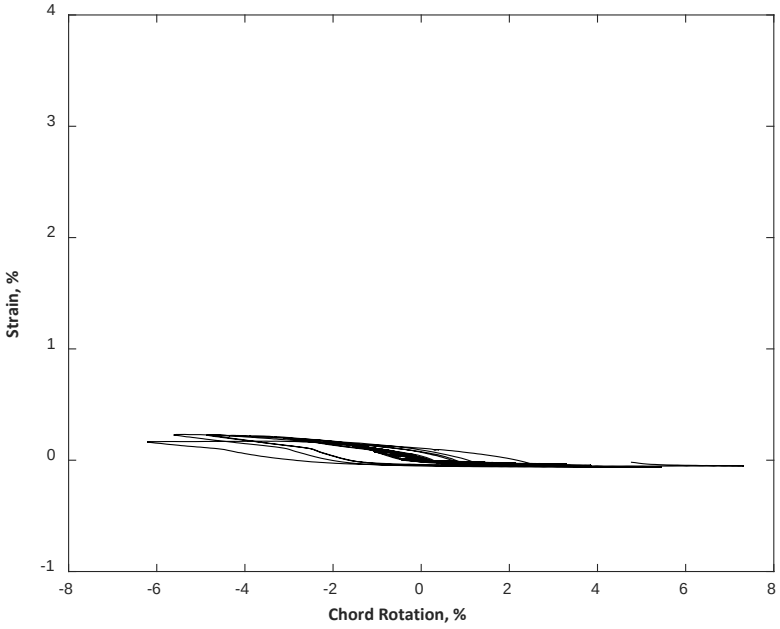

Figure D.10 – Strain measured with D2 for CB2AD

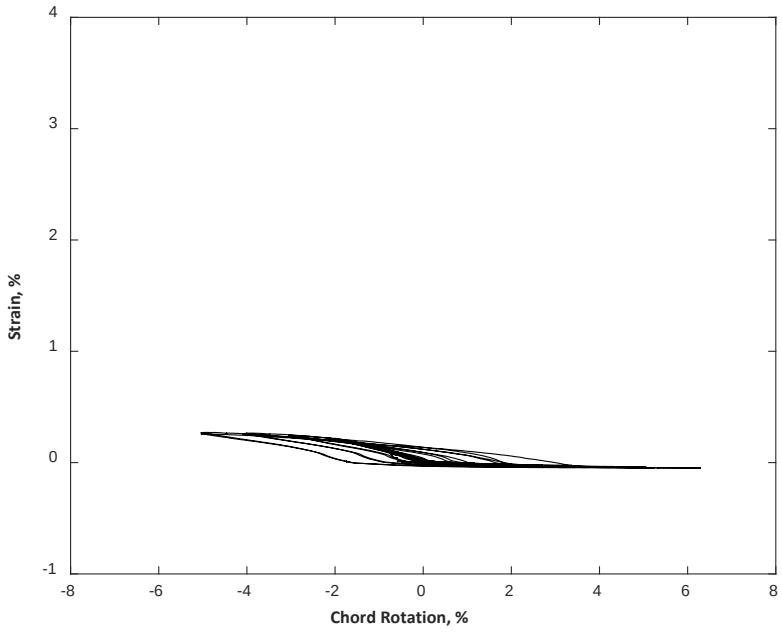

Figure D.11 – Strain measured with D2 for CB3D

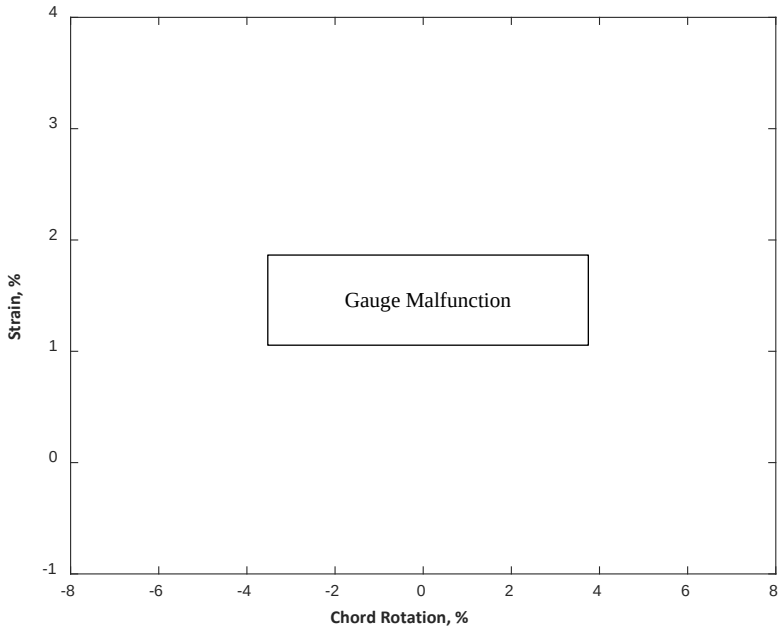

Figure D.12 – Strain measured with D3 for CB1

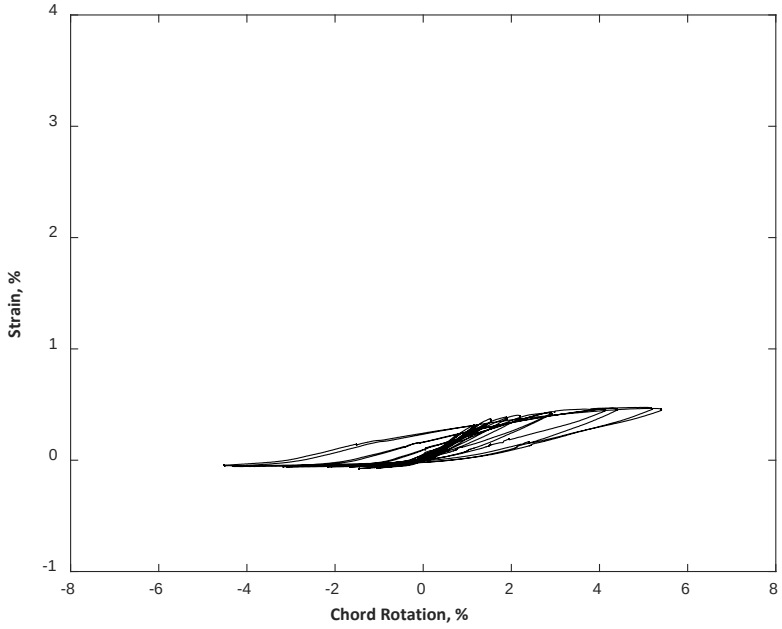

Figure D.13 – Strain measured with D3 for CB2

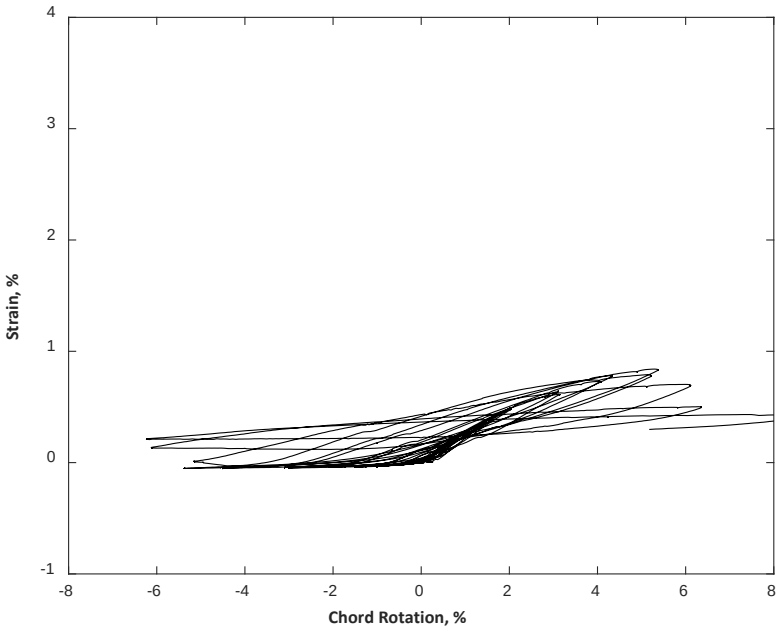

Figure D.14 – Strain measured with D3 for CB2D

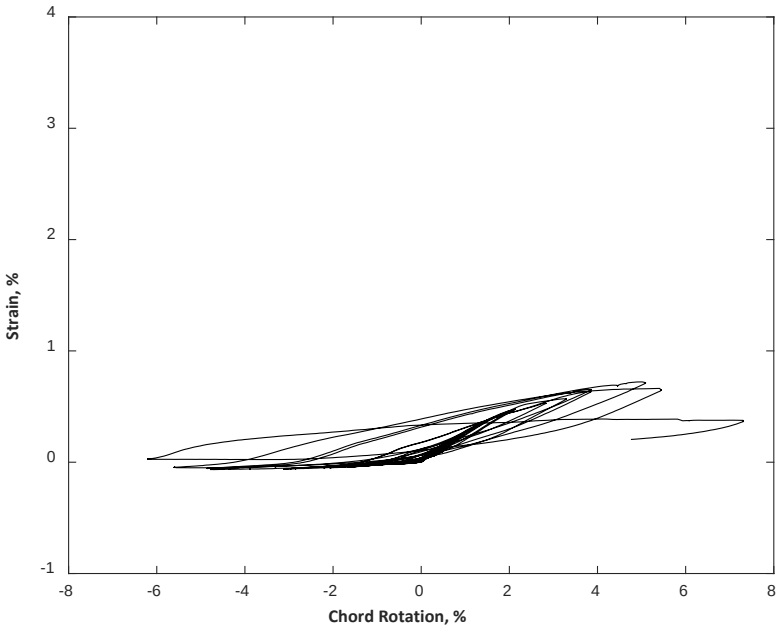

Figure D.15 – Strain measured with D3 for CB2AD

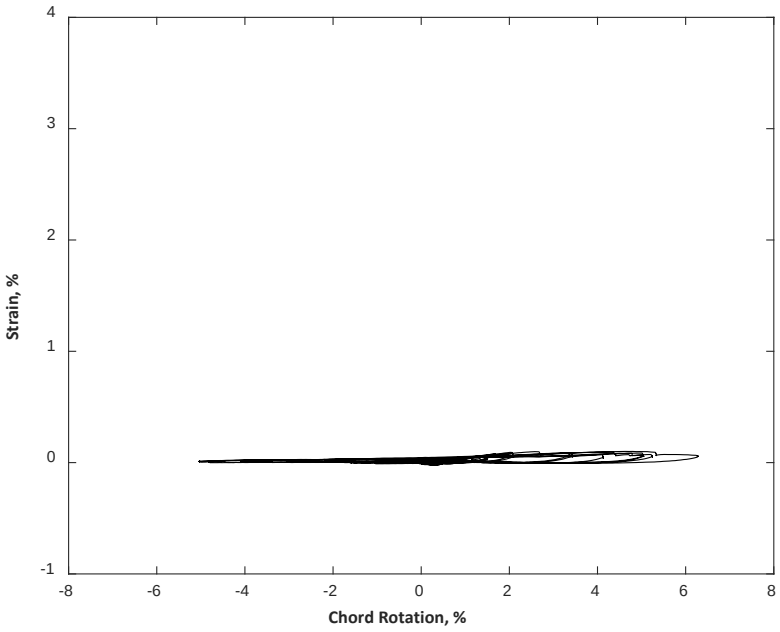

Figure D.16 – Strain measured with D3 for CB3D

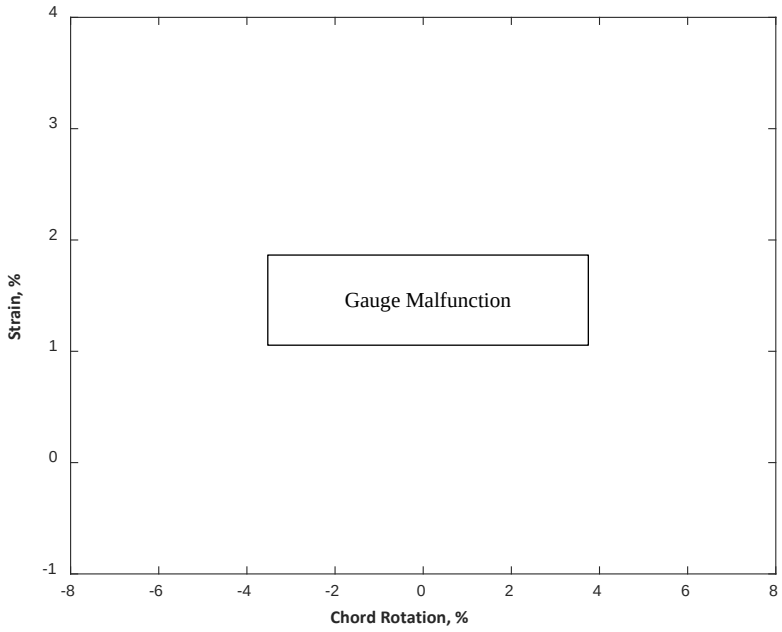

Figure D.17 – Strain measured with D4 for CB1

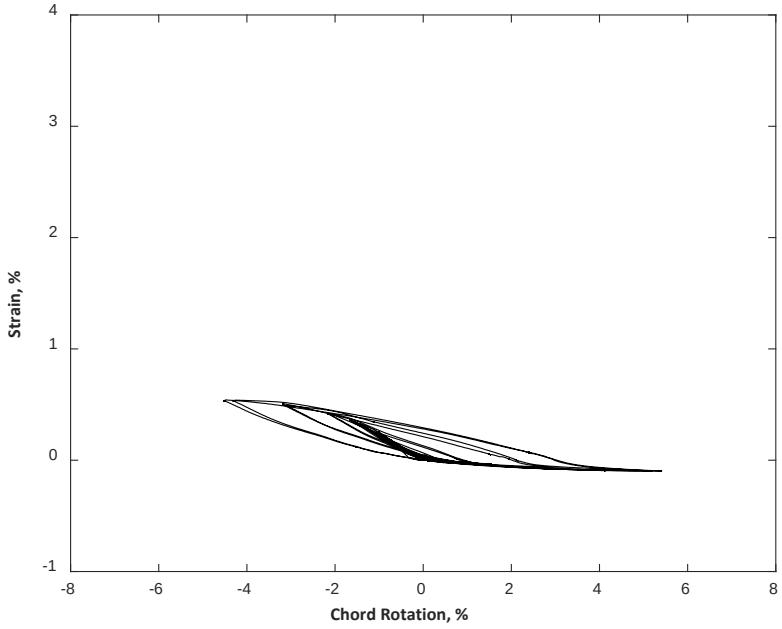

Figure D.18 – Strain measured with D4 for CB2

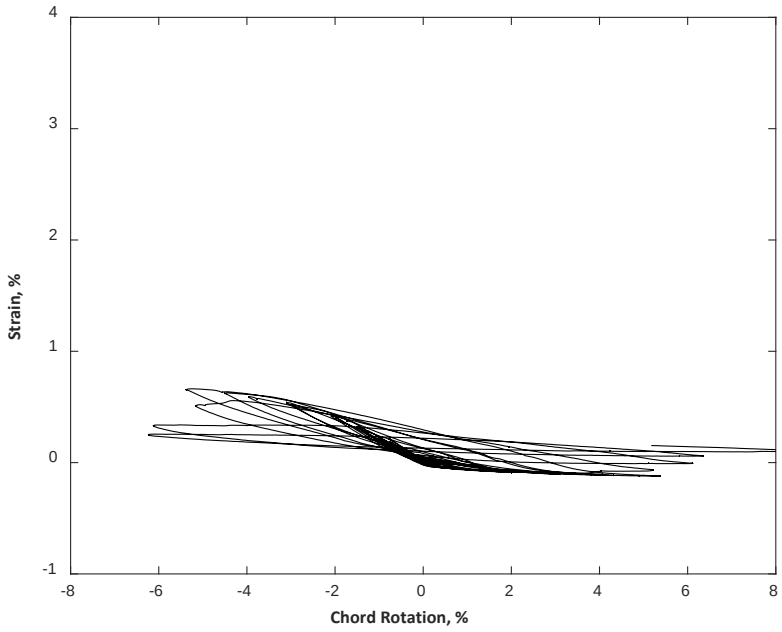

Figure D.19 – Strain measured with D4 for CB2D

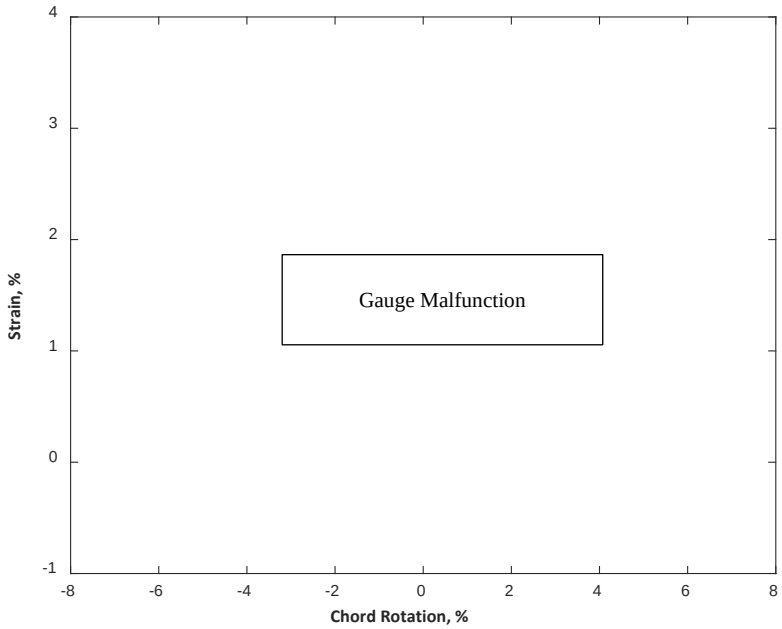

Figure D.20 – Strain measured with D4 for CB2AD

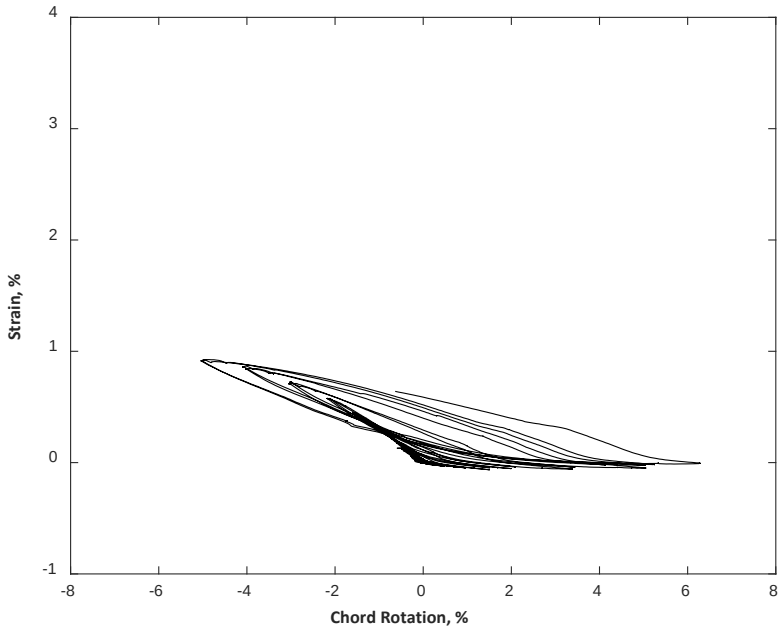

Figure D.21 – Strain measured with D4 for CB3D

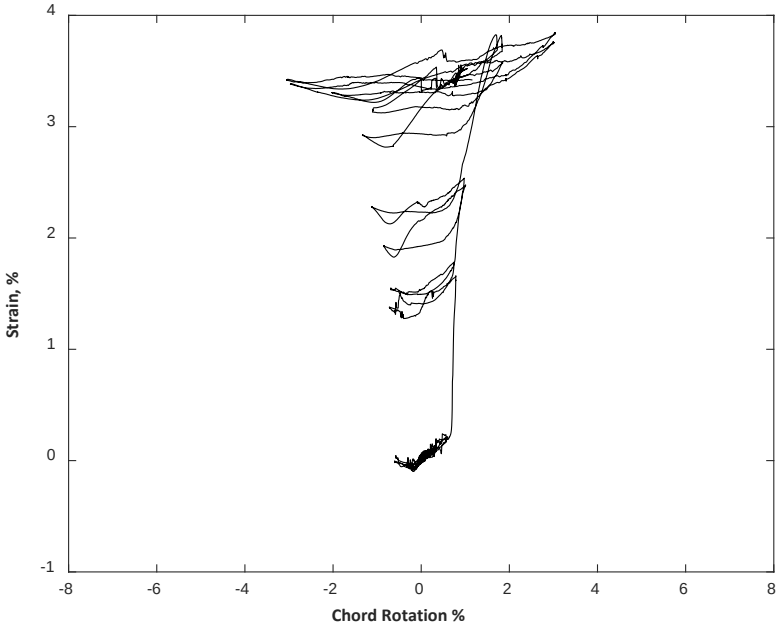

Figure D.22 – Strain measured with D5 for CB1

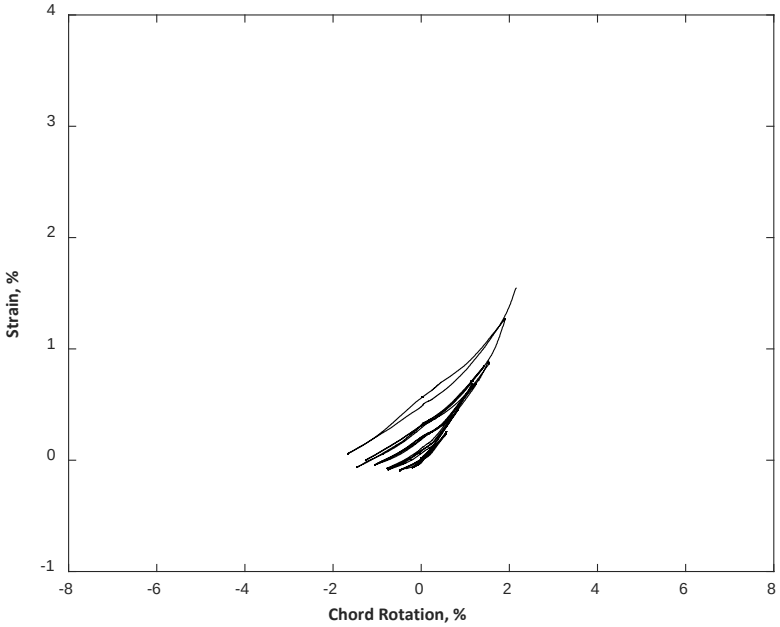

Figure D.23 – Strain measured with D5 for CB2

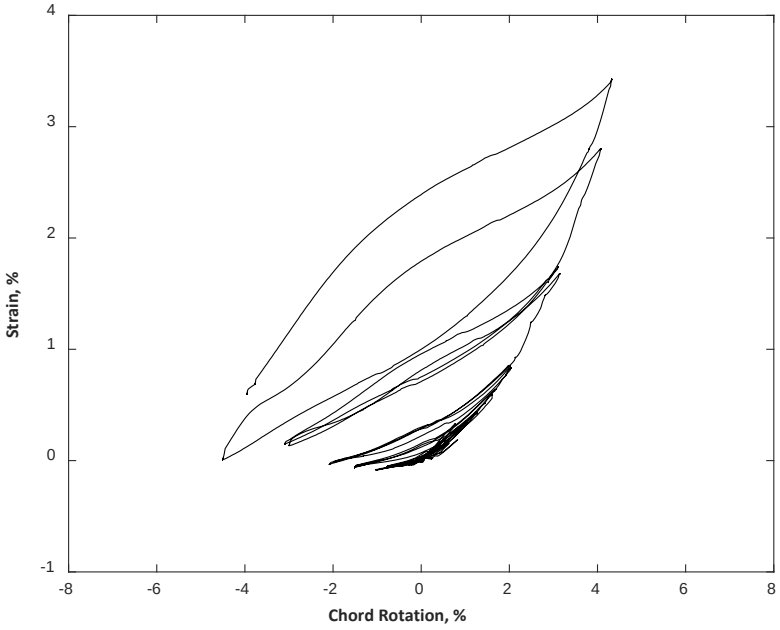

Figure D.24 – Strain measured with D5 for CB2D

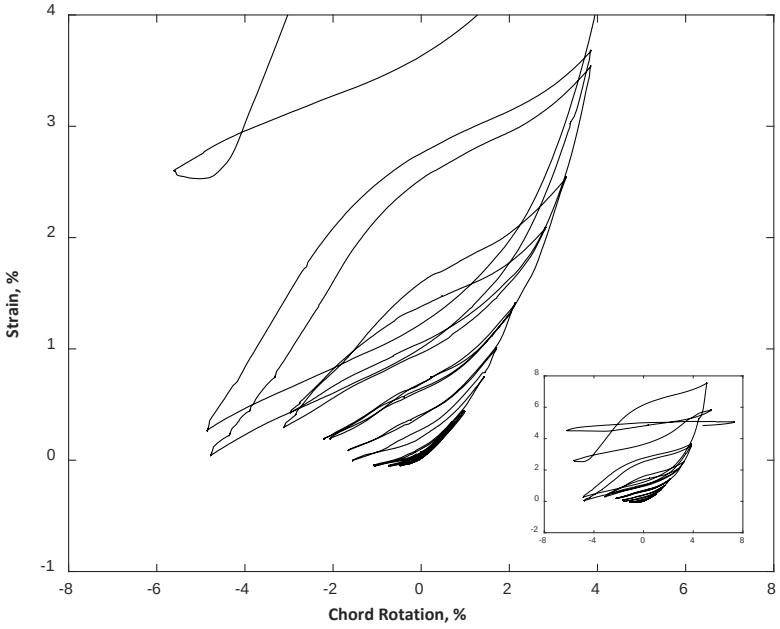

Figure D.25 – Strain measured with D5 for CB2AD

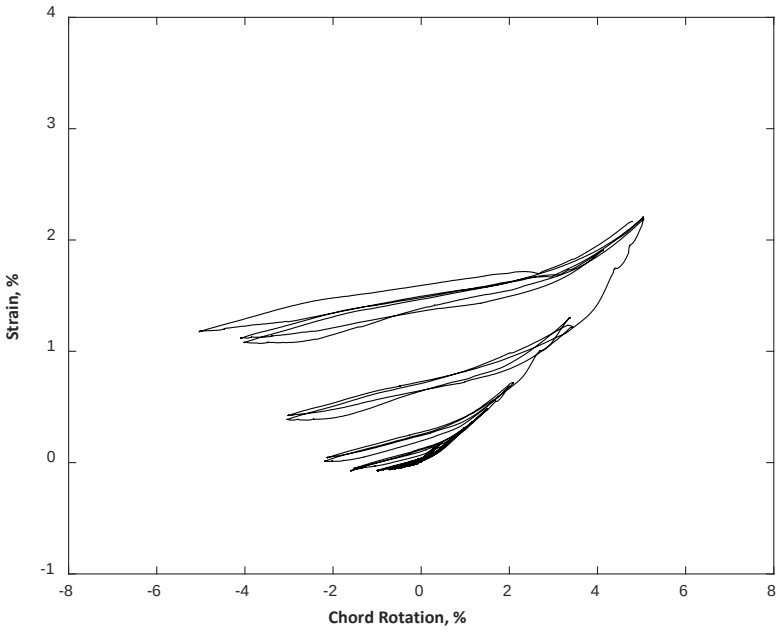

Figure D.26 – Strain measured with D5 for CB3D

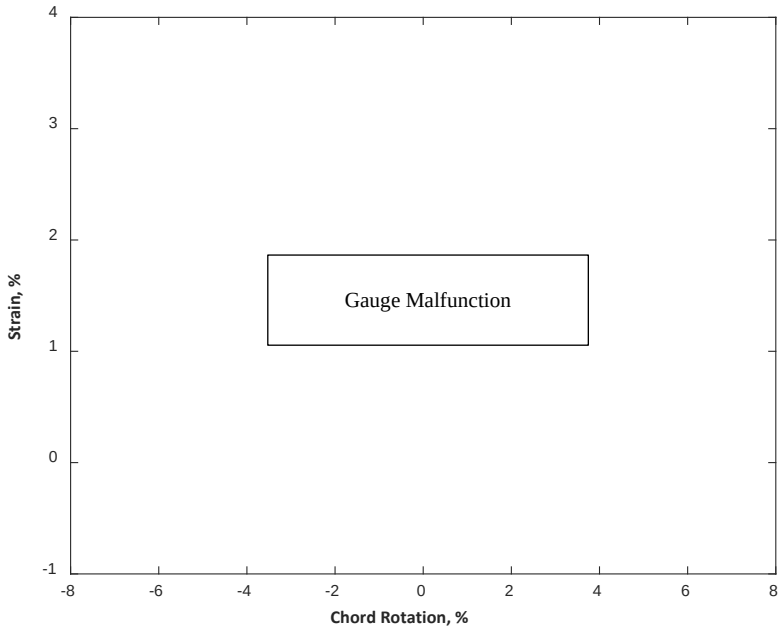

Figure D.27 – Strain measured with D6 for CB1

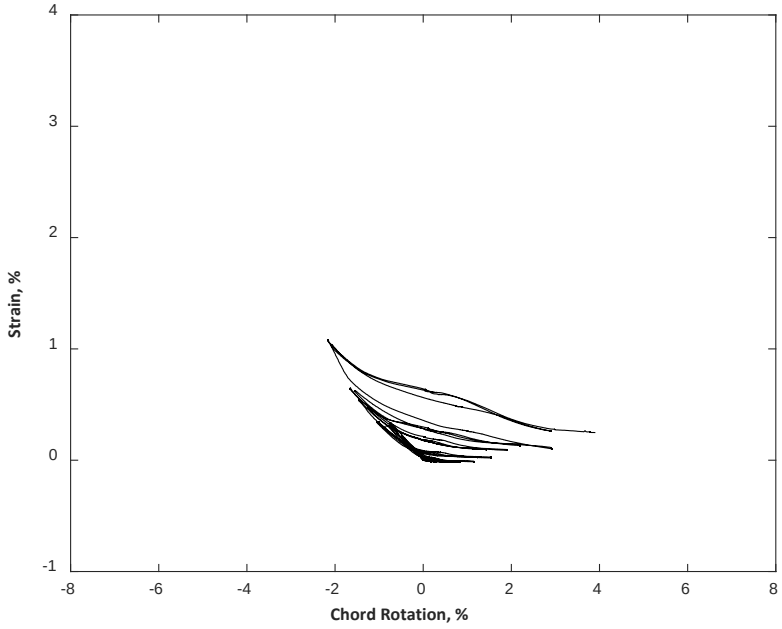

Figure D.28 – Strain measured with D6 for CB2

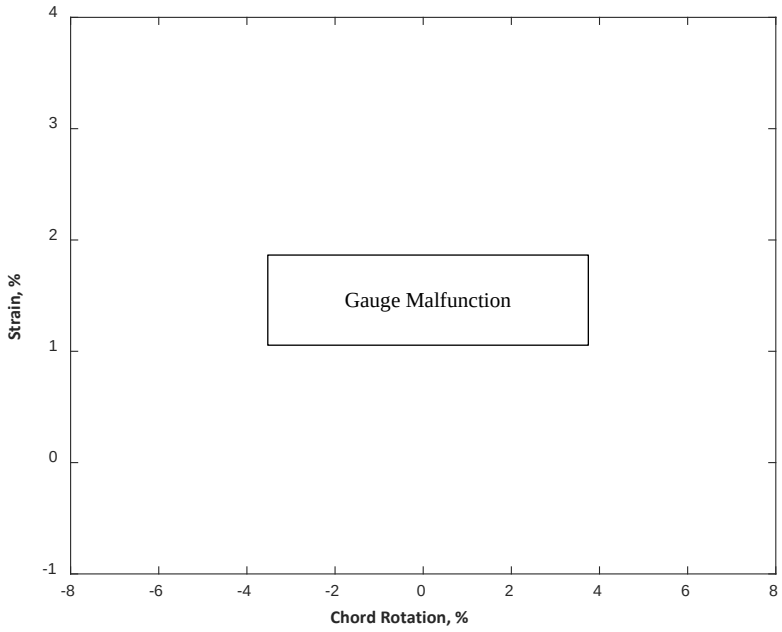

Figure D.29 – Strain measured with D6 for CB2D

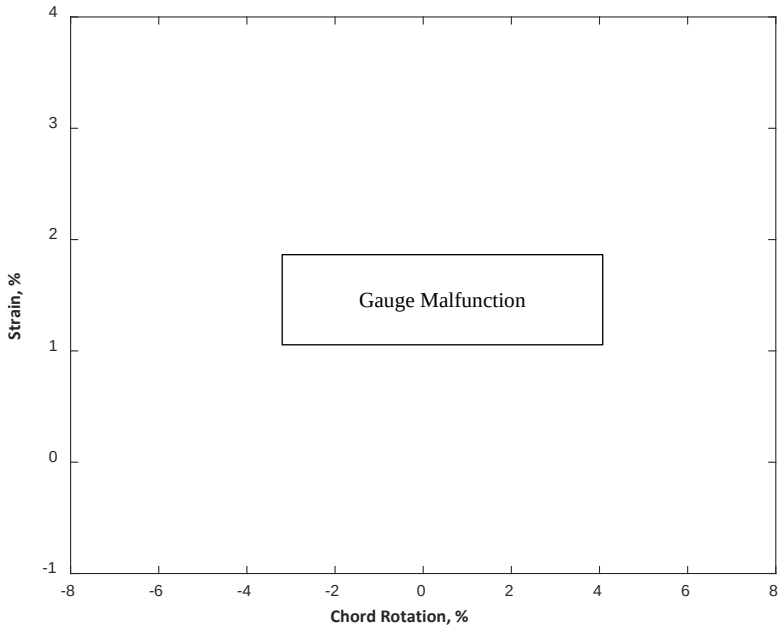

Figure D.30 – Strain measured with D6 for CB2AD

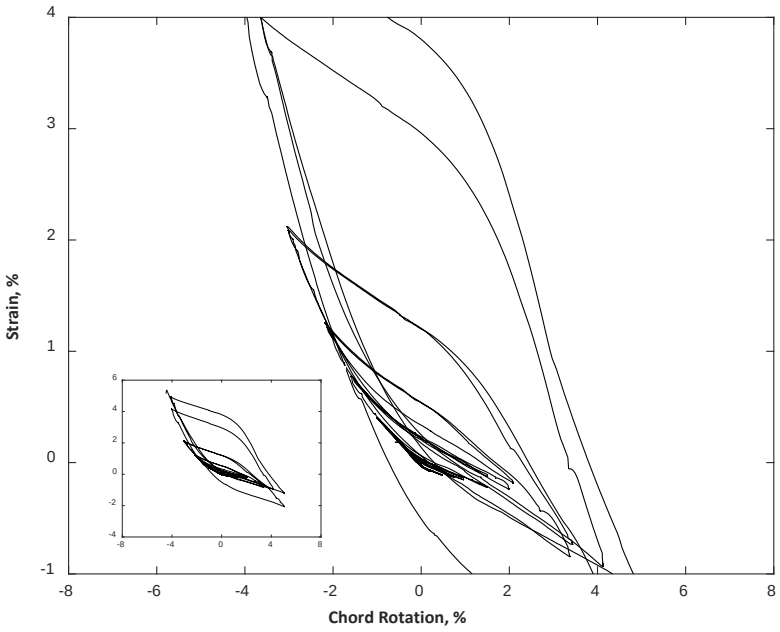

Figure D.31 – Strain measured with D6 for CB3D

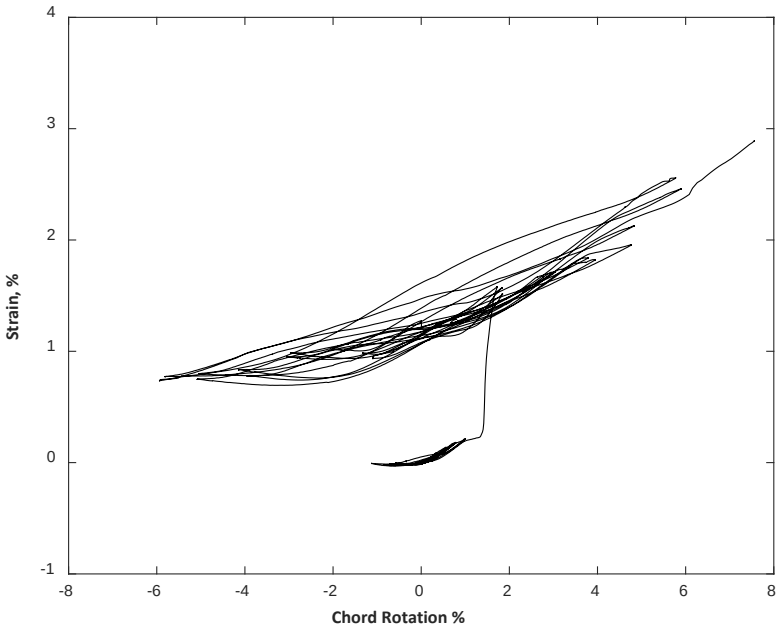

Figure D.32 – Strain measured with D7 for CB1

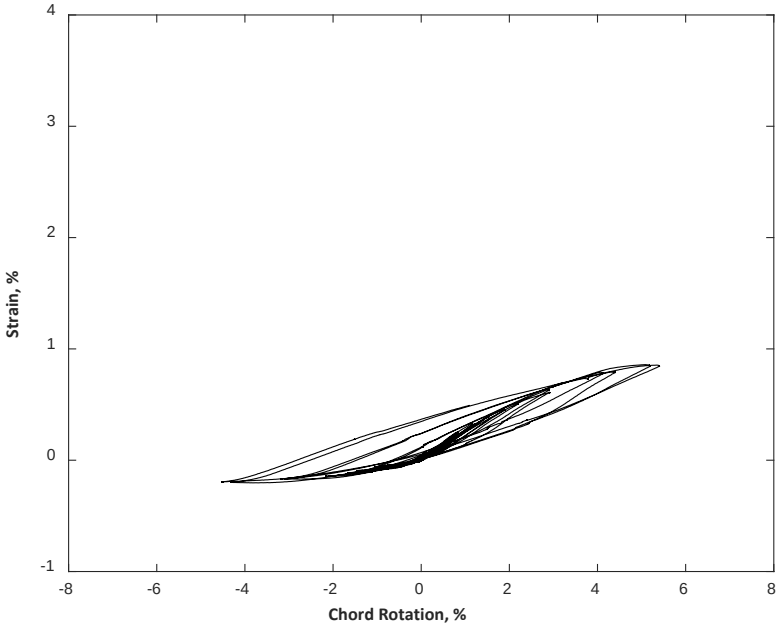

Figure D.33 – Strain measured with D7 for CB2

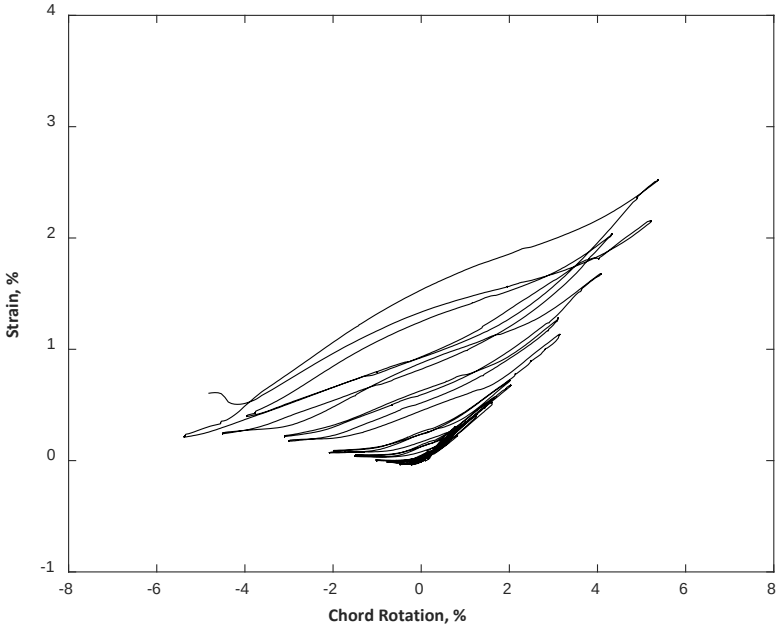

Figure D.34 – Strain measured with D7 for CB2D

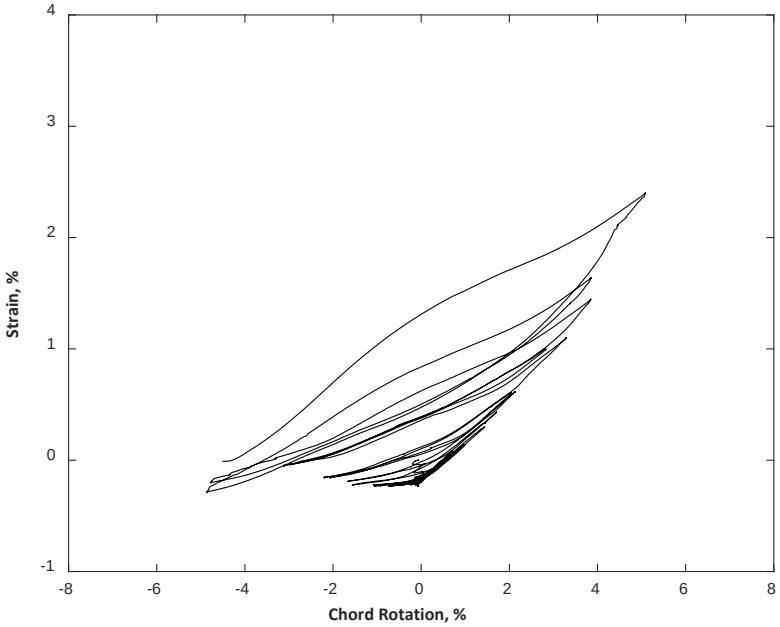

Figure D.35 – Strain measured with D7 for CB2AD

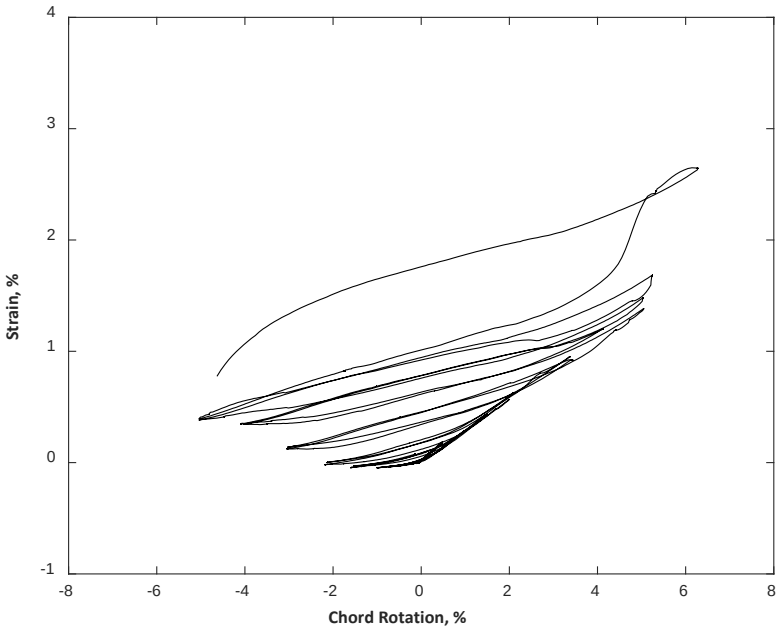

Figure D.36 – Strain measured with D7 for CB3D

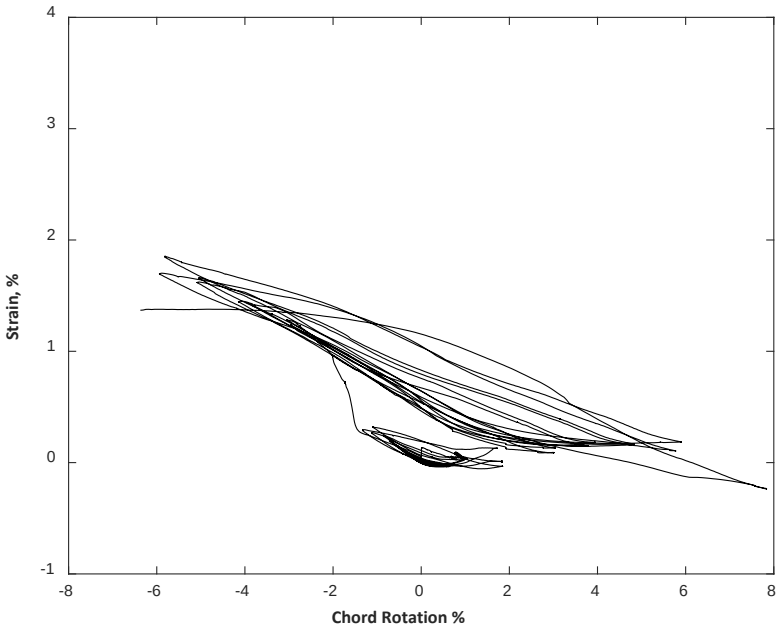

Figure D.37 – Strain measured with D8 for CB1

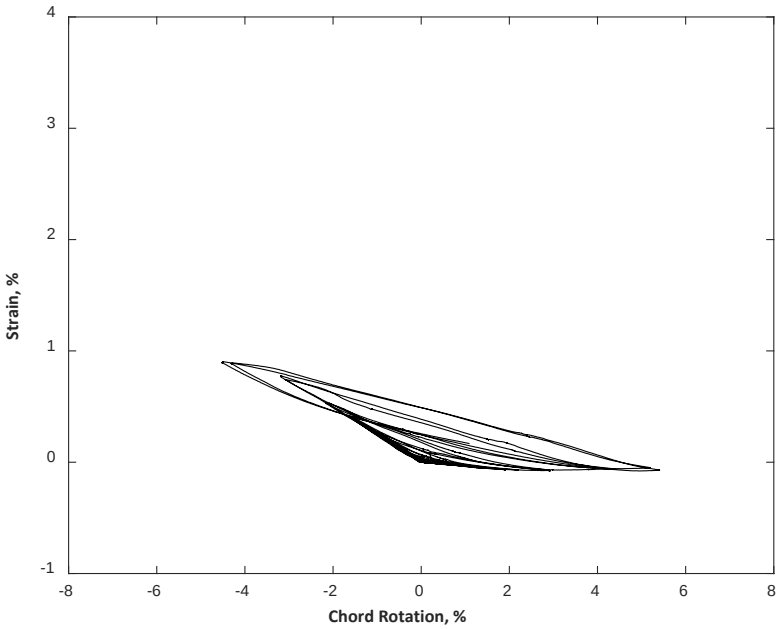

Figure D.38 – Strain measured with D8 for CB2

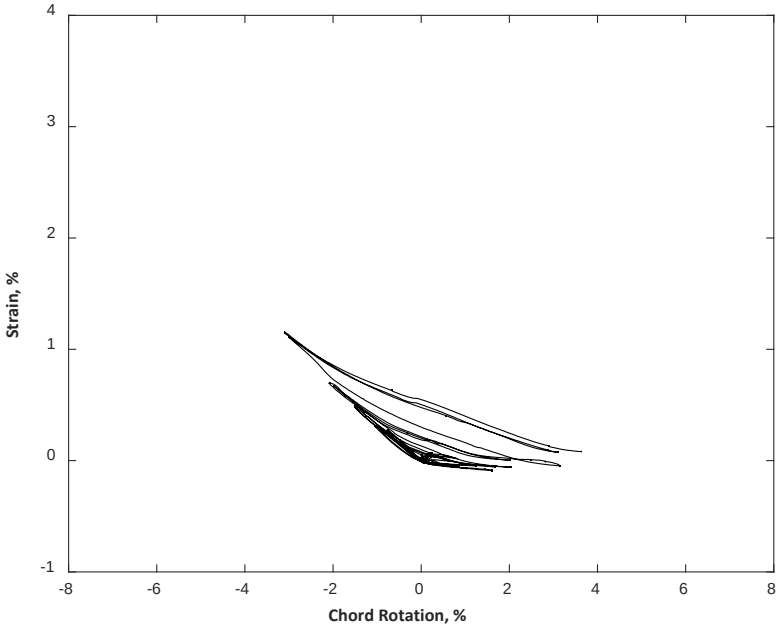

Figure D.39 – Strain measured with D8 for CB2D

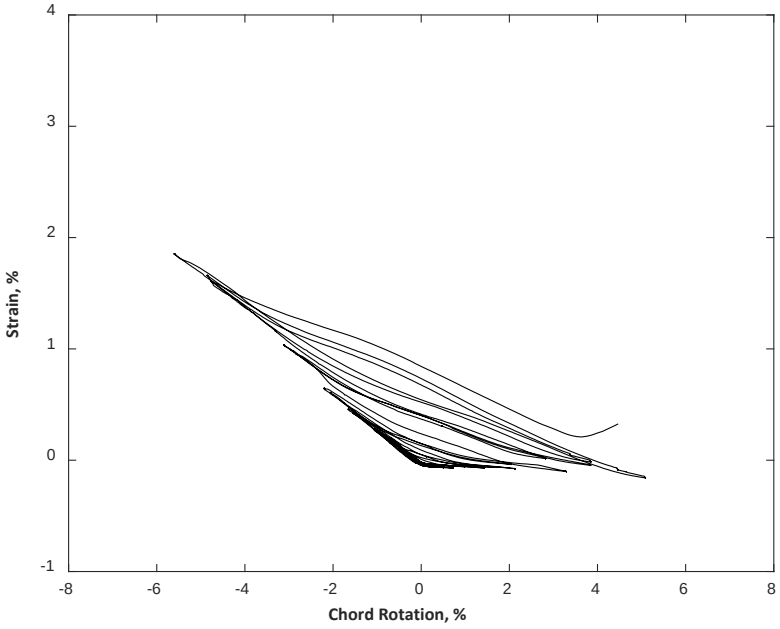

Figure D.40 – Strain measured with D8 for CB2AD

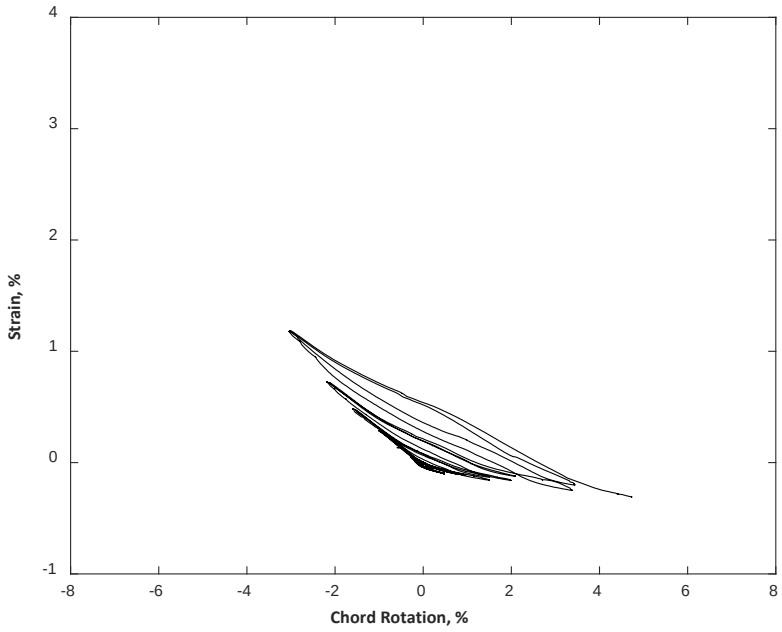

Figure D.41 – Strain measured with D8 for CB3D

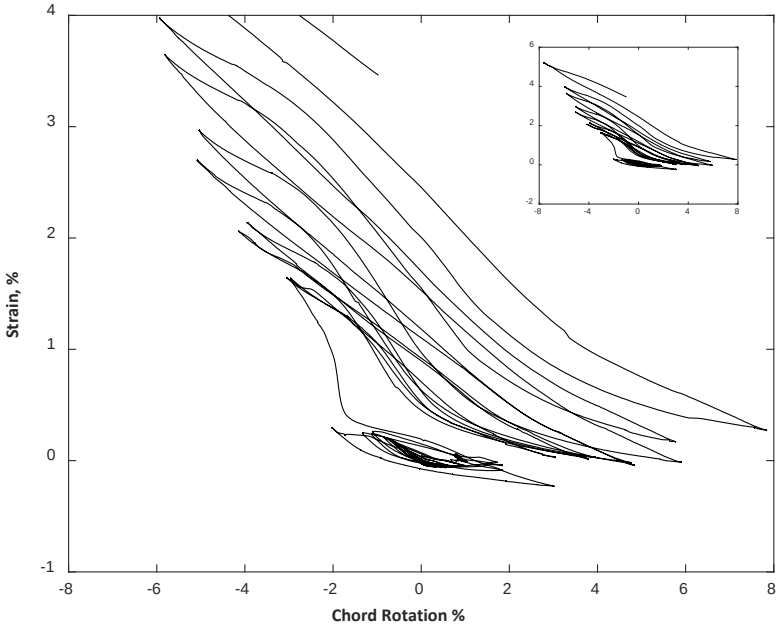

Figure D.42 – Strain measured with D9 for CB1

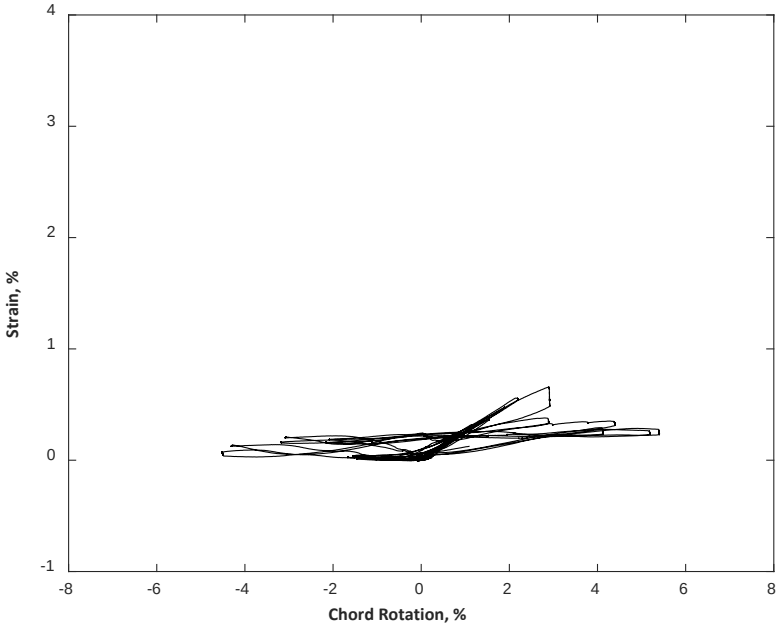

Figure D.43 – Strain measured with D9 for CB2

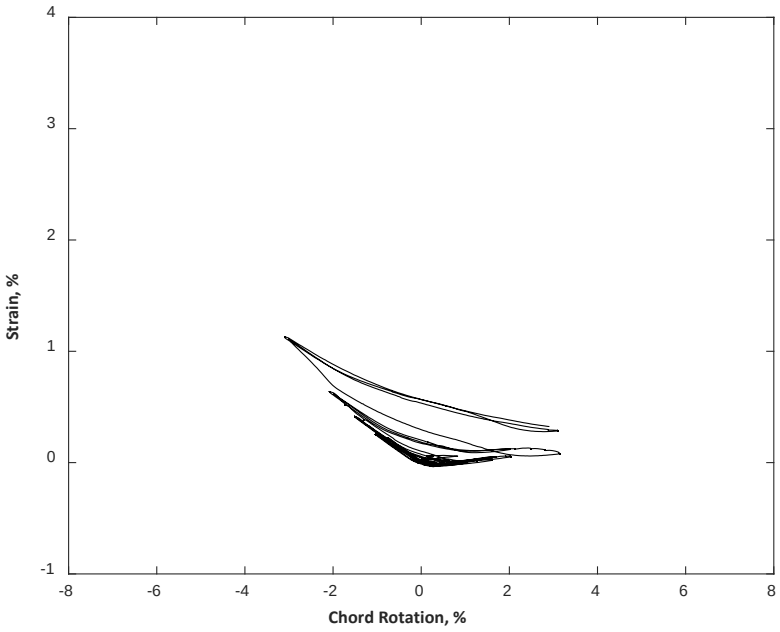

Figure D.44 – Strain measured with D9 for CB2D

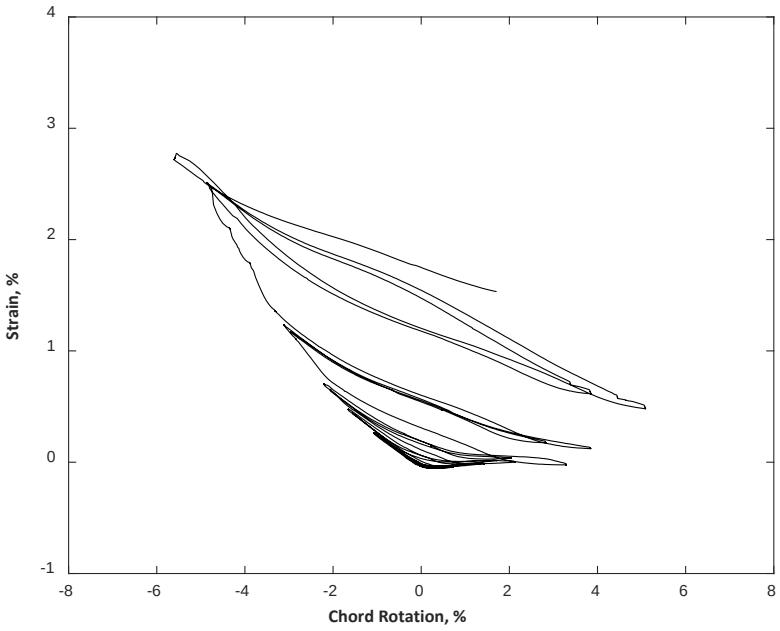

Figure D.45 – Strain measured with D9 for CB2AD

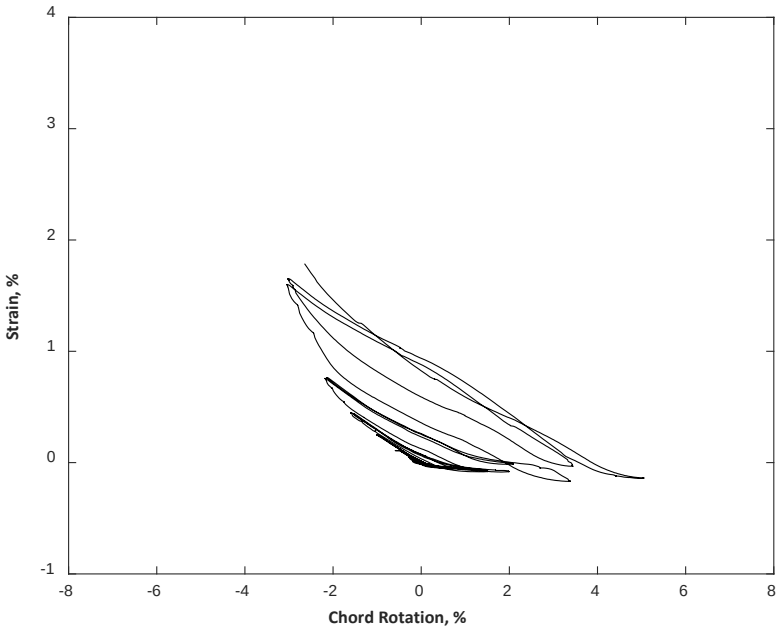

Figure D.46 – Strain measured with D9 for CB3D

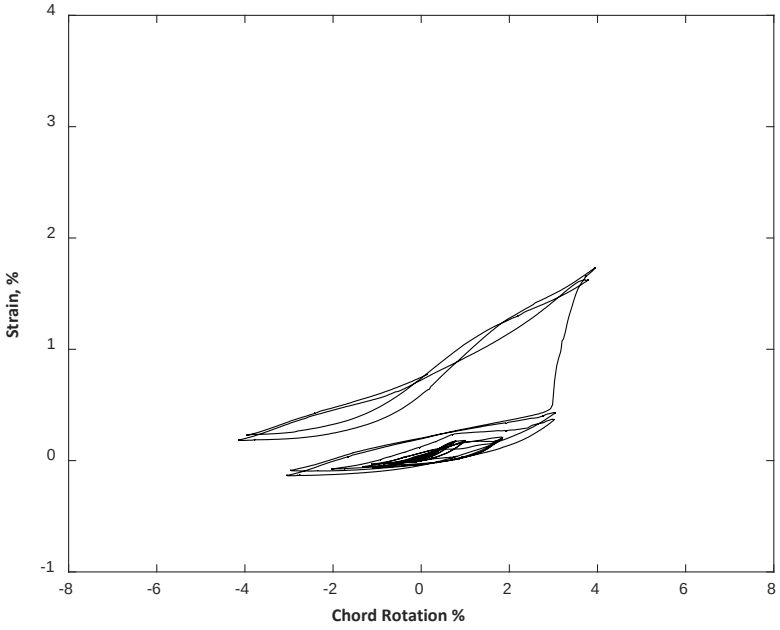

Figure D.47 – Strain measured with D10 for CB1

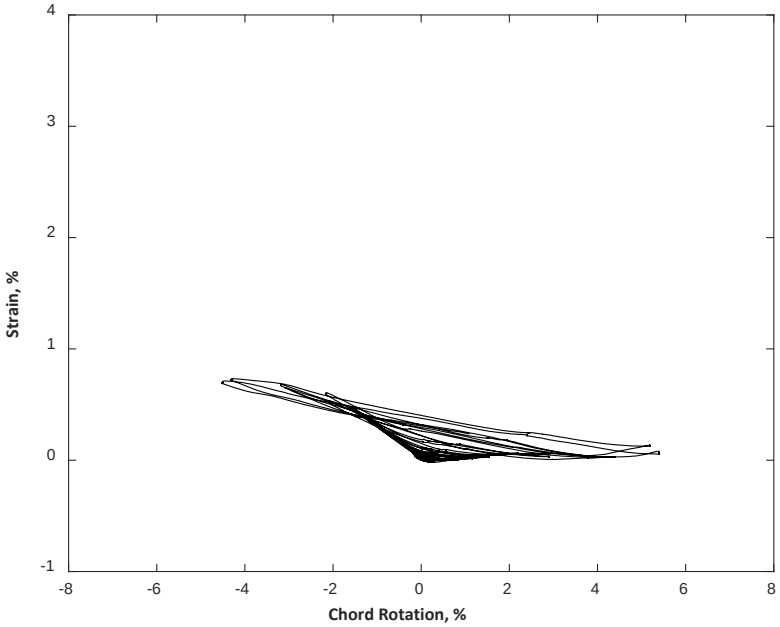

Figure D.48 – Strain measured with D10 for CB2

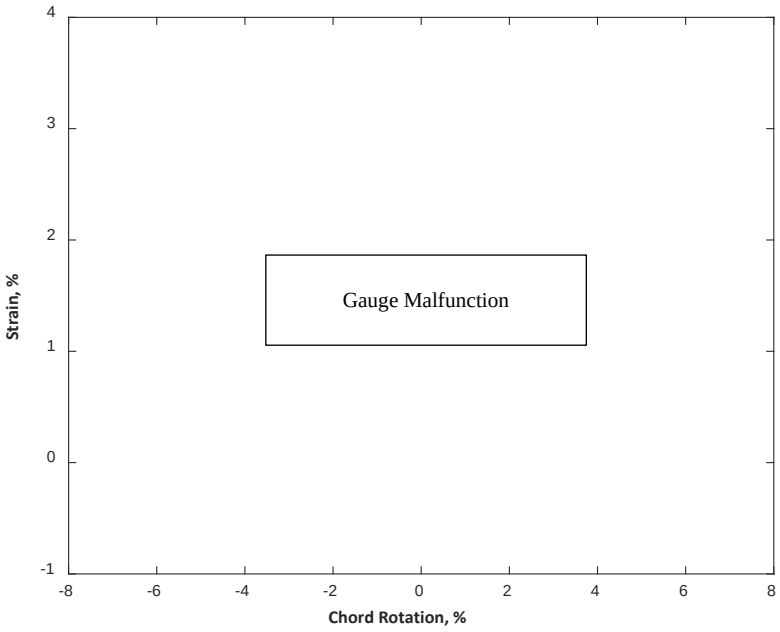

Figure D.49 – Strain measured with D10 for CB2D

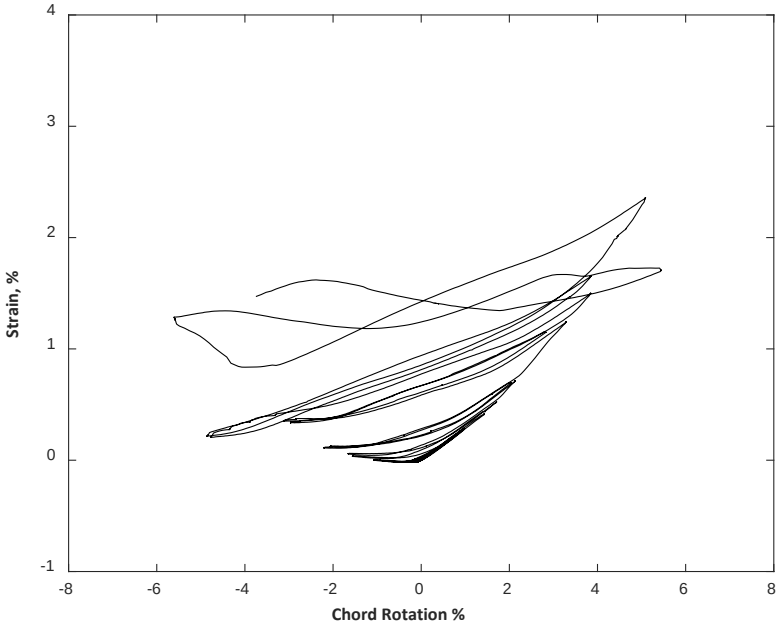

Figure D.50 – Strain measured with D10 for CB2AD

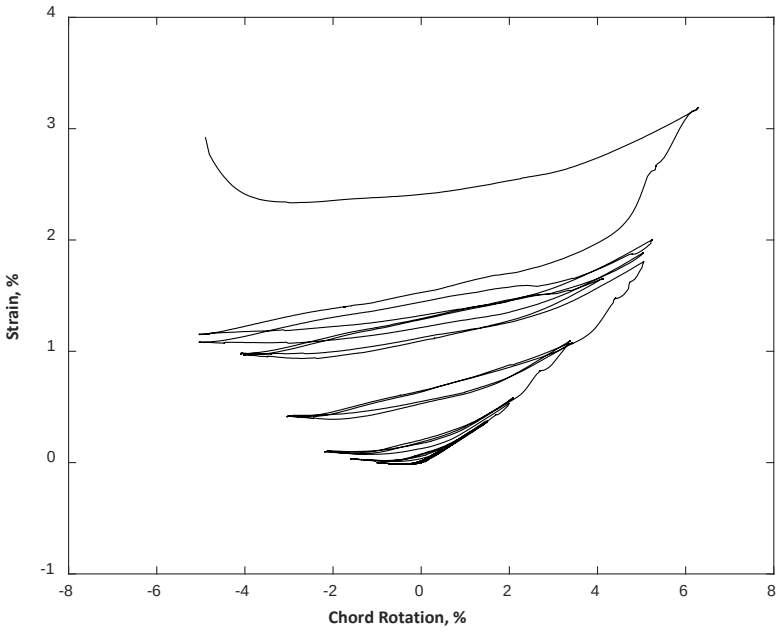

Figure D.51 – Strain measured with D10 for CB3D

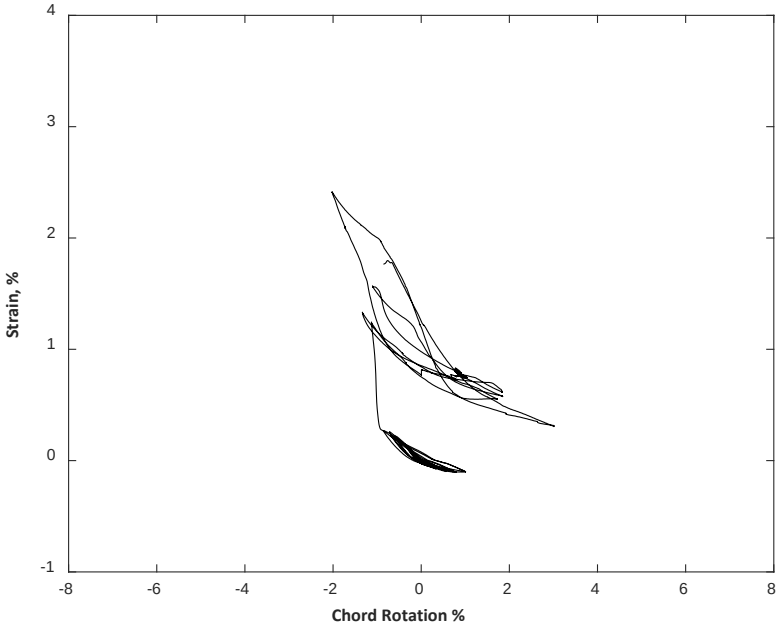

Figure D.52 – Strain measured with D11 for CB1

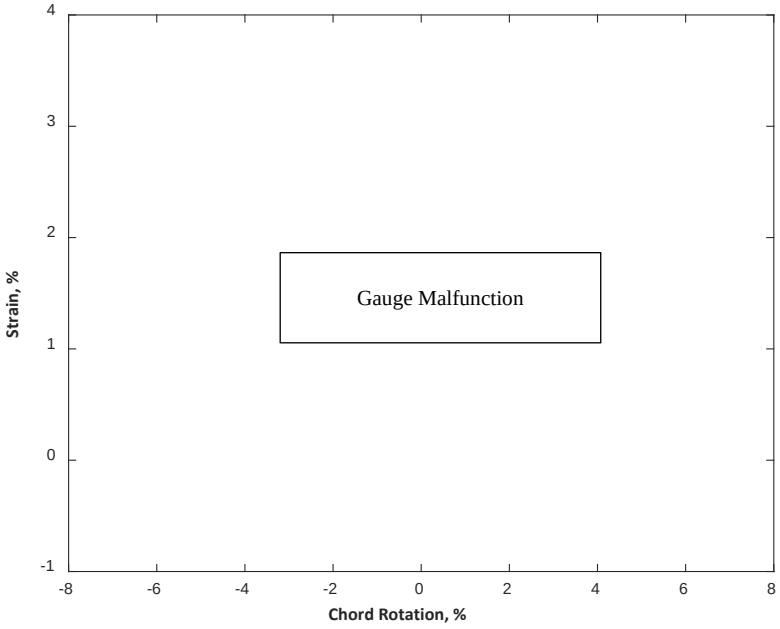

Figure D.53 – Strain measured with D11 for CB2

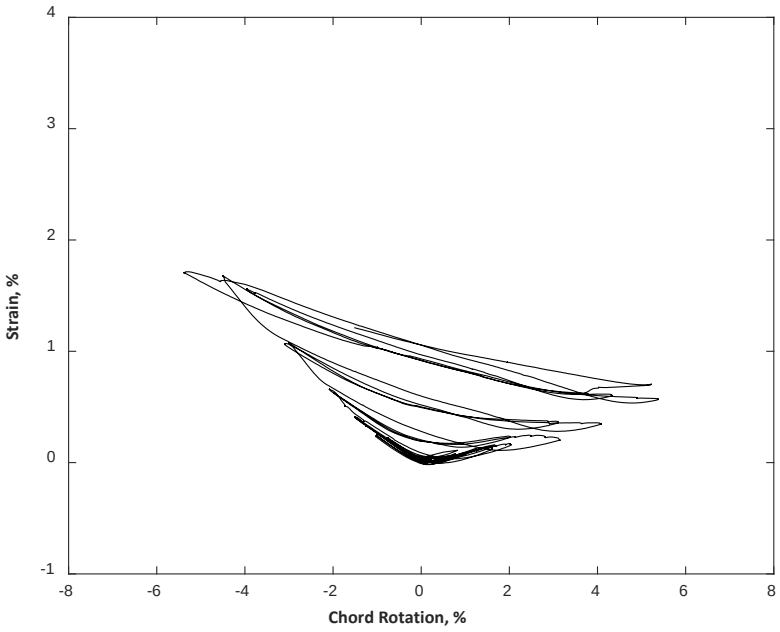

Figure D.54 – Strain measured with D11 for CB2D

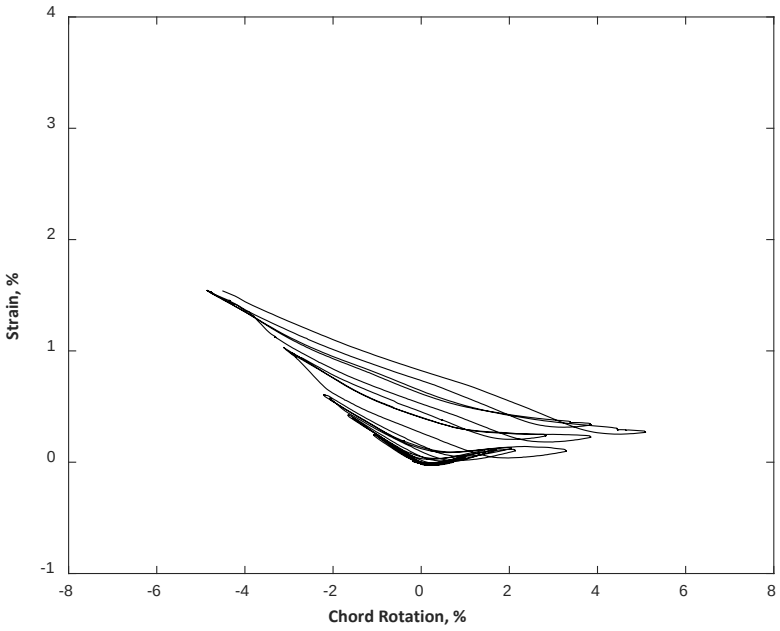

Figure D.55 – Strain measured with D11 for CB2AD

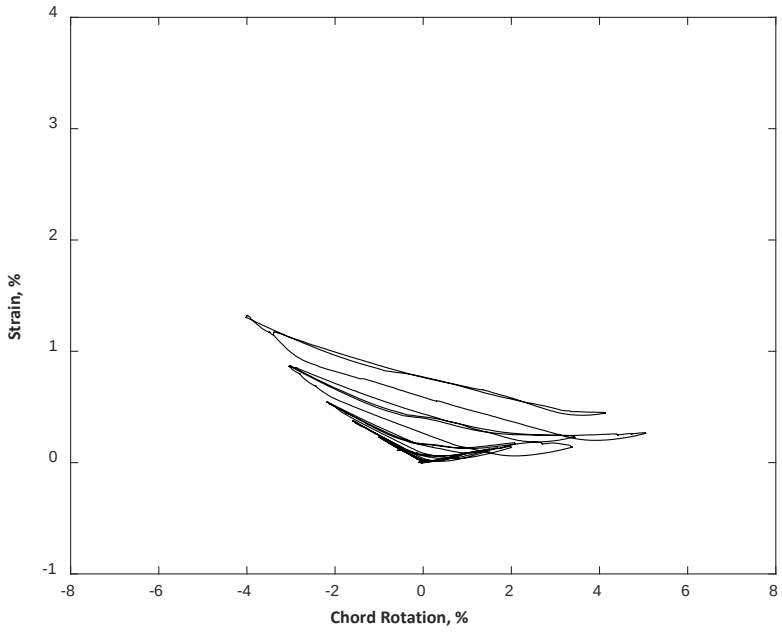

Figure D.56 – Strain measured with D11 for CB3D

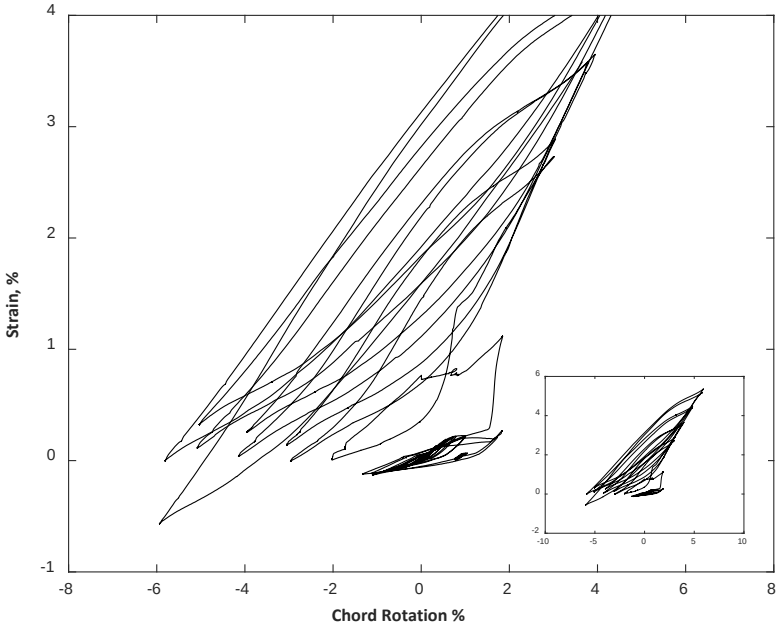

Figure D.57 – Strain measured with D12 for CB1

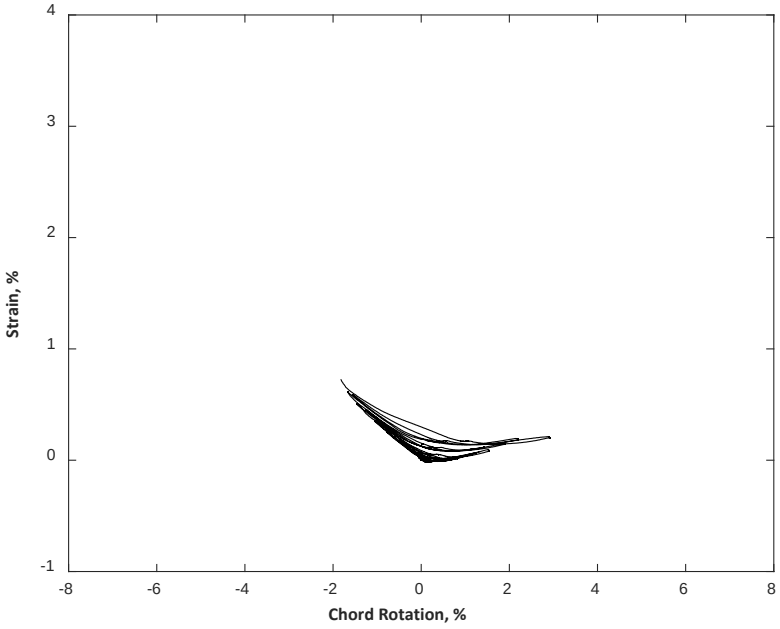

Figure D.58 – Strain measured with D12 for CB2

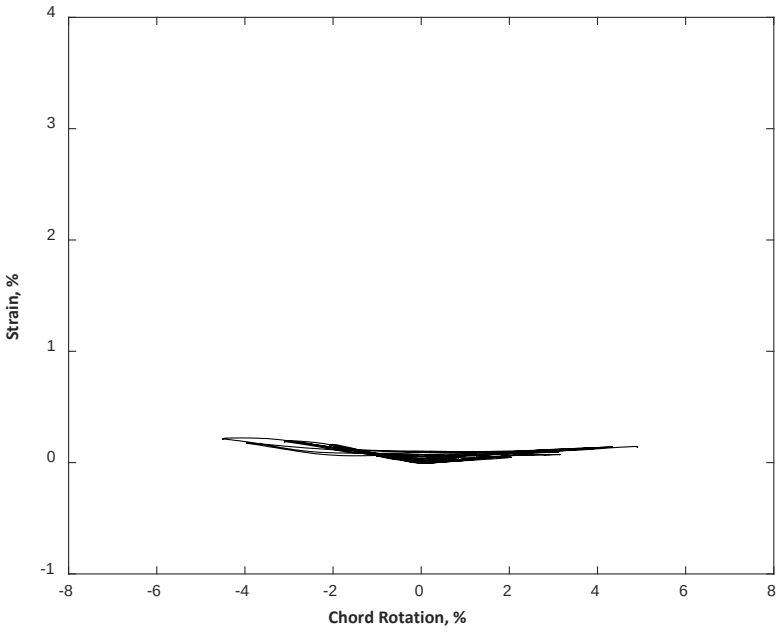

Figure D.59 – Strain measured with D12 for CB2D

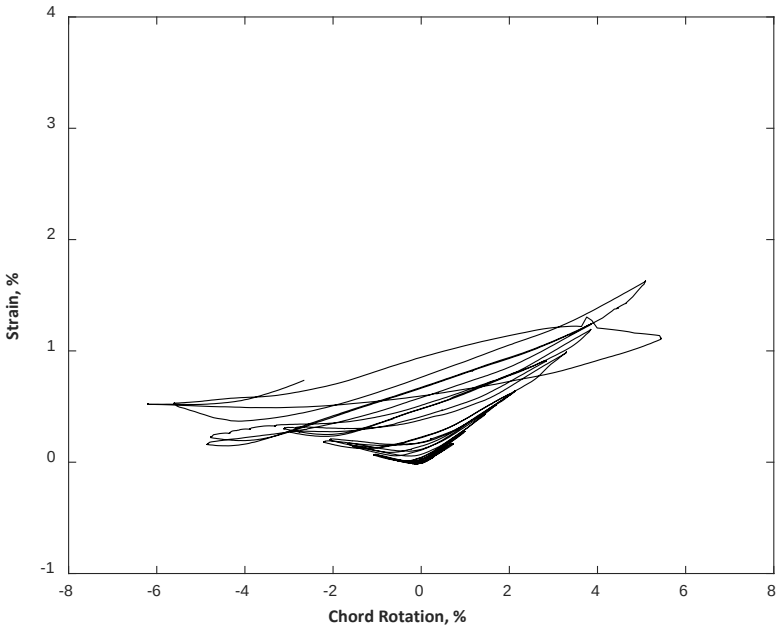

Figure D.60 – Strain measured with D12 for CB2AD

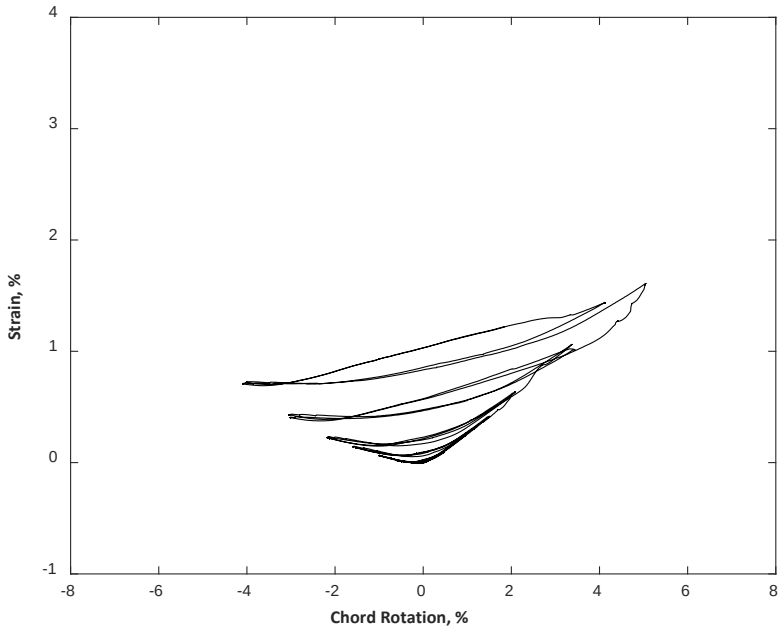

Figure D.61 – Strain measured with D12 for CB3D

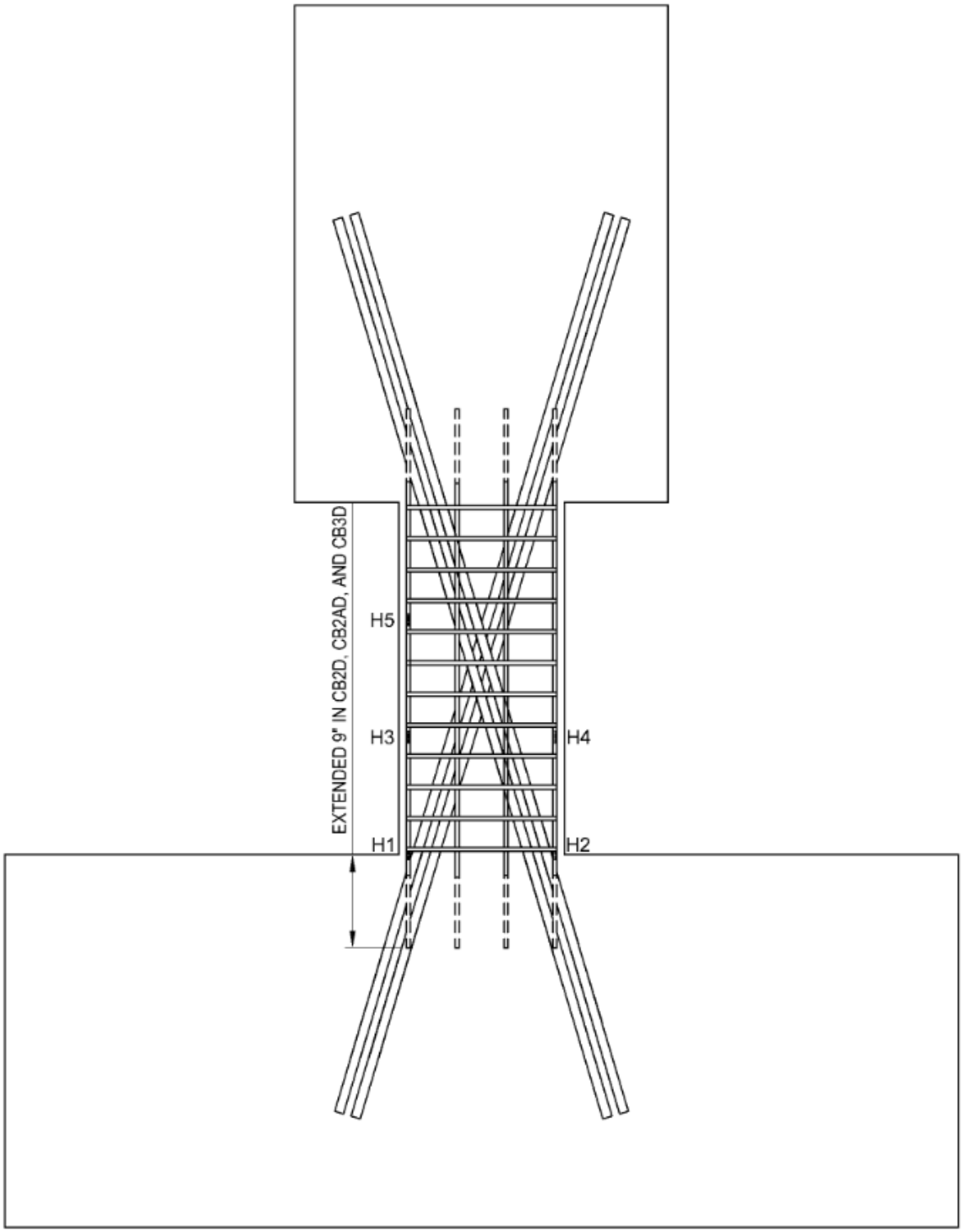

Figure D.62 – Location of strain gauges on secondary (non-diagonal) longitudinal bars

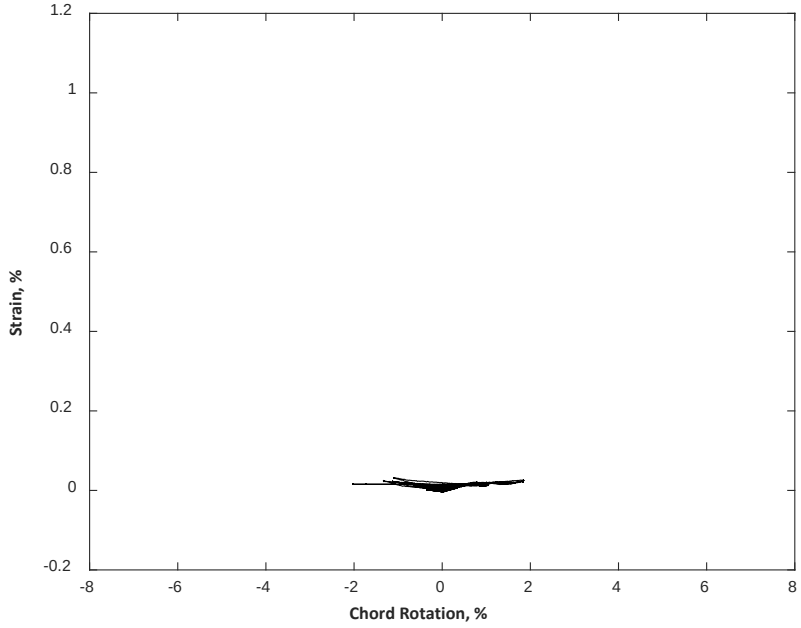

Figure D.63 – Strain measured with H1 for CB1

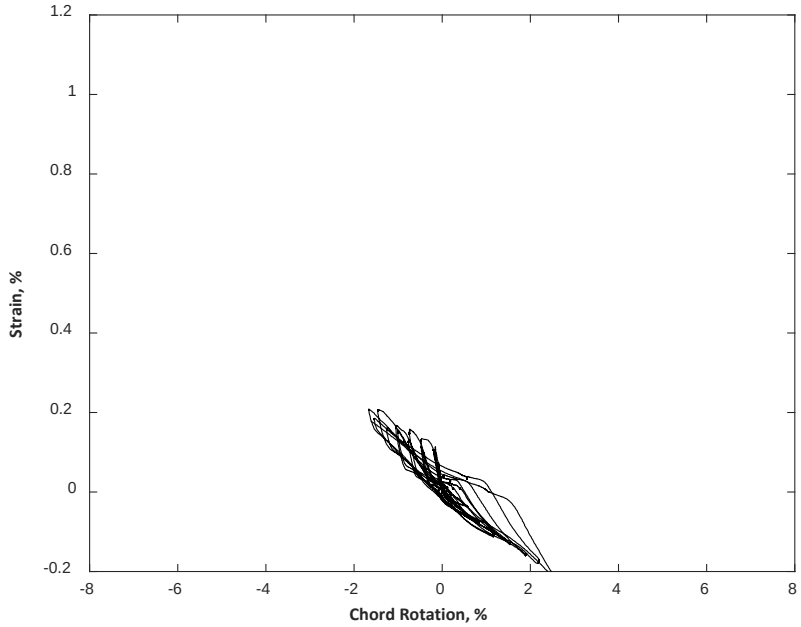

Figure D.64 – Strain measured with H1 for CB2

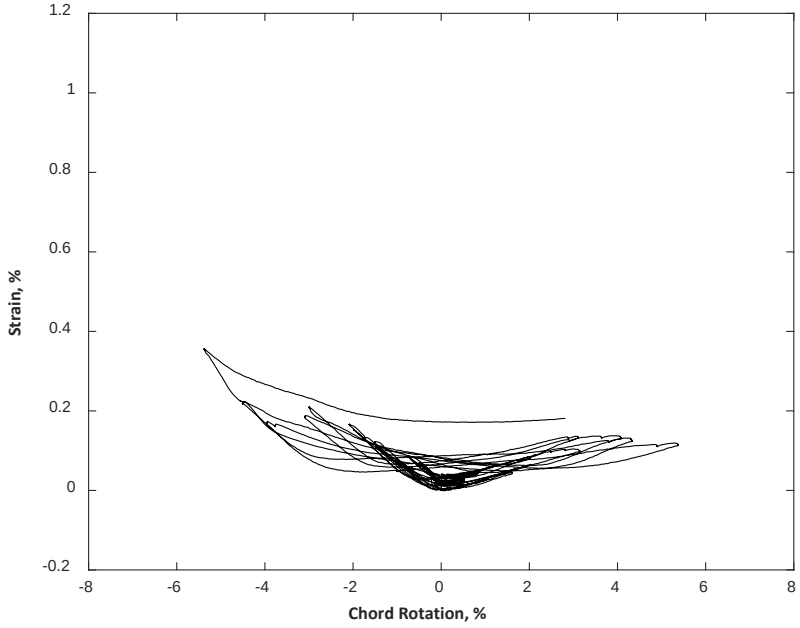

Figure D.65 – Strain measured with H1 for CB2D

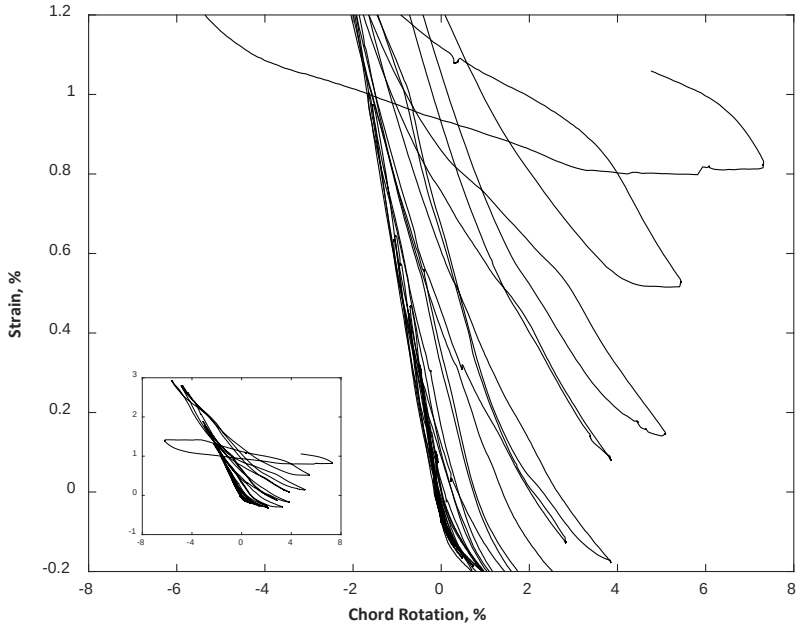

Figure D.66 – Strain measured with H1 for CB2AD

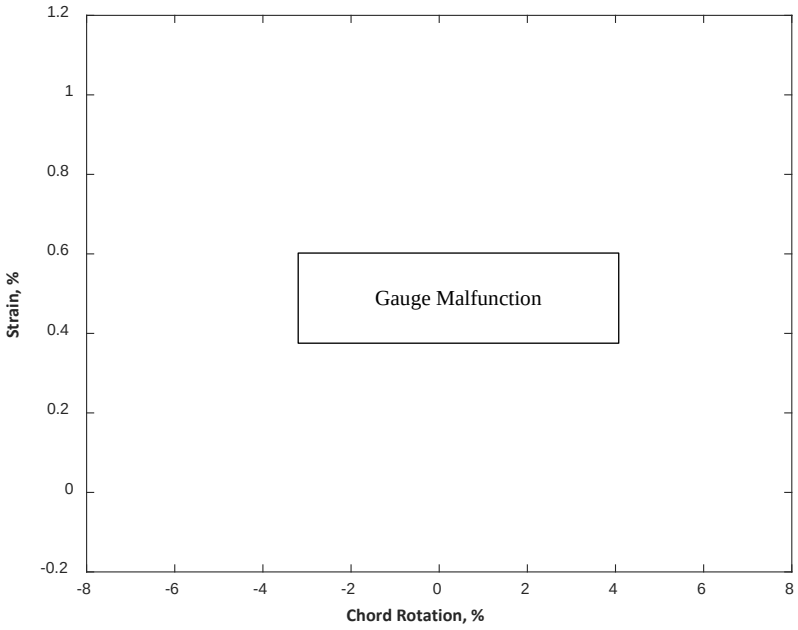

Figure D.67 – Strain measured with H1 for CB3D

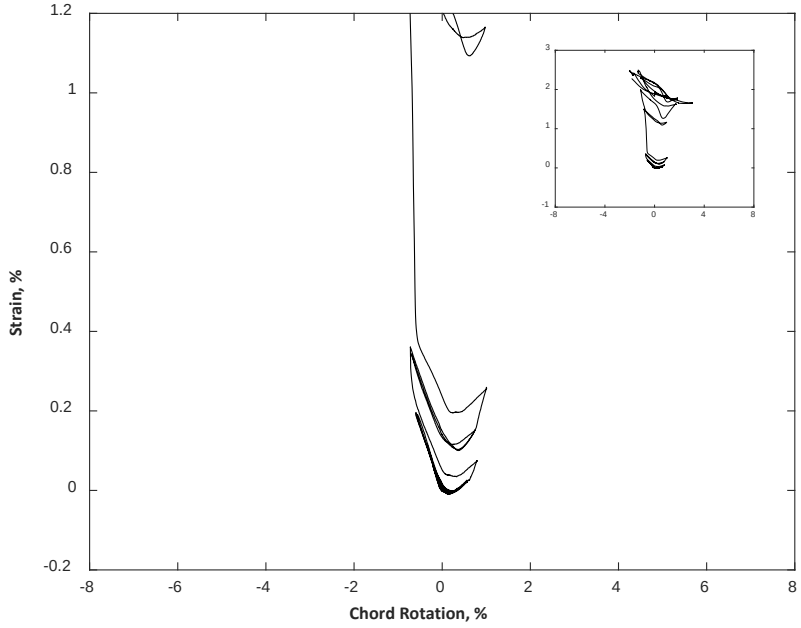

Figure D.68 – Strain measured with H2 for CB1

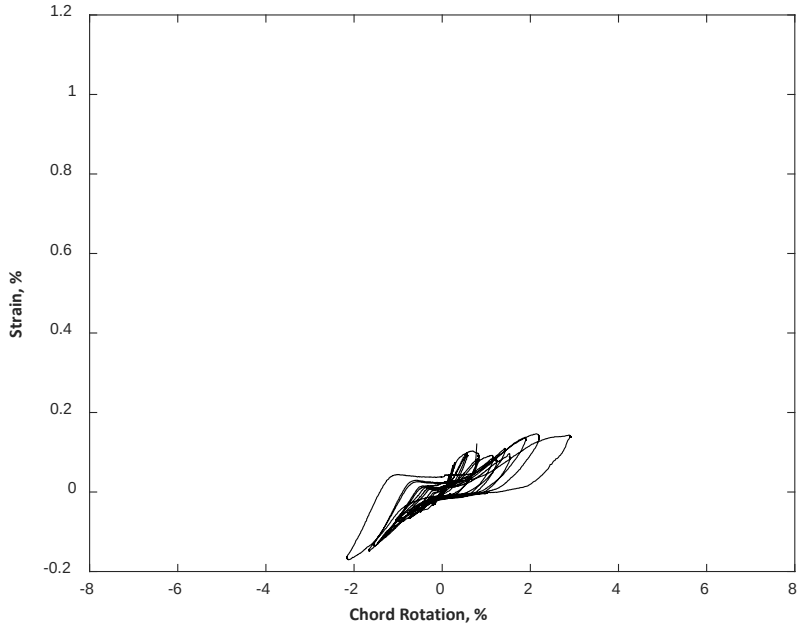

Figure D.69 – Strain measured with H2 for CB2

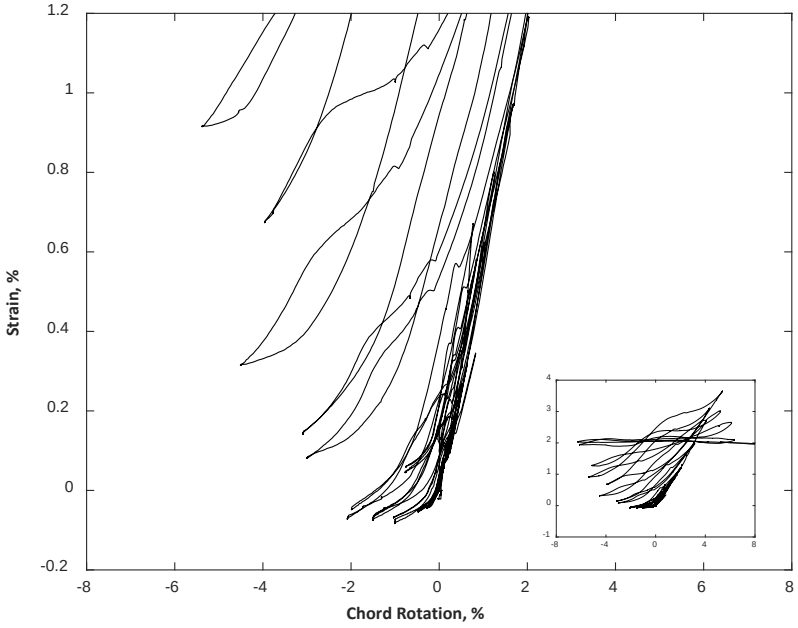

Figure D.70 – Strain measured with H2 for CB2D

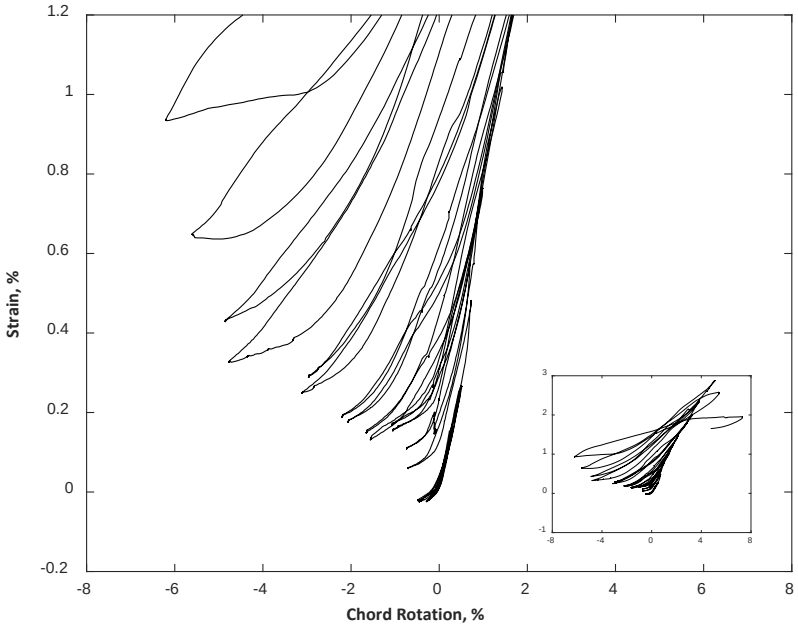

Figure D.71 – Strain measured with H2 for CB2AD

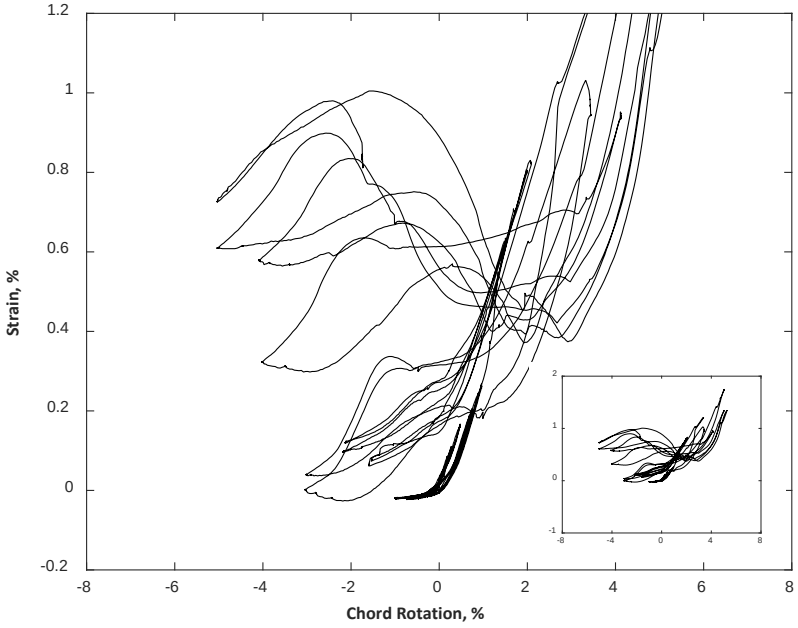

Figure D.72 – Strain measured with H2 for CB3D

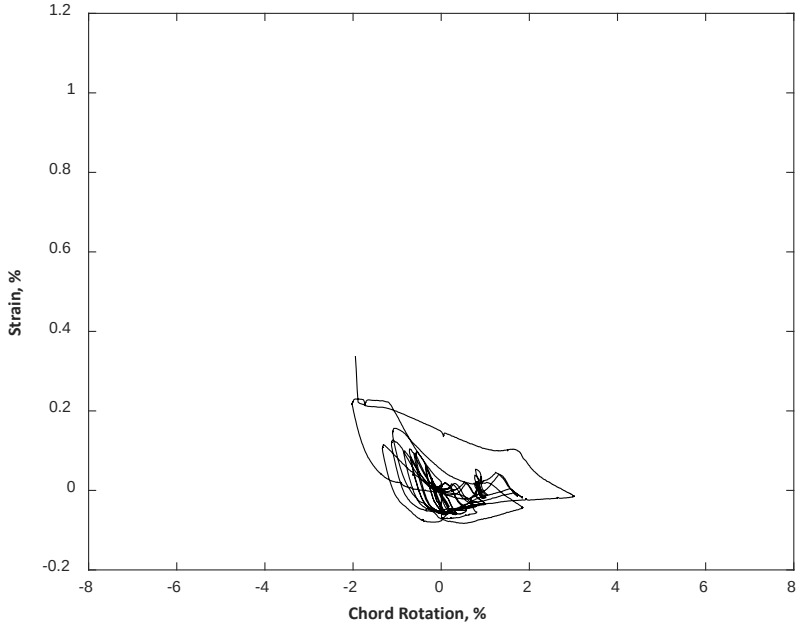

Figure D.73 – Strain measured with H3 for CB1

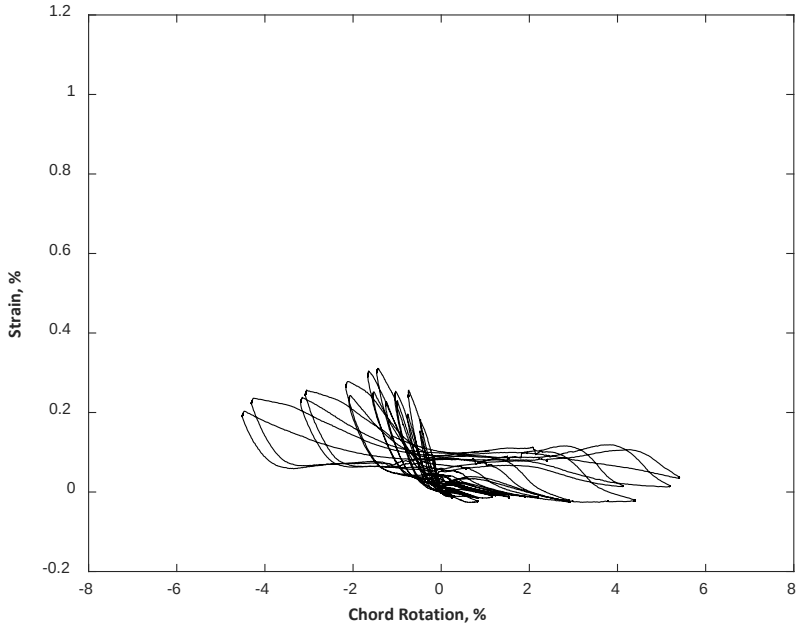

Figure D.74 – Strain measured with H3 for CB2

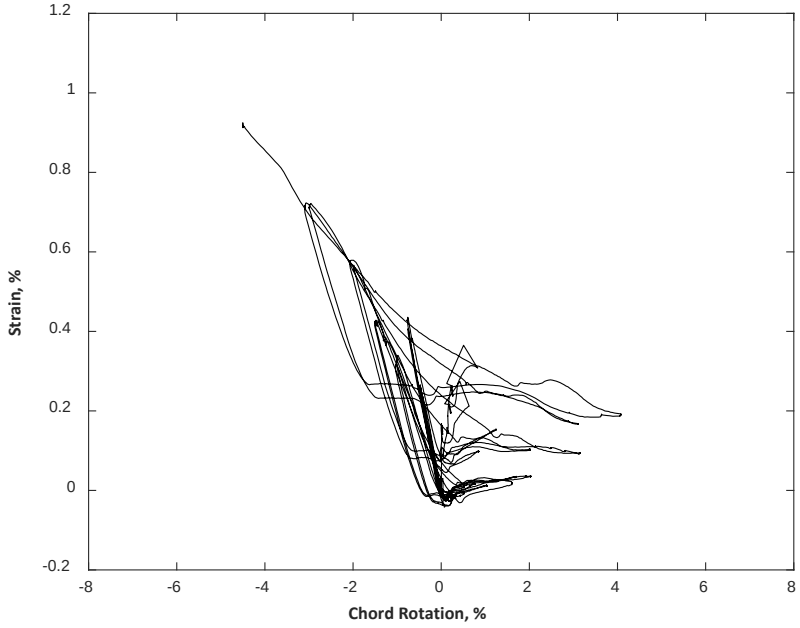

Figure D.75 – Strain measured with H3 for CB2D

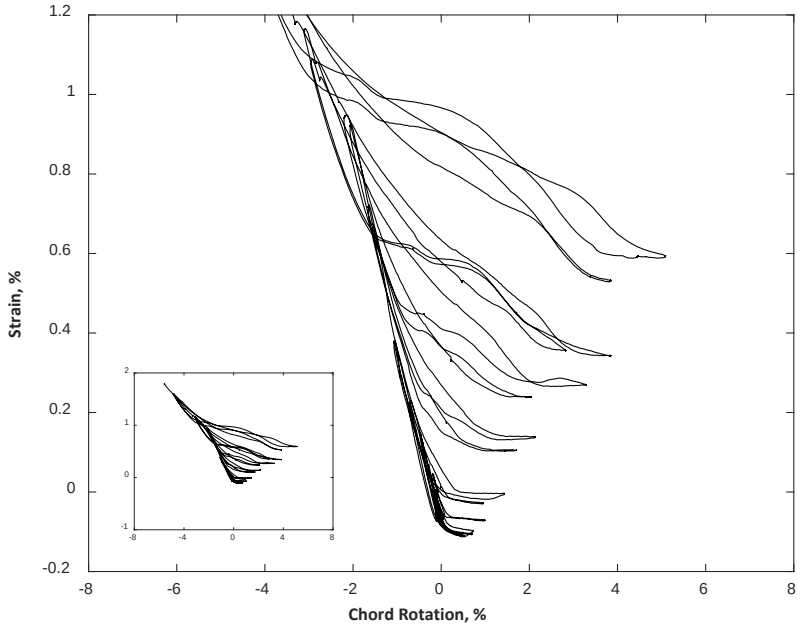

Figure D.76 – Strain measured with H3 for CB2AD

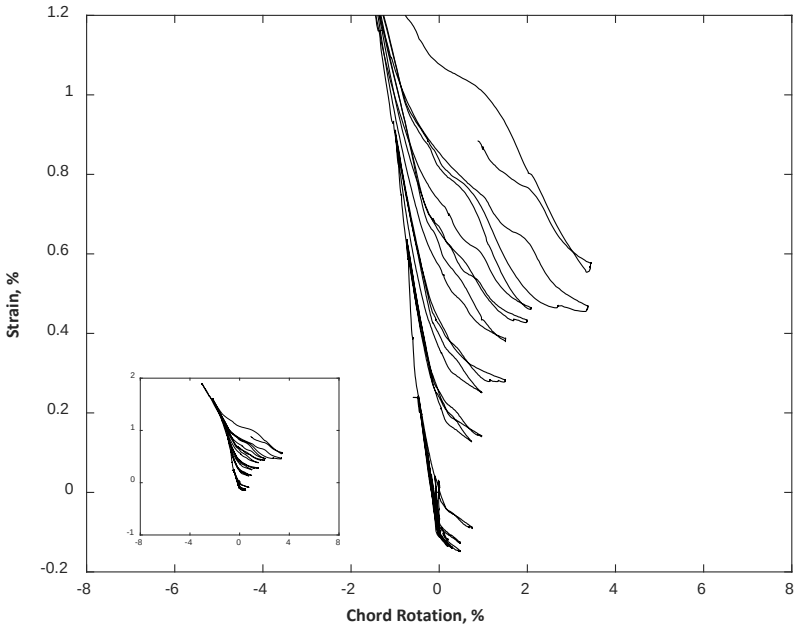

Figure D.77 – Strain measured with H3 for CB3D

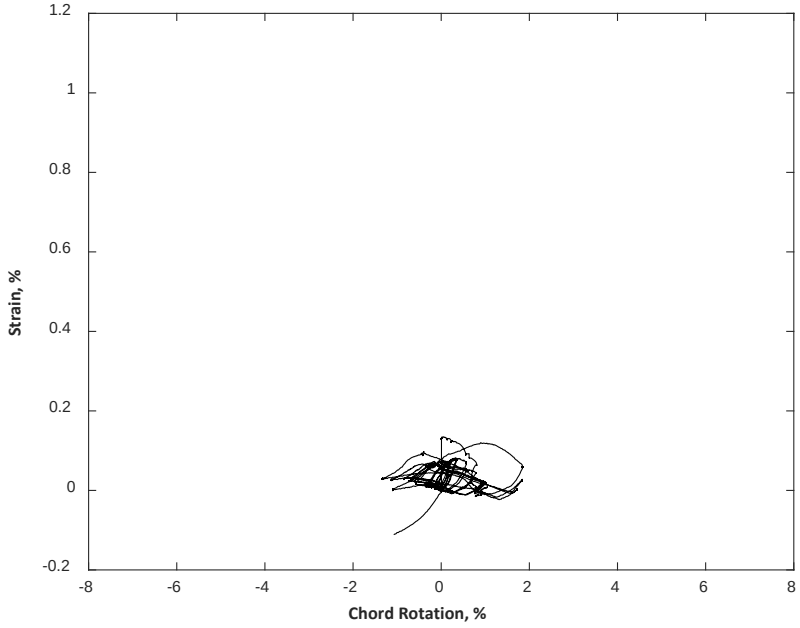

Figure D.78 – Strain measured with H4 for CB1

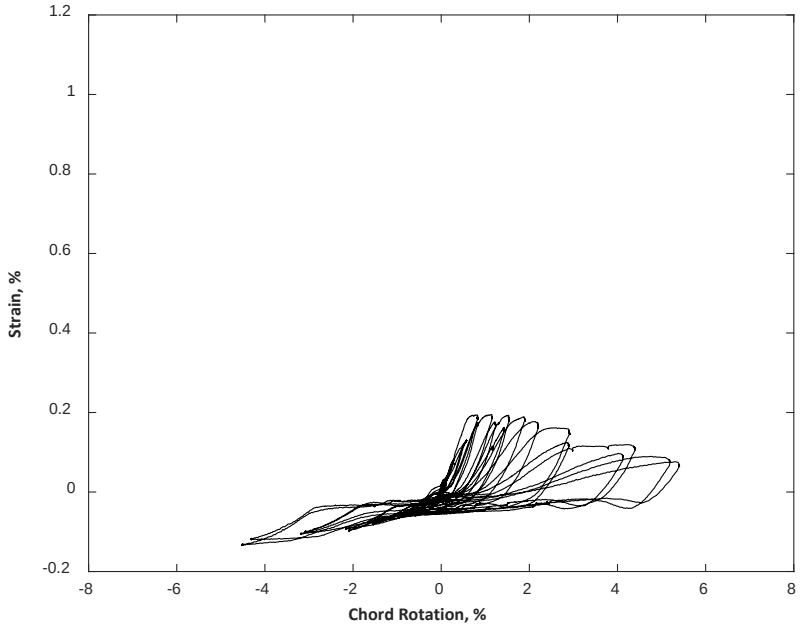

Figure D.79 – Strain measured with H4 for CB2

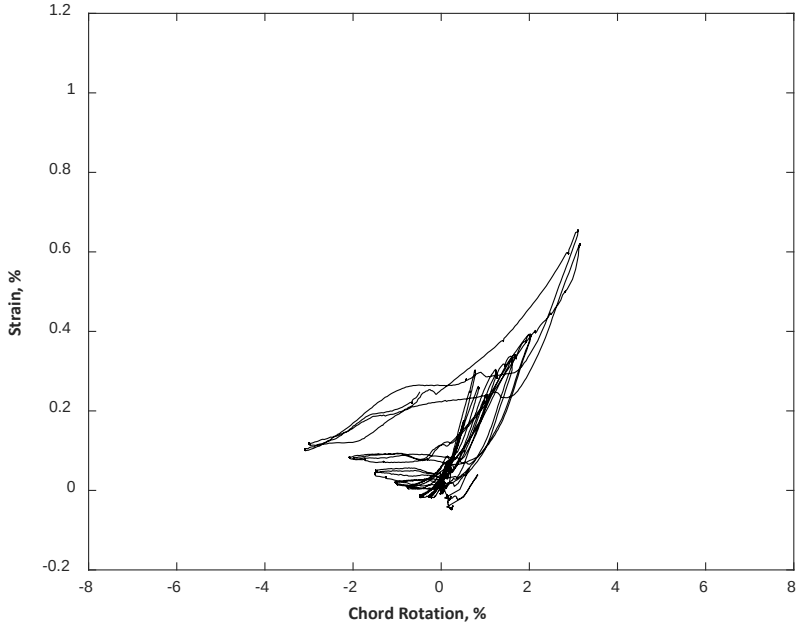

Figure D.80 – Strain measured with H4 for CB2D

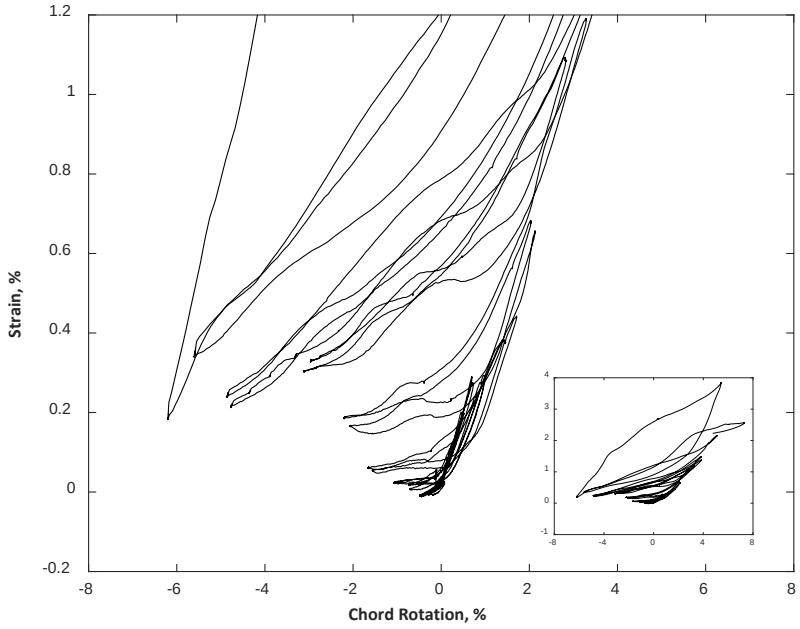

Figure D.81 – Strain measured with H4 for CB2AD

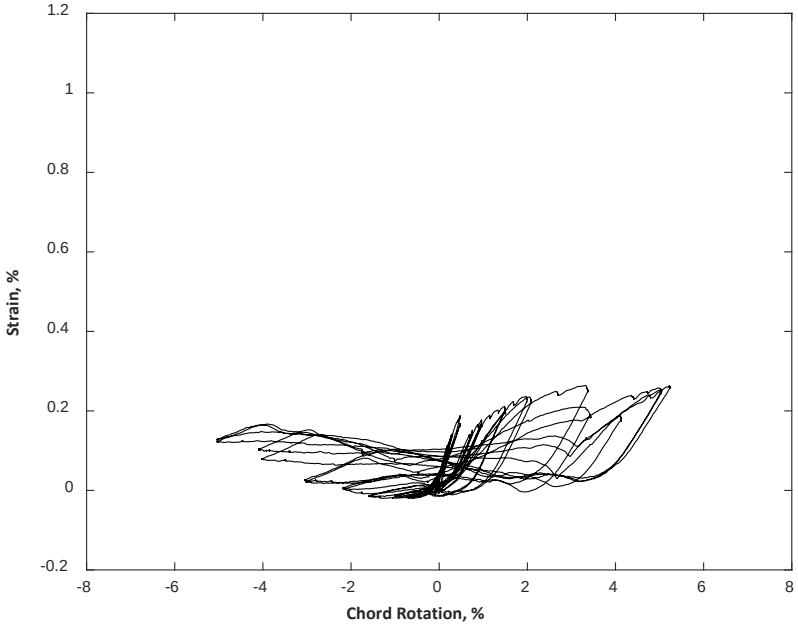

Figure D.82 – Strain measured with H4 for CB3D

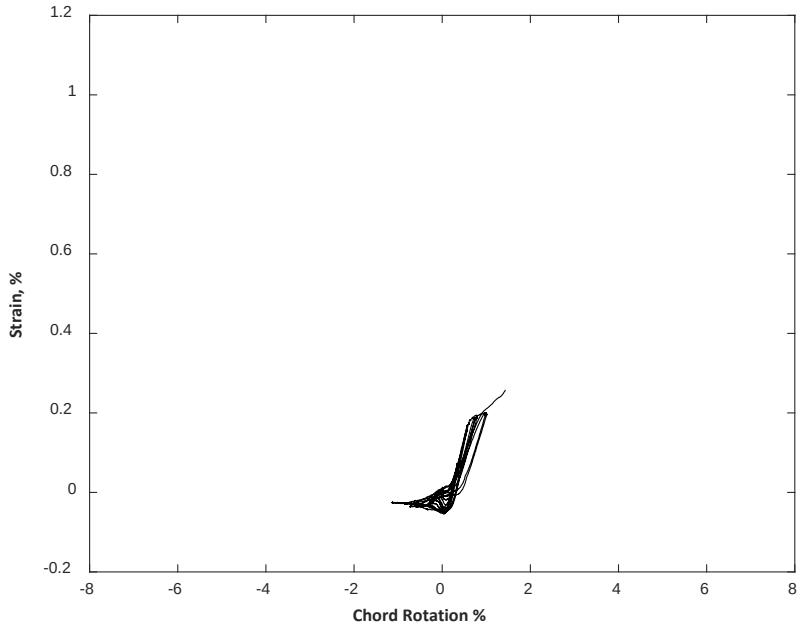

Figure D.83 – Strain measured with H5 for CB1

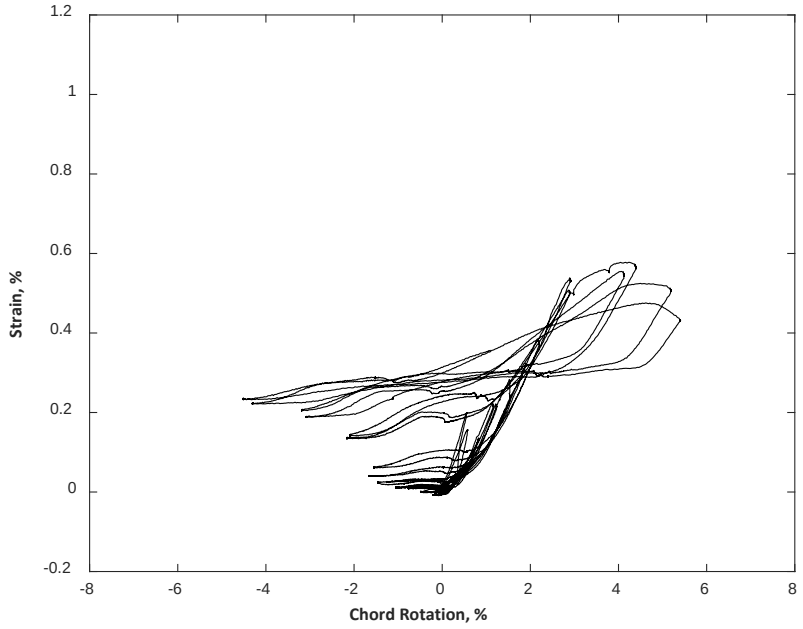

Figure D.84 – Strain measured with H5 for CB2

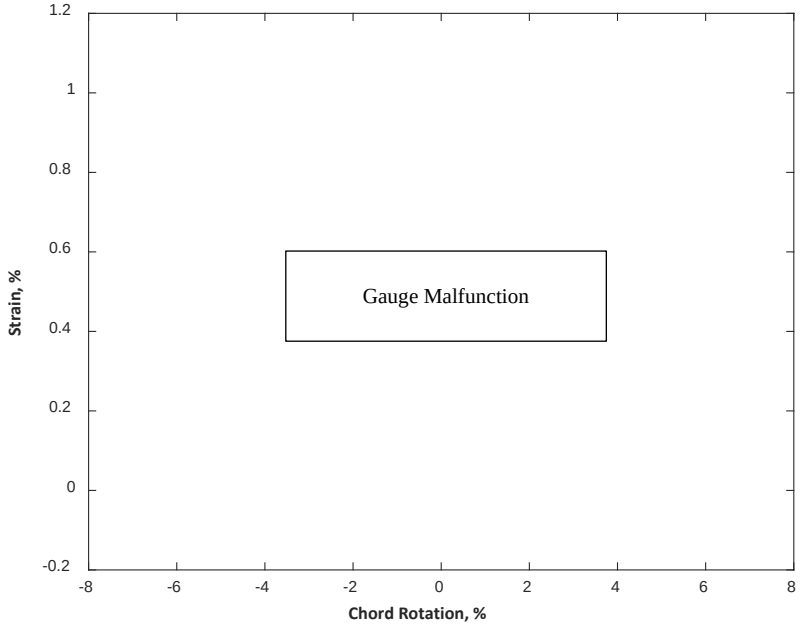

Figure D.85 – Strain measured with H5 for CB2D

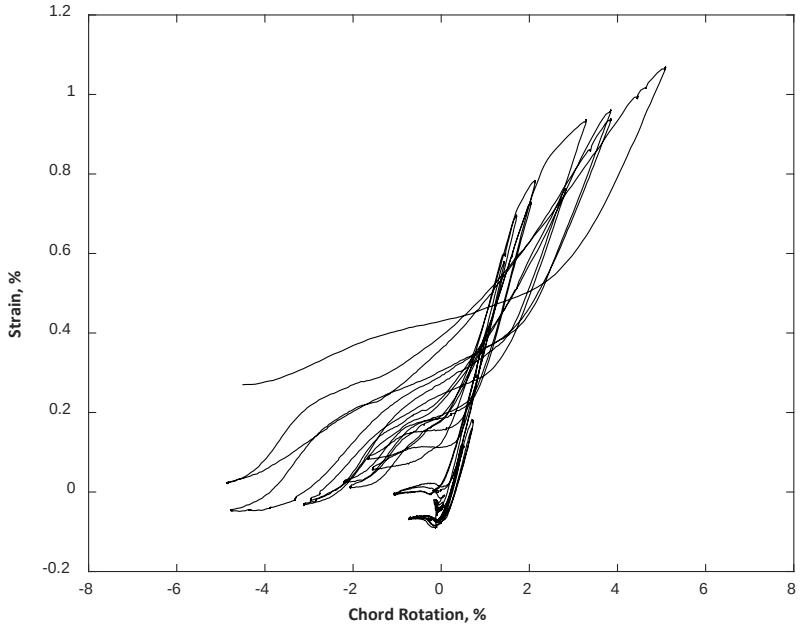

Figure D.86 – Strain measured with H5 for CB2AD

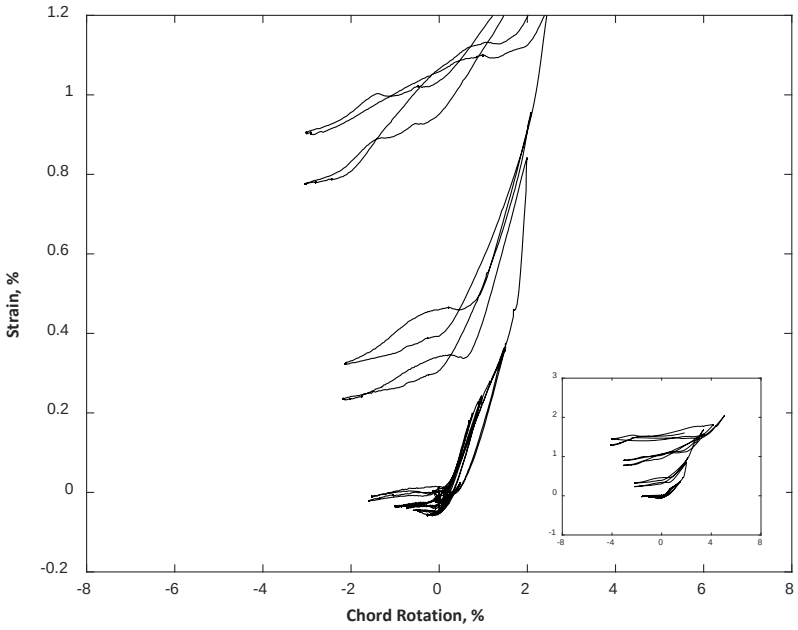

Figure D.87 – Strain measured with H5 for CB3D

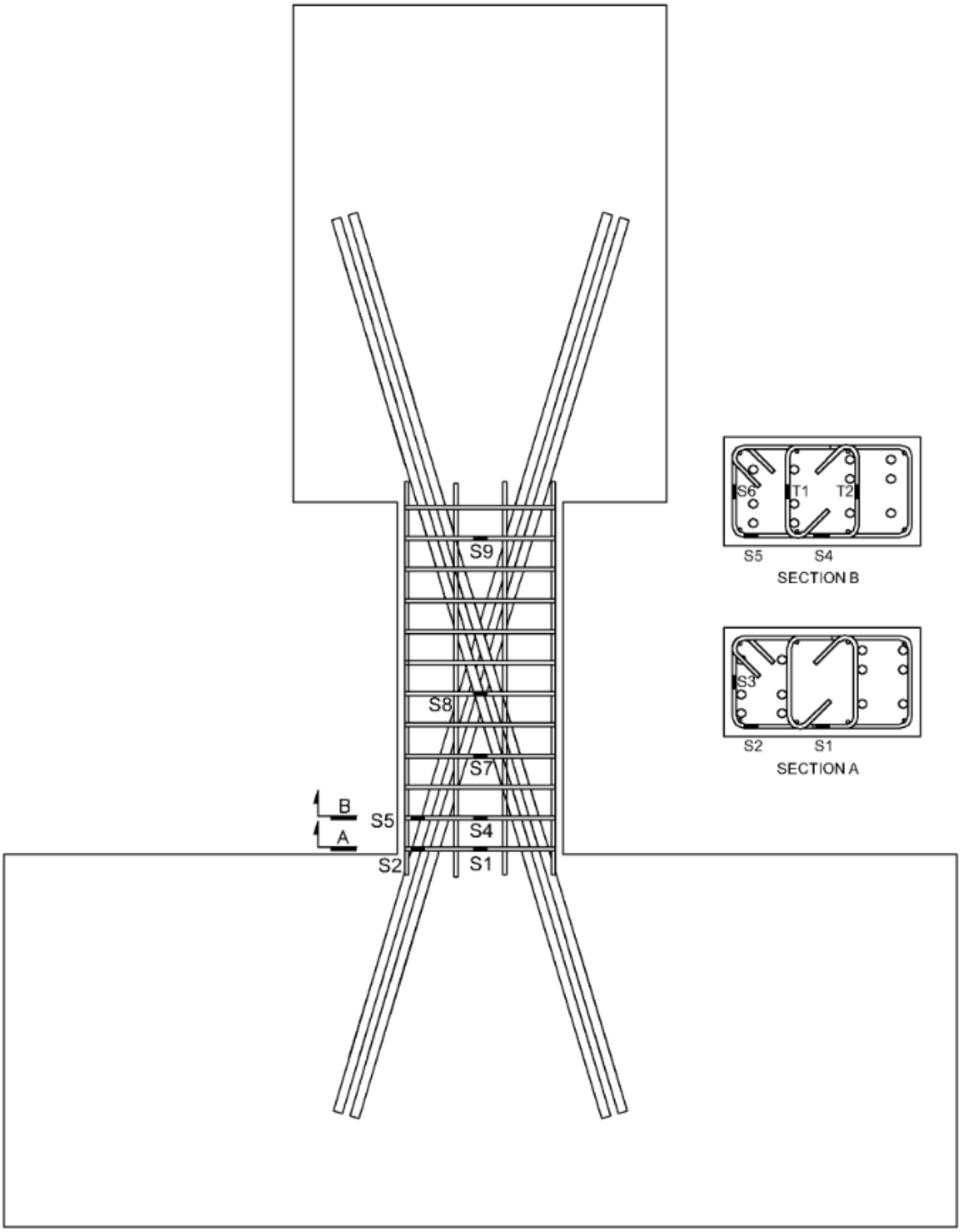

Figure D.88 – Location of strain gauges on transverse reinforcement (hoops and crossties)

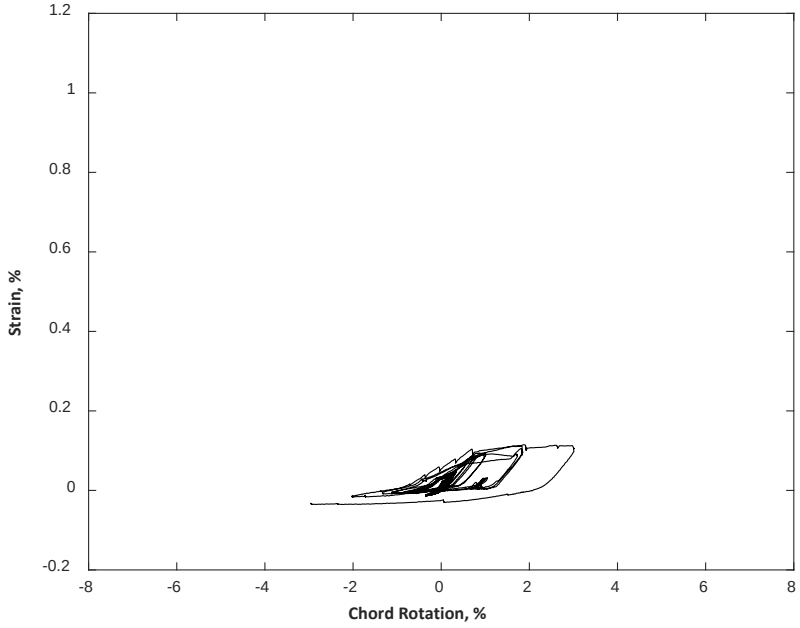

Figure D.89 – Strain measured with S1 for CB1

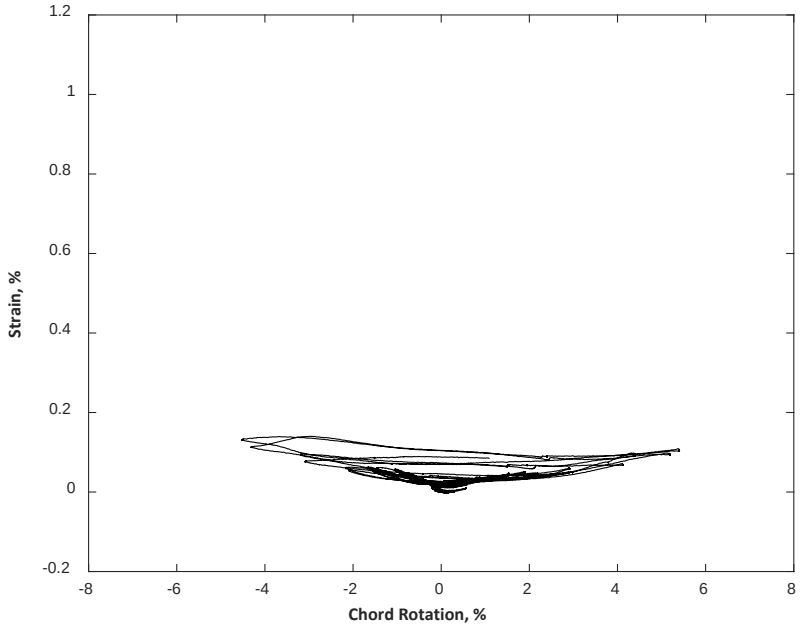

Figure D.90 – Strain measured with S1 for CB2

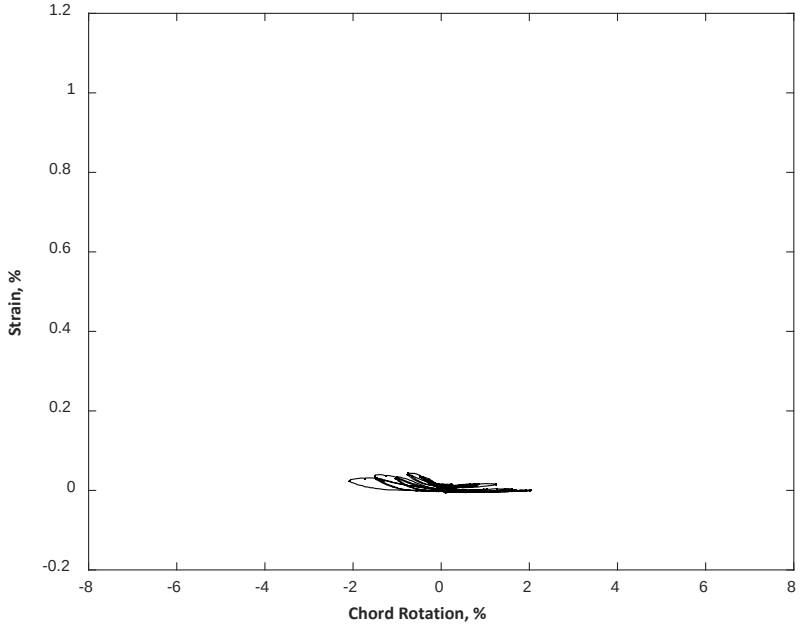

Figure D.91 – Strain measured with S1 for CB2D

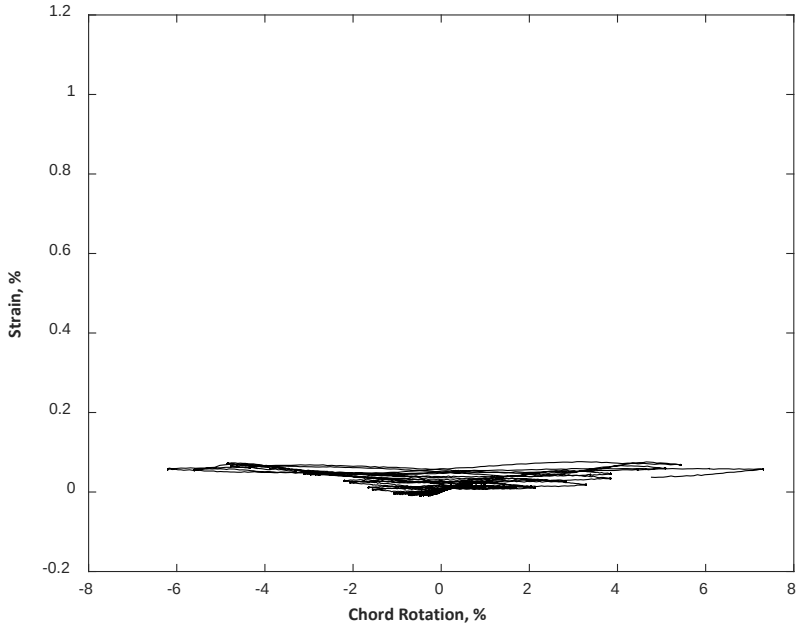

Figure D.92 – Strain measured with S1 for CB2AD

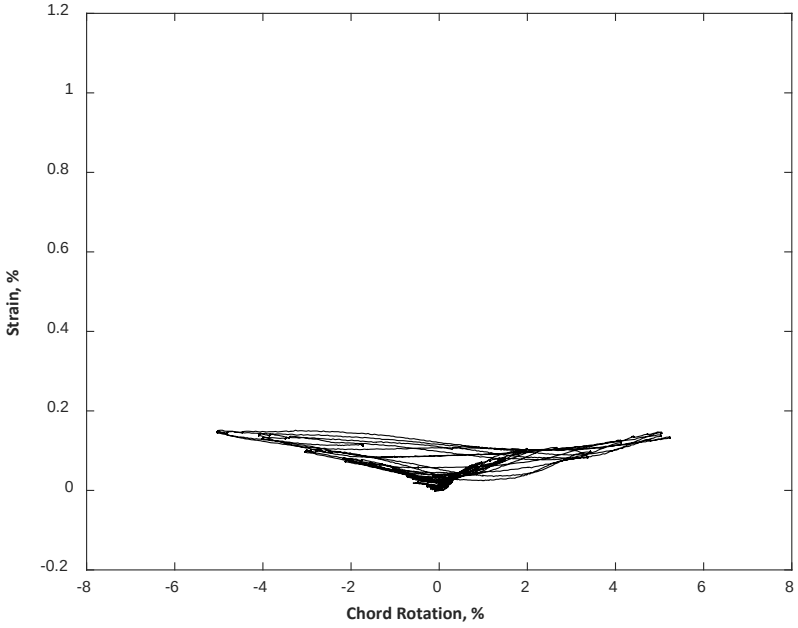

Figure D.93 – Strain measured with S1 for CB3D

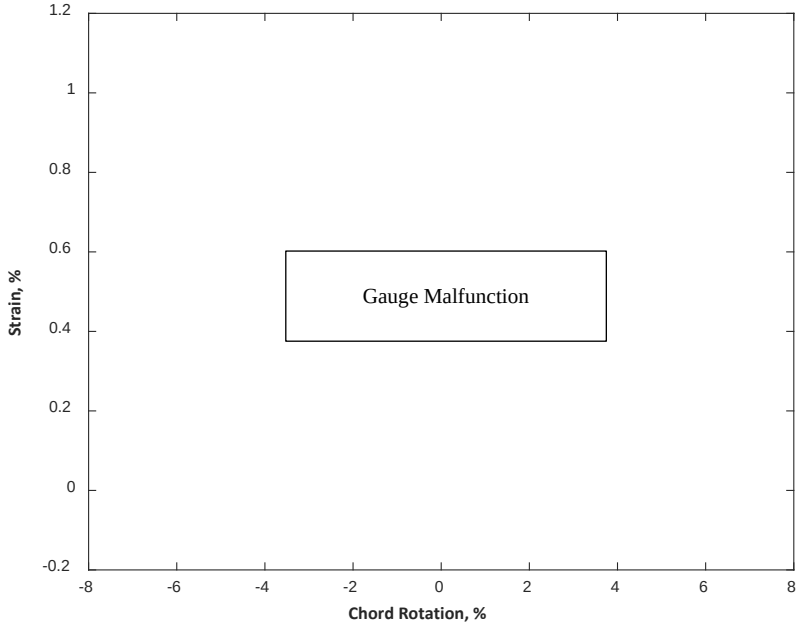

Figure D.94 – Strain measured with S2 for CB1

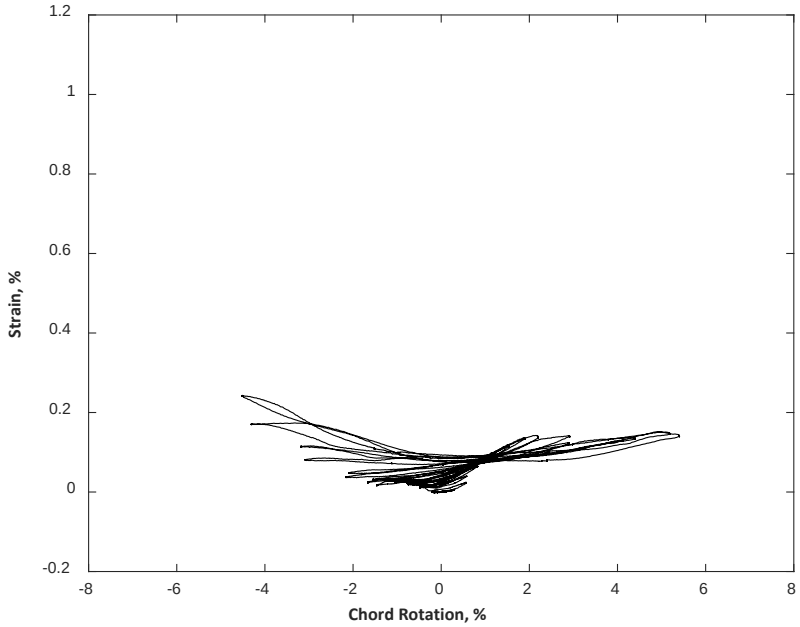

Figure D.95 – Strain measured with S2 for CB2

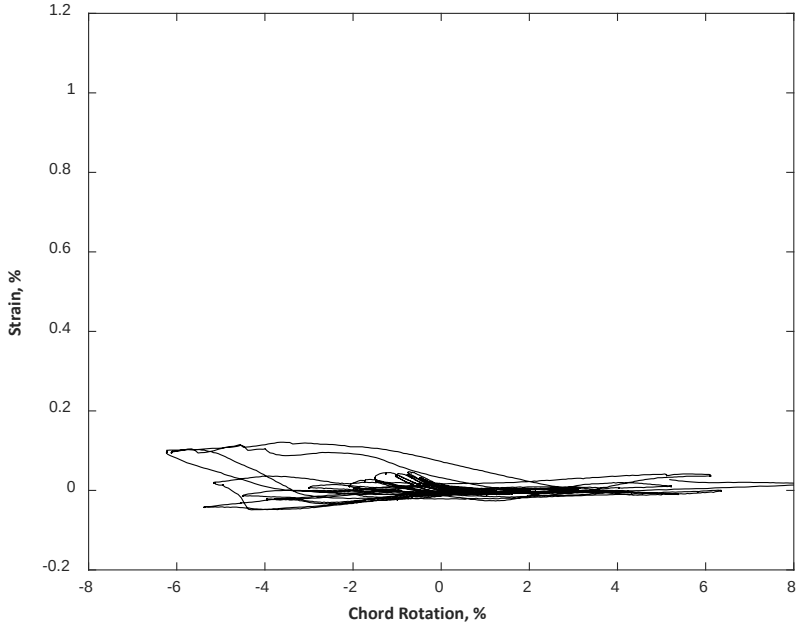

Figure D.96 – Strain measured with S2 for CB2D

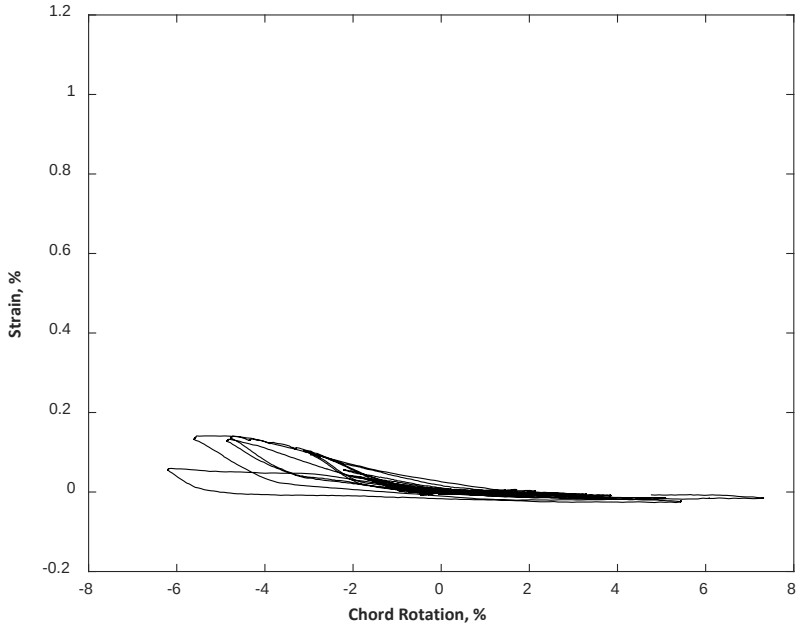

Figure D.97 – Strain measured with S2 for CB2AD

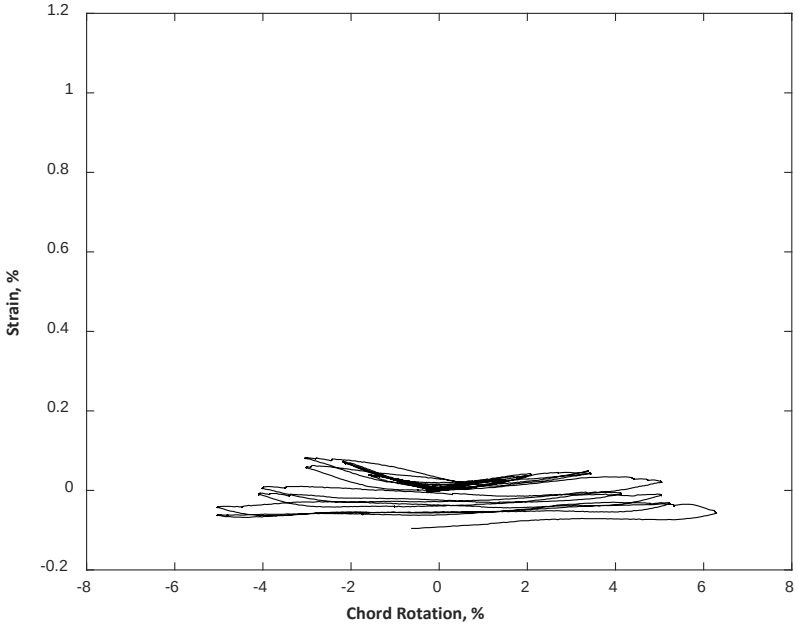

Figure D.98 – Strain measured with S2 for CB3D

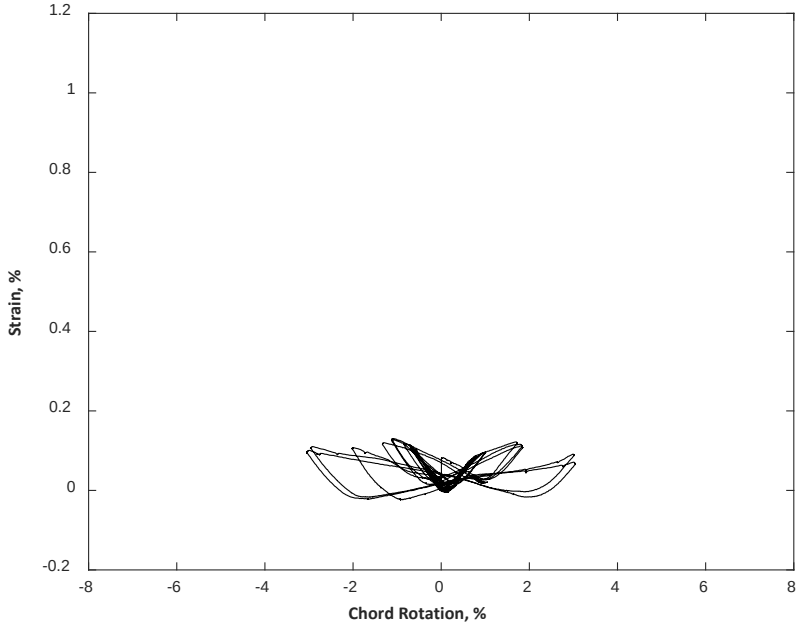

Figure D.99 – Strain measured with S3 for CB1

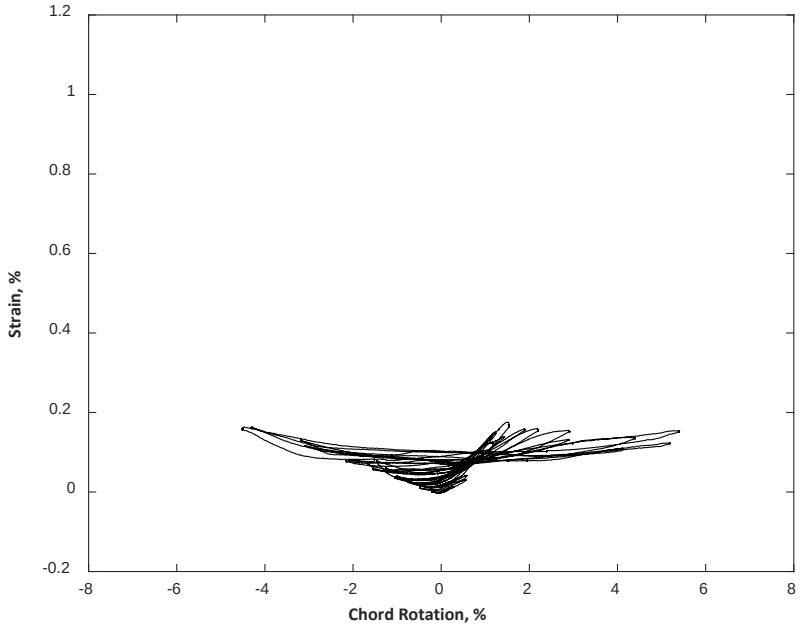

Figure D.100 – Strain measured with S3 for CB2

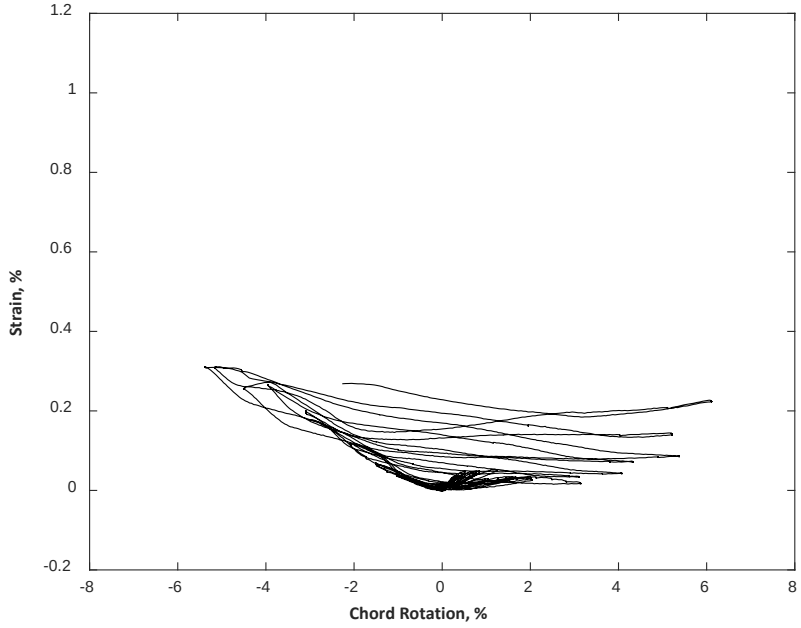

Figure D.101 – Strain measured with S3 for CB2D

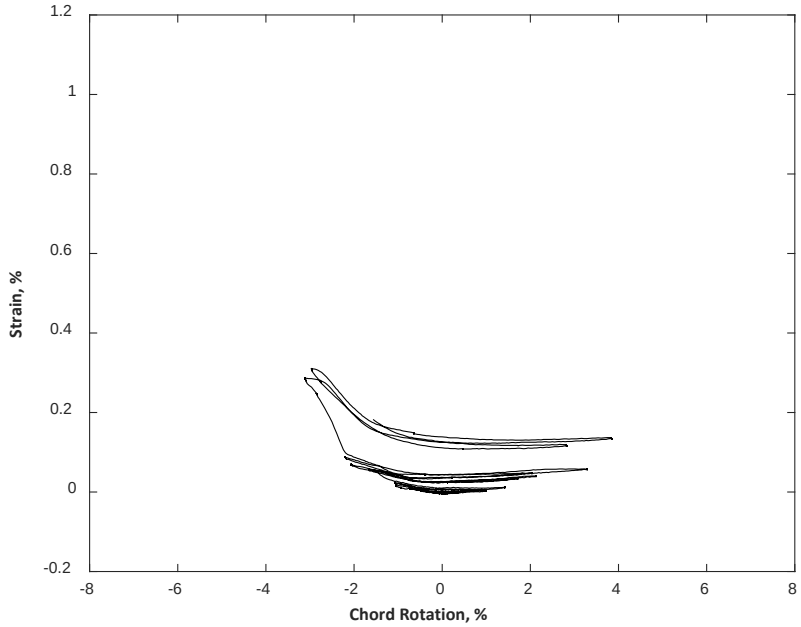

Figure D.102 – Strain measured with S3 for CB2AD

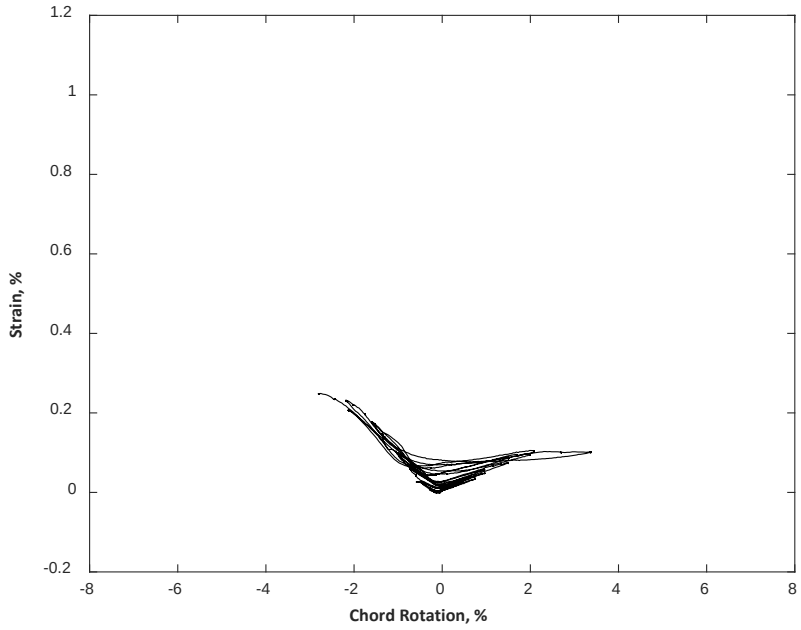

Figure D.103 – Strain measured with S3 for CB3D

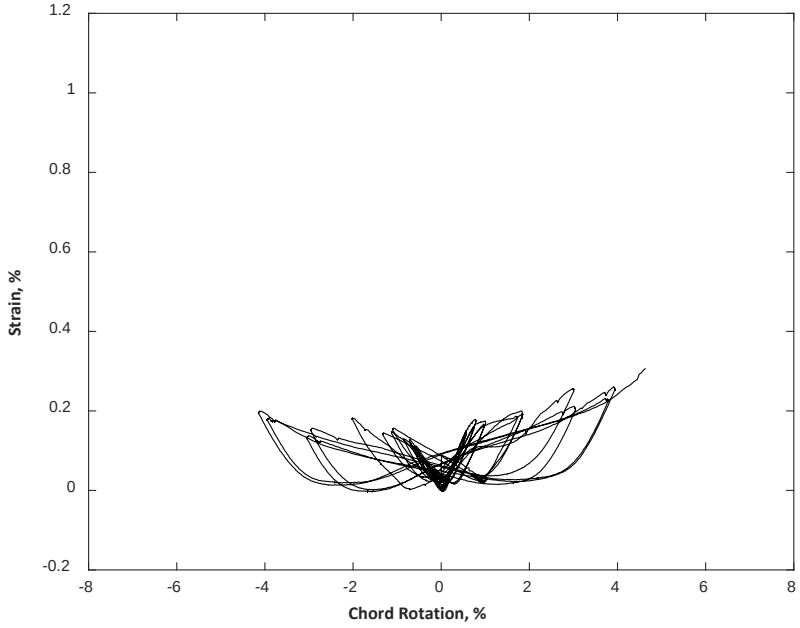

Figure D.104 – Strain measured with S4 for CB1

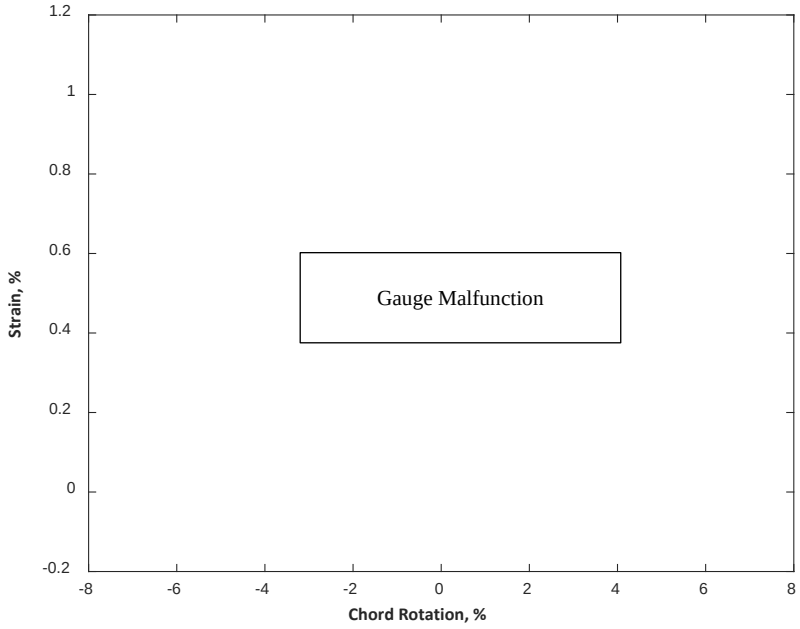

Figure D.105 – Strain measured with S4 for CB2

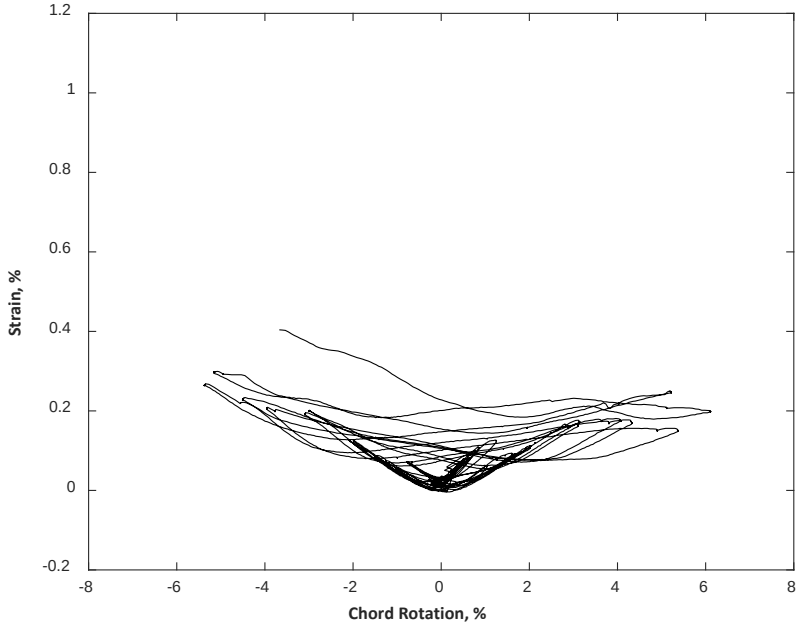

Figure D.106 – Strain measured with S4 for CB2D

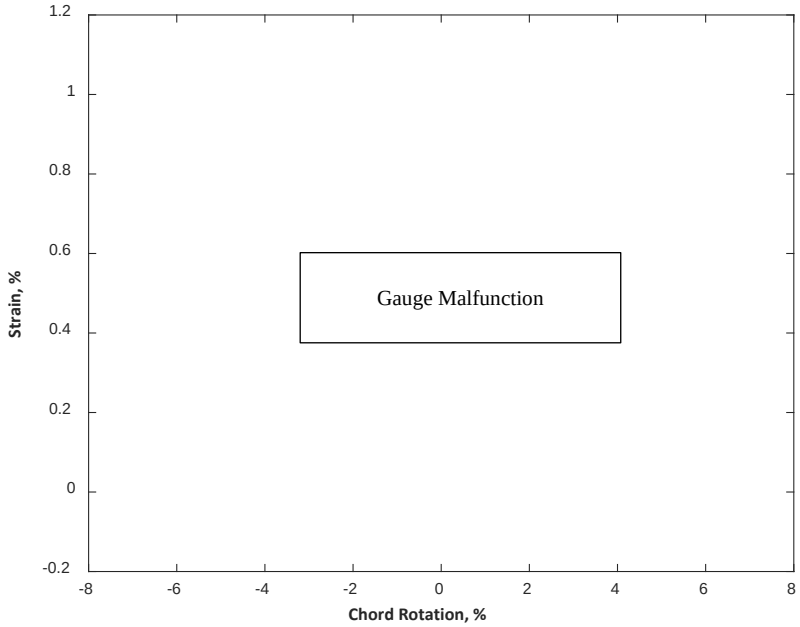

Figure D.107 – Strain measured with S4 for CB2AD

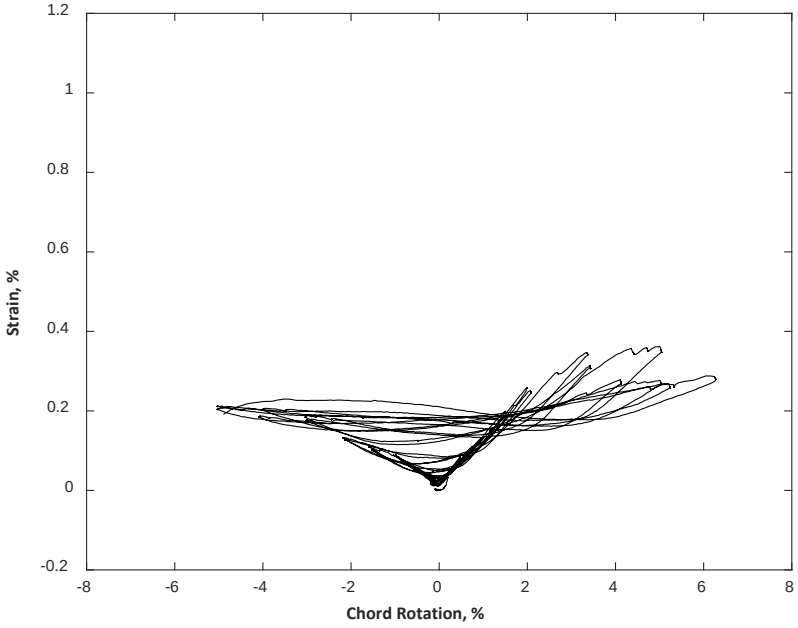

Figure D.108 – Strain measured with S4 for CB3D

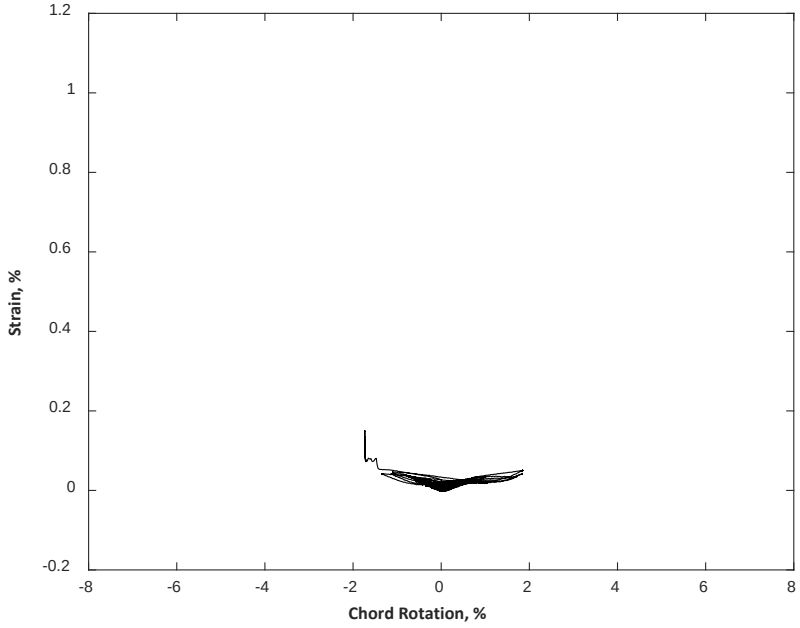

Figure D.109 – Strain measured with S5 for CB1

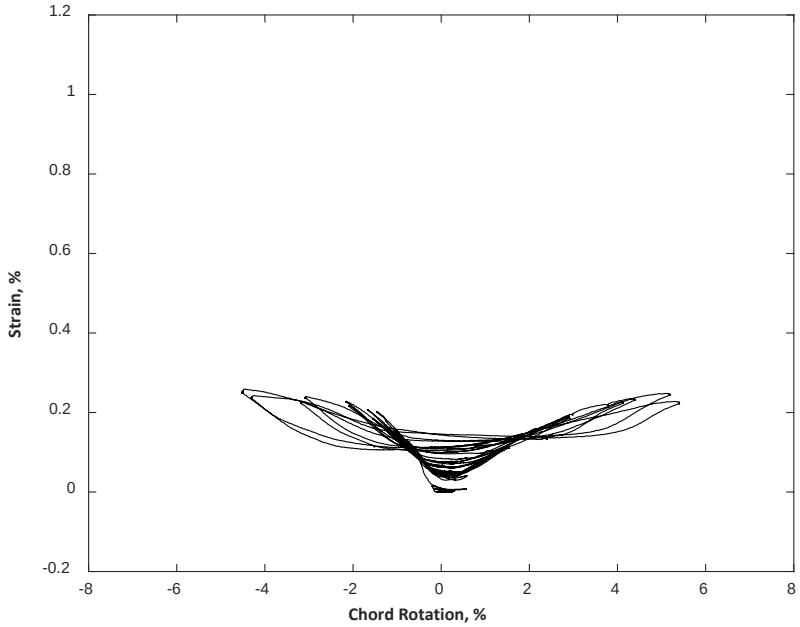

Figure D.110 – Strain measured with S5 for CB2

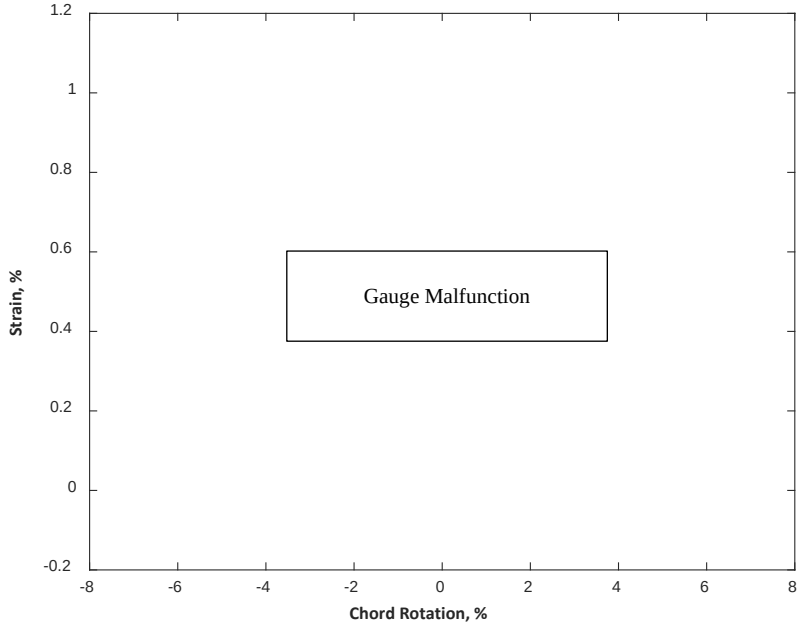

Figure D.111 – Strain measured with S5 for CB2D

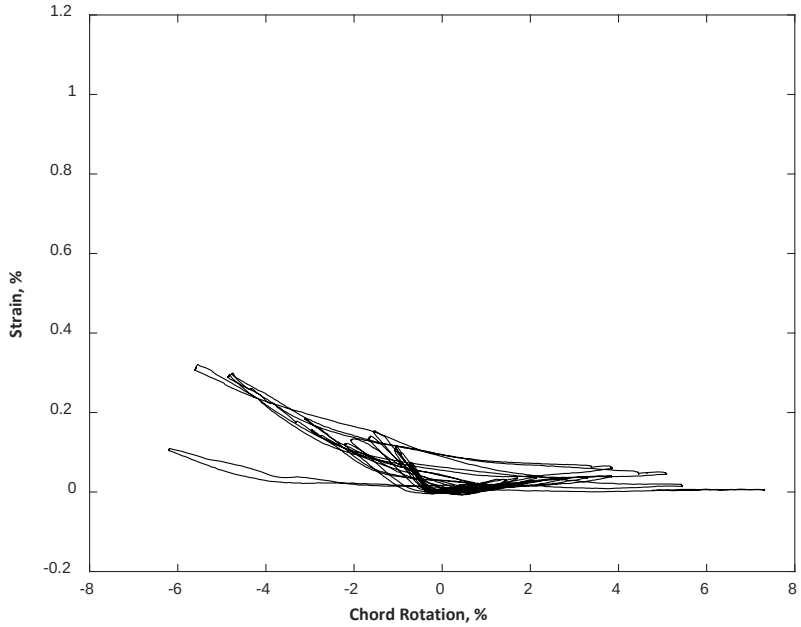

Figure D.112 – Strain measured with S5 for CB2AD

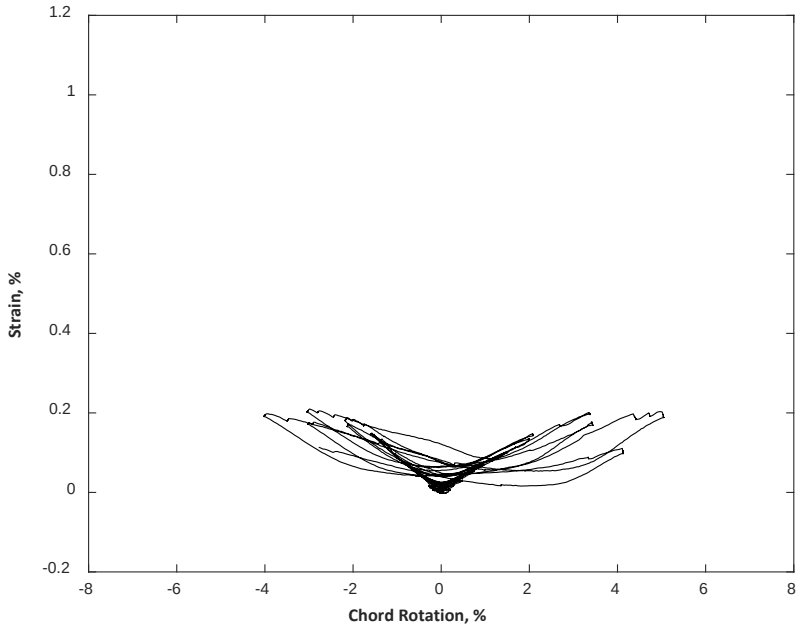

Figure D.113 – Strain measured with S5 for CB3D

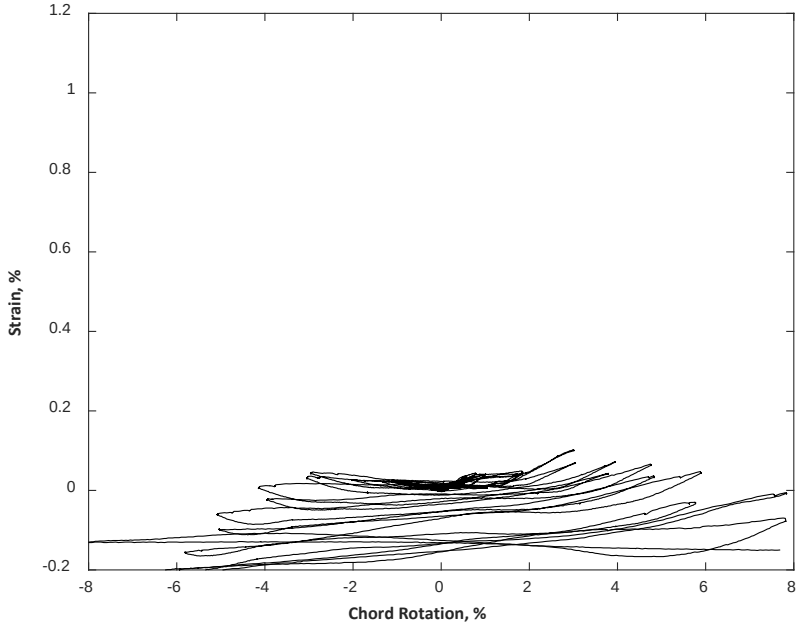

Figure D.114 – Strain measured with S6 for CB1

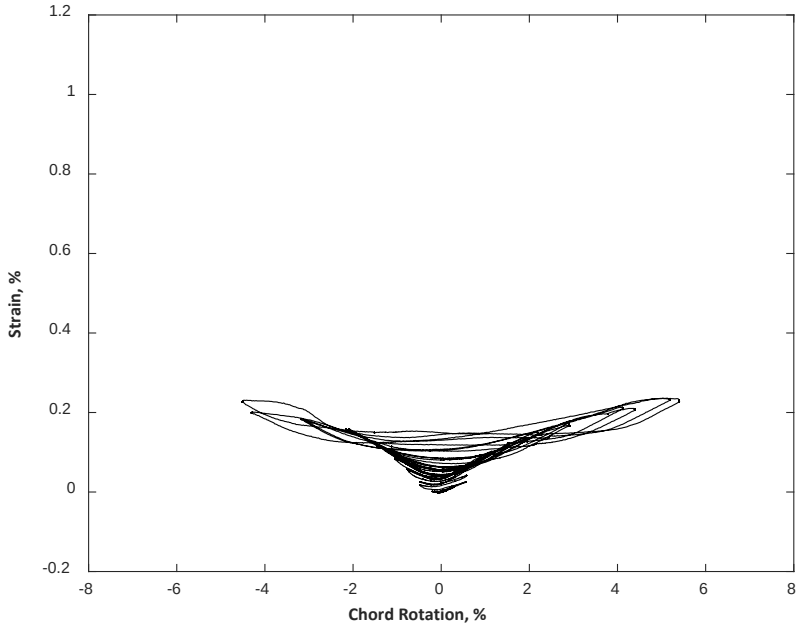

Figure D.115 – Strain measured with S6 for CB2

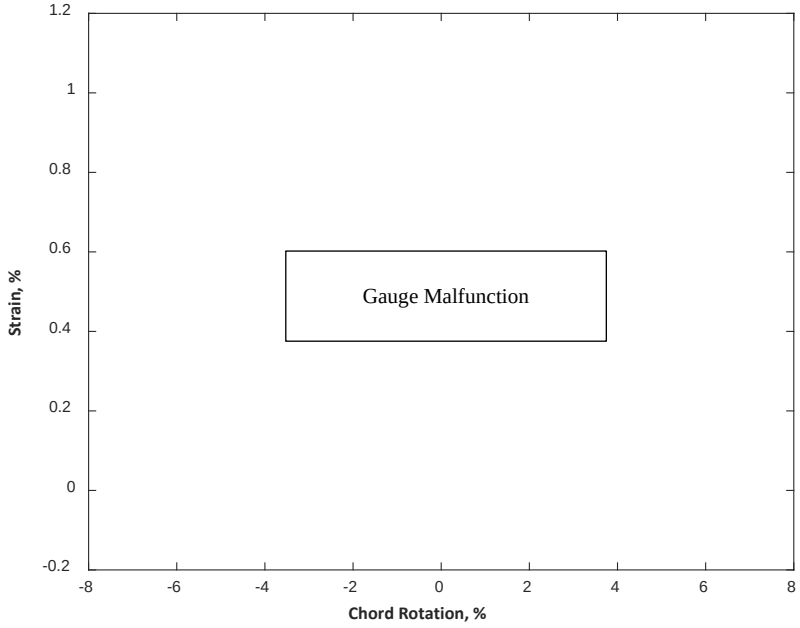

Figure D.116 – Strain measured with S6 for CB2D

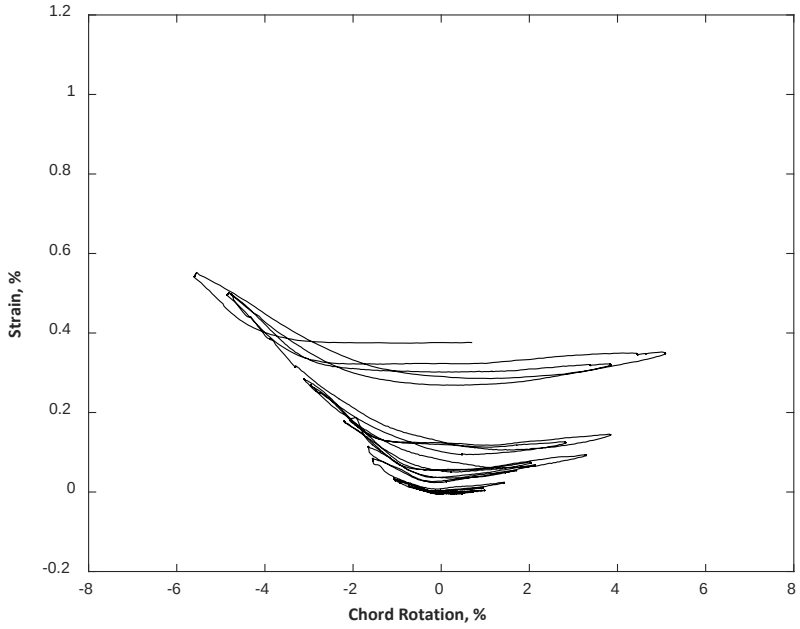

Figure D.117 – Strain measured with S6 for CB2AD

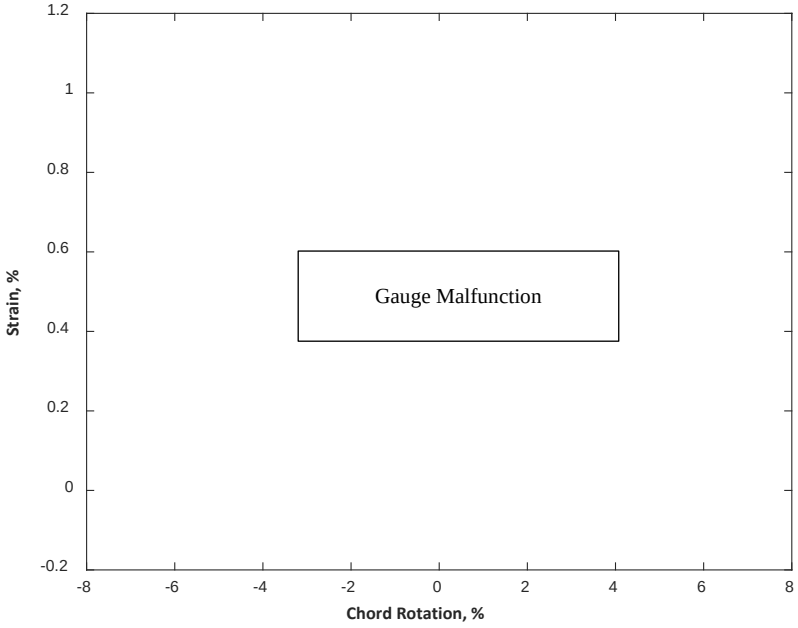

Figure D.118 – Strain measured with S6 for CB3D

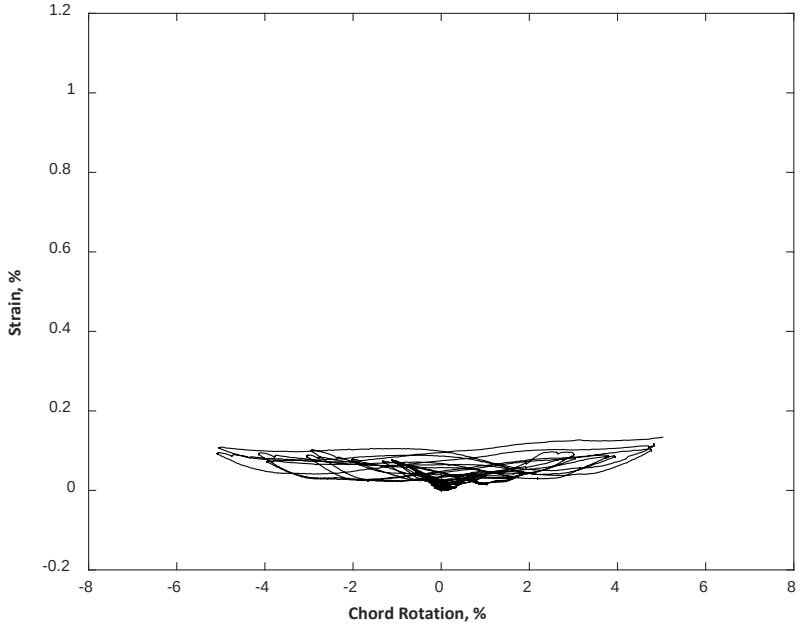

Figure D.119 – Strain measured with S7 for CB1

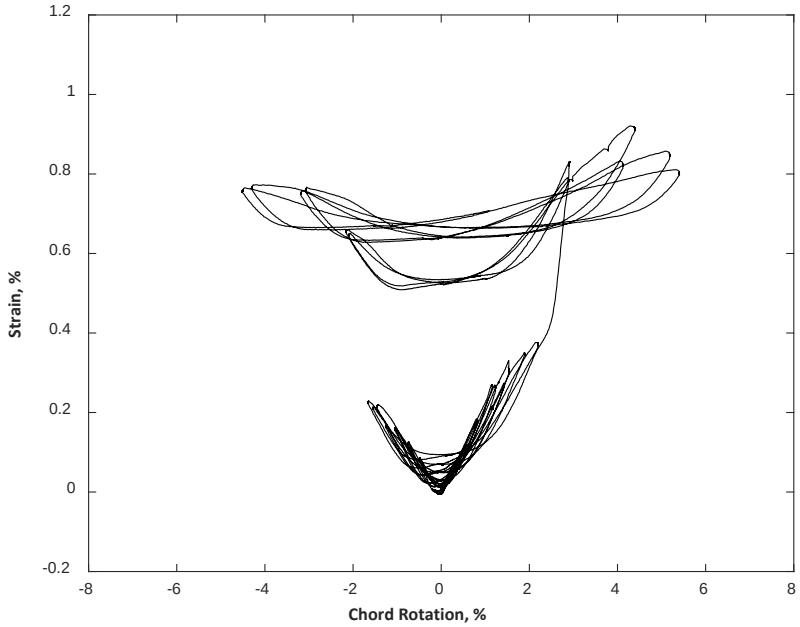

Figure D.120 – Strain measured with S7 for CB2

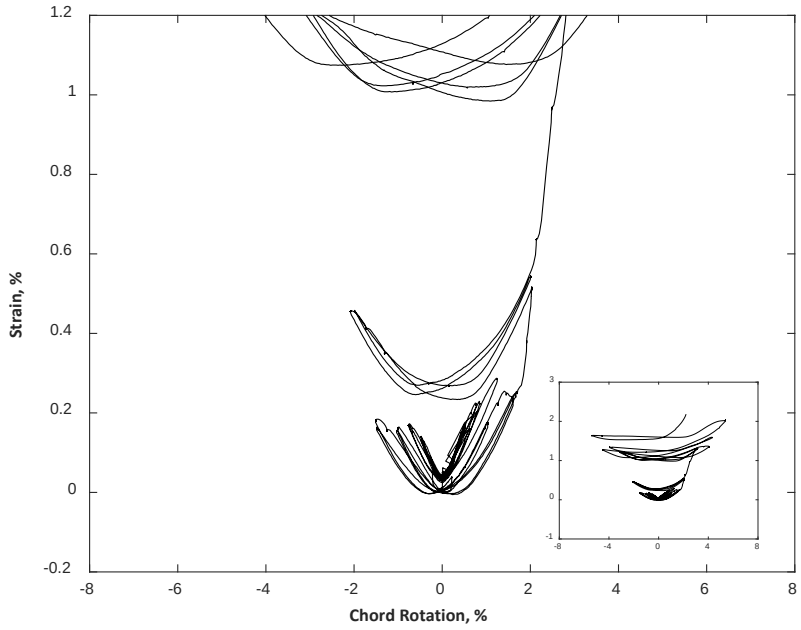

Figure D.121 – Strain measured with S7 for CB2D

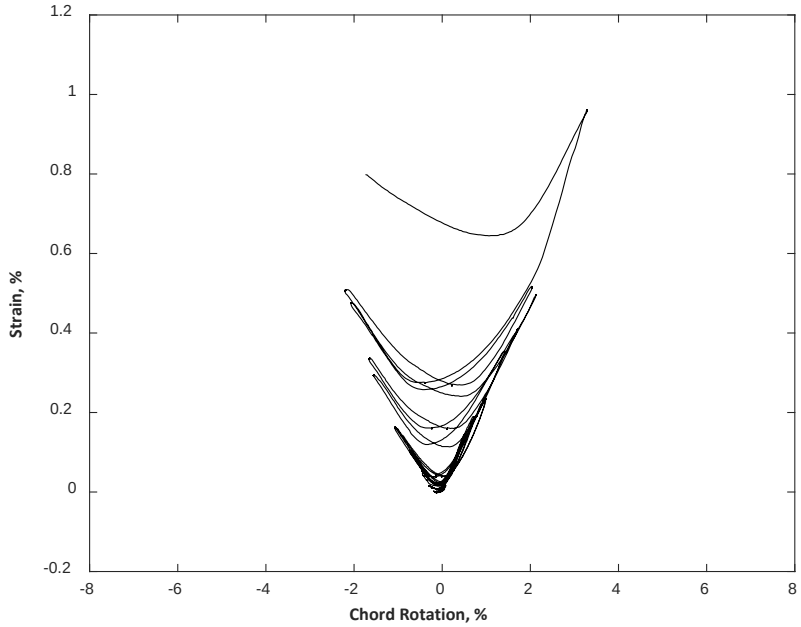

Figure D.122 – Strain measured with S7 for CB2AD

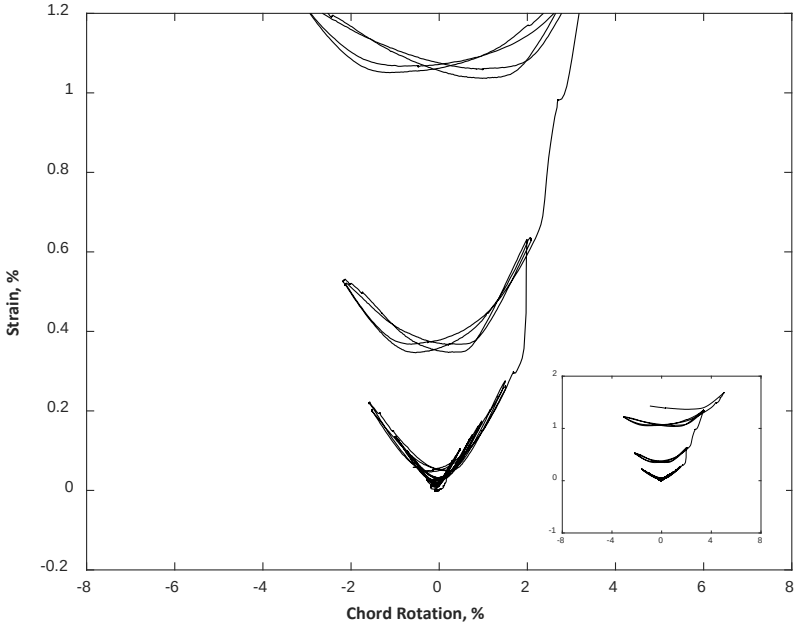

Figure D.123 – Strain measured with S7 for CB3D

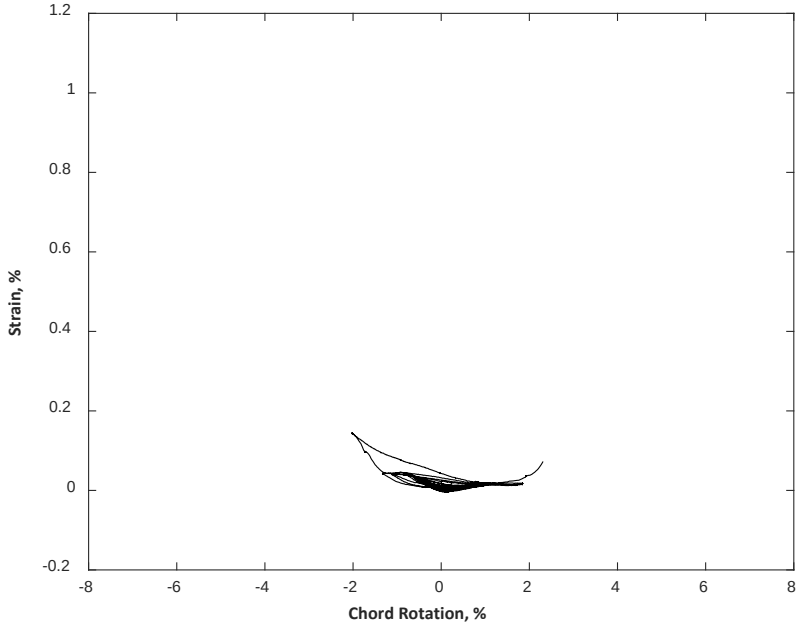

Figure D.124 – Strain measured with S8 for CB1

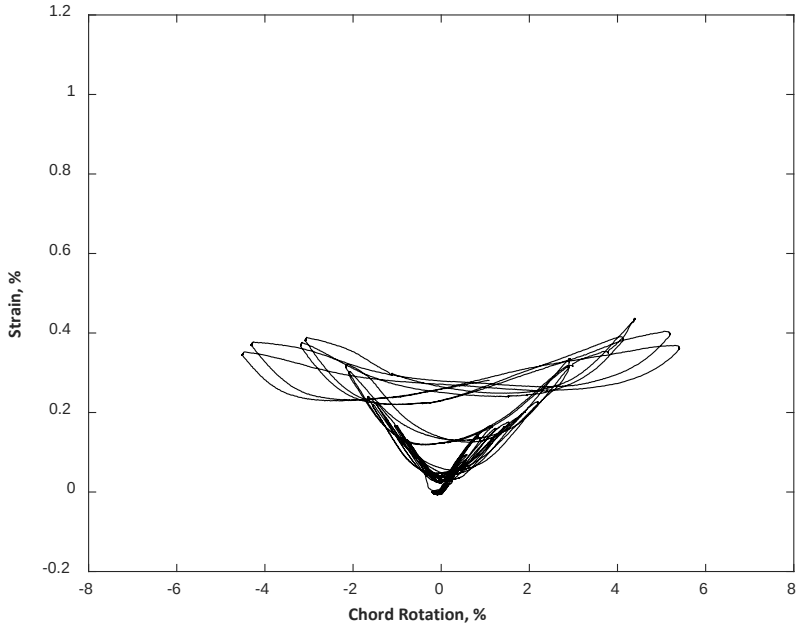

Figure D.125 – Strain measured with S8 for CB2

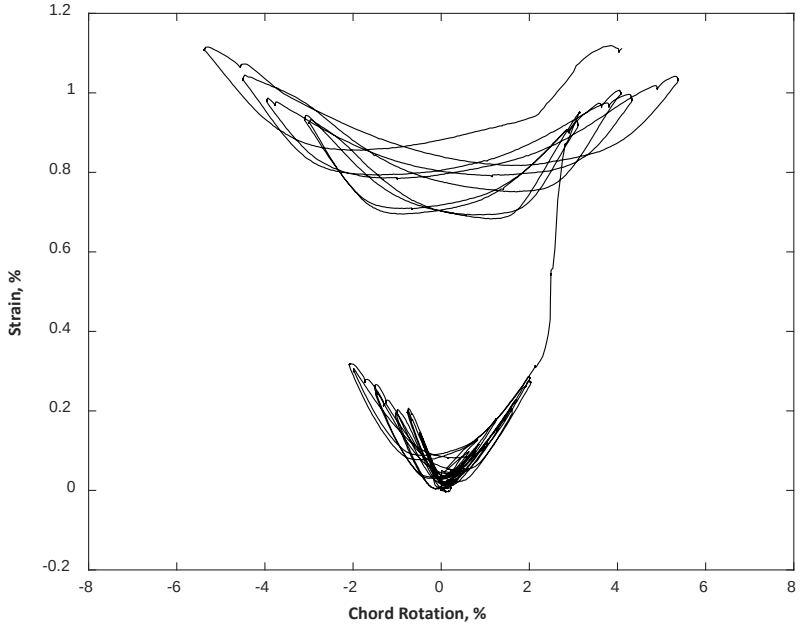

Figure D.126 – Strain measured with S8 for CB2D

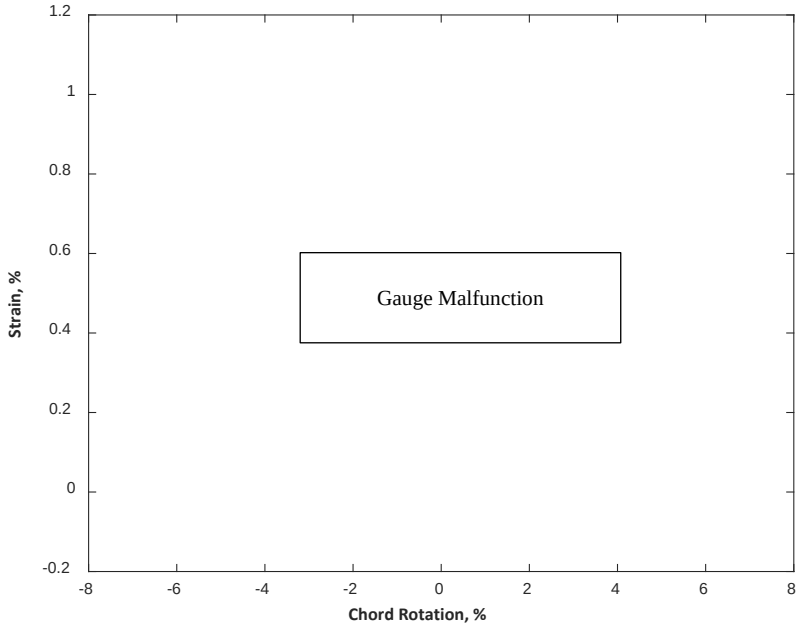

Figure D.127 – Strain measured with S8 for CB2AD

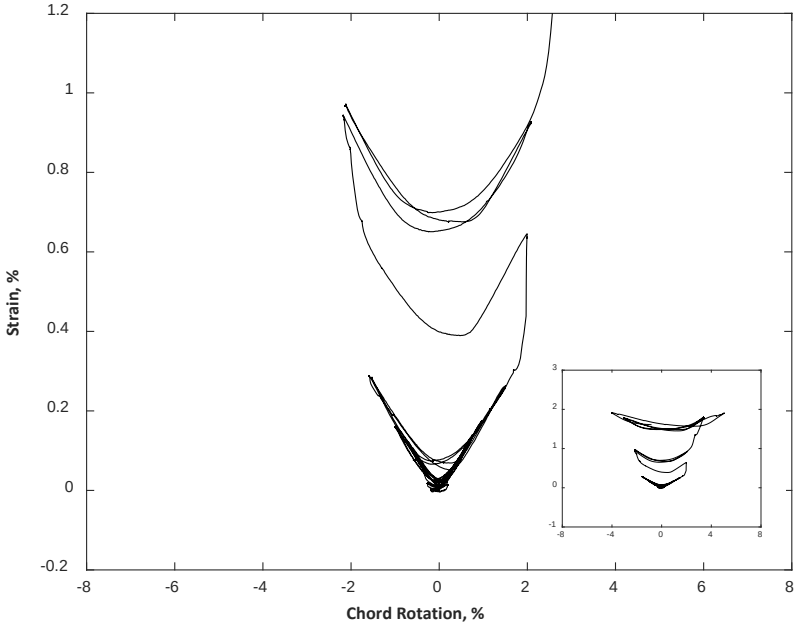

Figure D.128 – Strain measured with S8 for CB3D

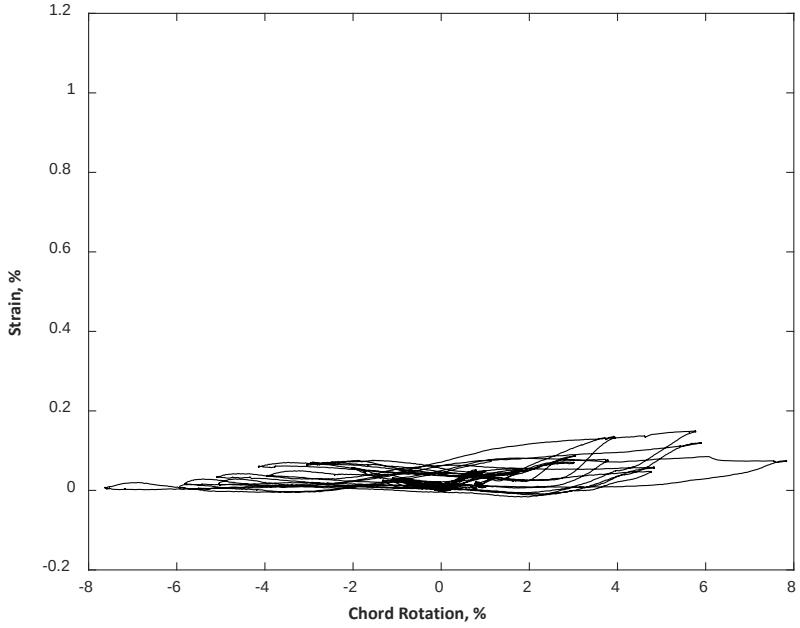

Figure D.129 – Strain measured with S9 for CB1

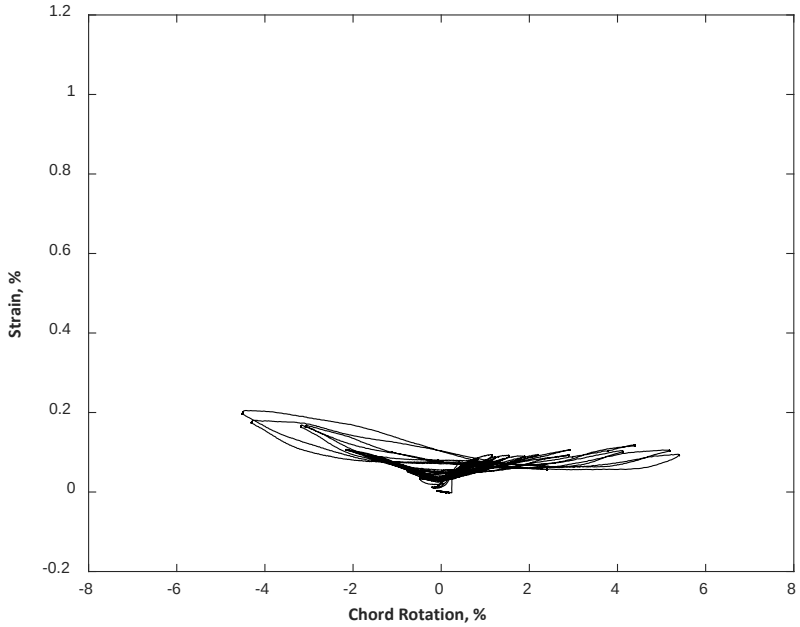

Figure D.130 – Strain measured with S9 for CB2

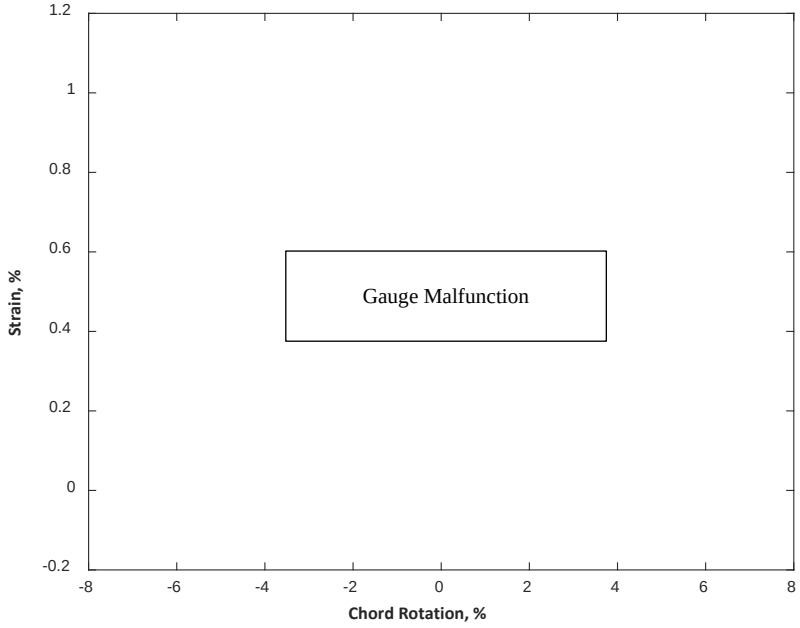

Figure D.131 – Strain measured with S9 for CB2D

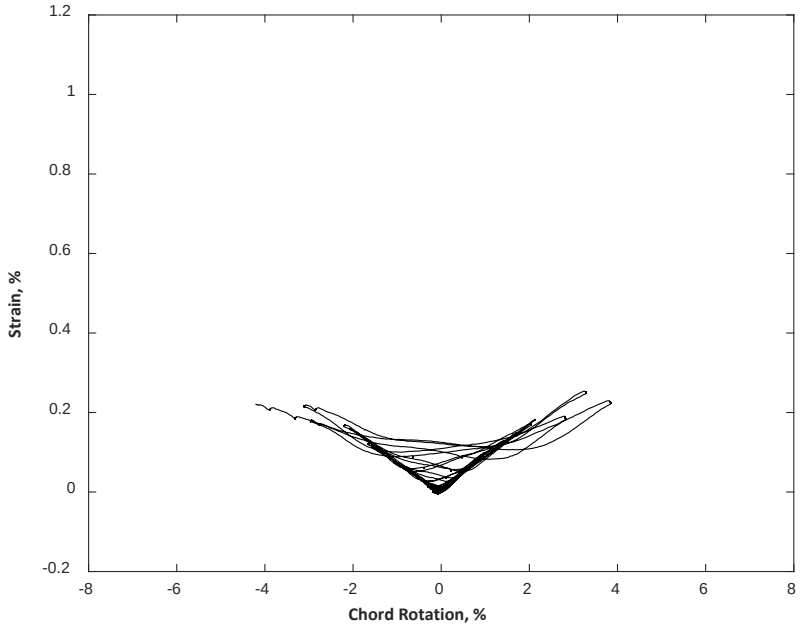

Figure D.132 – Strain measured with S9 for CB2AD

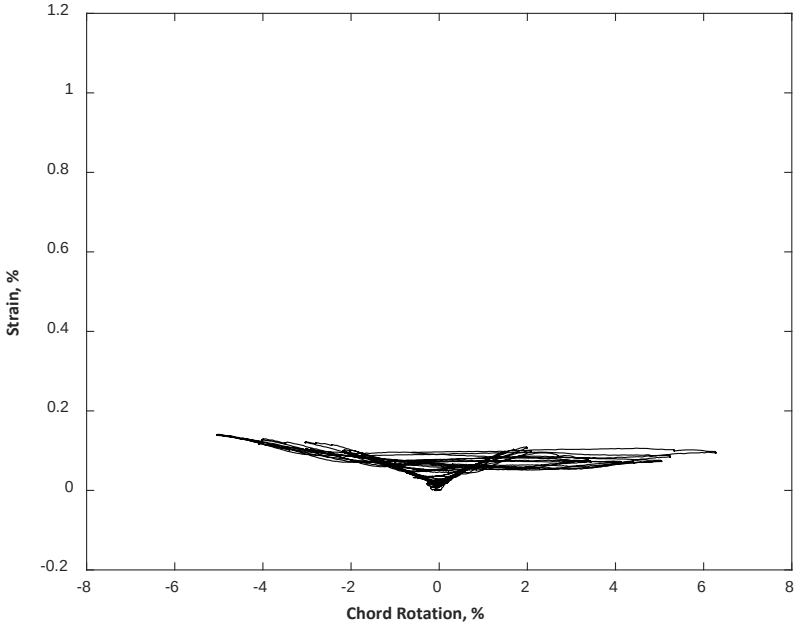

Figure D.133 – Strain measured with S9 for CB3D

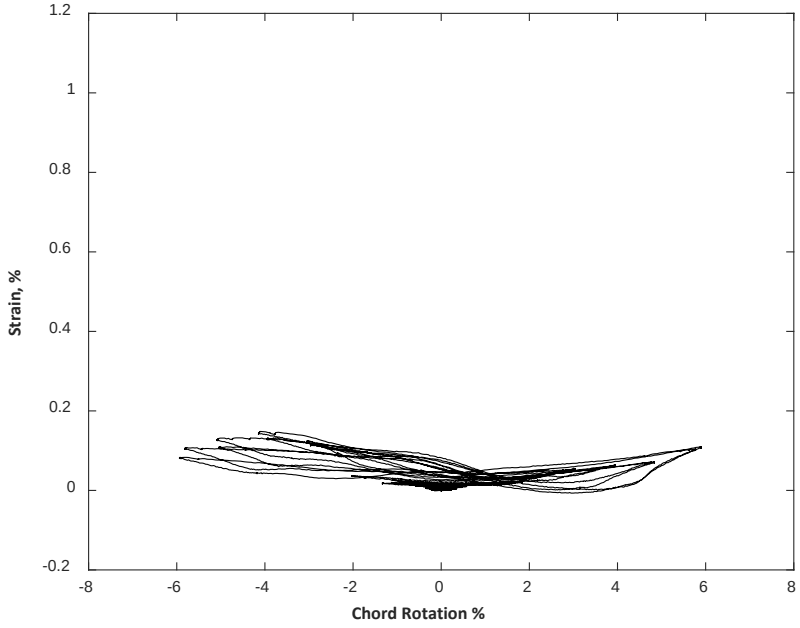

Figure D.134 – Strain measured with T1 for CB1

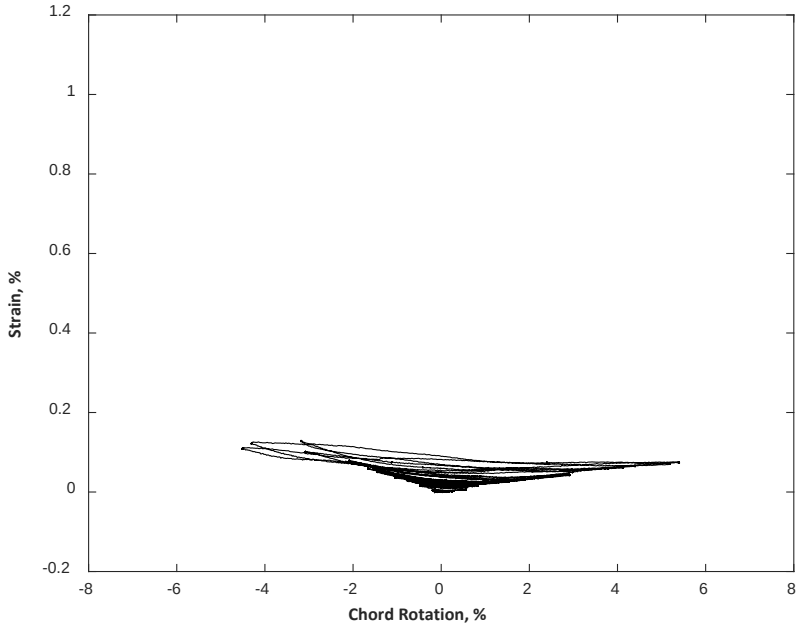

Figure D.135 – Strain measured with T1 for CB2

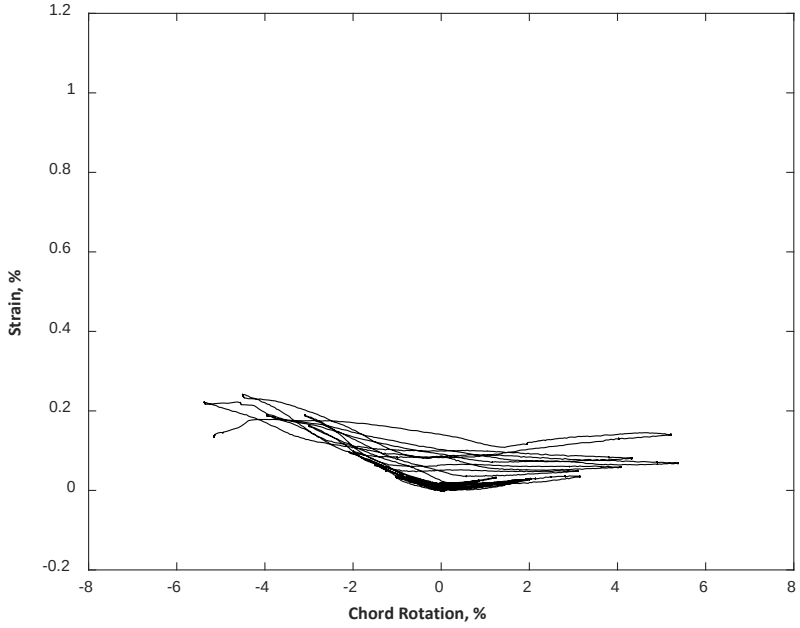

Figure D.136 – Strain measured with T1 for CB2D

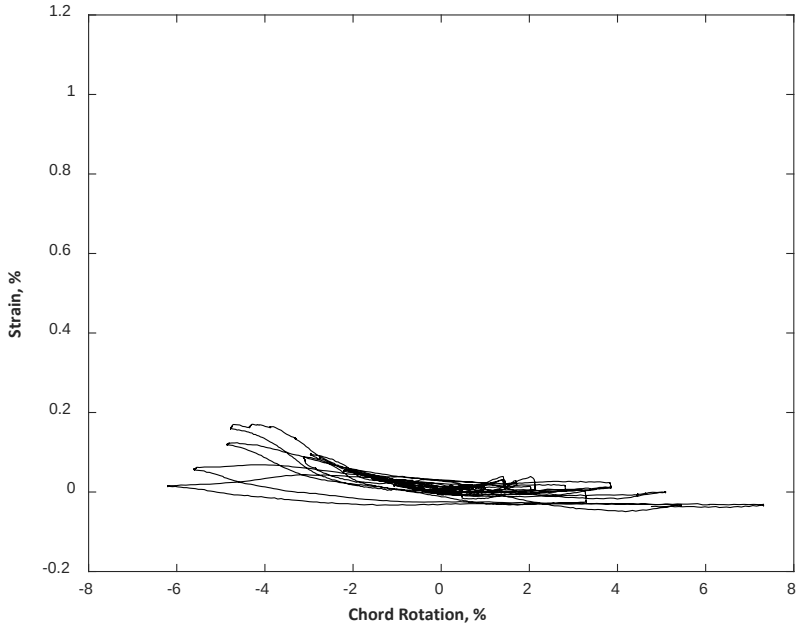

Figure D.137 – Strain measured with T1 for CB2AD

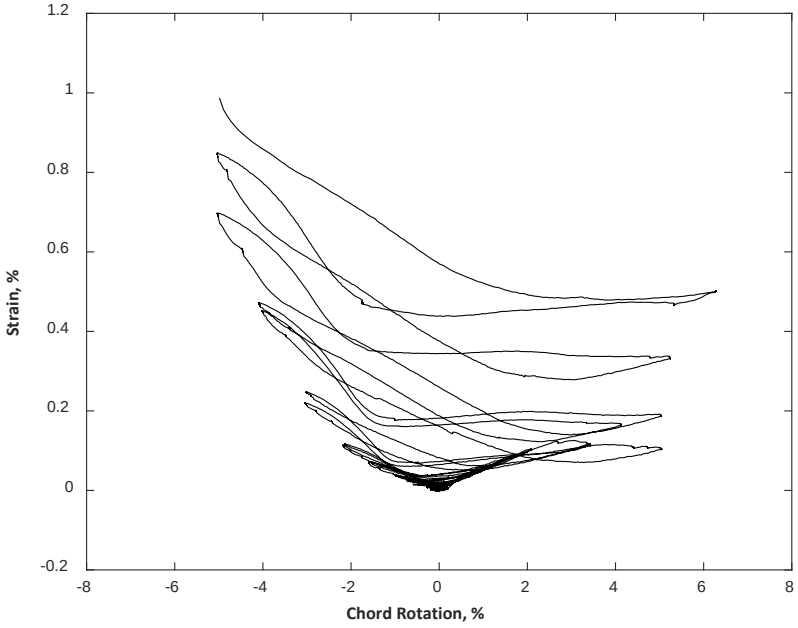

Figure D.138 – Strain measured with T1 for CB3D

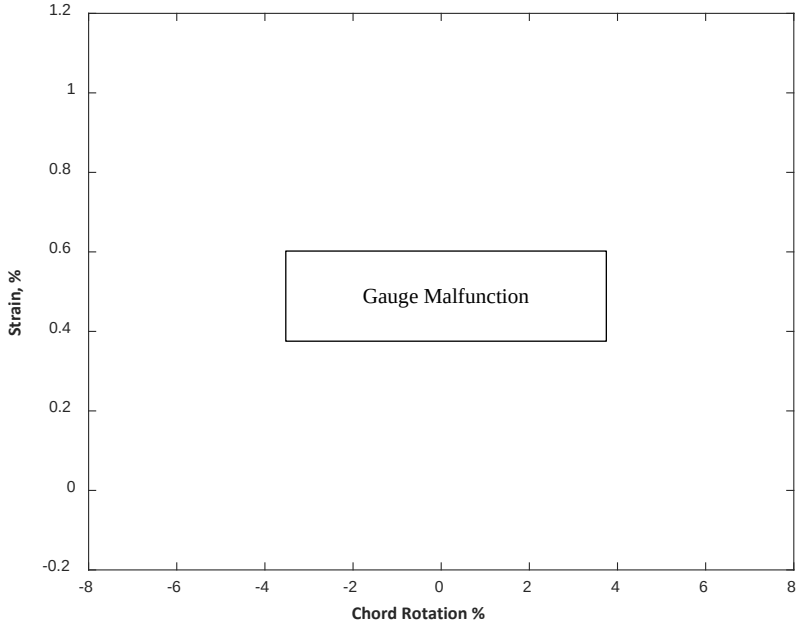

Figure D.139 – Strain measured with T2 for CB1

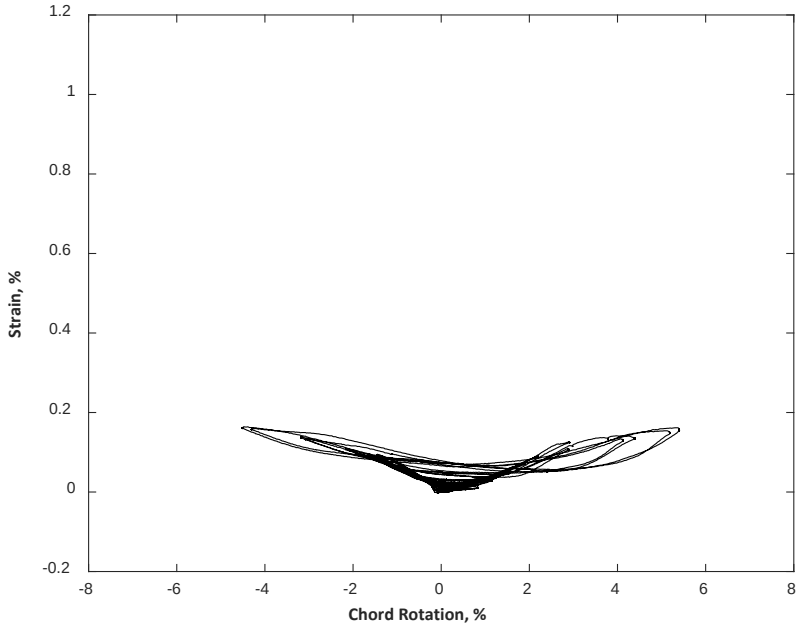

Figure D.140 – Strain measured with T2 for CB2

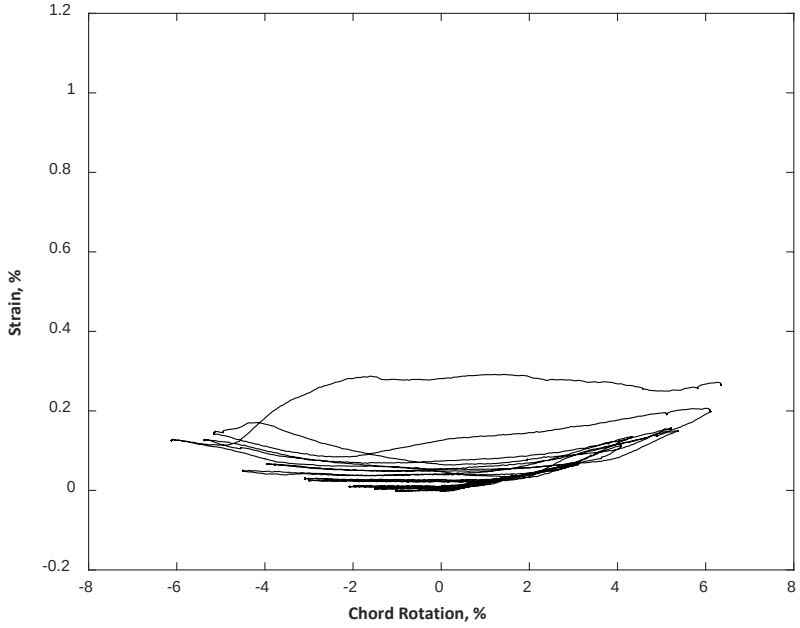

Figure D.141 – Strain measured with T2 for CB2D

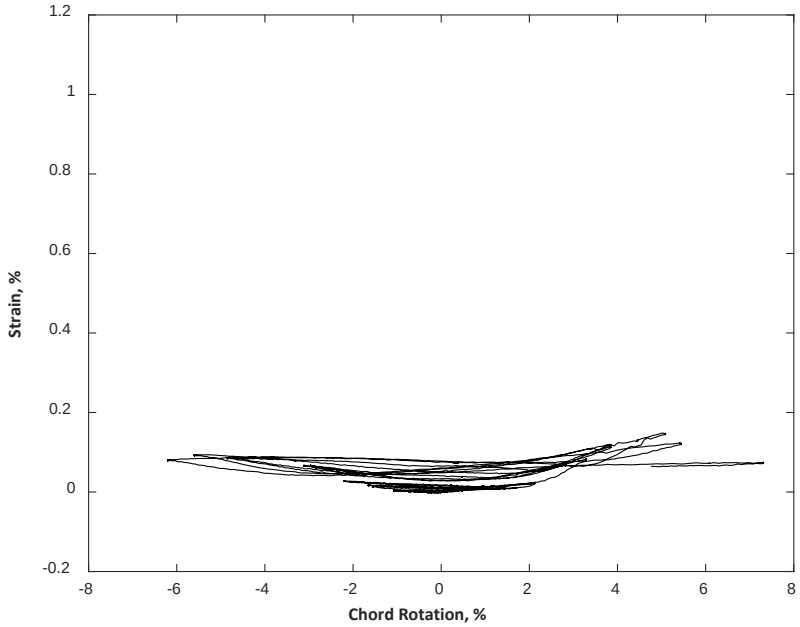

Figure D.142 – Strain measured with T2 for CB2AD

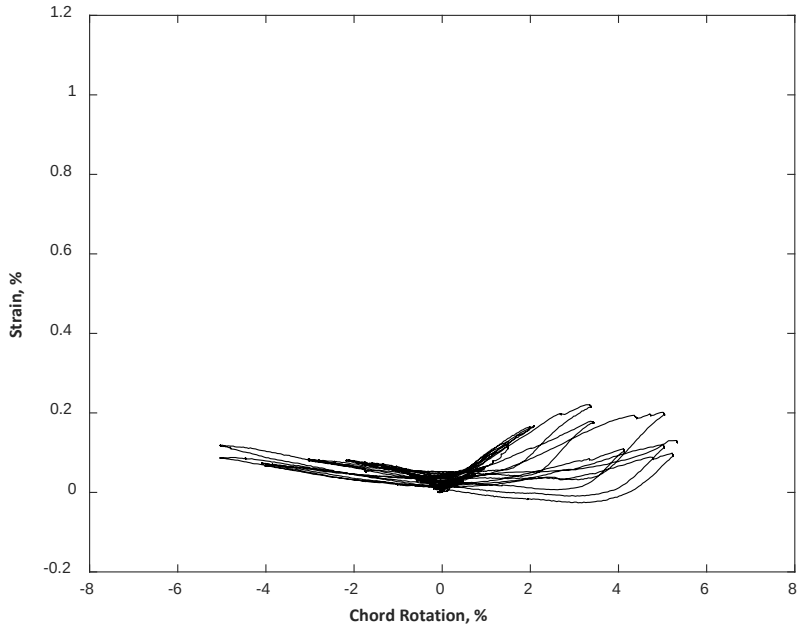

Figure D.143 – Strain measured with T2 for CB3D

APPENDIX E STIFFNESS

Table E.1 – Secant stiffness from measured shear-chord rotation envelope for CB1 during positive chord rotations (1 kip = 4.45 kN, 1 kip/in. = 0.175 kN/mm)

Chord Rotation, CR [a]	Shear, V	V/V_{max} [b]	Secant Stiffness, K [c]	Shear at $0.75V_{max}$	CR at $0.75V_{max}$	K_e [d]
%	kips		kips/in.	kips	%	kips/in.
0.33	86	0.47	755			
0.56	131	0.72	682			
0.77	153	0.84	584			
0.98	162	0.89	486			
1.69	164	0.90	287			
2.94	182	1.00	182	136	0.61	656
3.89	180	0.99	136			
4.69	178	0.98	112			
5.73	178	0.98	91.3			
7.69	151	0.83	57.6			

[a] Identifies chord rotation, *CR*, associated with peak force for each step (two cycles per step) of the loading protocol. Chord Rotation, *CR*, is defined as the relative lateral displacement between end blocks divided by the beam clear span and correcting for rotation of the bottom and top blocks.

[b] V_{max} is the maximum measured shear force per loading direction.

[c] K is calculated using $V/(CR \cdot l_n)$, where l_n is the clear span of the beam measured from the top of the bottom block to the bottom of the top block (Figure 4.1).

[d] K_e corresponds to the secant stiffness at $V = 0.75V_{max}$, based on linear interpolation.

Table E.2 – Secant stiffness from measured shear-chord rotation envelope for CB1 during negative chord rotations (1 kip = 4.45 kN, 1 kip/in. = 0.175 kN/mm)

Chord Rotation, CR [a]	Shear, V	V/V_{max} [b]	Secant Stiffness, K [c]	Shear at $0.75V_{max}$	CR at $0.75V_{max}$	K_e [d]
%	kips		kips/in.	kips	%	kips/in.
-0.33	-86	0.47	770			
-0.56	-131	0.71	693			
-0.72	-151	0.82	619			
-0.83	-150	0.82	534			
-1.31	-161	0.87	360			
-2.92	-179	0.97	180	-138	-0.63	667
-4.03	-184	1.00	134			
-4.96	-182	0.99	108			
-5.59	-172	0.93	90.5			
-6.88	-129	0.70	55.1			

[a] Identifies chord rotation, *CR*, associated with peak force for each step (two cycles per step) of the loading protocol. Chord Rotation, *CR*, is defined as the relative lateral displacement between end blocks divided by the beam clear span and correcting for rotation of the bottom and top blocks.

[b] V_{max} is the maximum measured shear force per loading direction.

[c] K is calculated using $V/(CR \cdot l_n)$, where l_n is the clear span of the beam measured from the top of the bottom block to the bottom of the top block (Figure 4.1).

[d] K_e corresponds to the secant stiffness at $V = 0.75V_{max}$, based on linear interpolation.

Table E.3 – Secant stiffness from measured shear-chord rotation envelope for CB2 during positive chord rotations (1 kip = 4.45 kN, 1 kip/in. = 0.175 kN/mm)

Chord Rotation, CR [a]	Shear, V	V/V_{max} [b]	Secant Stiffness, K [c]	Shear at $0.75V_{max}$	CR at $0.75V_{max}$	K_e [d]
%	kips		kips/in.	kips	%	kips/in.
0.24	50	0.24	609			
0.55	90	0.44	483			
0.83	121	0.59	430			
1.15	152	0.74	389			
1.53	171	0.83	329	154	1.23	384
1.89	185	0.90	288			
2.90	203	0.99	206			
4.34	205	1.00	139			
4.89	206	1.00	124			

[a] Identifies chord rotation, *CR*, associated with peak force for each step (two cycles per step) of the loading protocol. Chord Rotation, *CR*, is defined as the relative lateral displacement between end blocks divided by the beam clear span and correcting for rotation of the bottom and top blocks.

[b] V_{max} is the maximum measured shear force per loading direction.

[c] K is calculated using $V/(CR \cdot l_n)$, where l_n is the clear span of the beam measured from the top of the bottom block to the bottom of the top block (Figure 4.1).

[d] K_e corresponds to the secant stiffness at $V = 0.75V_{max}$, based on linear interpolation.

Table E.4 – Secant stiffness from measured shear-chord rotation envelope for CB2 during negative chord rotations (1 kip = 4.45 kN, 1 kip/in. = 0.175 kN/mm)

Chord Rotation, CR [a]	Shear, V	V/V_{max} [b]	Secant Stiffness, K [c]	Shear at $0.75V_{max}$	CR at $0.75V_{max}$	K_e [d]
%	kips		kips/in.	kips	%	kips/in.
-0.15	-47	0.25	920			
-0.47	-90	0.47	560			
-0.74	-122	0.64	487			
-1.04	-147	0.77	418			
-1.43	-173	0.90	355	-144	-0.97	428
-1.65	-178	0.93	317			
-2.14	-187	0.98	257			
-3.06	-192	1.00	184			
-4.27	-190	0.99	131			

[a] Identifies chord rotation, *CR*, associated with peak force for each step (two cycles per step) of the loading protocol. Chord Rotation, *CR*, is defined as the relative lateral displacement between end blocks divided by the beam clear span and correcting for rotation of the bottom and top blocks.

[b] V_{max} is the maximum measured shear force per loading direction.

[c] K is calculated using $V/(CR \cdot l_n)$, where l_n is the clear span of the beam measured from the top of the bottom block to the bottom of the top block (Figure 4.1).

[d] K_e corresponds to the secant stiffness at $V = 0.75V_{max}$, based on linear interpolation.

Table E.5 – Secant stiffness from measured shear-chord rotation envelope for CB2D during positive chord rotations (1 kip = 4.45 kN, 1 kip/in. = 0.175 kN/mm)

Chord Rotation, CR [a]	Shear, V	V/V_{max} [b]	Secant Stiffness, K [c]	Shear at $0.75V_{max}$	CR at $0.75V_{max}$	K_e [d]
%	kips		kips/in.	kips	%	kips/in.
0.21	51	0.25	717			
0.32	58	0.29	541			
0.51	83	0.41	475			
0.75	121	0.59	471			
1.24	150	0.74	358			
1.53	182	0.89	350	153	1.08	357
1.99	191	0.94	283			
3.05	204	1.00	197			
3.96	198	0.97	147			
5.16	189	0.93	108			
5.98	128	0.63	62.8			

[a] Identifies chord rotation, *CR*, associated with peak force for each step (two cycles per step) of the loading protocol. Chord Rotation, *CR*, is defined as the relative lateral displacement between end blocks divided by the beam clear span and correcting for rotation of the bottom and top blocks.

[b] V_{max} is the maximum measured shear force per loading direction.

[c] K is calculated using $V/(CR \cdot l_n)$, where l_n is the clear span of the beam measured from the top of the bottom block to the bottom of the top block (Figure 4.1).

[d] K_e corresponds to the secant stiffness at $V = 0.75V_{max}$, based on linear interpolation.

Table E.6 – Secant stiffness from measured shear-chord rotation envelope for CB2D during negative chord rotations (1 kip = 4.45 kN, 1 kip/in. = 0.175 kN/mm)

Chord Rotation, CR [a]	Shear, V	V/V_{max} [b]	Secant Stiffness, K [c]	Shear at $0.75V_{max}$	CR at $0.75V_{max}$	K_e [d]
%	kips		kips/in.	kips	%	kips/in.
-0.22	-51	0.26	685			
-0.28	-60	0.31	632			
-0.48	-88	0.45	547			
-0.74	-115	0.59	457			
-0.99	-141	0.72	416			
-1.44	-171	0.88	349	-146	-1.10	405
-1.93	-191	0.98	291			
-2.96	-194	1.00	193			
-4.45	-189	0.97	125			
-5.21	-174	0.90	98.4			
-5.94	-60	0.31	29.6			

[a] Identifies chord rotation, *CR*, associated with peak force for each step (two cycles per step) of the loading protocol. Chord Rotation, *CR*, is defined as the relative lateral displacement between end blocks divided by the beam clear span and correcting for rotation of the bottom and top blocks.

[b] V_{max} is the maximum measured shear force per loading direction.

[c] K is calculated using $V/(CR \cdot l_n)$, where l_n is the clear span of the beam measured from the top of the bottom block to the bottom of the top block (Figure 4.1).

[d] K_e corresponds to the secant stiffness at $V = 0.75V_{max}$, based on linear interpolation.

Table E.7 – Secant stiffness from measured shear-chord rotation envelope for CB2AD during positive chord rotations (1 kip = 4.45 kN, 1 kip/in. = 0.175 kN/mm)

Chord Rotation, CR [a]	Shear, V	V/V_{max} [b]	Secant Stiffness, K [c]	Shear at $0.75V_{max}$	CR at $0.75V_{max}$	K_e [d]
%	kips		kips/in.	kips	%	kips/in.
0.24	52	0.23	633			
0.46	86	0.38	548			
0.71	113	0.50	469			
0.97	150	0.66	454			
1.41	186	0.81	388	171	1.39	415
2.11	214	0.93	298			
3.24	229	1.00	208			
3.81	227	1.00	176			
5.06	221	0.97	129			

[a] Identifies chord rotation, *CR*, associated with peak force for each step (two cycles per step) of the loading protocol. Chord Rotation, *CR*, is defined as the relative lateral displacement between end blocks divided by the beam clear span and correcting for rotation of the bottom and top blocks.

[b] V_{max} is the maximum measured shear force per loading direction.

[c] K is calculated using $V/(CR \cdot l_n)$, where l_n is the clear span of the beam measured from the top of the bottom block to the bottom of the top block (Figure 4.1).

[d] K_e corresponds to the secant stiffness at $V = 0.75V_{max}$, based on linear interpolation.

Table E.8 – Secant stiffness from measured shear-chord rotation envelope for CB2AD during negative chord rotations (1 kip = 4.45 kN, 1 kip/in. = 0.175 kN/mm)

Chord Rotation, CR [a]	Shear, V	V/V_{max} [b]	Secant Stiffness, K [c]	Shear at $0.75V_{max}$	CR at $0.75V_{max}$	K_e [d]
%	kips		kips/in.	kips	%	kips/in.
-0.24	-52	0.22	643			
-0.45	-87	0.38	575			
-0.70	-116	0.50	490			
-1.03	-148	0.63	423			
-1.54	-185	0.80	354	174	-1.47	374
-2.03	-203	0.87	293			
-3.07	-225	0.97	216			
-4.73	-232	1.00	145			
-5.14	-201	0.86	115			

[a] Identifies chord rotation, *CR*, associated with peak force for each step (two cycles per step) of the loading protocol. Chord Rotation, *CR*, is defined as the relative lateral displacement between end blocks divided by the beam clear span and correcting for rotation of the bottom and top blocks.

[b] V_{max} is the maximum measured shear force per loading direction.

[c] K is calculated using $V/(CR \cdot l_n)$, where l_n is the clear span of the beam measured from the top of the bottom block to the bottom of the top block (Figure 4.1).

[d] K_e corresponds to the secant stiffness at $V = 0.75V_{max}$, based on linear interpolation.

Table E.9 – Secant stiffness from measured shear-chord rotation envelope for CB3D during positive chord rotations (1 kip = 4.45 kN, 1 kip/in. = 0.175 kN/mm)

Chord Rotation, CR [a]	Shear, V	V/V_{max} [b]	Secant Stiffness, K [c]	Shear at $0.75V_{max}$	CR at $0.75V_{max}$	K_e [d]
%	kips		kips/in.	kips	%	kips/in.
0.19	51	0.19	804			
0.27	61	0.22	660			
0.48	91	0.33	560			
0.75	132	0.48	519			
0.96	162	0.59	496			
1.49	217	0.79	428	205	1.39	442
1.98	243	0.89	363			
3.34	265	0.97	233			
5.01	274	1.00	161			
5.02	249	0.91	146			
5.78	254	0.93	129			

[a] Identifies chord rotation, *CR*, associated with peak force for each step (two cycles per step) of the loading protocol. Chord Rotation, *CR*, is defined as the relative lateral displacement between end blocks divided by the beam clear span and correcting for rotation of the bottom and top blocks.

[b] V_{max} is the maximum measured shear force per loading direction.

[c] K is calculated using $V/(CR \cdot l_n)$, where l_n is the clear span of the beam measured from the top of the bottom block to the bottom of the top block (Figure 4.1).

[d] K_e corresponds to the secant stiffness at $V = 0.75V_{max}$, based on linear interpolation.

Table E.10 – Secant stiffness from measured shear-chord rotation envelope for CB3D during negative chord rotations (1 kip = 4.45 kN, 1 kip/in. = 0.175 kN/mm)

Chord Rotation, *CR* [a]	Shear, *V*	V/V_{max} [b]	Secant Stiffness, *K* [c]	Shear at $0.75V_{max}$	*CR* at $0.75V_{max}$	K_e [d]
%	kips		kips/in.	kips	%	kips/in.
-0.19	-47	0.18	728			
-0.26	-62	0.23	692			
-0.49	-98	0.37	589			
-0.73	-140	0.53	563			
-0.98	-172	0.64	517			
-1.57	-227	0.85	424	-200	-1.27	468
-2.14	-252	0.94	346			
-3.00	-263	0.99	258			
-3.93	-267	1.00	200			
-4.98	-264	0.99	156			
-5.38	-116	0.43	63.0			

[a] Identifies chord rotation, *CR*, associated with peak force for each step (two cycles per step) of the loading protocol. Chord Rotation, *CR*, is defined as the relative lateral displacement between end blocks divided by the beam clear span and correcting for rotation of the bottom and top blocks.

[b] V_{max} is the maximum measured shear force per loading direction.

[c] *K* is calculated using $V/(CR \cdot l_n)$, where l_n is the clear span of the beam measured from the top of the bottom block to the bottom of the top block (Figure 4.1).

[d] K_e corresponds to the secant stiffness at $V = 0.75V_{max}$, based on linear interpolation.

Table E.11 – Unloading stiffness calculated from measured shear versus chord rotation for CB1 during positive chord rotations (1 kip = 4.45 kN, 1 kip/in. = 0.175 kN/mm)

Chord Rotation, *CR* [a]	*CR* at Zero Shear, CR_0 [b]	Shear, *V* [c]	Unloading Stiffness, K_u [d]
%	%	kips	kips/in.
0.16	0.00	35.6	646
0.22	-0.01	54.3	688
0.35	0.00	86.2	740
0.56	0.03	129	708
0.73	0.08	149	676
0.97	0.25	151	622
1.79	0.86	165	519
2.97	1.65	170	381
3.66	2.22	170	348
4.80	3.16	171	305
5.63	4.02	169	307

[a] *CR* corresponds to peak chord rotation during second cycle to a target chord rotation.
[b] CR_0 corresponds to chord rotation at zero shear after unloading from *CR*. Calculated based on a linear interpolation between chord rotations at ± 5 kips (± 22 kN).
[c] *V* corresponds to peak chord rotation, *CR*.
[d] K_u is calculated using $V/((CR - CR_0)\, l_n)$, where l_n is the clear span of the beam measured from the top of the bottom block to the bottom of the top block (Figure 4.1).

Table E.12 – Unloading stiffness calculated from measured shear versus chord rotation for CB1 during negative chord rotations (1 kip = 4.45 kN, 1 kip/in. = 0.175 kN/mm)

Chord Rotation, *CR* [a]	*CR* at Zero Shear, CR_0 [b]	Shear, *V* [c]	Unloading Stiffness, K_u [d]
%	%	kips	kips/in.
-0.15	-0.03	-36.4	894
-0.22	-0.03	-53.9	829
-0.35	-0.04	-86.6	827
-0.60	-0.07	-132	740
-0.69	-0.09	-136	670
-1.10	-0.36	-166	661
-1.93	-0.94	-182	540
-2.96	-1.69	-173	402
-3.91	-2.45	-171	345
-4.92	-3.42	-174	342
-5.73	-4.24	-159	315

[a] *CR* corresponds to peak chord rotation during second cycle to a target chord rotation.
[b] CR_0 corresponds to chord rotation at zero shear during unloading from *CR*.
[c] *V* corresponds to peak chord rotation, *CR*.
[d] K_u is calculated using $V/((CR - CR_0)\, l_n)$, where l_n is the clear span of the beam measured from the top of the bottom block to the bottom of the top block (Figure 4.1).

Table E.13 – Unloading stiffness calculated from measured shear versus chord rotation for CB2 during positive chord rotations (1 kip = 4.45 kN, 1 kip/in. = 0.175 kN/mm)

Chord Rotation, *CR* [a]	*CR* at Zero Shear, CR_0 [b]	Shear, *V* [c]	Unloading Stiffness, K_u [d]
%	%	kips	kips/in.
0.28	0.03	54.3	628
0.57	0.12	89.7	592
0.83	0.12	117	490
1.22	0.25	148	449
1.43	0.18	151	356
2.15	0.55	192	354
2.88	0.85	193	279
4.06	1.76	190	242
5.23	2.39	187	194

[a] *CR* corresponds to peak chord rotation during second cycle to a target chord rotation.
[b] CR_0 corresponds to chord rotation at zero shear during unloading from *CR*.
[c] *V* corresponds to peak chord rotation, *CR*.
[d] K_u is calculated using $V/((CR - CR_0)\, l_n)$, where l_n is the clear span of the beam measured from the top of the bottom block to the bottom of the top block (Figure 4.1).

Table E.14 – Unloading stiffness calculated from measured shear versus chord rotation for CB2 during negative chord rotations (1 kip = 4.45 kN, 1 kip/in. = 0.175 kN/mm)

Chord Rotation, *CR* [a]	*CR* at Zero Shear, CR_0 [b]	Shear, *V* [c]	Unloading Stiffness, K_u [d]
%	%	kips	kips/in.
-0.19	0.03	-52.2	684
-0.48	-0.01	-89.1	554
-0.76	-0.07	-118	502
-1.00	-0.02	-144	429
-1.26	-0.08	-141	353
-1.54	0.10	-161	287
-2.08	0.03	-176	246
-3.16	-0.46	-188	205
-4.47	-1.50	-182	180

[a] *CR* corresponds to peak chord rotation during second cycle to a target chord rotation.
[b] CR_0 corresponds to chord rotation at zero shear during unloading from *CR*.
[c] *V* corresponds to peak chord rotation, *CR*.
[d] K_u is calculated using $V/((CR - CR_0)\, l_n)$, where l_n is the clear span of the beam measured from the top of the bottom block to the bottom of the top block (Figure 4.1).

Table E.15 – Unloading stiffness calculated from measured shear versus chord rotation for CB2D during positive chord rotations (1 kip = 4.45 kN, 1 kip/in. = 0.175 kN/mm)

Chord Rotation, CR [a]	CR at Zero Shear, CR_0 [b]	Shear, V [c]	Unloading Stiffness, K_u [d]
%	%	kips	kips/in.
0.26	0.04	51.4	670
0.33	0.04	57.6	600
0.51	0.07	78.3	525
0.84	0.15	106	456
1.02	0.06	141	432
1.66	0.20	173	348
1.97	0.19	177	292
3.05	0.63	185	224
4.20	1.21	188	185
5.13	1.98	165	154
6.22	3.29	61	61

[a] CR corresponds to peak chord rotation during second cycle to a target chord rotation.
[b] CR_0 corresponds to chord rotation at zero shear during unloading from CR.
[c] V corresponds to peak chord rotation, CR.
[d] K_u is calculated using $V/((CR - CR_0)\, l_n)$, where l_n is the clear span of the beam measured from the top of the bottom block to the bottom of the top block (Figure 4.1).

Table E.16 – Unloading stiffness calculated from measured shear versus chord rotation for CB2D during negative chord rotations (1 kip = 4.45 kN, 1 kip/in. = 0.175 kN/mm)

Chord Rotation, *CR* [a]	*CR* at Zero Shear, CR_0 [b]	Shear, *V* [c]	Unloading Stiffness, K_u [d]
%	%	kips	kips/in.
-0.21	-0.02	-46.9	716
-0.27	-0.01	-56.5	652
-0.48	-0.03	-86.1	562
-0.76	-0.02	-120	480
-1.02	-0.12	-132	435
-1.48	-0.18	-161	362
-1.98	-0.33	-173	308
-3.01	-0.72	-183	236
-3.94	-1.02	-164	165
-4.24	-2.34	-126	194
-6.09	-3.70	-31.4	39

[a] *CR* corresponds to peak chord rotation during second cycle to a target chord rotation.
[b] CR_0 corresponds to chord rotation at zero shear during unloading from *CR*.
[c] *V* corresponds to peak chord rotation, *CR*.
[d] K_u is calculated using $V/((CR - CR_0)\, l_n)$, where l_n is the clear span of the beam measured from the top of the bottom block to the bottom of the top block (Figure 4.1).

Table E.17 – Unloading stiffness calculated from measured shear versus chord rotation for CB2AD during positive chord rotations (1 kip = 4.45 kN, 1 kip/in. = 0.175 kN/mm)

Chord Rotation, *CR* [a]	*CR* at Zero Shear, CR_0 [b]	Shear, *V* [c]	Unloading Stiffness, K_u [d]
%	%	kips	kips/in.
0.30	0.03	59.9	656
0.50	0.04	87.0	555
0.69	0.01	115	498
0.95	0.02	144	454
1.69	0.20	200	394
2.03	0.28	192	323
2.81	0.54	185	241
3.82	0.86	213	212
3.64	2.67	154	469

[a] *CR* corresponds to peak chord rotation during second cycle to a target chord rotation.
[b] CR_0 corresponds to chord rotation at zero shear during unloading from *CR*.
[c] *V* corresponds to peak chord rotation, *CR*.
[d] K_u is calculated using $V/((CR - CR_0)\, l_n)$, where l_n is the clear span of the beam measured from the top of the bottom block to the bottom of the top block (Figure 4.1).

Table E.18 – Unloading stiffness calculated from measured shear versus chord rotation for CB2AD during negative chord rotations (1 kip = 4.45 kN, 1 kip/in. = 0.175 kN/mm)

Chord Rotation, *CR* [a]	*CR* at Zero Shear, CR_0 [b]	Shear, *V* [c]	Unloading Stiffness, K_u [d]
%	%	kips	kips/in.
-0.29	-0.04	-62.5	739
-0.48	-0.06	-89.3	636
-0.73	-0.14	-114	572
-1.06	-0.23	-143	510
-1.64	-0.29	-183	402
-2.17	-0.44	-199	340
-2.94	-0.71	-201	265
-4.81	-1.99	-213	222

[a] *CR* corresponds to peak chord rotation during second cycle to a target chord rotation.
[b] CR_0 corresponds to chord rotation at zero shear during unloading from *CR*.
[c] *V* corresponds to peak chord rotation, *CR*.
[d] K_u is calculated using $V/((CR - CR_0)\, l_n)$, where l_n is the clear span of the beam measured from the top of the bottom block to the bottom of the top block (Figure 4.1).

Table E.19 – Unloading stiffness calculated from measured shear versus chord rotation for CB3D during positive chord rotations (1 kip = 4.45 kN, 1 kip/in. = 0.175 kN/mm)

Chord Rotation, *CR* [a]	*CR* at Zero Shear, CR_0 [b]	Shear, *V* [c]	Unloading Stiffness, K_u [d]
%	%	kips	kips/in.
0.19	0.00	46.9	719
0.30	0.02	60.7	647
0.47	0.04	87.5	596
0.74	0.05	128	551
0.96	0.05	158	515
1.50	0.10	209	437
2.07	0.23	237	380
3.33	1.02	240	305
4.11	1.37	220	236
5.21	1.95	249	224
6.54	3.88	63.0	70

[a] *CR* corresponds to peak chord rotation during second cycle to a target chord rotation.
[b] CR_0 corresponds to chord rotation at zero shear during unloading from *CR*.
[c] *V* corresponds to peak chord rotation, *CR*.
[d] K_u is calculated using $V/((CR - CR_0)\, l_n)$, where l_n is the clear span of the beam measured from the top of the bottom block to the bottom of the top block (Figure 4.1).

Table E.20 – Unloading stiffness calculated from measured shear versus chord rotation for CB3D during negative chord rotations (1 kip = 4.45 kN, 1 kip/in. = 0.175 kN/mm)

Chord Rotation, *CR* [a]	*CR* at Zero Shear, CR_0 [b]	Shear, *V* [c]	Unloading Stiffness, K_u [d]
%	%	kips	kips/in.
-0.19	-0.01	-47.3	756
-0.26	-0.00	-58.1	663
-0.47	-0.00	-97.0	612
-0.73	-0.05	-137	600
-0.99	-0.09	-167	547
-1.52	-0.14	-209	443
-2.11	-0.26	-232	368
-2.99	-0.48	-248	290
-4.05	-1.01	-255	246
-4.97	-1.77	-245	225

[a] *CR* corresponds to peak chord rotation during second cycle to a target chord rotation.
[b] CR_0 corresponds to chord rotation at zero shear during unloading from *CR*.
[c] *V* corresponds to peak chord rotation, *CR*.
[d] K_u is calculated using $V/((CR - CR_0)\, l_n)$, where l_n is the clear span of the beam measured from the top of the bottom block to the bottom of the top block (Figure 4.1).

APPENDIX F DATABASE

Table F.1 – Database of diagonally reinforced coupling beam specimens (1 in. = 25.4 mm, 1 ksi = 6.89 MPa, 1 psi = 0.00689 MPa, 1 kip = 4.45 kN)

Reference	Specimen ID (as stated)	b (in.)	h (in.)	l_n (in.)	$\frac{l_n}{h}$	Diagonal Reinforcement		
						No. [a]	d_b (in.)	f_y (ksi)
Paulay and Binney (1974)	316	6.00	31.0	40.0	1.29	4/3 [b]	0.875/1.0 [b]	41.8/41.7 [b]
	317	6.00	31.0	40.0	1.29	4/3 [b]	0.875/1.0 [b]	44.4/39.2 [b]
	395	6.00	39.0	40.0	1.03	4/3 [b]	0.875/1.0 [b]	37.6/41.9 [b]
Shiu, Barney, Fiorato, and Corley (1978)	C6	4.00	6.67	16.7	2.50	1/2 [b]	0.5/0.375 [b]	59.2/70.7 [b]
	C8	4.00	6.67	33.3	5.00	1/2 [b]	0.5/0.375 [b]	62.8/82.5 [b]
Tassios, Moretti and Bezas (1996)	CB-2A	5.12	19.7	19.7	1.00	4	0.375	73.1
	CB-2B	5.12	11.8	19.7	1.67	4	0.375	73.1
Galano and Vignoli (2000)	P07	5.91	15.7	23.6	1.50	4	0.375	82.2
	P12	5.91	15.7	23.6	1.50	4	0.375	82.2
Gonzalez (2001)	K	12.0	17.5	48.0	2.74	4	1.18	67.4
Kwan and Zhao (2002)	CCB11	4.72	23.6	27.6	1.17	6	0.315	75.0
Canbolat, Parra and Wight (2005)	Specimen 1	7.87	23.6	23.6	1.00	4	0.50	65.0
Fortney, Rassati, and Shahrooz (2008)	DCB-1	10.0	14.0	36.0	2.57	4	1.00	62.6
	DCB-2	10.0	12.0	36.0	3.00	4	0.875	69.2
Naish, Fry, Klemencic, and Wallace (2013)	CB24D	12.0	15.0	36.0	2.40	6	0.875	70.0
	CB33D	12.0	18.0	60.0	3.33	6	0.875	70.0
	CB24F	12.0	15.0	36.0	2.40	6	0.875	70.0
	CB33F	12.0	18.0	60.0	3.33	6	0.875	70.0
	CB24F-RC	12.0	15.0	36.0	2.40	6	0.875	70.0
	CB24F-PT	1.20	15.0	36.0	2.40	6	0.875	70.0
	CB24F-1/2-PT	12.0	15.0	36.0	2.40	6	0.875	70.0
Han, Lee, Shin, and Lee (2015)	SD-2.0	9.80	20.7	41.3	2.00	4	0.875	63.5
	SD-3.5	9.80	11.8	41.3	3.50	4	1.00	64.1
Lim, Hwang, Cheng, and Lin (2016)	CB30-DA	11.8	19.7	59.1	3.00	4	1.27	67.4
	CB30-DB	11.8	19.7	59.1	3.00	4	1.27	67.4
Lim, Hwang, Wang, and Chang (2016)	CB10-1	9.80	19.7	19.7	1.00	4	1.00	70.4
	CB20-1	11.8	19.7	39.4	2.00	4	1.128	67.6
Poudel (2018)	CB1A	10.0	18.0	34.0	1.89	6	0.875	63.0
Current study	CB1	10.0	18.0	34.0	1.89	6	0.875	63.0
	CB2	10.0	18.0	34.0	1.89	4	0.75	128
	CB2D	10.0	18.0	34.0	1.89	4	0.75	128
	CB2AD	10.0	18.0	34.0	1.89	4	0.75	128
	CB3D	10.0	18.0	34.0	1.89	6	0.75	128

[a] Number of bars in each diagonal group.
[b] Diagonal groups had different reinforcement detailing.

Table F.1 (continued)

Reference	Specimen ID (as stated)	Longitudinal Reinforcement				Transverse Reinforcement		
		No	d_b (in.)	f_y (ksi)	Condition	d_b (in.)	f_y (ksi)	s (in.)
Paulay and Binney (1974)	316	4	0.500	46.8	Cutoff	-	-	-
	317	4	0.250	-	Cutoff	0.250	-	4.0
	395	4	0.250	-	Cutoff	0.250	-	4.0
Shiu, Barney, Fiorato, and Corley (1978)	C6	4	D-3 wire	71.4	Cutoff	D-3 wire	71.4	1.3
	C8	4	D-3 wire	71.0	Cutoff	D-3 wire	71.0	1.3
Tassios, Moretti and Bezas (1996)	CB-2A	8	0.250	40.7	Developed	0.250	40.7	2.0
	CB-2B	8	0.250	40.7	Developed	0.250	40.7	2.0
Galano and Vignoli (2000)	P07	6	0.250	82.2	Developed	0.250	82.2	5.0
	P12	6	0.250	82.2	Developed	0.250	82.2	4.0
Gonzalez (2001)	K	4	0.44	-	Developed	0.44	-	4.0
Kwan and Zhao (2002)	CCB11	4	0.315	75.0	Developed	0.315	50.2	2.4
Canbolat, Parra and Wight (2005)	Specimen 1	10	0.250	-	Developed	0.250	-	3.0
Fortney, Rassati, and Shahrooz (2008)	DCB-1	4	0.750	60.7	Developed	0.375	60.6	3.0
	DCB-2	4	0.750	66.9	Cutoff	0.250	66.9	2.0
Naish, Fry, Klemencic, and Wallace (2013)	CB24D	10	0.250	70.0	Cutoff	0.375	70.0	2.5
	CB33D	12	0.250	70.0	Cutoff	0.375	70.0	2.5
	CB24F	10	0.375	70.0	Cutoff	0.375	70.0	3.0
	CB33F	12	0.375	70.0	Cutoff	0.375	70.0	3.0
	CB24F-RC	10	0.375	70.0	Cutoff	0.375	70.0	3.0
	CB24F-PT	10	0.375	70.0	Cutoff	0.375	70.0	3.0
	CB24F-1/2-PT	10	0.375	70.0	Cutoff	0.375	70.0	6.0
Han, Lee, Shin, and Lee (2015)	SD-2.0	14	0.500	73.4	Cutoff	0.500	73.4	4.7
	SD-3.5	10	0.500	73.4	Cutoff	0.500	73.4	4.3
Lim, Hwang, Cheng, and Lin (2016)	CB30-DA	4	0.500	63.9	Developed	0.375	68.9	5.9
	CB30-DB	10	0.375	68.9	Developed	0.375	68.9	3.9
Lim, Hwang, Wang, and Chang (2016)	CB10-1	10	0.375	-	Developed	0.500	67.9	3.9
	CB20-1	10	0.500	72.8	Developed	0.500	72.8	3.9
Poudel (2018)	CB1A	8	0.375	63.0	Cutoff	0.375	68.0	3.0
Current study	CB1	8	0.375	63.0	Cutoff	0.375	68.0	3.0
	CB2	8	0.375	63.0	Cutoff	0.375	68.0	3.0
	CB2D	8	0.375	63.0	Developed	0.375	68.0	3.0
	CB2AD	8	0.375	63.0	Developed	0.375	68.0	3.0
	CB3D	8	0.375	63.0	Developed	0.375	68.0	3.0

Table F.1 (continued)

Reference	Specimen ID (as stated)	Conf. Type	$\frac{s}{d_b}\sqrt{\frac{f_y}{60}}$	$A_{sh,\text{provided}}$		$A_{sh,\text{provided}}/A_{sh,\text{calculated}}$	
				(width)	(depth)	(width)	(depth)
Paulay and Binney (1974)	316	Full (min. reinf.)	-	-	-	-	-
	317	Diag.	3.80	0.007	0.005	0.450	0.290
	395	Diag.	3.70	0.007	0.005	0.610	0.390
Shiu, Barney, Fiorato, and Corley (1978)	C6	Full	3.70	0.013	0.007	3.90	2.21
	C8	Full	3.90	0.013	0.007	2.93	1.66
Tassios, Moretti and Bezas (1996)	CB-2A	Diag.	5.80	0.014	0.014	1.54	1.54
	CB-2B	Diag.	5.80	0.014	0.014	1.66	1.66
Galano and Vignoli (2000)	P07	Full	15.6	0.004	0.001	0.50	0.16
	P12	Diag.	12.5	0.007	0.007	0.99	0.99
Gonzalez (2001)	K	Diag.	3.60	0.016	0.016	1.12	2.25
Kwan and Zhao (2002)	CCB11	Diag.	8.4	0.023	0.011	2.32	1.16
Canbolat, Parra and Wight (2005)	Specimen 1	Diag.	6.20	0.008	0.008	1.03	1.03
Fortney, Rassati, and Shahrooz (2008)	DCB-1	Diag. (at ends)	3.10	0.015	0.017	1.78	2.09
	DCB-2	Diag.	2.50	0.010	0.012	0.93	1.09
Naish, Fry, Klemencic, and Wallace (2013)	CB24D	Diag.	3.10	0.016	0.022	1.84	2.50
	CB33D	Diag.	3.10	0.016	0.022	1.84	2.50
	CB24F	Full	3.70	0.012	0.011	1.31	1.23
	CB33F	Full	3.70	0.012	0.011	1.31	1.26
	CB24F-RC	Full (with RC slab)	3.70	0.012	0.011	1.23	1.16
	CB24F-PT	Full (with PT slab)	3.70	0.012	0.011	1.24	1.17
	CB24F-1/2-PT	Full (with ½ PT slab)	7.40	0.006	0.005	0.64	0.60
Han, Lee, Shin, and Lee (2015)	SD-2.0	Full	5.50	0.015	0.009	1.95	1.13
	SD-3.5	Full	4.50	0.017	0.018	2.12	2.29
Lim, Hwang, Cheng, and Lin (2016)	CB30-DA	Diag.	4.90	0.005	0.005	0.70	0.70
	CB30-DB	Full	3.30	0.008	0.006	1.13	0.85
Lim, Hwang, Wang, and Chang (2016)	CB10-1	Full	4.30	0.018	0.011	2.69	1.66
	CB20-1	Full	3.70	0.014	0.011	1.55	1.18
Poudel (2018)	CB1A	Full	3.50	0.009	0.009	1.09	1.12
Current study	CB1	Full	3.50	0.009	0.009	1.09	1.12
	CB2	Full	5.80	0.009	0.009	0.91	0.93
	CB2D	Full	5.80	0.009	0.009	1.03	1.07
	CB2AD	Full	5.80	0.009	0.009	1.16	1.20
	CB3D	Full	5.80	0.009	0.009	1.05	1.08

Table F.1 (continued)

Reference	Specimen ID (as stated)	f_{cm} (psi)	$V_{experiment}$ (kips)		$v_{experiment}$ ($\sqrt{f'_c}$, psi)	Chord Rotation (%)		
			-	+		-	+	capacity
Paulay and Binney (1974)	316	4800	124	151	11.7	0.9	6.1	3.5
	317	7350	120	130	8.2	6.2	3.8	5.0
	395	5150	120	146	8.7	1.0	5.8	3.4
Shiu, Barney, Fiorato, and Corley (1978)	C6	2600	13	13	9.8	6.1	6.1	6.1
	C8	3450	6	8	4.8	6.6	6.6	6.6
Tassios, Moretti and Bezas (1996)	CB-2A	4150	54	63	9.8	4.4	4.5	4.4
	CB-2B	3800	30	38	10.2	5.0	5.1	5.0
Galano and Vignoli (2000)	P07	7850	52	56	6.6	4.1	4.1	4.1
	P12	6050	53	56	7.5	2.5	3.9	3.2
Gonzalez (2001)	K	5150	221	206	14.6	6.6	8.2	7.4 [c]
Kwan and Zhao (2002)	CCB11	5500	74	78	9.1	5.3	5.4	5.3
Canbolat, Parra and Wight (2005)	Specimen 1	5950	95	106	7.1	4.0	3.5	3.8 [d]
Fortney, Rassati, and Shahrooz (2008)	DCB-1	5550	124	142	13.7	4.0	4.0	4.0
	DCB-2	8000	90	93	8.7	10.0	10.0	10.0
Naish, Fry, Klemencic,and Wallace (2013)	CB24D	6850	150	159	10.7	8.0	8.0	8.0
	CB33D	6850	118	121	6.7	6.0	7.0	6.5
	CB24F	6850	171	151	11.5	8.0	10.0	9.0
	CB33F	6850	115	124	6.9	8.0	8.0	8.0
	CB24F-RC	7300	190	191	12.4	10.0	10.0	10.0
	CB24F-PT	7250	200	212	13.8	8.0	8.0	8.0
	CB24F-1/2-PT	7000	180	190	12.6	8.0	8.0	8.0
Han, Lee, Shin, and Lee (2015)	SD-2.0	6400	251	245	15.5	5.2	6.2	5.7
	SD-3.5	6400	113	114	12.3	9.9	10.1	10.0
Lim, Hwang, Cheng, and Lin (2016)	CB30-DA	5750	150	151	8.6	8.0	7.7	7.8
	CB30-DB	5550	157	164	9.4	8.0	7.5	7.7
Lim, Hwang, Wang, and Chang (2016)	CB10-1	5000	315	325	23.8	5.8	5.8	5.8
	CB20-1	7600	241	230	11.9	7.3	7.3	7.3
Poudel (2018)	CB1A	6400	244	240	17.5	6.3	6.0	6.2
Current study	CB1	6000	184	182	13.2	6.3	8.0	7.1
	CB2	7200	192	207	13.6	4.5	5.6	5.1
	CB2D	6300	194	204	14.3	5.3	5.3	5.3
	CB2AD	5650	234	228	17.4	5.5	5.1	5.3
	CB3D	6200	268	275	19.4	5.0	6.3	5.6

[c] Average of chord rotation attained in one loading direction and chord rotation corresponding to peak shear force in the other loading direction.

[d] Average of maximum chord rotations attained in two directions, though in one direction shear force was less than 80%.

Table F.1 (continued)

Reference	Specimen ID (as stated)	Axial Restraint	Included in Derivation of Eq. 5.2	
		(Y/N)	(Y/N)	Reasons for Exclusions
Paulay and Binney (1974)	316	N	N	No systematic loading protocol
	317	N	N	No systematic loading protocol
	395	N	N	No systematic loading protocol
Shiu, Barney, Fiorato, and Corley (1978)	C6	N	N	Small scale specimens
	C8	N	N	Small scale specimens
Tassios, Moretti and Bezas (1996)	CB-2A	N	Y	
	CB-2B	N	Y	
Galano and Vignoli (2000)	P07	Y	N	s/d_b more than 6.0
	P12	Y	N	s/d_b more than 6.0
Gonzalez (2001)	K	Y	Y	
Kwan and Zhao (2002)	CCB11	N	N	s/d_b more than 6.0
Canbolat, Parra and Wight (2005)	Specimen 1	N	Y	
Fortney, Rassati, and Shahrooz (2008)	DCB-1	N	N	Diagonal confinement at ends only
	DCB-2	N	Y	
Naish, Fry, Klemencic, and Wallace (2013)	CB24D	N	Y	
	CB33D	N	N	Test was terminated early due to actuator limitations
	CB24F	N	Y	
	CB33F	N	Y	
	CB24F-RC	N	N	Specimen with slab
	CB24F-PT	N	N	Specimen with slab
	CB24F-1/2-PT	N	N	Specimen with slab
Han, Lee, Shin, and Lee (2015)	SD-2.0	Y	N	Stiff axial restraint
	SD-3.5	Y	N	Stiff axial restraint
Lim, Hwang, Cheng, and Lin (2016)	CB30-DA	N	Y	
	CB30-DB	N	Y	
Lim, Hwang, Wang, and Chang (2016)	CB10-1	N	Y	
	CB20-1	N	Y	
Poudel (2018)	CB1A	Y	N	Stiff axial restraint
Current study	CB1	N	Y	
	CB2	N	Y	
	CB2D	N	Y	
	CB2AD	Y	Y	
	CB3D	N	Y	